

**HYSTERETIC BEHAVIOR OF REINFORCED CONCRETE
STRUCTURAL WALLS**

By

**J. M. Vallenias
Research Assistant
Department of Civil Engineering
University of California, Berkeley**

**V. V. Bertero
Professor of Civil Engineering
Department of Civil Engineering
University of California, Berkeley**

and

**E. P. Popov
Professor of Civil Engineering
Department of Civil Engineering
University of California, Berkeley**

**Report to Sponsor:
National Science Foundation**

**Report No. UCB/EERC-79/20
Earthquake Engineering Research Center
College of Engineering
University of California
Berkeley**

August 1979

BIBLIOGRAPHIC DATA SHEET	1. Report No. NSF/RA-790350	2.	3. Recipient's Accession No. PB 80 165905	
4. Title and Subtitle Hysteretic Behavior of Reinforced Concrete Structural Walls			5. Report Date August 1979	
7. Author(s) J. M. Vallenias, V. V. Bertero, E. P. Popov			8. Performing Organization Rept. No. UCB/EERC-79/20	
9. Performing Organization Name and Address Earthquake Engineering Research Center University of California, Richmond Field Station 47th and Hoffman Blvd. Richmond, California 94804			10. Project/Task/Work Unit No. 0-21198	
12. Sponsoring Organization Name and Address National Science Foundation 1800 G Street, N.W. Washington, D.C. 20550			11. Contract/Grant No. EN76-04263	
15. Supplementary Notes			13. Type of Report & Period Covered	
16. Abstracts <p>The problem of understanding and modeling the behavior of reinforced concrete structural walls subjected to high shear earthquake loading conditions is studied. Results of eight earthquake simulation tests on 1/3 scale structural R/C wall subassemblage model specimens are presented.</p> <p>The prototypes were ten and seven-story buildings designed to current code provisions. Details of the test set up, the models tested, and the test procedure are summarized. The main experimental results are evaluated in terms of the hysteretic characteristics (strength, deformation, and energy dissipation capacity), the modes of failure, ease of construction, and effectiveness of repair.</p> <p>The parameters studied were: type of confinement in the boundary elements (hoop vs. spiral); wall cross-section (rectangular vs. framed where the boundary elements protrude from the surface of the wall); moment-to-shear ratios; monotonic and cyclic load programs; and repair procedures. Excellent behavior was obtained in well designed R/C structural walls. Slender walls with rectangular cross-section were found to have problems with out-of-plane stability.</p> <p>The analytical work included modeling of the wall behavior under monotonic loading and high shear conditions. The models developed included a breakdown of the overall deformation into three components: flexural, shear, and fixed end deformations. The possibility of extending these models to the case of cyclic loading is investigated.</p> <p>Present code design methods for walls are assessed, the seismic-resistant design implications of the results are discussed, and areas of further study are recommended.</p>			14.	
17b. Identifiers/Open-Ended Terms				
17c. COSATI Field Group				
18. Availability Statement Release Unlimited			19. Security Class (This Report) UNCLASSIFIED	21. No. of Pages
			20. Security Class (This Page) UNCLASSIFIED	22. Price

ABSTRACT

The problem of understanding and modeling the behavior of reinforced concrete structural walls subjected to high shear earthquake loading conditions is studied. Results of eight earthquake simulation tests on 1/3 scale structural R/C wall subassembly model specimens are presented.

The prototypes were ten and seven-story buildings designed to current code provisions. Details of the test set up, the models tested, and the test procedure are summarized. The main experimental results are evaluated in terms of the hysteretic characteristics (strength, deformation, and energy dissipation capacity), the modes of failure, ease of construction, and effectiveness of repair.

The parameters studied were: type of confinement in the boundary elements (hoop vs. spiral); wall cross-section (rectangular vs. framed where the boundary elements protrude from the surface of the wall); moment-to-shear ratios; monotonic and cyclic load programs; and repair procedures. Excellent behavior was obtained in well designed R/C structural walls. Slender walls with rectangular cross-section were found to have problems with out-of-plane stability.

The analytical work included modeling of the wall behavior under monotonic loading and high shear conditions. The models developed included a breakdown of the overall deformation into three components: flexural, shear, and fixed end deformations. The possibility of extending these models to the case of cyclic loading is investigated.

Present code design methods for walls are assessed, the seismic-resistant design implications of the results are discussed, and areas of further study are recommended.

ACKNOWLEDGMENTS

This report is based on the dissertation written by J. M. Vallenias, under the direct supervision of Professors V. V. Bertero and E. P. Popov, as partial fulfillment of the requirements for the degree of Doctor of Philosophy in Engineering.

The research reported herein was sponsored by the National Science Foundation under Grant No. EN76-04263, sub-project No. 0-21198. The tests were conducted in the Structural Engineering Laboratory of the Department of Civil Engineering, University of California, Berkeley.

The authors would like to express their gratitude to O. Hald, Professor of Mathematics, for being part of the dissertation committee. Thanks also to B. Lotz and D. Clyde who constructed the test specimens, the staff of the Davis Hall Structural Laboratory, M. Lamoroux who reduced the photogrammetric data, and L. Tsai and M. C. Randall who provided editorial assistance.

TABLE OF CONTENTS

	<u>Page</u>
ABSTRACT	iii
ACKNOWLEDGMENTS	v
TABLE OF CONTENTS	vii
LIST OF TABLES	xi
LIST OF FIGURES	xiii
1. INTRODUCTION	1
1.1 General Remarks	1
1.1.1 State of the Art in the Modeling of Material Properties	1
1.1.2 State of the Art in the Modeling of Behavior Mechanisms for Structural Walls	2
1.1.3 State of the Practice in the Design of Structural Walls	3
1.2 Objectives and Scope	4
1.2.1 Objectives of the Experimental Research Program	4
1.2.2 Analytical	5
2. TEST SPECIMENS	7
2.1 Prototype Buildings	7
2.2 Design of Prototype Buildings	7
2.2.1 Ten-Story Prototype	7
2.2.2 Seven-Story Prototype	8
2.3 Selection of Test Specimens	12
2.4 Mechanical Characteristics of Materials	12
2.4.1 Steel	12
2.4.2 Concrete	12
2.5 Fabrication of Specimens	13
2.6 Repair and Strengthening of Specimens	13
3. LOADING CONDITION OF WALL SPECIMENS, EXPERIMENTAL SET UP, AND TEST PROCEDURE	15
3.1 General	15
3.2 Parameters Contributing to Shear Failure	15
3.3 Critical Loading Condition of Walls	15
3.4 General Set up	16
3.5 Specimen Instrumentation and Data Acquisition System	16
3.6 Testing Procedure and Loading Sequence	16
4. EXPERIMENTAL RESULTS	17
4.1 General	17
4.2 Free Vibration Tests	17
4.3 Pseudo Static Tests	18
4.3.1 Virgin Framed Wall Subjected to Monotonic Loading (Specimen 3)	18

4.3.2	Framed Wall Subjected to Cyclic Loading (Specimen 4)	19
4.3.3	Repaired Framed Wall Subjected to Monotonic Loading (Specimen 4R)	20
4.3.4	Repaired Framed Wall Subjected to Cyclic Loading (Specimen 3R)	21
4.3.5	Virgin Rectangular Wall Subjected to Monotonic Loading (Specimen 5)	22
4.3.6	Virgin Rectangular Wall Subjected to Cyclic Loading (Specimen 6)	24
4.3.7	Repaired Rectangular Wall Subjected to Monotonic Loading (Specimen 6R)	24
4.3.8	Repaired Rectangular Wall Subjected to Cyclic Loading (Specimen 5R)	25
4.4	Photogrammetric Readings	26
4.4.1	Accuracy	26
4.4.2	Results	27
5.	EVALUATION OF EXPERIMENTAL RESULTS	29
5.1	Overall Hysteretic Behavior	29
5.1.1	Strength	29
5.1.2	Stiffness	33
5.1.3	Deformations of Structural Wall Specimens	37
5.1.4	Energy Absorption and Dissipation Capacity of Specimens	41
5.2	Failure Mechanisms	44
5.2.1	General	44
5.2.2	Buckling Mechanisms	44
5.2.3	Shear Failure Mechanisms	50
5.2.4	Failure of Repaired Specimens	51
5.3	Effect of Test Parameters on Overall Behavior	52
5.3.1	Wall Cross-Section	52
5.3.2	Confinement of Boundary Element	53
5.3.3	Loading Histories	54
5.3.4	Repair Procedure	55
6.	ANALYTICAL MODELING OF WALL BEHAVIOR	57
6.2	Tip Displacement Component Because of Flexural Deformations	57
6.2.1	Introduction	57
6.2.2	Solution Approach	58
6.2.3	Analytical Results	60
6.2.4	Cyclic Loading	61
6.3	Tip Displacement Component Because of Shear Deformations	62
6.3.1	Introduction	62
6.3.2	Analytical Solution for Monotonic Loading Based on a Simplified Model	63
6.3.3	Analytical Solution for Monotonic Loading of Rectangular Wall	69
6.3.4	Shear Deformations Under Cyclic Loading	71
6.4	Tip Displacement Component Because of Fixed End Deformations	74
6.4.1	Introduction	74
6.4.2	Solution Procedure	74

6.5	Evaluation of Analytical Results for Overall Force Deformation Relations	77
7.	CONCLUSIONS AND RECOMMENDATIONS	79
7.1	Conclusions	79
7.1.1	Main Parameters Controlling Seismic Behavior	79
7.1.2	Factors Affecting the Parameters that Control Seismic Behavior	81
7.1.3	Effect of Repair Technique	83
7.1.4	Effect of Moment-to-Shear Ratio	83
7.2	Implications of Results Obtained in Seismic Resistant Design	83
7.2.1	Evaluation of Critical Load Condition	83
7.2.2	Design Criteria	83
7.2.3	Selection of Wall Cross Section (Minimum Dimensions)	84
7.3	Recommendations for Future Research	84
7.3.1	Experimental	84
7.3.2	Analytical	84
	REFERENCES	87
	TABLES	93
	FIGURES	111
	LIST OF EERC REPORTS	235

LIST OF TABLES

<u>Table</u>		<u>Page</u>
2.1	Estimated Weight of Seven-Story Prototype Building	95
2.2	Specimen Types and Their Main Characteristics	96
2.3	Mechanical Characteristics of Materials	97
2.4	Concrete Mix Proportions	98
4.1	Shear Wall Tests	99
4.2	Experimental Frequencies and Damping Values for Structural Wall Models .	100
5.1	Strengths of Specimens (kN)	101
5.2	Comparison of Specimen Strengths	102
5.3	Curvatures	103
5.4	Secant Stiffness (MN/mm)	103
5.5	Secant Stiffness Components at First Yield (MN/mm)	104
5.6	Contribution of Different Sources of Lateral Deformation at Third-Floor Level	104
5.7	Story Drift Index R_i	105
5.8	Strength and Deformation Comparison for Virgin and Repaired Walls	106
6.1	Comparison of Experimental and Analytical Results for Flexural Deformation Models (Specimen 3)	107
6.2	Comparison of Predicted and Observed V_f Values	108
6.3	Comparison of Experimental and Analytical Results for Overall Deformations (Specimen 3)	109

LIST OF FIGURES

<u>Figure</u>	<u>Page</u>
2.1 Ten-Story Prototype Building	113
2.2 Seven-Story Prototype Building	113
2.3 Shear and Moment Diagram of Single N-S Wall of Ten-Story Building When Subjected to half of 1.4E and to 1.4 (Torsion) Code Forces	114
2.4a Dimensions and Details of Framed-Wall Specimens	114
2.4b Detailed Cross-Section of Framed Wall	115
2.5 Shear and Moment Diagrams of a Single N-S Wall of Seven-Story Building When Subjected to half of 1.4E and to 1.4 (Torsion) Code Forces	115
2.6a Dimensions and Details of Rectangular Specimens	116
2.6b Detailed Cross-Section of Rectangular Wall	116
2.7 Tensile Stress-Strain Diagram for Gage No. 7 Wire	117
2.8 Tensile Stress-Strain Diagram for No. 2 Reinforcing Bar	117
2.9 Tensile Stress-Strain Diagram for No. 5 Reinforcing Bar	118
2.10 Tensile Stress-Strain Diagram for No. 6 Reinforcing Bar	118
2.11 Tensile Stress-Strain Diagram for No. 7 Reinforcing Bar	119
2.12 Tensile Stress-Strain Diagram for No. 8 Reinforcing Bar	119
2.13 Tensile and Compressive Stress-Strain Diagrams for Machined No. 6 Reinforcing Bars	120
2.14 Typical Compressive Stress-Strain Diagram for Concrete Test Cylinders	120
2.15 Framed Walls During Construction	121
2.16 Reinforcement for Panel and Boundary Elements of Rectangular Wall	121
2.17 Dowels for Repair of First-Story Panel in Framed Wall Specimen	122
2.18 Buckled Wall Reinforcement During Repair Procedure	122
2.19 Framed Wall After Removal of Damaged Concrete and Placement of New Steel Reinforcement	122
2.20 Repaired Walls	123
3.1 Loading Conditions of Prototype and Model of Framed Wall for Ten- Story Building	124
3.2 Loading Conditions of Prototype and Model of Rectangular Wall for Seven-Story Building	125
3.3 Plan and General View of Testing Facility	126
3.4 External Instrumentation	127
3.5 Internal Instrumentation	127
3.6 Photogrammetric Reference Grid for Framed Walls	128
3.7 Photogrammetric Reference Grid for Rectangular Walls	128
4.1 Load Program for Framed Wall (Monotonic Loading) Specimen 3	129
4.2 Displacement at Third Floor of Framed Wall (Monotonic Loading) Speci- men 3	130
4.3 Displacement at Third Floor of Framed Wall (Monotonic Loading) Due to Shear Deformation, Specimen 3	130

4.4	Displacement at Third Floor of Framed Wall (Monotonic Loading) Due to Flexural Deformation, Specimen 3	131
4.5	Displacement at Third Floor of Framed Wall (Monotonic Loading) Due to Fixed-End Deformation, Specimen 3	131
4.6	Sequence of Crack Formation up to $\mu=1$, Specimen 3	132
4.7	Concrete Cover Spalling and Buckling in North Column, Specimen 3	132
4.8	Tension Cracks in South Panel and Column, Specimen 3	133
4.9	Buckling of South Column, Specimen 3	134
4.10	Views of Buckled South Column, Specimen 3	135
4.11	Second Panel at Conclusion of Test, Specimen 3	135
4.12	Displacement Component Diagrams	136
4.13	Load Program for Framed Wall (Cyclic Loading), Specimen 4	137
4.14	Displacement at Third Floor of Framed Wall (Cyclic Loading), Specimen 4	138
4.15	Displacement at Third Floor of Framed Wall (Cyclic Loading) Due to Shear Deformation, Specimen 4	138
4.16	Displacement at Third Floor of Framed Wall (Cyclic Loading) Due to Flexural Deformation, Specimen 4	139
4.17	Displacement at Third Floor of Framed Wall (Cyclic Loading) Due to Fixed-End Deformation, Specimen 4	139
4.18	Sequence of Crack Propagation, Specimen 4	140
4.19	Cracking at $\mu=2$, Specimen 4	140
4.20	Development of Failure Mechanism, Specimen 4	141
4.21	Specimen 4 After Failure	142
4.22	Displacement Components Diagram, Specimen 4	142
4.23	Load Program for Repaired Framed Wall (Monotonic Loading), Specimen 4R	143
4.24	Displacement at Third Floor of Repaired Framed Wall (Monotonic Loading), Specimen 4R	144
4.25	Displacement at Third Floor of Repaired Frame Wall (Monotonic Loading) Due to Shear Deformation, Specimen 4R	144
4.26	Displacement at Third Floor of Repaired Framed Wall (Monotonic Loading) Due to Flexural Deformation, Specimen 4R	145
4.27	Displacement at Third Floor of Repaired Framed Wall (Monotonic Loading) Due to Fixed-End Deformation, Specimen 4R	145
4.28	Specimen 4R at Initiation of Test	146
4.29	Sequence of Crack Propagation for First-Floor Panel, Specimen 4R	147
4.30	Rupture of Tension Reinforcement at Top of First-Floor Columns, Specimen 4R	148
4.31	Specimen 4R After Failure	148
4.32	Displacement Components Diagram at Third-Floor, Specimen 4R	148
4.33	Load Diagram for Repaired Framed Wall (Cyclic Loading), Specimen 3R	149
4.34	Displacement at Third Floor of Repaired Frame Wall (Cyclic Loading), Specimen 3R	150

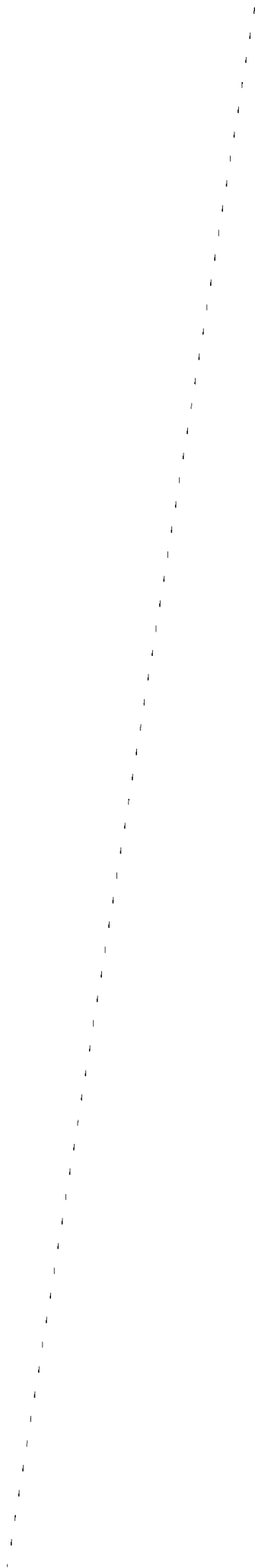
4.35 Displacement at Third Floor of Repaired Framed Wall (Cyclic Loading) Due to Shear Deformation, Specimen 3R	150
4.36 Displacement at Third Floor of Repaired Framed Wall (Cyclic Loading) Due to Flexural Deformation, Specimen 3R	151
4.37 Specimen 3R at Initiation of Test	151
4.38 Cracking at $\mu=1$, Specimen 3R	152
4.39 Cracking at $\mu=1$, Specimen 3R	152
4.40 Crack Between Third Floor Slab and Top of North Column, Specimen 3R	153
4.41 Cracking of Second Story Panel, Specimen 3R	153
4.42 Failure of Specimen 3R	154
4.43 Views of Failure at North Column Slab Connection	154
4.44 Displacement Components Diagram, Specimen 3R	155
4.45 Load Program for Rectangular Wall (Monotonic Loading), Specimen 5	156
4.46 Displacement at Third Floor of Rectangular Wall (Monotonic Loading), Specimen 5	157
4.47 Displacement at Third Floor of Rectangular Wall (Monotonic Loading) Due to Shear Deformation, Specimen 5	157
4.48 Displacement at Third Floor of Rectangular Wall (Monotonic Loading) Due to Flexural Deformation, Specimen 5	158
4.49 Displacement at Third Floor of Rectangular Wall (Monotonic Loading) Due to Fixed-End Deformation, Specimen 5	158
4.50 Sequence of Crack Propagation, Specimen 5	159
4.51 Buckling of Longitudinal Reinforcement at Base of North Column, Specimen 5	159
4.52 South Column Initiation of Buckling, Specimen 5	159
4.53 Flexural Shear Crack, Specimen 5	160
4.54 Displacement Components Diagram, Specimen 5	161
4.55 Load Program for Rectangular Wall (Cyclic Loading), Specimen 6	162
4.56 Displacement at Third Floor of Rectangular Wall (Cyclic Loading), Specimen 6	163
4.57 Displacement at Third Floor of Rectangular Wall (Cyclic Loading) Due to Shear Deformation, Specimen 6	163
4.58 Displacement at Third Floor of Rectangular Wall (Cyclic Loading) Due to Flexural Deformation, Specimen 6	164
4.59 Displacement at Third Floor of Rectangular Wall (Cyclic Loading) Due to Fixed-End Deformation, Specimen 6	164
4.60 Initial Cracking of Rectangular Wall (Cyclic Loading), Specimen 6	165
4.61 Crack Pattern at $\mu=3$ for Rectangular Wall (Cyclic Loading), Specimen 6	165
4.62 Buckling at Base of North Column, Specimen 6	165
4.63 Displacement Components Diagram, Specimen 6	166
4.64 Load Program for Repaired Rectangular Wall (Monotonic Loading), Specimen 6R	167
4.65 Displacement at Third Floor of Repaired Rectangular Wall (Monotonic Loading), Specimen 6R	168

4.66	Displacement at Third Floor of Repaired Rectangular Wall (Monotonic Loading) Due to Shear Deformation, Specimen 6R	168
4.67	Displacement at Third Floor of Repaired Rectangular Wall (Monotonic Loading) Due to Flexural Deformation, Specimen 6	169
4.68	Specimen 6R at Initiation of Test	169
4.69	Crack Sequence for First-Floor Panel, Specimen 6R	170
4.70	Main Crack in First Floor Panel, Specimen 6R	170
4.71	Crack Sequence for First Floor Panel When Loaded to the North, Specimen 6R	171
4.72	Displacement Component Diagram, Specimen 6R	171
4.73	Load Program for Repaired Rectangular Wall (Cyclic Loading), Specimen 5R	172
4.74	Displacement at Third Floor of Repaired Rectangular Wall (Cyclic Loading), Specimen 5R	173
4.75	Displacement at Third Floor of Repaired Rectangular Wall (Cyclic Loading) Due to Shear Deformation, Specimen 5R	173
4.76	Displacement at Third Floor of Repaired Rectangular Wall (Cyclic Loading) Due to Flexural Deformation, Specimen 5R	174
4.77	Crack Formation Sequence, Specimen 5R	174
4.78	Crack Formation Interfering with Reading of Linear Potentiometers, Specimen 5R	175
4.79	Failure of Specimen 5R	175
4.80	Displacement Components Diagram, Specimen 5R	175
4.81	Deformation Pattern of First Story, Specimen 3	176
4.82	Deformation Pattern of First Story, Specimen 4	176
4.83	Deformation Pattern of First Story, Specimen 4R	178
4.84	Deformation Pattern of First Story, Specimen 5	178
4.85	Deformation Pattern of First Story, Specimen 6	179
4.86	Deformation Pattern of First Story, Specimen 6R	180
4.87	Deformation Pattern of First Story, Specimen 5R	181
5.1	Cross Section of Walls Considered for Analytical Prediction of $M-\phi$ Relationship	182
5.2	Concrete Stress-Strain Relationship Considered for Analytical Prediction of $M-\phi$ Relationship	182
5.3	Comparison of Experimental and Analytical Curves for Specimen 3	183
5.4	Comparison of Experimental and Analytical Curves for Specimen 5	183
5.5	Position of Neutral Axis Under Monotonic Loading, Specimen 3	184
5.6	Reverse Shear Capacity of Deep Beams	184
5.7	Load Distribution on Rectangular Wall	185
5.8	Initial Stiffness, Specimen 3	186
5.9	Initial Stiffness, Specimen 5	186
5.10	Story Drift Geometry	187

5.11	Effect of Diagonal Crack	187
5.12	Curvature Distribution at Initiation of Yielding, Specimen 3	188
5.13	Curvature Distribution, Specimen 3	189
5.14	Curvature Distribution, Specimens 4, 5, and 6	190
5.15	Effect of Fixed-End Rotation on Tip Displacement	191
5.16	Energy Absorption Diagrams	191
5.17	Comparison of Energy Dissipation for Different Specimens	193
5.18	Concrete Strain at Base of North Column (Gage C1), Framed Wall (Monotonic Loading), Specimen 3	194
5.19a	Cross Section of Rectangular Boundary Element	194
5.19b	Stability Failure Due to Asymmetric Cover Spalling	195
5.20a	Load and Displacement Histories for the Last Three Cycles at Ductility Four and Buckling, Specimen 6	196
5.20b	Strain Histories	196
5.20c	Clip Gage Location	196
5.21	Average Strain Distribution Along South Column, Specimen 3	197
5.22	Crack Spacing	198
5.23	Effective Compressive Section for Boundary Element of Specimen 3 at LP 80	198
5.24	Average Stress-Strain History for Steel in South Boundary Element of Specimen 3	199
5.25	Shear Slippage at Crack	199
5.26	Variation of Axial Force Components and Crack Width Along South Boundary Element at LP 81, Specimen 3	200
5.27	Comparison of $V-\delta_3$ Diagrams for Specimens 1 and 3	201
5.28	Transverse Hoops in Critical Regions of Panel	201
5.29	Development of Crushing Band	202
5.30	Strain History for Gage W31, Specimen 4	203
5.31ab	Curvature Distribution at Maximum Displacement	203
5.31cd	Curvature Distribution at LP 151	204
5.32	Rotational Ductility Demand in Repaired Walls	204
5.33	Comparison of $V-\delta_3$ Diagrams for Specimens 1, 4, and 3	204
5.34	Comparison of $V-\delta_3$ Diagrams	205
5.35	Confinement Arrangements for Boundary Elements of Structural Walls	206
5.36	Comparison of $V-\delta_3$ Diagrams, Specimens 5 and 6	207
5.37	Comparison of $V-\delta_3$ Diagrams, Specimens 4 and 3R	207
5.38	Comparison of $V-\delta_3$ Diagrams, Specimens 3 and 4R	208
5.39	Comparison of $V-\delta_3$ Diagrams, Specimens 4 and 4R	209
5.40	Comparison of $V-\delta_3$ Diagrams, Specimens 5 and 6R	209
5.41	Comparison of $V-\delta_3$ Diagrams, Specimens 6 and 5R	209
5.42	Comparison of $V-\delta_3$ Diagrams, Specimens 6 and 6R	210

6.1	Finite Element Modelling of Framed Wall for Monotonic Loading	211
6.2	Idealized Cyclic Stress-Strain Curve for No. 6 and No. 2 Steel Bars	212
6.3	Stress-Strain Diagram for Confining Reinforcement (Gage No. 7 Wire)	212
6.4	$\frac{f_c}{f_c'}$ vs. ϵ_L for Boundary Element	213
6.5	$\frac{f_c}{f_c'}$ vs. ϵ_L for Boundary Element	213
6.6	$\frac{f_c}{f_c'}$ vs. ϵ_L for Plain Concrete	214
6.7	Tensile Softening	214
6.8	Effect of Different Assumptions on $M-\delta$ Relation for Specimens	215
6.9a	Analytical Force-Displacement Curve, Specimen 3	215
6.9b	Experimental Force-Displacement Curve, Specimen 3	216
6.10	Comparison of Experimental and Analytical Flexural Displacement Component, Specimen 3	216
6.11a	Crack Pattern Analytical Prediction, Specimen 3	217
6.11b	Experimentally Obtained Crack Pattern, Specimen 3	217
6.12	Finite Element Modelling of Framed Wall for Displacement-Controlled Cyclic Loading	218
6.13	Comparison of Experimental and Analytical Flexural Deformations, Specimen 4	218
6.14	Concrete Failure Surface in Three-Dimensional Stress Space	219
6.15	Kinking Action in Panel Steel	219
6.16	Internal Shear Resisting Mechanisms	220
6.17a	Comparison of Experimental and Analytical Third-Floor Displacement Due to Shear Deformations, Specimen 3	221
6.17b	Comparison of Experimental and Analytical First-Floor Displacements Due to Shear Deformations, Specimen 3	221
6.18a	Idealized Crack Pattern and Shear Deformation of Cracked Wall	222
6.18b	Shear Deformation (Before Yield)	222
6.18c	Williot's Diagram	222
6.19a	Shear Deformation for First-Story Framed Wall (Monotonic Loading), Specimen 3	223
6.19b	Shear Deformation for Second-Story Framed Wall (Monotonic Loading), Specimen 3	223
6.20	Flexural Displacement at First-Floor of Framed Wall (Monotonic Loading), Specimen 3	224
6.21	Shear-Yielding Mechanism	224
6.22	Comparison of Shear Stiffness (Third-Floor Displacement), Specimen 5	225
6.23	Hysteretic Rule for Cyclic Shear Deformations	225
6.24	Schematic Deformations of Panel with Open Diagonal Cracks	227
6.25	Shear Deformation for First-Story Framed Wall (Cyclic Loading), Specimen 4	227

6.26 Comparison of Experimental and Analytical Cyclic Shear Displacements, Specimen 4	228
6.27 Displacement Due to Fixed-End Deformations	228
6.28 Embedment Conditions for Longitudinal Reinforcement in the Foundation	229
6.29 Determination of Tip Displacement Due to Fixed-End Rotations	230
6.30 Comparison of Experimental and Analytical Fixed-End Deformation Curves, Specimen 3	231
6.31a Comparison of Strain Distribution Curves for Ref. 20 and Present Investigation	231
6.31 Bond Stress Distribution for No. 6 Bar, Ref. 20	232
6.32 Idealized Stress-Strain Distribution Along Embedded Bar for $\epsilon_s^o > \epsilon_s^y$	233
6.33 Comparison of Experimental/Analytical Results for Overall Deformations	234
7.1 Cracking Idealization	234



1. INTRODUCTION

1.1. General Remarks

Efficient design of earthquake resistant structures requires a good scientific background, experience, and judgment on the part of engineers. The structural engineer must design for both serviceability and safety and, at the same time, satisfy architectural demands as well as economic restraints.

It is widely recognized [1,2,3] that seismic code provisions underestimate the forces that can be introduced in a relatively rigid structure by a severe earthquake motion. A rational design is not always a straight forward task. Some of the biggest problems the engineer faces when trying to make a rational design are the uncertainties regarding the nature and magnitude of seismic disturbances, the characteristics of building materials, the workmanship involved in construction, and the realistic behavior of structures. Furthermore the magnitude (intensity) of forces that can be developed during a severe earthquake ground motion are so high that they make it economically unfeasible to design structures that will remain elastic under all circumstances. It is then necessary to place reliance on the behavior of structures in their inelastic range. Designers should take advantage of the potential ductility, energy absorption, and dissipation capacities of structural members for the building to survive major ground motions.

The current state of knowledge in inelastic design indicates that three fundamental characteristics are required for the satisfactory behavior of a structure: stiffness, strength, and stable hysteretic behavior with large energy dissipation capacity (large ductility under stable strength and stiffness). In medium to high rise reinforced concrete buildings, these desirable characteristics can be efficiently obtained by using combinations of structural walls with space frames.

Structural walls can provide structures under service loading with sufficient stiffness, minimizing deformations and damage to nonstructural elements. Under severe excitations, they can provide sufficient strength, energy absorption, and dissipation capacities to prevent collapse and loss of life. Despite considerable progress in earthquake engineering in the last few decades, there are still many uncertainties in the prediction of the mechanical behavior of structures under severe seismic actions, particularly in the case of wall-frame reinforced concrete structural systems.

In order to carry out an adequate inelastic design of wall-frame R/C structural systems, it is necessary to estimate the earthquake energy input and then understand the manner in which the system absorbs and dissipates this energy. It is also necessary to estimate the deformation, energy absorption, and energy dissipation capacities of the structural system. Ideally all these should be achieved by using basic principles of solid mechanics, starting from the mechanical behavior of the structural materials. However with the present state of knowledge these are not yet possible to achieve with the reliability and accuracy desired. Further experimental and analytical work is required to improve such knowledge.

1.1.1. State of the Art in the Modeling of Material Properties

The complete load-deformation behavior of concrete under stresses and strains that can be developed under earthquake excitations is not clearly understood. Concrete is a non-linear, strain-softening, discrete cracking material. Its properties change with the state of stress, strain-rate and age [4].

Moreover, in order to obtain good hysteretic behavior (strength, ductility, and energy dissipation) in earthquake resistant structures, it is necessary to reinforce and confine the concrete. The use of confined reinforced concrete involves understanding the behavior of reinforcing steel, the behavior of confined concrete, the mechanisms of bond between concrete and steel [5,6], and the behavior of cracked concrete, especially in regards to the shear transfer at the cracks (aggregate interlock and dowel action). The mechanical characteristics of confined

concrete subjected to axial monotonic loading has been studied [7,8,9.], but more work is needed in this area, particularly on the effect of cyclic load reversals, use of different materials, i.e. light-weight aggregate, and different confinement arrangements.

Some promising attempts have been made to formulate general constitutive relations for concrete [10] using the endochronic theory of inelasticity and failure introduced by Valanis [11] although its extension to problems of cyclic loading and high shear must await further development.

In recent years the search for a constitutive relation for steel has received a good deal of attention [6,12,13,14,15,16]. For most practical purposes, both monotonic and random cyclic stress-strain relations for reinforcing steel can be sufficiently and accurately formulated.

The bond-slip of reinforcing steel and concrete requires further investigation, particularly as it applies to cyclic loading. A review of the relevant work to date was done by Popov [6] , who also recommended further studies on a number of parameters, including load rate, history of loading, bar deformation patterns, and others.

Recent experimental work in this area [17,18,19,20,21,22] and subsequent empirical formulae shed some light on this matter, and further progress is expected.

1.1.2. State of the Art in the Modeling of Behavior Mechanisms for Structural Walls

The current state of knowledge in the mechanical characteristics of the three elements concrete, steel, and bond slip, is reflected in the progress achieved in the modeling of the deformational behavior for structural walls.

The flexural behavior of R/C members has been modeled with reasonable accuracy for monotonic loading and low shear stresses, assuming linear variations of strain along a section and idealized stress-strain curves for steel and concrete [1,23,24,25]. The implementation of these results under high shear conditions and in predicting moment-curvature relations under load reversals has some limitations. Diagonal cracking under high shear conditions causes a redistribution of stresses that affects the curvature distribution along the wall. This generally causes an increase in the flexural deformations with respect to those obtained in a similar specimen subjected to the same flexural moment, but much lower shear stresses. While this effect has been observed by other researchers, it has not been accounted for analytically.

As is discussed in detail in Refs. [1,24], in the case of flexural structural elements subjected to high shear because of residual tensile cracks, when the load is reversed there is a temporary reduction in the moment of inertia. This leads to a decrease in stiffness and a pinching effect is observed in the moment-curvature diagrams. This effect starts to disappear when, after increasing the load, the cracks gradually close. Shear slippage in the direction parallel to the crack plane causes the irregular crack surfaces to contact. This in turn causes an increase in the flexural stiffness over that predicted by certain analytical models that have attempted to include the effect of crack opening in predicting the observed reduced stiffness. The possibility of stability problems because of wall slenderness and reinforcement detailing must be considered. Such problems are particularly likely in the case of damaged structures where large residual tensile cracks in the concrete and Bauschinger effects on the reinforcement cause a reduction in the effective EI of the region that could result in instability.

The problem of determining the effects of flexure in the shear resistance and shear deformations remains a difficult one. Opening of flexural cracks causes a significant drop in the contribution of concrete to shear stiffness and strength. Because of the large number of flexural cracks, and the jaggedness of the crack surfaces, this effect is hard to quantify analytically. The interaction of flexural and shear mechanisms, the effect of bond on cracking, aggregate interlocking and dowel actions, and the effect of reversals must all be considered in a complete model [24].

The deformational behavior of walls with a dominant shear mechanism has been modeled for monotonic loading by a finite element program developed by Wang, et al., accounting for tensile cracking [1]. Although reasonable agreement is observed in the initial

portion of the force-deformation diagram before yield, the latter portion indicates an overestimation of the strength and an underestimation of the deformation.

Ma, et al. [24] developed a model capable of adequately predicting the shear degradation which occurred at the initiation of load reversals at a displacement ductility of one, but was not able to account for the degradation of the shear resistance elements, i.e. aggregate interlocking, tie resistance across cracks, and dowel action of the main bars, at larger displacement ductilities. Bazant and Bhat [26] have applied the newly developed endochronic theory of concrete for predicting moment rotation and force deformation curves with promising results. They accounted for the shear strains producing volume dilatancy and transverse stresses and strains, and they used a fixed shear transfer factor α (originally introduced by Suidan and Schnobrich [27]). It is questionable, however, whether this assumption can be applied successfully to predicting behavior of elements under high shear.

Cervenka and Gerstle [28] and Darwin and Pecknold [29] have also used the nonlinear finite element approach to study the behavior of R/C structures. They have obtained good analytical agreement with the experimental results for two shear panels whose behavior was controlled by tensile steel. Their results show the importance of modeling the axial stress-strain behavior of steel and concrete, and the need to account for the concrete tension cracking. Further studies are needed before the results can be applied under high shear conditions.

1.1.3 State of the Practice in the Design of Structural Walls

In designing structural walls the designer needs to know which is the maximum possible shear that can be developed, and what is the pattern of seismic forces that causes the maximum shear-moment ratio. The designer also needs to know which are the critical regions so as to avoid the premature flexural behavior deterioration and failure due to shear.

In determining the shear force the UBC-73 code [30] uses the expression:

$$V = ZKCW \quad (1.1)$$

where:

V is the base shear for the structure, Z is the seismic zone coefficient, C is a numerical coefficient specified in Section 2312 (d) of the code, W is the total dead load as defined in Section 2301 of the UBC, and K is a numerical coefficient as specified in Table No. 23-1 of the code, as a function of the type and arrangement of the resisting elements.

The K coefficient was introduced in the 1959 SEAC recommendations [31]. The value of K ranges from 0.67 to 1.33, as a function of the available ductility of the structural system. All other things remaining equal the code specifies that: a framed structure satisfying requirements for ductile moment-resisting frames will have to be designed for a base shear computed on the basis of $K = 0.67$; a dual frame-wall structure will have to be designed for $K = 0.8$; and a box structure is required to be designed for $K = 1.33$ which is a 100% increase over the base shear specified for a ductile moment-resisting space frame structure. The SEAOC recommendations [31] justify these K values stating that shear walls lack high ductility. As shown in Ref. [1], structural wall systems can develop large ductilities, comparable to those in framed structures. Furthermore, the nonlinear behavior of structural wall systems is better than that of framed structures, where partial collapse mechanisms can take place with the energy being absorbed by only a few hinges. A wall-frame system, on the other hand, properly designed, can offer much more energy absorption capacity.

While the 1976 UBC code [32], and the 1974 SEAOC [33] maintain the same values of K set in the 1959 SEAOC [31], the new ATC recommendations [34] present some change. The design base shear is specified as:

$$V = C_s W \quad (1.2)$$

where C_s is a factor which is a function of, among other things, $1/R$. The ATC specifies a value of $R = 8$ for wall-frame systems, $R = 7$ for ductile space frames and $R = 4.5$ for bearing wall

systems where the lateral resistance is provided by reinforced concrete shear walls. In other words, the ATC recommendation (which have not been introduced in the codes yet) imply a better seismic performance for wall-frame systems than that of reinforced concrete ductile space frames, but consider box systems to have a relatively poor nonlinear seismic performance.

As mentioned before, it is widely recognized [1,2,3] that seismic code provisions underestimate the forces that can be introduced in a relatively rigid structure by a severe earthquake motion. This fact, together with the desire to prevent structural failure, dictates the need to provide structural walls with a shear capacity greater than the maximum shear that could be developed with the available moment capacity. For this reason, it is most important to determine as accurately as possible, or at least in an approximate but conservative manner, the flexural capacity of the critical wall cross-section and the effective shear span of the forces acting on the wall.

The codes tend to underestimate the sections' flexural strength by: using specified strengths of materials, a reduction factor $\phi=0.90$, neglecting the increase in steel strength because of strain hardening and the actual concrete strength which is generally higher than the specified f'_c .

The M/V ratio, computed according to the code assumptions (which do not account for the effect of the higher modes of vibration in a proper way and neglect the effect of the nonlinear structural response) tends to be overestimated.

The codes compensate in some way for this situation, by specifying higher factors for the forces used in designing members for flexure. The UBC [30] specifies the earthquake forces E to be multiplied by a factor of 2.8 when designing for shear (rather than 1.4 E specified when designing for flexure). This factor is further increased dividing it by $\phi=0.85$. The ACI 71 and 77 codes [35,36], specify 1.4 E (same as for flexure) with $\phi=0.85$ and the ATC recommendations specify specify 1 E with $\phi=0.6$ which gives an end result similar to the ACI.

Although these factors (particularly those in the UBC 73 [30]) could be sufficiently high to compensate for the underestimation of the actual shear that can be developed in the critical regions of certain wall structures, in general they do not represent a sound design philosophy and can lead to considerable underestimation of the actual shear forces developed in extreme earthquakes. A more logical design philosophy is to design against shear according to flexural wall capacity and largest expected shear-moment ratio. This would be consistent with the present code philosophy of ductile moment-resistant space frames. Better understanding of wall behavior will facilitate the implementation of these procedures.

1.2 Objectives and Scope

Experimental and analytical objectives were considered.

1.2.1 Objectives of the Experimental Research Program

The experimental program focused on the hysteretic behavior of walls. The effect of the following parameters was studied:

1. Rectangular hoop confinement for the columns rather than circular spiral confinement as used in Ref. [1].
2. Walls having a rectangular cross-section with embedded columns rather than framed walls (barbell-shape) in which the boundary elements protrude from the surface of the wall panel.
3. Different moment-to-shear ratios.
4. Monotonic and cyclic load programs, and
5. Repair Procedures

The characteristics of the hysteretic behavior studied were: stiffness, strength, ductility, the contribution of the different mechanisms to the overall deformation, the energy dissipation capacity and modes of failure. Also studied were the variation of the critical damping ratio and the frequency characteristics of the wall at different levels of damage.

The experimental program consisted of testing four three-story wall specimens similar to those reported by Wang in Ref. [1]. The specimens represented the lower portion of the shear walls of wall-frame structural systems of a ten- and seven-story building. The experiments simulated, in a pseudo-static manner, the dynamic loading conditions which could be induced in subassemblages of buildings during actual earthquake shaking. After incipient failure, all the specimens were repaired and retested. Free vibration tests were conducted on the specimens, first undamaged and later at different stages of damage.

An additional experimental investigation was carried out to study the longitudinal stress-strain relation for the hoop confined concrete of the boundary elements in the framed walls and is reported in detail in Ref. [9].

1.2.2 Analytical

The analytical work includes the detailed interpretation of the experimental results. These results are compared with theoretical values predicted by the code and different analysis methods.

Analytical models for the behavior of structural walls under high shear stresses are presented. These models consider a breakdown of the overall deformations into three components: flexural, shear, and fixed end deformations.

In the flexural deformation model, a finite element technique is used. A concrete model developed by de Villiers [37], based on Bazant and Bhat's work on the endochronic theory [26], was chosen for this purpose. This model can adequately represent the behavior of confined and unconfined concrete under axial compression, and the stress redistribution after tensile cracking. The element as written by de Villiers has the major limitation of not being able to account for the shear slippage along the tensile crack surfaces. This limitation is important when there is a significant contribution of shear deformation as is the case in the walls tested. Also the constants for the application of the endochronic theory to concrete, as determined by Bazant and Bhat, were not adequate for the case of hoop confinement of the type used in experiments. These limitations were overcome by modifying the confined concrete stress-strain relations on the basis of the work described in Ref. [9].

The shear deformations were accounted for with a multilinear model in which the wall behavior at different stages (uncracked, diagonally cracked, and yielding) was defined under monotonic loading. In the latter part, the interaction with the flexural mechanism was found to be important and was included in the model. The fixed end deformations, which in the case of the specimens tested is rather small, were accounted for with a simplified bond slip model.

The possibility of extending the models to the case of cyclic loading was also investigated.

2. TEST SPECIMENS

2.1. Prototype Buildings

The idealized prototypes adopted in this investigation are shown in Figs. 2.1 and 2.2. A ten-story and a seven-story building were designed having similar floor plans. The buildings are symmetric with respect to both directions, thus minimizing the seismic torsional forces, and include four walls along the E-W direction and two walls along the N-S direction.

The use of only two walls in one direction is not desirable because the failure of one could bring about the collapse of the structure. The use of a greater number of walls would minimize this possibility. For this reason the AIJ code specifications [38,39] require a minimum number of four walls. Only two walls were used here in order to obtain the largest story shear per wall.

In this study, the walls of the ten-story building have protruding boundary elements with rectangular hoop rather than the spiral confinement used in Ref. [1]. Since one of the objectives of the experimental program was to induce high shear stresses in the walls, in order to maintain the same high shear stresses as those in the framed wall structure, a seven-story building was designed with rectangular walls. In a rectangular wall, the moment-to-shear capacity ratio is generally lower than in a framed wall. Thus, a shorter building with a lower moment-to-shear ratio acting on the walls will have shear stresses of magnitudes similar to those induced by seismic shaking in the walls of a ten-story building.

2.2. Design of Prototype Buildings

The design of the prototype buildings was done according to the provisions of the 1973 UBC [30]. The buildings were assumed to be located in Seismic Zone Number 3, and the horizontal force factor, K , was obtained from Table No. 23-1 of that code as 0.8. The material properties were specified as:

$$f'_c = 414 \text{ MPa}$$

$$f'_t = 27.58 \text{ MPa}$$

2.2.1. Ten-Story Prototype

Estimation of the weight of this building, together with the design of the wall panel, is presented in Ref. [1]. Item 2 of Table 23-1 of the code requires that the walls resist the total lateral force, acting independently of the ductile moment-resisting portions of the space frame. This load condition produces the maximum moment and shear at the base of the wall, and is the one used here.

(a) Wall Panel

The shear and moment diagrams for a single N-S wall when subjected to the factored code forces are shown in Fig. 2.3. The panel designed according to Section 2627(a) of the 1973 UBC has a thickness of $t = 0.306$ m. The horizontal wall dimension l_w was selected as 7.164 m, and a double layer of #6 bars spaced vertically and horizontally at 0.230 m was used. The panel steel ratios are

$$\rho_h = \rho_v = 0.0082$$

(b) Boundary Element

According to Section 2627(c) of the 1973 UBC, vertical boundary elements should be designed to carry all the vertical loads resulting from the specified horizontal earthquake force, plus the tributary dead and live loads.

1) Tension

$$\frac{P_u}{\phi} = \frac{1.4E - 0.9D}{\phi} \quad (2.1)$$

where the factor ϕ for axial tension is 0.9 (UBC Section 2609[c]), and E is the earthquake load including torsion effects.

From Figs. 2.1 and 2.3:

$$E = \frac{64386 \text{ kN-m}}{(1.4)(6.401 \text{ m})} = 7189 \text{ kN}$$

$$\frac{P_u}{\phi} = \frac{(1.4)(7189) - (0.9)(3263)}{0.9} = 7920 \text{ kN}$$

Using eight #18 bars:

$$\frac{P_u}{\phi} = (.414 \text{ kN/mm}^2) (8) (2605 \text{ mm}^2) = 8628 \text{ kN}$$

2) Compression

$$\frac{P_u}{\phi} = \frac{1.4(E + D + L)}{\phi} \quad (2.2)$$

where the factor ϕ for the column in axial compression with hoop confinement is 0.7. Thus:

$$\frac{P_u}{\phi} = \frac{1.4(7189 + 3263 + 329)}{.7} = 21562 \text{ kN}$$

Using a 0.762 m x 0.762 m column with eight #18 bars:

$$P_u = [(A_g - A_s)f'_c + A_s f_y] \quad (2.3)$$

$$= [(580644 - 20840)(.85)(27.58) + (20840)(414)](10^{-3}) \text{ kN}$$

$$= 21751 \text{ kN}$$

and the longitudinal reinforcement ratio is taken as:

$$\rho = 0.0353$$

3) Transverse Reinforcement

The design of the transverse reinforcement was carried out according to UBC requirements and is described in Ref. [9]. The code requirement can be satisfied with the use of a double hoop of #4 bars with 102 mm spacing; the hoop arrangement for the model is shown in Fig. 2.4 (b) and yields:

$$\rho'' = 0.0154$$

2.2.2. **Seven-Story Prototype**

According to Eqs. 14-3, 14-2, and 14-1, in Chapter 23 of the UBC and the dimensions shown in Fig. 2.2:

$$T = \frac{0.05 h_n}{\sqrt{D}} = \frac{(0.05)(66)}{\sqrt{61}} = 0.422 \text{ sec} \quad (2.4)$$

where h_n and D are in feet.

$$C = \frac{0.05}{T^{1/3}} = 0.066 \quad (2.5)$$

$$V = ZKW = (1)(.8)(.066)(60233) = 3180 \text{ kN} \quad (2.6)$$

(The estimation of the total weight of building W is given in Table 2.1.)

According to Section 2314(g) of the UBC, the walls should be capable of resisting a torsional moment:

$$M_t = (0.05)(54.9)(3180) = 8730 \text{ kN-m}$$

In order to estimate the shear force that the torsional moments cause in the walls, it is conservatively assumed that all the torsional moments are resisted by the N-S walls alone:

$$\text{total base shear per wall} = \frac{1}{2}(3180) + \frac{8730}{42.7} = 1794 \text{ kN}$$

where 42.7 m is the distance between the walls.

This assumption is conservative in that it neglects the contribution to the torsional resistance provided by the E-W walls and the columns. But the evaluation of the torsional moment according to the code assumptions will underestimate the torsional moments that would take place when one of the two N-S walls reaches yielding. The distribution of the total base shear along the height of the wall is in accord with Eqs. 14-4 and 14-5, Chapter 23 of the UBC. Figure 2.5 shows the lateral earthquake forces including torsion, multiplied by the load factor 1.4. The base axial force appears unfactored because it is believed that, during severe earthquake ground shaking, the probability of an increase of 1.4 in either the vertical live or dead load existing on the building is very small. The effects of the vertical component of the acceleration were not accounted for.

(a) Wall Panel

From Section 2627(a) of the UBC, when calculating the shear stresses in shear walls of buildings without a 100% moment-resisting space frame, the following factors should be used:

$$U = \frac{V_u}{\phi} = \frac{(2.8)E}{0.85} = 3.294 E \quad (2.7)$$

This shear load factor is twice as large as that required for flexure, and it is intended to prevent undesirable, brittle shear failure.

The code does not account for certain realistic factors, such as: 1) The effects of the frame-wall interaction and of higher modes in the dynamic response, which can lower the effective shear span in the wall (h_v in Fig. 2.5). 2) Higher yielding strength and strain-hardening of the reinforcing bars, and concrete strengths higher than those specified in the design, which can increase the shear introduced in the wall. (This increased shear is compensated for by an increase in the shear capacity of the wall). The code also neglects the deterioration of shear strength due to shear reversals. Since all these factors may contribute to the possibility of brittle shear failure, the 3.294 overall shear load factor may not be conservative in all cases.

1) Wall Cross Section

Using a 0.343-m thick wall panel, the effective depth, d , of the wall is taken to be $0.8 l_w$:

$$d = 0.8 l_w = (0.8)(7.239) = 5.791 \text{ m} \quad (2.8)$$

and the shear stress is:

$$\begin{aligned} v_u &= \frac{V_u}{\phi h d} = \frac{(3.294)(1.794 \text{ MN})}{(0.343 \text{ m})(5.791 \text{ m})} \\ &= 2.97 \text{ MPa} = .57\sqrt{f'_c} \text{ MPa} = (6.83 \sqrt{f'_c} \text{ psi}) \\ &(\leq 10 \sqrt{f'_c} \text{ psi}) \end{aligned} \quad (2.9)$$

Thus, the 0.343 m thick panel is acceptable.

2) Horizontal Wall Panel Reinforcement

Using Eq. 11-33 of Section 2611 of the UBC

$$v_c \leq 0.6 \sqrt{f'_c} + \frac{l_w \left[1.25 \sqrt{f'_c} + (0.2) \left(\frac{N_u}{l_w h} \right) \right]}{\frac{M_u}{V_u} - \frac{l_w}{2}} \quad (2.10)$$

where f'_c is in psi, l_w and h are in inches, M_u is in lb-in., V_u is in lb, and, according to Section 2611(g): $N_u = 0$.

$$v_c \leq 38 + \frac{285 \left[(1.25)(63.24) \right]}{\frac{224941}{403.32} - \frac{285}{2}}$$

$$v_c \leq 92.3 \text{ psi}$$

Using UBC Eq. 11-32:

$$v_c \leq 3.3 \sqrt{f'_c} + \frac{N_u}{4 l_w h} \quad (2.11)$$

$$v_c \leq 208.7 \text{ psi}$$

According to Section 2611(q):

$$v_c \leq 2 \sqrt{f'_c} = 126.5 \text{ psi} \quad (= 0.872 \text{ MPa})$$

Therefore, the nominal permissible shear stress carried by steel (v_s) is :

$$v_s = v_u - v_c \quad (2.12)$$

$$= 2.97 \text{ MPa} - 0.872 \text{ MPa} = 2.1 \text{ MPa}$$

Using #6 bars in a double layer:

$$s \leq \frac{A_v f_v}{v_s h} = \frac{(568 \text{ mm}^2)(414 \text{ MPa})}{(2.1 \text{ MPa})(343 \text{ mm})} = 326 \text{ mm} \quad (2.13)$$

Thus, a spacing of $s = 305 \text{ mm}$ can be used, and:

$$\rho_h = \frac{568}{(343)(305)} = 0.0054$$

satisfies the requirement of $\rho_h \geq 0.0025$ from UBC Section 2611(e).

3) Vertical Wall Panel Reinforcement

According to Eq. 11-34, Section 2611(e), the vertical shear reinforcement shall be:

$$\rho_n \geq 0.0025 + 0.5 \left(2.5 - \frac{h}{l_w} \right) (\rho_h - 0.0025) = 0.0021 \quad (2.14)$$

or:

$$\rho_n \geq 0.0025 \quad (2.15)$$

but ρ_n need not be greater than ρ_h .

According to the SEAOC [33], however, the value of ρ_n shall be the same as that for ρ_h .

(b) Boundary Elements

The columns embedded in the edges of the wall were designed according to Section 2627(c) of the UBC.

1) Tension

From Eq. 2.1:

$$\frac{P_u}{\phi} = \frac{(1.4)(3970) - (0.9)(2272)}{0.9} = 3903 \text{ kN}$$

where

$$3970 = \frac{35585 \text{ kN-m}}{1.4 (6.401 \text{ m})} \quad (\text{Fig. 2.4})$$

Using four #18 and four #14 bars (required by compression):

$$\frac{P_u}{\phi} = 0.141 \left[(4)(2605) + (4)(1552) \right] = 6883 \text{ kN}$$

2) Compression

From Eq. 2.2:

$$\frac{P_u}{\phi} = \frac{1.4(3970 + 2272 + 218)}{0.7} = 12920 \text{ kN}$$

Using a (0.838-m x .343-m) column with four #18 and four #14 bars, from Eq. 2.3:

$$\begin{aligned} \frac{P_u}{\phi} &= [(287434 - 15632)(0.85)(27.58) + (16632)(414)](10^{-3}) \\ &= 13234 \text{ kN} \end{aligned}$$

The column dimensions should satisfy Section 2626(f) of the UBC; thus:

$$\frac{b}{h} = 0.409 \geq 0.4 \quad (2.16)$$

and

$$\rho = 0.0567 \leq 0.06 \quad (2.17)$$

3) Transverse Reinforcement

According to Section 2626(f) of the code, the design of the transverse reinforcement can be computed by:

$$A_{sh} \geq 0.3 s_h h_c \frac{f'_c}{f_{yh}} \left[\frac{A_g}{A_{ch}} - 1 \right] \quad (2.18)$$

$$A_{sh} \geq 0.12 s_h h_c \frac{f'_c}{f_{yh}} \quad (2.19)$$

According to the above formulae, for 102-mm spacing: from Eq. 2.18

$$A_{sh} \geq 23.22 \text{ mm}^2$$

and from Eq. 2.19

$$A_{sh} \geq 225.18 \text{ mm}^2 \quad (\text{this controls})$$

Because Section 2607(m)3 requires the use of at least #4 deformed bars for stirrup, and the area of the #4 bars is 129 mm^2 , hoops of #4 bars with 102 mm spacing are used. Section 2607(m)3 of the code also states that the ties shall be arranged such that every corner and alternate longitudinal bar is laterally supported by the corner of a tie having an angle of no more than $(3/4)\pi$ radians and that no bar is further than 152 mm from such a laterally supported bar. The arrangement of the hoops for the model is illustrated in Fig. 2.6 (b).

2.3. Selection of Test Specimens

The selection of the model scale and basic subassemblage for the test specimens is elaborated upon in Ref. [1]. The dimensions of the specimens correspond to one-third the dimensions of the prototype. The dimensions of the specimens and the details of its reinforcement are shown in Figs. 2.4 and 2.6.

Since there is no one-third scale reinforcing bar equivalent to the #14 bars used in the prototype, nine #5 bars were used in the rectangular wall model. The model columns therefore have $\rho=0.0557$ rather than $\rho=0.0567$ computed for the prototype. Gage No. 7 undeformed wire with a diameter of 4.5 mm was used to model the #4 column transverse reinforcing steel of the prototype, yielding $\rho''=0.0184$. The wall design parameters are summarized in Table 2.2.

2.4. Mechanical Characteristics of Materials

2.4.1. Steel

The specified yield strength of steel was 414 MPa. In order to obtain homogeneity in the material properties, bars of similar size were purchased at one time and from the same heat. The actual material mechanical characteristics are summarized in Table 2.3 and shown in Figs. 2.7-2.13. The stress-strain relations shown in Figs. 2.7-2.12 were obtained from tests on reinforcing bars used in the model. These tensile bar specimens were not machined. The strains were recorded along a 51 mm gage length using linear variable differential transformers (LVDT's). At the initiation of steel necking the LVDT's were removed to prevent damage to the equipment. The tests were then continued until the tensile specimens were ruptured. ϵ_r is the residual strain measured along the initial 25 mm gage length where rupture took place.

The stress-strain relation shown in Fig. 2.13 was obtained from tests on machined bar specimens. In order to delay buckling, the specimens in compression had a length-to-diameter ratio of 3-to-1. Comparing Figs. 2.13 and 2.10, it can be seen that the machined bars have a higher strength after yield. This agrees with Ma et al.'s observations [24]. Figure 2.13 also shows that, in compression, the yielding strength is 11% higher than in tension, and that the stresses are higher for strains beyond the strain-hardening level. These results are consistent with other experimental data [20,40].

It can be seen that the stress-strain relationship for the Gage No. 7 wire (Fig. 2.7) used to model the lateral reinforcement in the columns differs significantly from the typical stress-strain relationship of reinforcing bars. This is because the wire strain-hardened during fabrication. Another significant violation of the similitude law is that the wire used had no deformations resembling those of the #4 bar in the prototype.

2.4.2. Concrete

The specified strength of concrete was 27.58 MPa; the actual mechanical characteristics are shown in Table 2.3 and Fig. 2.14. The concrete mix proportions are shown in Table 2.4. Although the 28-day compression strength was close to the specified value, at the time of testing the concrete compressive strength for the original specimens varied from 32.4 MPa to 38 MPa. This variation was due to the different ages at the time of testing. The concrete mix proportions are shown in Table 2.4.

The confined concrete in the boundary elements of the framed walls was the subject of a detailed investigation reported in Ref. [9]. An empirical relation developed in that reference takes into account the increase in the concrete's strength and ductility because of the confining effect of the hoops and the longitudinal reinforcement.

The specimens were repaired by removing the damaged concrete in the first floor panel and columns, and by pouring a mix with high cement content in order to obtain an early high strength and to complete the tests in the shortest possible time. The concrete strength in the repaired sections varied from 45.8 MPa to 51.7 MPa.

2.5. Fabrication of Specimens

The specimens were cast story by story in their vertical position as explained in Ref. [1]. Figure 2.15 shows the framed walls during construction, and Fig. 2.16 is a close-up photo showing details of the reinforcement for the panel and boundary elements of the rectangular wall.

In the framed wall specimens, in order to facilitate repair, #2 bar dowels were left embedded in the columns and the slabs around the first story panel (Fig. 2.17).

The fabrication of the columns with hoop confinement required significantly more effort than the columns of Ref. [1] with spiral confinement. Each hoop had to be fabricated by hand. In order to provide a good lateral restraint for the longitudinal bars, very tight tolerance requirements (± 2.5 mm) were specified for the hoop dimensions.

2.6. Repair and Strengthening of Specimens

Damage to the walls was concentrated on the first story. It included crushing of the concrete in the panel, buckling of the wall and column reinforcement, and, after rupturing of the confining reinforcement, crushing of the concrete in the column under compression and shear. Damage also included large residual tensile cracks, especially in the boundary elements.

The strengthening and repair procedure included increasing the moment and shear capacity of the first floor so that, when retested, most of the damage would occur in the second story. This would prevent excessive ductility demands in the first floor panel, which had already been subjected to very high strain levels.

The strength capacity of the first story of the models was increased by placing some additional longitudinal reinforcement in the first story, considering that:

$$\frac{\text{realistic moment requirements at foundation level}}{\text{realistic moment requirements at first floor level}} =$$

$$1.368 \quad \text{for framed wall (from [1])}$$

$$1.442 \quad \text{for rectangular walls (from Section 3.2)}$$

In order to displace the critical section of the wall to the second story, and considering that the column and some of the panel reinforcement in the second story has already been strain-hardened, the moment capacity of the first story had to be increased by at least 37% and 44% for the framed and rectangular walls, respectively, and the shear capacity should be increased by at least the same factor.

As a consequence of this strengthening of the first story, the second panel will be subjected to a lower M/V ratio, this will increase the shear demands in that panel. It was considered of interest to observe the behavior of the panel under this lower M/V ratio, because as shown in [1] during the nonlinear response of the structure to a realistic earthquake, the actual M/V ratio could go below that indicated by the linear elastic analysis used as basis for the tests (Section 3.2).

Assuming that the external moment is carried by the boundary elements using two additional #8 bars with $A_s = (2)(507) = 1014$ mm², the ratio of this additional area to the original steel in the models is:

$$\frac{1014}{2316} = 0.438 > 0.368 \quad \text{for framed walls}$$

$$\frac{1014}{1782} = 0.569 > 0.442 \quad \text{for rectangular walls}$$

The shear capacity can be increased by increasing the thickness of the repaired panel. Casting new 50-mm and 75-mm thick panels (increasing the total thicknesses to 152 and 189 mm), the ratio of this additional thickness to the original thickness of the panel cross-section is:

$$\frac{50}{102} = 0.49 \quad \text{for framed walls}$$

$$\frac{75}{114} = 0.657 \quad \text{for } \textit{rectangular walls}$$

In this way the increase in the shear capacity is larger than the increase in the moment capacity

$$0.490 > 0.438 \quad \text{for } \textit{framed walls}$$

and

$$0.657 > 0.569 \quad \text{for } \textit{rectangular walls}$$

The repair procedure was carried out in the following steps:

1. Removal of the damaged concrete in the panel, and removal of the column concrete that had been crushed or showed large residual tensile cracks.
2. Straightening of the buckled column bars (Fig. 2.18), and restoration of the original wall geometry. Since some of the reinforcement had large residual tensile deformations, and some of the lateral reinforcement in the column had to be replaced, the column longitudinal bars were cut and shortened, and new lateral reinforcement was placed where needed.
3. Welding of new panel reinforcement. In the framed walls panel reinforcing bars were welded to the dowels left in place for that purpose. In the rectangular walls they were welded to the old panel reinforcement.
4. Lap splicing of the column longitudinal reinforcement, and welding of additional longitudinal reinforcement to increase the moment capacity of the section (Fig. 2.19).
5. Casting of new concrete. To accelerate the test schedule, it was desirable to obtain an early high strength. It was also important to prevent, or at least minimize, the shrinkage cracks in concrete. To obtain an early high strength, a concentrated mix (high cement content per cubic meter of concrete) was used, although there were some inconveniences with its use. As one example, the high temperature developed in a concentrated mix can produce cracks. To control this, crushed ice was used with water to keep the mix at approximately 10°C. A high cement content mix will also tend to shrink; this required the use of a low water-cement ratio, with high density aggregate (Table 2.4), and curing was carefully done, keeping the concrete moist.

3. LOADING CONDITION OF WALL SPECIMENS, EXPERIMENTAL SET UP, AND TEST PROCEDURE

3.1. General

In order to check on the validity of the maximum shear stresses allowed by the codes, it was considered of particular interest to subject the specimen to the highest shear forces that could be expected in a severe earthquake ground motion.

3.2. Parameters Contributing to Shear Failure

It is well known that the shear developed in a structural member or system during extreme earthquake ground motions, depends upon the flexural strength capacity built into the structure. Therefore there are several factors that contribute to a brittle type of shear failure which are not explicitly considered in the code specifications. These can be classified in three groups:

1. Factors which cause an increase in the moment capacity and, consequently, an increase in the shear force that can be developed by the section.
2. Factors which reduce the moment-to-shear ratio for the lateral forces acting on the wall, so as to increase the shear required to produce the flexural (bending moment) strength at the critical section (region).
3. Factors that can reduce the shear strength capacity.

In the first group are included:

(a) Realistic stress-strain diagrams for the reinforcing steel. These show that the maximum stress level that can be developed in a steel bar is of the order of 60% above the specified yield strength of the bar (Figs. 2.8-2.13).

(b) Vertical web reinforcement in the shear wall. This reinforcement increases the flexural capacity of the section.

(c) Axial force in a flexural member. In a shear wall, for example, compressive axial forces cause an increase in its flexural capacity because usually the axial load acting on the member is smaller than the balanced load [1].

(d) A value of f'_c higher (e.g. 35 MPa) than specified (say, 27.58 MPa) generally results in reinforced concrete structural elements of higher strength than that intended (this effect will be compensated by an increase in the concrete shear capacity of the wall).

The second group of factors include:

(a) The effect of higher modes of vibration in the response of a structure to a realistic earthquake motion.

(b) The interaction of the frame and wall systems [1].

(c) The nonlinear response of a real structure, particularly the reduction of stiffness in the lower story [1].

In the third group it is necessary to consider:

(a) The effect of the axial tensile forces which is partial because they also reduce the moment capacity.

(b) The effect of loading reversals. Under reversals of load, there is a drop in the shear capacity of the R/C member [41,42].

3.3. Critical Loading Condition of Walls

For a fixed ultimate moment capacity, the critical loading condition of the wall is that which induces development of the highest shear stresses. The loading condition used for the wall of the ten-story prototype was taken from Ref. [1] and is shown in Fig. 3.1, together with the condition specified by the code. The critical loading condition employed corresponds to the

elastic analysis of the structure subjected to the ground accelerations of the 1940 El Centro earthquake. A realistic nonlinear analysis would give a more severe loading condition, i.e. smaller effective shear spans. But, in order to facilitate comparison of the results with those obtained in Ref. [1], a loading condition similar to that used there was adopted.

For the seven-story prototype, analyses were performed with the computer program, TABS [43]. The results are shown in Fig. 3.2. The critical loading condition employed is shown in Fig. 3.2 (ii) and corresponds to the ground motion of the San Fernando earthquake. The simplified loads to be used in the test were normalized to the ultimate moment capacity obtained using the computer program, RCCOLA [23]. The axial forces in the walls (Figs. 3.1 and 3.2) were obtained from the TABS analysis and kept constant. Note that the wall axial forces shown in Figs. 2.3 and 2.5 and described in Section 2.2 were obtained assuming the walls carried the loads corresponding to their tributary areas (6.1 m x 12.501 m).

3.4. General Setup

The general test setup is shown in Fig. 3.3 and elaborated upon in Ref. [1]. The two smaller lateral jacks (667 kN) were used only in the tests of the models with rectangular walls corresponding to the seven story building. In this shorter building, the shear in the lower three stories is not constant. The moment distribution in the lower three panels of the structural wall is not linear and is better represented by a trilinear moment diagram (Figs. 2.5 and 3.2).

3.5. Specimen Instrumentation and Data Acquisition System

With some minor differences from specimen to specimen, the instrumentation was similar to that used in the previous investigation [1], and is shown schematically in Figs. 3.4 and 3.5. Continuous plots were made of chosen data acquisition channels by means of X-Y and X-Y-Y' recorders. Sequential records of all channels at short time intervals were made by means of a low-speed data acquisition system for the first two tests (tests number 3 and 4 in Table 2.3[b]). A new high-speed data acquisition system was employed for all the other tests.

Photogrammetric readings were made at the initiation of the tests, and at selected load points during the load cycles. The gridlines used are shown in Fig. 3.6 and 3.7. In addition, photographic records were taken with 35 mm cameras.

3.6. Testing Procedure and Loading Sequence

The testing procedure used in the earlier investigation [1] was repeated, and similar loading sequences implemented. When testing each pair of wall specimens, one was subjected to a monotonic load program, and the other underwent cyclic loading. After repair, the specimens were retested. the specimen originally tested under monotonic loading was subjected to cyclic loading, and vice versa. In this way, it was possible to keep the total number of shear reversals similar in both specimens.

Free vibration tests were performed on the specimens in their undamaged state, after reaching a ductility level of 3, and after failure. The initial displacement was induced by either a hammer blow or by introducing an initial displacement at the top of the specimen - pulling it with a cable, and suddenly releasing it (snap test).

4. EXPERIMENTAL RESULTS

4.1. General

A total of eight tests were performed on four structural wall models; these are enumerated in Table 4.1 together with the main experimental results. The main experimental data obtained are reported in this chapter. Some additional experimental results are presented in Chapters 5 and 6.

Because of the large amount of data involved, the data reduction process was automated whenever possible. Computer programs were developed to plot the scanner data points, and to handle the photogrammetric data.

There is some repetition in the test procedures and results from specimen to specimen. The analysis and interpretation of the experimental results is done in detail in the next chapter. Most of the present chapter should then be regarded as backup material for the ones to come.

The hysteresis diagrams presented in this chapter are functions of the total base shear V . Due to the lateral movement of the specimen, the net axial force on the columns has a horizontal component ΔV_3 acting on the specimen as shown in Fig. 4.1. Although the direction in which $V_{i=1,2,3}$ is applied does not remain horizontal during the test, the corrections were negligible. The total base shear in the framed wall specimens is then

$$V = V_3 + \Delta V_3 \quad (4.1)$$

In the case of the rectangular walls, two additional jacks (Fig. 3.3) introduced lateral forces at the first and second floor levels (V_1 and V_2). The total base shear in these walls is then:

$$V = V_1 + V_2 + V_3 + \Delta V_3 \quad (4.2)$$

4.2. Free Vibration Tests

The results of the free vibration tests are shown in Table 4.2. The fundamental period of the specimens was measured under three types of excitations: (1) ambient vibrations (with peak accelerations of the order of 7×10^{-7} g); (2) hammer impact using a 7 kg hammer; and (3) pull and sudden release (an initial tip displacement was introduced by pulling with a #4 reinforcing bar attached to the specimen and a pulley set up, introducing a force of approximately 50 kN).

The measured frequency consistently decreased with the maximum ductility level and with the number of cycles beyond yield level reached previously. The reduction was of the order of 50% for $\mu = 3$. This can be attributed to the deterioration in stiffness due to the opening of cracks in concrete.

The critical damping ratio was computed from the decay in the accelerograph records. In the virgin specimens the critical damping ratio ranged from 0.0183 to 0.0261 for excitation type (3), with an average value of 0.022. These values are in general agreement with those obtained by other researchers [1,44] and those recommended in practice [45,46]. Damping increased after the specimens underwent yield deformations, and changed at different levels of damage. The values, however, were generally higher than those for the virgin specimens. Larger amplitude cycles usually resulted in higher damping values. This can be attributed to energy dissipation along the cracks.

The results obtained in these tests cannot be directly extrapolated to a real structure for the following reasons:

1. When performing the free vibration tests, there was no axial load on the specimens. In a real structure the axial load would decrease the opening in the horizontal cracks. Smaller crack widths would tend to close earlier, increasing the stiffness of the specimen.
2. Structural walls are only one element of a structural system. The dynamic characteristics of a real structure are also affected by the frames, the nonstructural elements, and the soil conditions (soil-structure interaction).
3. The amplitude of vibration in a structure subjected to a strong ground motion is larger than that used in a free vibration test. Thus, the dynamic characteristics of a structure subjected to a strong ground motion will also differ.
4. Realistic testing is hard to achieve with a scaled model. The damping characteristics appear to be very sensitive to the crack widths, and it is questionable that the use of scaled down aggregates is enough to obtain an equivalent damping effect.

Realistic testing would require the use of full or large scale models, in which the effect of axial loads, non structural elements etc. is accounted for. The use of forced vibration excitations would allow large amplitude displacements to be reached.

For these reasons, the data obtained provide insight on the dynamic characteristics of structural walls, and their variation with the damage state, but the actual dynamic characteristics would be different in a real structure.

4.3. Pseudo Static Tests

The main experimental results (mostly in the form of hysteresis loops) are presented in this section. A detailed analysis and discussion is given in Chapter 5.

4.3.1. Virgin Framed Wall Subjected to Monotonic Loading (Specimen 3)

This specimen was subjected to the loading program shown in Fig. 4.1. This loading program is similar to that used in Ref. [1]. The main force deformation diagrams are shown in Figs. 4.2 - 4.5.

LP 0-16 Gravity loads of 434 kN (Fig. 3.1) per column were gradually applied to the specimen. Loads in both vertical jacks were maintained within a 45-kN difference so as to avoid unbalanced moments. Small lateral load cycles (± 45 kN) were applied for checking the loading and data acquisition systems. This load was small enough so as not to cause any cracking or permanent deformations.

LP 16-32 The specimen was cycled at a lateral force level of 222 kN, the load at which the first tensile crack in the south column was observed. (The north and south directions for the specimen are defined in Fig. 3.3. The north direction is taken as positive for all tests). The overall displacement for these cycles was 2.3 mm.

LP 32-77 The lateral load was increased monotonically to the north. At a load of 311 kN, corresponding to a nominal shear stress of $v_{det} = 0.267 \sqrt{f'_c}$, the first hairline diagonal cracks observable to the eye appeared in the panel. The outermost tension bar in the column reached yielding strains at the top of the first story, with a load of 761 kN and a third floor displacement of 12.2 mm. The same bar yielded at the base of the first floor when the load reached 800 kN and the third floor displacement reached 13.5 mm. The reason for the bar yielding first at the top is related to the stress redistribution with diagonal cracking and is elaborated upon in Chapter 5. But even if the outermost bar had yielded, the overall force deformation diagram does not indicate yielding. In Fig 4.2 it can be observed that, while there is a change in the slope of the overall force-deformation diagram at 800 kN, overall yielding does not take place until a load of 898 kN is reached (LP 49). This is the load at which all the reinforcement in the column cross-section at the base of the tension column yields (as indicated by gages C3 and C4 of Fig. 3.5). The nominal displacement ductility ratio of one, obtained from the overall force deformation diagram (Fig 4.2), was taken as 18 mm at a lateral load of 898 kN (LP 49) (Figs. 4.2 and 4.6). At a nominal displacement ductility level of three (lateral displacement at the third floor $\delta_3 = 54$ mm), and a lateral load of 996k kN, spalling initiated at the base of the

north compressive column (LP 52 Fig. 4.7[a]). Cracks in the tensile column had a uniform spacing of approximately 36 mm with average widths of 0.8 mm. During this monotonic cycle, the specimen withstood loads up to 1090 kN at LP 58, and reached a top floor displacement of 147 mm at LP 59. At this load point, the test was interrupted, and the lateral load had to be removed because the linear potentiometer monitoring the top floor displacement and feeding the electronic signal for the displacement control of the test had reached its maximum displacement.

Upon resumption, the specimen was reloaded to the north, this time reaching a peak load of 1090 kN (LP 75). Soon afterwards, the cover at the base of the north compression column completed spalling with the longitudinal reinforcement buckling, and the confining hoops at the base of the north column rupturing (Fig. 4.7[b]).

At this point the lateral load was returned to zero to prevent the collapse of the specimen.

LP 77-82 The lateral load was reversed increasing monotonically in the south direction. At a load of -360 kN, there were a large number of residual tensile cracks still open in the south column (Fig. 4.8). These, together with the Bauschinger effect in the longitudinal reinforcement, caused a reduction in the effective EI of the column cross-section, and initiation of buckling was observed (LP 80 in Figs. 4.2 and 4.9[a]). Subsequently, the load was able to increase only slightly, up to -365.6 kN at LP 81 when the column completely buckled. At this point the reading for the lateral displacement at the third floor level showed a residual north deformation of 107 mm. This failure marked the end of the test.

The buckled column, including part of the panel, is shown in Fig. 4.10. Figure 4.11 shows the second panel and boundary elements at the conclusion of the test. Figure 4.12 shows the displacement components increasing almost linearly with the tip displacement.

4.3.2. Framed Wall Subjected to Cyclic Loading (Specimen 4)

The specimen was subjected to the cyclic loading program shown in Fig. 4.13. Figures 4.14–4.17 show the main force-deformation diagrams.

LP 0-21 The same gravity loads applied to Specimen 3 were used for Specimen 4. Checking of the loading and data acquisition systems was done using a run of small 45 and 133 kN cycles

LP 21-33 Cracking load cycles of 222 kN were run. The first hairline cracks in the tensile columns (shown in Fig. 4.18[a]) were observed at LP 22 (222 kN). Overall displacement for these cycles was 2.84 mm.

LP 33-45 The specimen was cycled at a working load level of ± 400 kN. As will be elaborated upon in the next chapter, this load was analytically determined to be the load at which the tensile reinforcement reaches a stress of 165.5 MPa or $.4f_y$, which is the allowable stress for steels with an f_y of 414 MPa or more.

At a load of 355 kN the specimen developed several diagonal hairline cracks spaced 86 mm apart in the tension region of the wall panel (Fig. 4.18[b]). The tensile column developed hairline cracks with 38-76 mm spacing. When the load was reversed new cracks were observed in a symmetrical way (Fig. 4.18[c]). The overall displacement in these cycles was 8.33 mm. The hysteresis loops were stable (no degradation) and exhibited little energy dissipation.

LP 45-57 The specimen was cycled at a displacement amplitude of ± 18 mm corresponding to a nominal ductility ratio value of one (Section 4.3.1). During this series of cycles, the longitudinal steel in the columns yielded, and cracking continued to propagate, opening new cracks. Some energy dissipation was observed, and the strength of the specimen dropped by 5% between the first and third cycles.

LP 57-81 The specimen was cycled at ductility values of two and three. During the cycle at a ductility level of two, the lateral load reached 970 kN. Upon reversal a horizontal flexural crack propagated into the panel (Fig. 4.19[a]), with the upper panels also undergoing extensive cracking (Fig. 4.19[b]). The loss of strength from the first to the third cycle was 6% at a

nominal displacement ductility $\mu=2$ and 7% at $\mu=3$.

During cycles at $\mu=3$, the crack at the base of the specimen over the foundation opened 1.5 mm wide and an overall slippage of 3 mm was observed along this crack. The largest diagonal cracks in the panel and the tensile column reached also a width of 1.5 mm.

LP 81-96 The specimen was loaded to a displacement of 71 mm or a displacement ductility of 4, which was reached at a load of 970 kN. Crushing initiated along the horizontal flexural cracks in the panel, indicating shear slippage along this horizontal crack (Fig. 4.20[a]). Upon reversing the load to the south for the second time at this displacement ductility level, the horizontal panel reinforcement at the base of the wall buckled, causing the concrete in the south region of the panel to spall (Fig. 4.20[b]). When loading the specimen to the north, the lateral load reached 938 kN; upon its reversal to the south again, the damaged panel region was not capable of withstanding the compressive stresses, and at a peak load of 742 kN, the compressive region of the panel crushed. The lateral load dropped to a load of 640 kN at a displacement ductility of -4 (Fig 4.20[c])

LP 96-99 An attempt was made to reload the specimen to the north, but at 410 kN all the concrete along the lower part of the first floor panel crushed, and the load dropped to 205 kN at a displacement of 91 mm. At this point the columns buckled (Fig. 4.21) and the test was concluded.

The displacement components are shown in Fig. 4.22, and a significant difference can be observed when comparing it to Fig. 4.12. For Specimen 4 the ratio of shear deformation to flexural deformation components increases with the tip displacement. The deterioration mechanisms under load reversals that cause this are discussed in the following chapter.

4.3.3. Repaired Framed Wall Subjected to Monotonic Loading (Specimen 4R)

Specimen 4 was repaired (Sect. 2.5), renamed Specimen 4R and subjected to the monotonic loading program shown in Fig.4.23. The main force deformation diagrams are shown in Figs. 4.24-4.27. The repaired first floor panel, and the status of the damaged upper panels at the initiation of the test is shown in Fig. 4.28.

LP 0-58 The same gravity loads applied to the undamaged specimens were used here. Small cycles of ± 45 kN and 133 kN were initially run in order to check the loading and data acquisition systems.

LP 58-108 Loads of 222 kN were cycled in order to compare the response of this specimen with the response of Specimens 3 and 4 at the same load level.

LP 108-211 The overall displacement for this cycle was 7.38 mm which is an increase of 2.6 times greater than the displacement under the same cyclic load level of Specimen 4. This indicates that significant damage remained in the upper floors which had not been repaired.

The specimen was loaded monotonically to the north. The nominal displacement ductility of one used in this test was 18 mm, (same as for virgin Specimens 3 and 4). At a load of 427 kN, several diagonal hairline cracks were observed in the lower panel and corresponding tensile column (Fig.4.29[a]). Cracks continued to appear and propagate in the column and panel as shown in Figs. 4.29[b] and 4.29[c]. At a displacement ductility of 3 and a lateral load of 1262 kN, the concrete cover at the top of the north column in the first floor started to spall and the tensile cracks at the second story reached widths of 2.5 mm. At this point the lateral load was returned to zero and free vibration tests were performed.

LP 211-258 A series of 222 kN load cycles with an overall displacement of 13.36 mm was run. This overall displacement is 59% larger than the displacement obtained for the same load level cycles at the initiation of the test (LP's 0-58), and 4.7 times the displacement corresponding to Specimen 4.

LP 258-343 Loading to the north continued with damage increasing in all three panels. The crack at the top of the first floor's south column reached 3.2 mm at a peak load of 1297 kN. At this load the third story panel started crushing, with a crack opening between the third

floor slab and the top of the specimen's columns. At a top floor displacement of 117 mm, and a lateral load of 1008 kN, two tensile #6 reinforcement bars ruptured at the top of the first story where the bars had been welded during repair (Fig. 4.30) and the load was returned to zero.

LP 343-355 A 222 kN cycle with an overall displacement of 20 mm was introduced. This overall displacement represents an increase of 2.7 times the one obtained initially for the same load level cycles for this specimen, and an increase of 7 times over that corresponding to Specimen 4.

LP 355-397 The specimen was loaded in the south direction with damage increasing in the third floor panel and the crack between the columns and the third floor slab opening.

At a load of -914 kN and a displacement of -26.7 mm, the third floor panel crushed and the lateral load was returned to zero. The specimen was still capable of resisting the axial gravity load.

LP 39-445 The specimen was cycled at 222 kN. The overall displacement was 45.6 mm, which is an increase of 5 and 16 times over the displacements obtained during similar load level cycles at the initiation of this test, and the test on the original virgin specimen (Specimen 4) respectively.

Views of the third story panel after failure and of the separation between the third floor slab and the top of the columns are shown in Fig. 4.31(a).

The shear deformation at the third floor panel was monitored with linear potentiometers attached to the slabs, and the third floor displacement was monitored with a potentiometer attached to the column. A large crack opened between the third floor slab and the column (Fig. 4.31[b]), and caused significant differences in the readings of the displacement components (Fig. 4.32). A similar situation took place in Specimen 3R and is discussed in the next section.

4.3.4. Repaired Framed Wall Subjected to Cyclic Loading (Specimen 3R)

Specimen 3 was repaired, renamed Specimen 3R, and subjected to the cyclic loading program shown in Fig. 4.33. The main hysteresis diagrams are shown in Figs. 4.34 to 4.36. Views of the panel at the initiation of the test are shown in Fig. 4.37.

LP 0-103 The gravity loads were the same as those applied to Specimen 3 (Section 4.3.1). Small loads (45 and 113 kN) were cycled in order to check the loading and data acquisition systems.

LP 102-128 Load cycles at 222 kN, the cracking load for Specimen 4 (Section 4.3.2) were run for comparison. The overall displacement was 7.3 mm, this is an increase of 3.2 times over the corresponding value for Specimen 3. Note that this drop in stiffness is similar to the one observed for Specimen 4R. This was caused by the unrepaired damage in the second and third stories.

LP 128-164 The specimen was cycled at 400 kN, the working load level corresponding to Specimens 3 and 4. The overall displacement was 14.3 mm, which is an increase of 1.72 times over the total displacement obtained under equivalent cycles in Specimen 4 (Section 4.3.2)

LP 164-438 The specimen was loaded to the north, reaching a displacement of 18 mm at 937 kN. Cracking developed in the first floor panel, and only two small new cracks appeared in the second floor panel (Fig 4.38). When the load was reversed, the specimen reached -18 mm at a lateral load of -846 kN. Since the original Specimen 3 had not been subjected to such a high south load, new cracks formed in all three panels (Fig 4.39). The specimen was cycled two more times at this displacement level (corresponding to $\mu = \pm 1$ in the virgin specimen). The next cycles were at $\mu = \pm 2$. In the first cycle at this displacement ductility level, the lateral load reached 1300 kN (LP 276), and when reversing the load to the south (LP 300) a crack opened at the interface between the third floor slab and the top of the specimen's north column (Fig 4.40). This crack was a consequence of the "tearing action" on that connection (Fig. 4.40[c]). In order to prevent it from opening more, the south displacement in the following

load reversals was limited to a nominal displacement ductility value of -2. Upon reloading to the north a load of 1096 kN was reached (a drop of 16% in the specimen's strength). Cycling was repeated for a total of three cycles at this displacement ductility level.

LP 438-866 The specimen was cycled three times from a maximum positive displacement ductility of 3 to a maximum negative ductility of -2. During this cycling, crushing initiated at the base of the second floor panel (Fig. 4.41). The north displacement was then increased to $\mu = 4$ with the lateral load reaching 1092 kN. Upon reversal to $\mu = -2$ (with a load of 860 kN and a displacement of -41 mm), some buckling was noticed on the south column reinforcement at the base of the second floor.

The second floor panel underwent failure while reloading in the north direction to a displacement of 55 mm and a lateral load of 763 kN (LP 726). Buckling of the horizontal reinforcement and concrete crushing took place (Fig. 4.41[b]). After the strength stabilized at 595 kN, the load was increased again to 727 kN which brought about failure of the connection between the third floor slab and the north column. Two subsequent cycles were performed at this displacement ductility level, showing a large drop in the specimen's strength, and completing the damage as shown in Figs. 4.42 and 4.43.

The diagram of displacement components is shown in Fig. 4.44. As was the case in Specimen 4R (Section 4.3.3) this diagram shows considerable differences between the recorded overall third floor displacement component and the sum of the displacement components. This is caused by the separation between the third floor slab and the north column.

Figures 4.43(c) and 4.43(d) show the instrumentation used for measuring the third floor displacement and the locations of that used to monitor the shear deformations at the third story. These are attached at different points (A and B in Fig. 4.43[d]). While normally the distance between these points is expected to remain constant throughout the test, in the case reported the crack between the slab and the column caused distance AB to change. This rendered the readings for the shear deformations at the third story inaccurate after LP 300. The shear displacement at the third floor (Fig. 4.35) was computed based on the measured shear deformations of the individual panels, and is consequently inaccurate for the readings after LP 300.

4.3.5. Virgin Rectangular Wall Subjected to Monotonic Loading (Specimen 5)

This rectangular wall model was subjected to the loading program shown on Fig. 4.45. The main force deformation diagrams are shown in Figs. 4.46 to 4.49.

LP 0-28 Gravity loads of 229 kN per column (Fig. 3.2) were applied to the specimen, maintaining the loads in both vertical jacks within ± 45 kN to avoid unbalanced moments.

LP 28-72 The lateral jacks were connected, and small lateral load cycles (± 45 kN) were applied. The stresses generated by these loads were very small so as not to cause any cracking or permanent deformations. These cycles were applied for the purpose of checking the loading setup and the data acquisition system.

LP 72-134 The specimen was cycled eight times at working load level (279 kN). The first tensile crack in the columns were observed at ± 110 kN. A long diagonal crack was observed in the panel at 250 kN. At the conclusion of these cycles several horizontal hairline cracks were observed in the columns with a spacing of approximately 70 mm. Some of the cracks penetrated the lower part of the panel. The overall displacement in these cycles was 5 mm.

LP 134-202 Lateral loads were increased monotonically. At 613 kN, diagonal hairline cracks with 100-140 mm spacing were observed in all panels (Fig 4.50). The outermost tensile bar in the south column reached yield strain at a lateral load of 709 kN (LP 159) and a 12 mm displacement at the third floor level. In members with more than one layer of vertical reinforcement, not all the tensile reinforcement yields simultaneously. The force displacement diagram does not indicate overall yielding (Fig. 4.46) until after all the tensile column reinforcement yields. At a load of 788 kN (LP 170) the force displacement diagram shows overall yielding of the subassemblage (wall). A nominal value of 12.7 mm was taken for the initial

yielding of the force displacement curve of Fig. 4.46.

The strain readings are referred to a reference zero reading obtained at the initiation of the test and the true strains in the reinforcing bars may differ from the test recorded values because of initial construction and shrinkage strains. On the average these strains reach $200 \mu\epsilon$ in compression. If the third floor displacement recorded when the outermost tensile reinforcement yielded (LP 159), had been the one used as a reference yield displacement, the values of overall displacement ductility would be 7% higher. Initial concrete crushing at the base of the compression column was observed immediately after yielding of the specimen.

When a top floor displacement of 37 mm was reached (LP 198), the lateral load was returned to zero to perform free vibration tests and service load cycles.

LP 202-250 A series of three working load cycles was performed. The overall displacement in these cycles was 11.9 mm. Comparing it to the 5 mm obtained in the working load cycles for the virgin specimen (LP's 72-134), the ratio, $11.9/5 = 2.34$, indicates a smaller reduction in stiffness than that determined from the free vibration tests, where (on basis of the natural frequencies measured) this ratio is $(1.77)^2 = 3.15$ (Table 4.2). The smaller ratio of reduction is due to the larger displacement amplitude and the axial load acting on the specimen, both of which contributed to the closing of the cracks and the increase in the EI of the section.

LP 250-355 The specimen was reloaded, and this time yielding was more gradual (Fig. 4.46). At 840 kN (LP 273), the column in compression initiated spalling, and the compression region panel showed initial crushing. The spalling was not symmetric around the column, it was concentrated on only one surface causing some eccentricity in the cross-section. At a displacement of 74.8 mm, the peak load of 916 kN was reached (LP 309), and rupturing of steel was heard at the base of the compressive column indicating rupture of a lateral confinement hoop. The load dropped to 742 kN, and, when loading was continued to the north, buckling of the longitudinal bars at the base of the north compressive column was observed. A further drop in the load to 296 kN occurred. Some hairline cracks appeared in the panel, indicating out of plane deformations (shown as dashed lines, Fig 4.51). At this point, in order to prevent the collapse of the specimen, the load was returned to zero. The specimen was still capable of sustaining the axial gravity load.

LP 355-440 A series of service load cycles was performed. These were unstable in the north direction. The overall displacement in these cycles was 29.5 mm, which gives a reduction in stiffness with respect to the service load cycles in the virgin specimen, (LP's 72-134) of $29.5/5 = 5.9$.

LP 440-600 Loading in the south direction (Fig. 3.3) introduced compression in the south column and panel, which had a large number of residual open tensile cracks. Some cracks reached 3.5 mm opening and, consequently, the specimen's cross-section had a reduced EI. At a load of -378 kN (LP 451), a small out of plane deformation of the panel and compression column along the first floor span was observed (Fig. 4.52). Upon increased loading (at -847 kN LP 526), a flexural shear crack initiated at the buckled region of the north column and the zone of crushed concrete in the northern portion of the panel propagated all the way through the specimen (Fig. 4.53). At this point the load dropped to -251 kN, and the displacement reached -74 mm.

The third floor displacement was then returned to zero in order to facilitate repairs. In this last phase, the lateral load could barely reach 70 kN. Nevertheless, the specimen was still supporting the vertical loads on the columns.

Figure 4.54 shows the displacement component diagrams for the third and first floor levels. From this figure, it can be observed that the percentage of shear deformation with respect to the total deformation tends to rise as the deformations and damage in the specimen increase, particularly in the story where the damage is concentrated.

The contribution of the shear deformation component is relatively higher for the first story than for the third. There are two reasons for this. First, the flexural rotations at the base cause larger displacements at sections higher above the foundation. Secondly, the flexural and

shear cracks are concentrated in the first panel, and shear deformations are higher for that panel.

4.3.6. Virgin Rectangular Wall Subjected to Cyclic Loading (Specimen 6)

The specimen was subjected to the loading program shown in Fig. 4.55 and the main force deformation diagrams are shown in Figs. 4.56 to 4.59

LP 0-18 Gravity loads identical to those applied to Specimen 5 were applied to the specimen.

LP 18-61 Cycles ± 45 kN were applied in order to check the loading and data acquisition systems.

LP 61-118 The next three cycles were applied at the working load level (279 kN). In the first cycle, cracking was initiated in the specimen, with the first flexural crack being observed at 123 kN and the first diagonal crack propagating from the column into the panel at 140 kN (Fig. 4.60). A diagonal crack did not penetrate all the way into the panel until a load of 279 kN was reached. The overall displacement at the top of the specimen for this working cycles was 5.1 mm, which is similar to that of Specimen 5 (Section 4.3.5). At the end of this work cycle, the test was transferred from load to displacement control.

LP 118-471 The specimen was cycled up to yielding at a nominal yield displacement of 12.7 mm, (which is the displacement at which yielding was noted in the overall load deformation diagram, for Specimen 5), and at a load of 729 kN.

The specimen was then cycled three times at ductility one, developing flexural cracks in both columns and throughout the panel. In the next series of cycles, $\mu = 2$ was reached at a load of 828 kN. In the second cycle at this ductility level, the load dropped by 6%. The subsequent deterioration is shown in the hysteretic diagram of Fig. 4.56. Also at $\mu = 2$ the concrete cover in the compression region of the specimen started to spall, and flexural-shear cracks up to 1.8 mm in width opened in the tensile region. The spalling at the base of the column disrupted the instrumentation used to measure the fixed end deformations. A large crack opened between the wall and the foundation. This crack reached a width of 1 mm.

Under cycling at $\mu = 3$, tensile cracks up to 2.6 mm opened, with the specimen showing widespread cracking. As can be seen in Fig. 4.61, there were numerous, closely spaced tensile cracks in the columns. These cracks remained open even after the columns went into compression.

LP 471-522 At the conclusion of the $\mu = 3$ cycles three working load cycles were applied. The overall displacement for these cycles was 25.8 mm, which is greater than the overall displacement in the initial working cycles by a factor of 5.06.

LP 522-696 In the next cycle at a $\mu = 4$, tensile cracks in the column opened up to 3.2 mm and the crack between the wall and the foundation opened up to 5 mm. In the second cycle at this ductility level, when loading to the south with -500 kN, the south column cover spalled on only one side of the specimen (Fig. 4.62) causing the column to buckle, taking part of the wall panel along with it. This type of failure is similar to the one observed in Specimen 5, and is elaborated upon in Chapter 5. At this point the lateral load capacity of the specimen dropped to 256 kN, and the test was considered completed. Figure 4.63 shows the displacement component diagrams. There is a large error in the fixed end deformation readings after concrete spalling at the base of the column took place. This spalling interfered with the instrumentation used.

4.3.7. Repaired Rectangular Wall Subjected to Monotonic Loading (Specimen 6R).

Specimen 6 was repaired, renamed 6R, and subjected to the loading program shown in Fig. 4.64, which is similar to the program used on Specimen 5. The main force-deformation diagrams are shown in Figs. 4.65 - 4.67. The damage state at the initiation of the test is shown in Fig. 4.68.

LP 0-41 Gravity loads were applied to the specimen, and cycles of ± 45 kN were run for checking the loading and data acquisition systems.

LP 41-65 Service load cycles were performed (279 kN) with an overall displacement of 5.83 mm, which indicated that the total original stiffness of the specimen had nearly been restored, with the repaired stiffness being only 14% lower than that of virgin Specimen 6 (Section 4.3.6). Even if the overall specimen stiffness had been the same, however, the EI distribution along the specimen would still be very different: the first story would still be fairly stiff, with more steel area and uncracked concrete; and the upper stories much softer, because of the previous damage (Fig. 4.68).

LP 66-106 The specimen was monotonically loaded in the north direction up to a nominal ductility value of $\mu = 3$. A displacement of 12.7 mm was taken as the nominal ductility one displacement in order to facilitate comparison with the virgin specimens.

At LP 76, with $\mu = 1$ and a load of 892 kN, a crack opened at the top of the first floor between the wall and the slab, propagating diagonally into the panel (Fig. 4.68). This was to be the main crack in the following stages.

At a load of 1130 kN, a displacement of 38.15 mm was reached (LP 92 Fig. 4.69). At that point, the main cracks in the panel and the top of the south column reached a width of 3 mm.

LP 106-130 Service load cycles were applied with an overall displacement of 11.83 mm, an increase of 2.03 times the one obtained at the initiation of the test.

LP 130-180 Loading to the north was continued, reaching a maximum load of 1162.5 kN at a displacement of 50 mm. At LP 168, with a displacement of 63 mm, the main diagonal crack in the first floor panel reached a width of 14 mm (Fig. 4.70), and the main diagonal crack in the second floor panel reached a width of 2 mm. Several steel rupturing sounds were heard at this point indicating rupture of the vertical reinforcement in the wall. The lateral load capacity of the wall dropped (LP 172 Fig. 4.65) and the lateral load was subsequently returned to zero. The specimen was still capable of resisting the gravity axial loads.

LP 180-207 A series of service load cycles was run. The overall displacement was 14.68 mm or an increase of 2.52 times over the displacement at the initiation of the test.

LP 207-313 Upon loading to the south, the concrete cover at the base of the south column started to spall at -779 kN, and the two outer bars at the base of the south column in the second floor showed signs of initial buckling. Diagonal cracks propagated through the panel and formed a grid with the cracks previously noted (Fig. 4.71). At a load of -1158 kN, the crack at the top of the north column reached a width of 4 mm. At this point, the vertical wall steel started rupturing, followed by the rupture of some column longitudinal bars. Loading to the south was continued until the lateral strength of the specimen dropped to -588 kN at -126 mm (Fig. 4.65). In this last stage, the top of the south column in the first floor panel crushed with buckling of the longitudinal bars and rupturing of the hoop confinement.

LP 313-340 A last series of service load cycles was run with an overall displacement of 28.4 mm or an increase of 4.9 times the displacement at the initial working load cycles. A diagram of the displacement components is shown in Fig. 4.72.

4.3.8. Repaired Rectangular Wall Subjected to Cyclic Loading (Specimen 5R)

Specimen 5 was repaired, renamed 5R, and subjected to the loading program shown in Fig. 4.73, which is similar to that corresponding to Specimen 6. The main force deformation diagrams are shown in Figs. 4.74 to 4.76.

LP 0-43 Gravity loads were applied to the specimen. Loads at ± 45 kN were cycled for checking the loading and data acquisition systems.

LP 43-82 Three service load cycles (± 279 kN) were performed with an overall displacement of only 5.68 mm, indicating a stiff first story.

LP 82-408 The specimen was cycled three times at a nominal ductility of one with a displacement of 12.7 mm (Section 4.3.7). In the first half-cycle at $\mu = 1$, hairline cracks appeared in the tension column and propagated into the panel (Fig. 4.77[a]). One of the cracks at the top of the first story panel propagated horizontally half-way through the panel and then diagonally across. When the load was reversed, similar cracks appeared in the opposite direction (Fig. 4.77[b]). In the first reversal at $\mu = 2$ (LP 219), rupturing of reinforcement was heard in the south column in tension, most likely indicating rupture of the #5 bars at the top of the first story where it had been welded in the repair procedure. Spalling of the concrete cover also started at this ductility level at the top of the first story, causing a crack to open and extend into the first floor slab. The widening of this crack during cycling at $\mu = 3$ rendered the readings obtained at the first floor and middle of the first story unreliable (Fig. 4.78).

The drop in strength from the first to the third cycle was 29 kN (3.5%) for $\mu = 1$, 128 kN (12%) for $\mu = 2$ (where the #5 bar ruptured), and 177 kN (17%) for $\mu = 3$ (where several vertical reinforcement panel bars ruptured at the welds). In the last cycle at $\mu = 3$, slippage on the horizontal crack at the top of the first panel was 14.5 mm.

LP 408-429 Three cycles of service loads were applied, having an overall displacement of 32.47 mm or an increase of 5.8 times the initial service load cycles. This high ratio (>4) indicates extensive damage in the specimen.

LP 4299-575 Three cycles at a ductility of ± 4 were performed (note that the ductility for the story where the damage is concentrated is larger). Between the first and second cycles at this ductility, the north load dropped 205 kN. In the third cycle, more bars ruptured, and the south load dropped 366 kN to 277 kN, marking the end of this test. The overall horizontal slippage in the crack at the top of the first panel was 25 mm. The failure at the top of the first panel is shown in Fig. 4.79. Figure 4.80 shows the displacement components. As shown in the latter figure, shear deformation significantly increased during the three cycles at $\mu = 3$.

4.4. Photogrammetric Readings

4.4.1. Accuracy

Kodak Tri-X panchromatic 100 mm x 125 mm glass plates were used for the photogrammetric readings in all specimens, with the exception of Specimens 3R and 4R in which celuloid plates were used.

The specimens appear in the photographic emulsion at a scale of 1/24.36. The comparator used to read the photogrammetric plates has a maximum accuracy of one micron ($10^{-6}m$), which corresponds to 0.0244 mm in the specimen. Unfortunately this ideal accuracy cannot be easily obtained.

When several careful readings for the same target in the emulsion are taken in the comparator, discrepancies of 10 to 15 microns are found even at a sharp point. Consequently the best accuracy that can be expected under ideal conditions is on the order of 0.24 to 0.36 mm in the specimen. This accuracy deteriorates very fast with bad quality of the photographic plates (over or under exposure and or development, fuzziness of the targets etc.) and the errors can reach 1.2 mm or more. The fuzziness of the targets seems to be caused by three reasons: 1) the relatively large grain size in the emulsion used; 2) an apparent out of flat field that renders the targets in the center of the specimen sharp, but the ones in the outer part out of focus; and 3) a general unsharp focus because of human error. The first problem could be minimized somewhat by using a finer grain emulsion, and the other two by closing the diaphragm in the photogrammetric cameras to a minimum for greater depth of field. This requires a corresponding increase in the exposure times.

Since the lines in the photogrammetric grids are spaced at 152 mm, the error in the readings is equivalent to a strain of:

$$\begin{aligned}\epsilon &\approx 0.0016 \text{ m/m} && \text{for a sharp point} \\ \epsilon &\approx 0.008 \text{ m/m} && \text{for a fuzzy point}\end{aligned}$$

This error is too gross to attempt the computation of strain distributions on the basis of photogrammetric data. Even at the load points corresponding to the largest deformations, where the strains in localized regions are very large, the use of these data for determining the strain distributions is not recommended because in general targets are lost in regions of large strain and damage concentration. On the other hand, these errors are relatively small when compared to the values of displacement observed in the specimens during the test.

In conclusion, the photogrammetric data can be used to compute deformation patterns, but is unsatisfactory to compute strain distributions.

4.4.2. Results

The deformed configurations for all the specimens are shown in Figs. 4.81 to 4.87.

Figure 4.81(a) shows the lengthening of the south column, and the compression and pivoting at the base of the north column of Specimen 3 (see also Fig. 4.7[b]). The neutral axis position indicates that only a small portion of the panel undergoes compressive stresses. Figure 4.81(b) shows the deformed configuration at the point of buckling of the south boundary element, indicating the existence of very large residual tensile strains, and a double curvature for that element.

Figure 4.82 shows the deformation pattern at different stages during the last cycle at ductility four in Specimen 4. Load points 83S and 83T were chosen as the points where the slope in the shear-shear displacements diagram (Fig. 4.15) changes drastically. The elastic rebound when unloading (Fig. 4.14 LP 82-83) is shown in Figs. 4.82(a) and (b); it can be observed that the column in compression rebounds more than the column in tension. This is because cracks in reinforced concrete tend to remain open when shear slip along the crack takes place. This phenomenon will be discussed later. From LP 83S to LP 83T there is a significant lateral deformation with only a very small variation in the axial lengths of the boundary elements. This is a range in which most of the deformation is accounted for by shear slippage along the open cracks. From LP 83T to 84 the lateral deformation brings along a significant variation in the axial length of the boundary elements, with a significant increase in the lateral force level (Fig. 4.15). From LP 84 to LP 85 there is an elastic rebound similar to that from LP 82 to LP 83.

Figure 4.83 shows the deformation pattern for Specimen 4R. The large distortion at the top of the boundary element agrees with the crack pattern shown in Fig. 4.29.

Figure 4.84 shows the deformation pattern for Specimen 5. From LP 312 to LP 342 local buckling at the base of the north boundary element took place, (Section 4.3.2), and a considerable shortening can be observed in this element (Fig. 4.84[b]). Note that large tensile strains remain in the south boundary element and most of the panel. Figure 4.84(c) shows the deformation pattern after flexural shear failure with a large shear displacement along a horizontal flexural crack at the base of the panel took place.

Figure 4.85 shows the deformation pattern for Specimen 6. At LP 149 yielding of the specimen was just reached, and the deformations are small and regular, with the neutral axis practically at the edge of the boundary element. At LP 532 large tensile strains were observed in the south boundary element and most of the panel. When the load was reversed, the north boundary element in turn showed large tensile strains. When comparing the deformations for LP 532 and LP 638, it can be observed that the residual tensile strains accumulate, and that there was an overall lengthening of the specimen. (The north boundary element shows residual lengthening while subjected to compression). LP's 561 and 670 correspond to the same ductility level, but at LP 670 the south boundary element has buckled, and a large strain concentration can be observed at its base.

Figure 4.86 shows the deformation pattern for Specimen 6R. At LP 168 a very large crack was observed running horizontally at the top of the first panel, and then diagonally into the panel (Fig. 4.17). When reversing the load, at LP 300, loss of confinement and crushing took place at the top of the south boundary element, damaging the concrete and interfering with the photogrammetric readings.

Figure 4.87 shows the deformations for Specimen 5R. In this specimen a large crack opened at the top of the first floor panel and residual tensile deformations were observed horizontally in the upper region of the first floor panel under load reversals.

5. EVALUATION OF EXPERIMENTAL RESULTS

The experimental results are interpreted and compared to theoretical values predicted by the code and different analysis methods. The results studied are: the overall hysteretic behavior, the failure mechanisms, and the effect of the test parameters in the overall behavior.

5.1. Overall Hysteretic Behavior

The behavior characteristics studied are the strength, stiffness, deformation capacity and energy absorption and dissipation capacities. Comparison is made between values predicted according to code assumptions and values predicted according to different analysis methods. In several cases the agreement between the experimental and analytical methods is not very good. Better prediction methods are developed and presented in the next chapter.

5.1.1. Strength

The strength at different load levels: flexural cracking, shear cracking, working, yield and maximum strength is studied.

(a) Flexural Cracking Load

According to UBC's Eq (9-5) the flexural cracking load can be computed as:

$$M_{cr} = \frac{f_r I_g}{Y_t} \quad (5.1)$$

where:

f_r = Modulus of rupture of concrete

I_g = Moment of Inertia of the gross concrete cross-section neglecting the reinforcement

Y_t = Distance from centroid to extreme tension fiber

This equation yields:

$$M_{cr} = 0.631 \times 10^9 \text{ N}\cdot\text{mm} \quad \text{or} \quad V_{cr} = \frac{M_{cr}}{4383 \text{ mm}} = 144 \text{ kN}$$

for the framed wall specimens, and

$$M_{cr} = 0.386 \times 10^9 \text{ N}\cdot\text{mm} \quad \text{or} \quad V_{cr} = \frac{M_{cr}}{3849 \text{ mm}} = 100.3 \text{ kN}$$

for the rectangular wall specimens.

Comparing the code values to those obtained experimentally (Table 5.1):

$V_{cr} = 222 \text{ kN}$ for specimens 3 and 4

$V_{cr} = 110 \text{ kN}$ for specimen 5

$V_{cr} = 123 \text{ kN}$ for specimen 6

it can be observed that the code assumptions underestimate the specimen's flexural cracking strength. If instead of neglecting the longitudinal reinforcement, a correction to the code equation is made by computing the moment of inertia of the composite reinforced concrete cross-section, a better agreement with the experimental results is obtained.

$V_{cr} = 175 \text{ kN}$ for the framed walls, and

$V_{cr} = 130 \text{ kN}$ for the rectangular walls.

(b) Flexural Shear Cracking Load

According to Eq. (11-11) for prestressed concrete members, in Chapter 26 of the UBC code, the flexural cracking load can be obtained from (modifying the equation to put it in terms of SI units):

$$v_{cr} = 0.049 \sqrt{f_c} + \frac{V_d + \frac{V_l M_{cr}}{M_{\max}}}{b_w d} \quad (5.2)$$

where:

- v_{ci} = shear stress at diagonal cracking (MPa)
- V_d = shear force at section due to dead load
- V_l = Shear force at section occurring simultaneously with M_{max}
- M_{max} = Maximum bending moment due to applied design loads

This equation yields:

- $v_{ci} = 1.099$ MPa which can be expressed as
- $V_{ci} = 352.6$ kN for the framed walls, and
- $v_{ci} = .8273$ MPa, which can be expressed as
- $V_{ci} = 227$ kN for the rectangular walls

where:

$$V_{ci} = v_{ci} b_w d \text{ is the total base shear at diagonal cracking.}$$

The experimentally observed diagonal cracking loads are shown in Table 5.1 and are in general agreement with the computed values. It should be noted that the tensile cracking strain for concrete is very small (on the order of $300 \mu\epsilon$), and since the shrinkage strains can be of that order of magnitude they can significantly affect the load at which initial cracking takes place.

(c) Working Load

The working load level can be ascertained from the definitions given in Section 2608 J of the UBC [30] code. It is specified that under working load the tensile stresses in the steel shall not exceed the specified allowable stress of 165.5 MPa (for steels with an f_y of 414 MPa or more), and the extreme concrete compressive strength shall not exceed $0.45 f'_c$. In the walls studied the tension reinforcement reaches a strain corresponding to $0.40 f_y$ before the concrete in compression reaches $0.45 f'_c$. The theoretical working loads (assuming pure flexure effects, plane sections remaining plane, linear strain distributions, and the experimentally observed material properties) were 400 kN and 292 kN for the framed and the rectangular walls respectively.

These values are shown in Table 5.1, together with the experimentally observed values. The measured working load values were estimated on basis of the largest of the strains indicated by strain gages C3, C4 and C5 (Fig. 3.5) and the experimentally obtained stress strain relationship for the reinforcement (Figs. 2.9 and 2.10).

(d) Initial Yield Load

The initial yield load is that at which the tensile steel reaches the yielding strain value. The walls having distributed vertical reinforcement show a somewhat gradual variation of slope in the overall force deformation diagram. This causes problems in defining a "yield point". Until a unified criterion for this definition is reached, care should be exercised in interpreting reported ductility values. For example, for Specimen 3 the outermost tension bar yielded at a third floor displacement of $\delta_3 = 12.2$ mm and the whole column cross-section at the base yielded at $\delta_3 = 19.8$ mm (Section 4.3.1). It should also be noted that the yielding of the steel was determined on basis of the strain gage readings obtained during the test, and that these readings are referred to a zero reading at the initiation of the test, which does not necessarily correspond to a zero stress condition in the steel bar. In general the bar has an initial strain because of shrinkage which in the specimens tested was on the average $200 \mu\epsilon$ (or an initial stress of 42 MPa) in compression.

The initial yield values observed experimentally together with those computed with the assumption of linear distribution of strains, plane sections remaining plane, and realistic material properties, are shown in Table 5.1. The experimental initial yielding strains were estimated on basis of the strains recorded by gages C3, C4 and C5. (Because of the stress redistribution after diagonal cracking, the strains at C5 can be of the same magnitude as the strains

at C3 and C4, this phenomenon is elaborated upon in a latter section.)

(e) Maximum Flexural Strength

The philosophy most commonly used in earthquake resistant design is intended to prevent the possibility of brittle failure (i.e. shear failure). The elements are thus designed so that their force resistance is limited by their flexural strength, and the intended failure mode is ideally ductile (i.e. rupture of the tensile reinforcement).

For this reason it is important to be able to determine the flexural strength of the specimens with reasonable accuracy.

1) Analysis Using the Code Assumptions

The maximum flexural strength was computed using the specified material properties, assuming linear variation of strains along a section, and the equivalent concrete stress block suggested by the ACI. The effect of the axial load was accounted for. The results are presented in Table 5.2. It can be seen that the code consistently underestimates maximum flexural strength.

2) Approximate Analysis:

The maximum flexural strength can be estimated by the following formula

$$M_{\max} = (A_{s \text{ col}} f_{\max} + D/2) d \quad (5.3)$$

where

$A_{s \text{ col}}$ = Cross-sectional steel area in boundary element

f_{\max} = Maximum stress of longitudinal reinforcement

D = Axial dead load in specimen

d = Effective depth of section, taken here as the center to center distance between boundary elements

This formula does not consider compatibility, nor the effect of concrete or the vertical panel reinforcement, and is intended to give only an estimation of the maximum moment capacity without demanding much computational effort. For an accurate estimation of the maximum moment capacity a more refined analysis should be used as explained in the next section.

The basis for this simplified formula is the assumption that the flexural strength of the specimen is controlled by the tensile strength of the longitudinal reinforcement. This means that buckling has been delayed, and the strength of the compression element (steel and confined concrete), is greater than the tensile strength of the tension element. It is also assumed that when this tensile strength is reached, the resultant of the compression forces is very close to the axis of the compression boundary element, and the contribution of vertical panel reinforcement to flexural strength is negligible when compared to that of the boundary elements.

This simplified equation yields the following results:

For the framed walls:

$$M_{\max} = [(2315.5 \text{ mm}^2)(639 \text{ MPa}) + 434 \text{ kN}] 2.134 \text{ m} = 4084 \text{ kN-m}$$

which in terms of the base shear V is:

$$V_{\max} = \frac{M_{\max}}{4.383} = 931 \text{ kN}$$

where 4.383m is the effective moment arm of the forces acting on the wall.

For the rectangular walls:

$$M_{\max} = [(1780.6 \text{ mm}^2)(687 \text{ MPa}) + 299 \text{ kN}] 2.134 \text{ m} = 3249 \text{ kN-m}$$

which in terms of the base shear is

$$V_{\max} = \frac{M_{\max}}{3.849} = 844 \text{ kN}$$

3) Refined Analysis

The maximum flexural strength was calculated by using a more refined analysis. The cross-sections shown in Fig 5.1 were analysed to obtain the corresponding moment curvature relations. The computer program RCCOLA [23] was used and the following assumptions were made:

- a) Plane sections remain plane
- b) Bond slippage effects are not accounted for.
- c) The stress-strain relations used for the steel are shown in Figs. 2.9 and 2.10, for the rectangular and the framed walls respectively. The panel steel was assumed to have identical material properties as the column reinforcement (RCCOLA allows only one steel stress-strain relation to be defined). This assumption is believed to introduce only a small error.
- d) Different stress-strain relations were used for the confined and the unconfined concrete (Fig. 5.2), these were based on the results obtained in Ref. [9].
- e) The tensile strength of concrete is neglected.
- f) The redistribution of stresses because of the shear cracks is not accounted for.

The resulting moment curvature relations are shown in Figs. 5.3 and 5.4 and compared to the curvatures experimentally observed in Specimens 3 and 5 (the data used was that recorded with clip gages K1 and K11 in Fig. 3.4). It should be noted that the experimental curvature values do not include the fixed end rotations. It can be seen on Fig. 5.3 that the analysis was able to predict the moment curvature relations for Specimen 3 with excellent accuracy up to the point of maximum strength. After this point there is a drop in the experimental strength mainly because of the spalling of the concrete cover, and the confined concrete's reduction in load carrying capacity (see Table 5.2). This causes the position of the neutral axis to shift back (Fig. 5.5) and some of the concrete and steel in the specimen's cross-section to undergo load reversal.

Since the computer program used does not have the capability of handling unloading, it cannot accurately predict the moment curvature diagram beyond the maximum strength point.

Figure 5.4 shows the moment diagrams for Specimen 5. It can be seen in Table 5.2, that the maximum specimen strength obtained experimentally is 7% less than that predicted using assumptions similar to those in the analysis of Specimen 3. Specimen 5 was not able to reach the ductility at which the maximum strength was expected, because the unsymmetric spalling of the cover in the boundary element caused the specimen to have an early stability failure (Section 4.3.5).

Table 5.3 shows the analytical value of the curvature at the base of the specimen when the maximum strength is reached. The agreement with the experimental results for the case of Specimen 3 is very good. For the case of Specimen 5, it is shown that the maximum strength could not be reached because of premature failure.

(f) Maximum Shear Strength

According to the UBC code assumptions the shear strength of the specimens can be ascertained from (see Section 2.2).

$$V_u = \phi(0.8 \ell_w b_s v_c + 0.8 \ell_w b_w \rho_h f_y) \quad (5.4)$$

Using the specified values for f_y and f'_c , and:

$$v_c = 2\sqrt{f'_c \text{ psi}} (= .166\sqrt{f'_c \text{ MPa}}):$$

1) For the framed wall specimens

$$\frac{V_u}{\phi} = [(.8)(2387.6)(101.6)(.166 \sqrt{27.53}) + (.8)(2387.6)(101.6)(.0082)(413)] = 826. \text{ kN}$$

2) For the rectangular wall specimens

$$\frac{V_u}{\phi} = [(.8)(2413)(114.3)(.16608 \sqrt{27.53}) + (.8)(2413)(113.3)(.0054)(413)] = 684. \text{ kN}$$

Table 5.2 shows the observed specimen strengths to be higher than those obtained with the code assumptions. The reason for this difference is that the UBC code neglects the actual material properties, the contribution of the boundary elements, the strain hardening of the wall steel, and the effect of the floor slabs in restraining the opening of the shear cracks.

In this way the code provisions for shear strength are conservative for monotonic loads. This agrees with the comparison made by Cardenas et al. of the ACI code provisions [35] with experimental results for walls under monotonic loading [47]. But it should be noted that for the case of cyclic loading the shear strength can drastically drop and the code provisions are not intended to take this into account.

(8) Maximum Shear Strength Compared to Ordinary Beams

It is interesting to note that the maximum shear stress levels obtained in the structural wall specimens are in general higher than those obtained for ordinary beams [24,41]. While under cyclic load conditions v_u values of $1.116 \sqrt{f'_c}$ MPa were obtained in this investigation for $\mu_\delta=4$. For this same μ_δ the upper bound for beams is of the order of $0.55 \sqrt{f'_c}$ MPa. Several factors account for this better performance.

1. The arch or truss action (the flow of compressive stresses that can develop between the load and the support), is most effective in the case of deep beams and is similar to the flow of compressive stresses in structural walls. Experiments in panels with no reinforcement [48] have shown that the shear strength decreases with the slenderness ratio (Fig. 5.6).
2. When large lateral forces are applied, the region of the cross-section in the compression side of the neutral axis is subjected to high shear and axial compressive stresses. In a structural wall the confined concrete boundary element in this region is very effective in taking shear stresses.

5.1.2. Stiffness

(a) Uncracked Stiffness

The material nonlinearities at load levels below the flexural cracking load can be assumed to be small enough to allow the use of linear elastic methods. The elastic deformation at the third floor level δ_3^e can be expressed as:

$$\delta_3^e = \delta_3^e_{shear} + \delta_3^e_{flexural} + \delta_3^e_{fixed\ end} \quad (5.5)$$

1) Flexural Stiffness (see Fig. 5.7)

$$\delta_3^e_{flexural} = \int_0^{h_3} \frac{M(h) [h_3-h] dh}{E_c I} \quad (5.6)$$

$$= \frac{V}{E_c I} \left[\frac{h_3^3}{3} + (h_v - h_3) \frac{h_3^2}{2} \right] \quad (5.7)$$

for the framed walls, and

$$= \frac{V}{E_c I} \left[1.799 \frac{h_3^3}{3} + (h_v - h_3) \frac{h_3^2}{2} \right]$$

$$+ \frac{0.1038(h_2^3)}{3} + \frac{0.0974(h_1^3)}{3} \\ + \frac{0.1038}{2} \frac{h_2^2}{(h_3-h_2)} + \frac{0.0974}{2} \frac{h_1^2}{(h_3-h_1)}$$

for the rectangular walls (see Fig. 5.7).

In these equations:

$$h_3 = \text{height of third floor slab over the foundation level} = 3001 \text{ mm}$$

$$h_v = \text{effective shear span} = 4383. \text{ mm}$$

$$I = 248 \times 10^9 \text{ mm}^4 \text{ (framed wall)}$$

$$= 172 \times 10^9 \text{ mm}^4 \text{ (rectangular walls)}$$

$$E_c = 21300 \text{ MPa} \text{ (this value is taken Ref. [9])}$$

The flexural stiffness can then be computed as

$$\delta_3^{\xi}{}_{flex} = 2.88 \text{ mm/MN}$$

$$K_3^{\xi}{}_{flex} = 0.346 \text{ MN/mm}$$

for the framed walls, and replacing:

$$h_v = 3851 \text{ mm}$$

$$h_2 = \text{height of second floor slab over foundation level} = 1829 \text{ mm}$$

$$h_1 = 1219 \text{ mm}$$

For the rectangular walls it can be obtained:

$$\delta_3^{\xi}{}_{flex} = 2.984 \text{ mm/MN}$$

$$K_3^{\xi}{}_{flex} = 0.436 \text{ MN/mm}$$

2) Shear Stiffness

$$\delta_3^{\xi}{}_{shear} = \frac{F}{G A_v} \int_0^{h_3} V(h) dh \quad (5.8)$$

Where F is a form factor that for I sections can be taken as 6/5. A_v can be taken as the area of the web:

$$A_v = 243 \times 10^3 \text{ mm}^2 \text{ (Framed walls)}$$

$$A_v = 280 \times 10^3 \text{ mm}^2 \text{ (Rectangular walls)}$$

and

$$G = \frac{E_c}{2(1+\nu)} \quad (5.9)$$

From Ref. [9] the value of ν is taken as 0.2 for confined concrete.

$$G = \frac{21300}{2(1+0.2)} = 8875 \text{ MPa}$$

$$\delta_3^{\xi}{}_{shear} = 1.66 \text{ mm/MN}$$

$$K_3^{\xi}{}_{shear} = 0.600 \text{ MN/mm}$$

for the framed walls, and

$$K_3^{\xi}{}_{shear} = 0.743 \text{ MN/mm}$$

for the rectangular walls.

3) Total Stiffness

The fixed end rotation deformation component is small enough so that its contribution to the total stiffness can be neglected.

The total stiffness can then be estimated as:

$$K_3^c = \frac{1}{\frac{1}{K_3^c \text{ flex}} + \frac{1}{K_3^c \text{ shear}}} \quad (5.10)$$

$$= 0.220 \text{ MN/mm} \quad \text{for the framed walls}$$

$$= 0.230 \text{ MN/mm} \quad \text{for the rectangular walls}$$

Figures 5.8 and 5.9 show the initial portion of Figs. 4.2 and 4.46 greatly enlarged, with the initial stiffness values shown. Table 5.4 shows the comparison of the analytical and experimental results. It can be observed that the agreement is good.

(b) Cracked Stiffness

The stiffness of the wall after flexural cracking can be ascertained assuming that the concrete does not take tension stresses.

Analysis was made accounting for the realistic stress-strain characteristics of materials, the contribution of the vertical wall panel reinforcement, the effect of axial load, and by assuming a linear strain distribution along the wall cross-section, and a linear curvature distribution along the height of the wall.

1) Flexural Stiffness

The flexural stiffness for the framed walls is:

$$K_3^c \text{ flex} = 0.201 \text{ MN/mm}$$

which is a decrease in flexural stiffness of 1.718 times.

The flexural stiffness for the rectangular walls is:

$$K_3^c \text{ flex} = 0.197 \text{ MN/mm}$$

which is a decrease in flexural stiffness of 1.692 times.

2) Shear Stiffness

Assuming that the flexural cracks do not interfere with the shear stiffness, the procedure used in section 6.1.2.1 gives:

$$K_3^c \text{ shear} = 0.600 \text{ MN/mm}$$

for the framed walls, and

$$K_3^c \text{ shear} = 0.743 \text{ MN/mm}$$

for the rectangular walls.

3) Overall Stiffness

The specimen's overall stiffness, according to Eq. 5.10 is

$$K_3^c = 0.151 \text{ MN/mm}$$

for the framed walls, and

$$K_3^c = 0.156 \text{ MN/mm}$$

for the rectangular walls.

Comparing experimental and analytical values (see Table 5.4), it can be concluded that while for framed walls there was a good agreement, for the rectangular walls the agreement

was not so good (15% difference).

(c) Stiffness at Initiation of Yielding

At the point initial yielding took place, the walls in this investigation presented widespread diagonal cracking. This type of cracking is characteristic of deep members subjected to high shear stresses, and significantly affects the stiffness values.

1) Flexural Stiffness

Assuming a linear variation of curvature along the height of the wall, and on the basis of results of the analytical determination of the moment-curvature relation (Figs. 5.3 and 5.4):

$$K_{3\ flex}^y = 0.147\ MN/mm$$

is obtained for the framed walls, and

$$K_{3\ flex}^y = 0.150\ MN/mm$$

is obtained for the rectangular walls.

2) Shear Stiffness

As previously mentioned, at the point of initial yielding there is widespread flexural and diagonal tension cracking. Under these conditions, the initial uncracked deep shear beam mechanism is no longer effective. Most of the shear strength is provided by compression stresses developed along diagonal concrete struts, and by tension in the wall reinforcement. There is also a contribution of interface shear transfer and the dowel action.

At this stage, the determination of the shear stiffness is a difficult problem: there is not much useful knowledge in the available bibliography concerning this subject, which is further pursued in the next chapter, where a possible solution is suggested.

In the present Section, a rough estimate of the shear stiffness is made by recognizing that at the point of initial yielding there is widespread flexural tension cracking in the tension boundary element, and there are also diagonal shear cracks in the panel (Fig. 4.6). The assumption that only the portion of the concrete that remains uncracked is effective in taking shear stress, (that is, the effective shear area is the portion of the cross-section at the base of the specimen which is in the compression side of the neutral axis) neglects the contribution to the shear strength given by the wall reinforcement, the interface shear transfer, and the dowel action. The shear stiffness can be calculated as:

$$K_{3\ shear}^y = 0.213\ MN/mm$$

for the framed walls and

$$K_{3\ shear}^y = 0.226\ MN/mm$$

for the rectangular walls

3) Overall Stiffness

The overall stiffness values are shown in Tables 5.4 and 5.5. Note that the overall stiffness found in the basis of the observed third floor displacements does not agree with that obtained by adding the individual observed deformation component stiffness. The reason for this is the limited range of accuracy of the instrumentation used to measure the shear deformations. The stiffness found in the basis of the third floor displacements is more reliable.

(d) Comparison With Experimental Results, and Observations on Stiffness Values

The experimentally observed values for the secant stiffness are shown in Figs. 5.8 and 5.9 and compared to the computed values in Table. 5.4, with a breakdown of these stiffness values into components shown in Table 5.5.

While a very good agreement is obtained for the initial uncracked section stiffness, the computed values in general overestimate the observed results.

1) Flexural Stiffness

The main difficulty is that the curvature distribution is a function not only of the moment distribution, but also of the shear. Diagonal shear cracking reduces the effective EI of the cross sections above the foundation. As shown in Fig. 5.11, in order to maintain equilibrium after losing the concrete tensile stresses, the axial force T_C at the top of the boundary element increases, and approaches the value of the axial force at the base of the wall T_B . This can be interpreted as a truss effect, and is also illustrated in Figs. 5.12 and 5.13. In Fig. 5.12 it can be observed that the actual curvature distribution resembles that of the beam theory only at the sections where diagonal cracking is restrained (i.e. at the foundation and floor slabs). At the upper portion of each panel, where the diagonal cracks are open, the actual curvature distribution resembles that found by using a "truss analogy" in which the stresses in the boundary elements are constant along each span. The flexural stiffness values computed by beam theory agree with the observed ones (Table 5.5) because the differences in curvature distribution average out. Figure 5.14 shows curvature distributions for Specimens 4,5, and 6 following a similar pattern.

2) Shear Stiffness

The largest error in the estimation of the specimens' stiffness is in the shear stiffness (Table 5.5). This indicates that the shear resisting mechanism is more flexible than that assumed in the computation.

Is very hard to ascertain the degree of restraint that the slab, cracked panel and boundary elements present to the shear deformations. This is the subject of one section in the next chapter.

5.1.3. Deformations of Structural Wall Specimens

In this section the deformations observed in the test specimens are discussed. Emphasis is made on the deformation components and on the maximum deformations. The accurate analytical prediction of deformations in reinforced concrete members subjected to high shear stresses is very difficult. The deformation at different loading stages can be computed on the basis of the strengths and stiffnesses determined in the previous sections (Sections 5.1.1. and 5.1.2.). Figures 5.8 and 5.9 show the deformations at: 1) flexural cracking, 2) diagonal shear cracking, and 3) initial yielding. It can be observed that the agreement with the experimental results after shear cracking takes place is not very good. Better procedures are suggested in the next chapter.

There is a need to predict the maximum deformation capacity of a structural wall because it gives an indication of the ductility available under extreme loading conditions. This maximum deformation is defined as the deformation that can be reached before failure or a significant drop in strength is reached (the lateral load strength dropping below that corresponding to the working load strength). The failure mechanisms limiting the deformation capacity are discussed in Section 5.2.

(a) Observed Behavior

Some of the observed maximum specimen displacements are listed in Table 4.1. But in order to discuss in a more systematic manner the deformation capacities of the specimens, Table 5.6 presents the deformations in terms of the deformation components at different stages defined by nominal ductility levels, and Table 5.7 presents the deformations in terms of the story drift index at the onset of failure for various panels. The inter-story drift indexes are computed on the basis of the measured differences in the horizontal floor displacements between the adjoining floors divided by the story height and are defined as:

$$R_i = \frac{\delta_{i+1} - \delta_i}{h_{i+1} - h_i} \quad (5.11)$$

The story drift index R_i , computed this way has two components at a given story i (see Fig 5.10): R_{θ_i} , the rotational drift index caused by the rigid body rotation (the accumulated

effect of the rotations in stories below the i^{th} floor level), and the tangential drift index R_{Ti} , caused by the deformations in the i^{th} story. Because of this the story drift computed for the second and third story does not exactly represent the panel deformations corresponding to those stories. Nevertheless the R_i values shown are important because the structural walls are the main lateral force resisting elements in the prototype building, and these values give an idea of the actual inter-story drifts that the space frame columns in the prototype must undergo.

It is important to know the maximum panel deformations that can be obtained. For this reason the tangential drift index R_{Ti} is presented in the same table, for the panels where failure took place. In the virgin walls, failure always took place in the lower part of the first story panel, while in the repaired walls failure was obtained in the second or third story panels.

1) Deformation at first yield of reinforcement

The tangential drift index at which initial yield was obtained ranged from 0.0035 to 0.0039 with an average of 0.0036.

2) Maximum Deformation

The maximum observed story drift index is that corresponding to the first story in Specimen 3, which reached 0.0623 under monotonically increasing loading (corresponding to a nominal story drift ductility of 16). In a realistic case, the columns in the prototype's first story frames are subjected to a high axial force, and they will require excellent detailing in order to develop the ductility to accommodate this deformation.

Specimen 4 reached a story drift index of 0.0261, with an overall cyclic story drift (the sum of the maximum overall story drift to the north and the maximum overall story drift to the south) index of 0.0518 (0.0257 + 0.0261) before developing a flexural shear failure. The rectangular cross-section walls were not able to develop as large deformations because of the stability failures associated with their geometric characteristics as will be elaborated upon in Section 6.2. Specimen 5 developed buckling of the boundary element at a story drift index of 0.0238 and at an overall cyclic story drift index of 0.0244. Specimen 6 subjected to load reversals developed buckling of the boundary element at a story drift index of 0.0193 with a nominal story drift ductility of 5.34.

The repaired walls as shown in Table 5.7 developed the largest story drifts in the upper panels. The reason for this was the stiffening and strengthening of the first story during the repair procedure. In general the repaired walls were not able to develop as large a story drift index. The main reason for this is that the longitudinal reinforcement had been previously strain hardened and welded, and consequently had a much lower ductility capacity. Several of the failures (Section 5.2) included rupture of the tensile reinforcement.

3) Comparison With Code Values.

All walls yielded before reaching the UBC [32] and SEAOC [33] allowable story drift index of $0.005K = 0.004$. In other words, the level of deformation that can be reached in the specimens before yield is smaller than that specified by the codes. While the UBC and SEAOC drift limitations are for deformations under the lateral forces specified by the code, the ATC recommendations specify the expected drift value during nonlinear response as being less than $C_d \delta_{xe} / \Delta h$ where C_d is a coefficient specified by the code as 6.5 for dual wall-frame systems, and $\delta_{xe} / \Delta h$ is the drift obtained from an elastic analysis for the ATC forces. This elastic drift is specified to be always less than 0.0023 for dual systems. In this way according to ATC the expected drift during nonlinear response is at most 0.015. The maximum drift values observed in the tests of the virgin specimens (Table 5.7) were in all cases greater than 0.015. This means that if the ATC limit was based only on a maximum inelastic strain that the wall can supply, ATC indeed underestimates the maximum drift that can be supplied by these walls.

(b) Deformation Components

The deformation capacity of a structural wall is controlled by the failure mechanisms that can develop (Section 5.2). In specimens under strictly monotonic loading and properly

designed so they can resist the shear corresponding to the maximum moment capacity, the type of failures most likely to take place are the rupture of the tensile steel and/or an instability failure in the compression element. These failures are related to the axial strains in the boundary elements. The moment and curvature corresponding to these limiting strains can be predicted from beam theory (Section 5.1.1). This is better done if the effect of load reversals, because of the shifting back of the neutral axis when the specimen strength drops, is taken into account (see Fig. 5.5). But determining the moment curvature relationship for the cross-section, or the maximum curvature that the specimen can undergo, is not enough to determine the overall force deformation nor the maximum deformation capacity of the specimen. To achieve this it is necessary to determine the curvature distribution along the specimen, the shear deformations along the specimen, and the fixed end rotation caused by the bond slip of the tensile reinforcement embedded in the foundation. While the latter is not as important in the case of the specimens tested, the other two components are very significant, and interact with each other closely.

In specimens subjected to cyclic loading conditions the deformations are limited because of deterioration of concrete, and the development of cyclic failure mechanisms associated with the load history and characteristics of the specimens (Section 5.2). As a general rule the overall cyclic deformation (the total deformation during a full loading reversal) under cyclic loading was found to be at least 75% of the deformation reached under monotonic loading. For the framed and rectangular walls 78% and 74.5% were obtained respectively, while Wang [1] reports 75% for framed walls. Since the cyclic load history with full reversals used in testing the specimens was very severe, and not likely to take place in practice, the overall deformation capacity under a realistic ground motion could be expected to be over 75% of the deformation capacity under monotonic loading conditions.

1) Curvature Distribution

As mentioned in Section 5.1.2, the curvature distribution along an element subjected to high shear stress is affected by the redistribution of stresses when cracking takes place. In Fig. 5.11, taking moment equilibrium about point A at the onset of diagonal cracking, and repeating the procedure with the same external forces, but with the diagonal crack opened, it can be seen that the disappearance of the tensile concrete stresses f_t causes an increase in the tensile force T_c , so it approaches the value of T_B . There is also an increase in the tensile stress of the wall reinforcing steel f_s , but in order to simplify the presentation the force introduced by these stresses is neglected. (The difference between T_B and T_c was estimated as between 2 and 14%). The condition of $T_B \approx T_c$ can be conceptually represented by an equivalent truss (see Fig. 5.12). In this truss there is no element taking diagonal tension, and the force along BC is constant. Consequently, as shown in the same figure, the curvature distribution in the framed wall approximates the curvature distribution in an "equivalent truss".

The geometry of this equivalent truss is such that the slope of the compression diagonals θ follows the direction of the compressive stress trajectories. Since the stress distribution changes with the development of the cracks, the angle θ , or the topology of the "equivalent truss" in general, changes with the load level and the crack propagation. This phenomenon can be observed in Fig. 5.13 where the curvature distribution at the initiation of yielding, and at the maximum displacement level is shown. At larger displacements widespread cracking causes the curvature distribution to be more uniform, but still the curvature values at the sections away from the fixed end are higher than those predicted by the beam theory (Fig 5.13(b)). Note that the moment curvature relationship computed for the section at the base of the wall is in better agreement with the observed values because the foundation block restrains the opening of the diagonal cracks.

The curvature distribution at high load levels, is shown in Fig. 5.14 for Specimens 4,5, and 6. The distribution patterns in them also resembles that of the truss analogy. This is further pursued in the next chapter on analytical modeling.

2) Fixed End Rotation

This deformation mechanism (bond slippage of the reinforcement at the fixed end) is not as important in the case of structural walls as it is in the case of ordinary beams [24, 49]. As shown in Table 5.6 the third floor displacements because of fixed end deformations amount to 7 to 11% of the total third floor displacement. There are several reasons for this:

- a) For the same amount of bond slip the displacement of the free end in a deep beam is less than in a normal slender beam (Fig. 5.15).
- b) The longitudinal reinforcement in the specimens tested was well anchored into the foundation.

Note that the models were designed according to the code requirements for the prototype. According to the UBC code, Section 2612(f), the basic development length shall be (modifying the equations for SI units):

For a #6 bar (using the design values)

$$l_d \geq 0.019 A_b \frac{f_y}{\sqrt{f_c}} = 424.2 \text{ mm}$$

$$\geq 0.058 d_b f_y = 457.1 \text{ mm}$$

For a #18 bar

$$l_d \geq 33.65 \frac{f_y}{\sqrt{f_c}} = 2651 \text{ mm}$$

But for either case, according to Section 2626(e) not less than 609.6mm. Scaling down the requirements for the #18 bar:

$$l_{d \text{ model}} = \frac{l_{d \text{ prototype}}}{3} = 883 \text{ mm}$$

which is larger than the development length required for the #6 bars. The actual development length used in the specimens was over 1000 mm.

- c) The structural wall has vertical reinforcement distributed in the panel. This reinforcement contributes to the effective surface area of the tension reinforcement
- d) While the maximum tensile reinforcement ratio in a flexural member is limited by $\rho_t \leq 0.025$ [UBC Section 2626(e)], the reinforcement in the boundary element of a structural wall is limited by $\rho \leq 0.06$, [UBC Section 2626(f)]. But if the average steel ratio ρ for the whole structural wall cross-section is calculated, a low steel ratio is obtained. For the walls tested $\rho = 0.0191$ for the framed walls, and $\rho = 0.0170$ for the rectangular walls were obtained.

Since the uncracked walls have the same amount of steel in tension as in compression (if the axial load is neglected), the tensile steel ratio can be assumed to be $\rho_t \approx \rho/2 = 0.0096$ for the framed walls, and 0.0085 for the rectangular walls. This value is under the 0.025 maximum the code specifies for flexural members (if the effects of axial loads and cracking are considered, the ρ_t values reach 0.012 and 0.011 respectively).

- e) The very good confinement provided for the columns was continued into the foundation, and prevented the formation of splitting cracks around the longitudinal bars.

3) Shear Deformations

The shear deformations along a specimen are very hard to ascertain. While in specimens subjected to monotonic loading they are almost a constant factor of the flexural deformations ($\delta_{3 \text{ shear}} = 0.46 \delta_{3 \text{ flexural}}$ for Specimen 3, and $\delta_{3 \text{ shear}} = 0.43 \delta_{3 \text{ flexural}}$ for Specimen 5 before failure takes place as shown in Figs. 4.12 and 4.54). In the case of specimens subjected to cyclic loading, this ratio increases with the number of load reversals and intensity of the deformation. As shown in Figs. 4.18 and 4.60, when the maximum deformations are reached, the shear deformations $\delta_{3 \text{ shear}}$ reach values of 0.87 and 0.53 $\delta_{3 \text{ flex}}$ for Specimens 4 and 6

respectively.

There is a need to better understand the mechanisms of shear deformations and shear transfer, and their interaction with the moment and axial force. It is necessary also to take into account the change in topology and the redistribution of stresses with cracking. These subjects are further pursued in the next chapter.

5.1.4. Energy Absorption and Dissipation Capacity of Specimens

(a) External Energy Input

The energy transferred to the specimen is the total work done by the external loads. The external loads on the specimens tested are the forces in the lateral and vertical jacks, and the friction forces in the teflon sliding pads supporting the specimen. The work done by the friction forces is believed to be negligible, the work done by the net axial force is also small (10% of the total deformations before yield. When the flexural loads cause inelastic deformations and lengthening of the boundary elements, the net work done by this external compressive force may become negative [1]).

(b) Internal Energy Dissipation

The internal energy dissipated by the specimens is computed by integrating the stresses multiplied by the corresponding strains over the whole volume and over the whole time domain:

$$Internal\ Energy = \int_t \int_v \sigma_{ij} \dot{\epsilon}_{ij} dv dt$$

where v is the volume of the specimen, and ij are the directional indexes. For a two dimensional beam subjected to shear, axial force, and in plane bending moment, using the assumption that plane sections remain plane, this equation can be simplified as in [1]:

$$\begin{aligned} Internal\ Energy &= D \cdot \delta h + \int_t \int_h M(h) \dot{\phi}(h) dh dt + \int_t \int_v \tau \dot{\gamma} dv dt \\ &= D \cdot \delta h + \int_t dt \sum_{i=1}^7 (M_i)_{av} (\dot{\phi}_i)_{av} l_i + \int_t dt \sum_{i=1}^3 V_i (\dot{\gamma}_i)_{av} l_i + \int_t M_o \dot{\theta}_{fixed\ end} dt \end{aligned} \quad (5.12)$$

where D is the dead load on the specimen,

δh is the net axial deformation of the specimen,

$(M_i)_{av}$, $(\dot{\phi}_i)_{av}$ and l_i are the average moment, rate of average curvature and length of the i^{th} region respectively (Fig 3.4).

V_i , $(\dot{\gamma}_i)_{av}$ and l_i are the shear force, rate of shear deformation and length of panel respectively, M_o is the moment at the base and

$\dot{\theta}_{fixed\ end}$ is the rate of rotation produced by the slippage of the vertical reinforcement inside the footing of the specimens.

This equation can be modified again replacing:

$$(M_i)_{av} \text{ by } V_i(h_v - h_{i\ av}),$$

$$(\dot{\phi}_i)_{av} l_i \text{ by } \frac{\delta_3\ flexural\ i}{h_3 - h_{i\ av}},$$

$$(\dot{\gamma}_i)_{av} \text{ by } \frac{\delta_3\ shear\ i}{l_i}$$

$$M_o \text{ by } V\ h_v \text{ and } \dot{\theta}_{fixed\ end} \text{ by } \frac{\delta_3\ fixed\ end}{h_3}$$

where:

$\dot{\delta}_{3 \text{ flexural } i}$ and $\dot{\delta}_{3 \text{ shear } i}$ are the rate of flexural and shear displacement at the third floor level, caused by the flexural and shear deformations at span i respectively.

h_v and $h_{i \text{ av}}$ are the shear and the average height of the i^{th} region over the foundation respectively, and

h'_3 is the height of the third story.

A new expression is then obtained:

$$\begin{aligned} \text{Internal Energy} = & D \cdot \dot{\delta} h + \int_t dt \sum_{i=1}^7 V_i \dot{\delta}_{3 \text{ flexural } i} \frac{h_v - h_{i \text{ av}}}{h'_3 - h_{i \text{ av}}} \\ & + \int_t dt \sum_{i=1}^3 V_i \dot{\delta}_{3 \text{ shear } i} + \int_t dt V \dot{\delta}_{3 \text{ fixed end}} \end{aligned} \quad (5.13)$$

In this way the internal energy can be computed by integrating the area under the base shear-third floor displacement curves presented in Section 4.3.

Figure 5.16 shows the energy absorption characteristics for the different specimens at selected cycles. For Specimen 3 in Fig 5.16(a) it can be observed that while the internal energy is absorbed before yielding almost equally by the shear resisting mechanism and the flexural mechanism, after the specimen yields, the largest internal energy absorption component is the flexural one. Also, the rate of increase in the total energy absorption of the system is almost a linear function of the tip displacement δ_3 .

In order to observe the effect of load reversals in the energy absorption characteristics of the specimens, Fig 5.16(b) is presented for Specimen 4 after it was subjected to a cycle with a nominal deformation ductility of 4. The variation of the internal and external energy absorption characteristics when reloading in the second cycle at ductility 4 (LP 85-86 in Fig 4.14) is shown. The most striking difference with Specimen 3 is the total energy, which is much lower than for the monotonic case, and increases almost parabolically with the overall displacement (the displacement δ_3 is referred to the residual third floor deformation at LP 85). It can be seen that for the initial deformation range the main energy absorption mechanism is the shear deformation. This is so because most of the deformation in this range is by shear sliding along open cracks with only a small increase in the lateral load strength of the specimen. When the open cracks in the compression region start closing and the strength of the specimen increases, the main energy absorption mechanism becomes the flexural one.

The effect of the repair procedure can be observed by comparing Figs. 5.16(a) to 5.16(c). While the total energy curve for Specimen 4R is almost as steep as the original monotonic Specimen 3, it does not have as much energy absorption capacity in the initial range of deformations. This is because the second floor panel in that specimen had already been damaged (Fig. 4.28). Since the cracks in that panel are small, it takes only a relatively short deformation to close them, and the energy absorption characteristics of the specimen improve. One striking difference in the way the internal energy is being absorbed is that in the repaired specimen the flexural and the shear absorption mechanisms contribute almost equally to the internal energy absorption, while in the original specimens the shear mechanism was not as effective. The reason for this is that in Specimen 4R most of the energy is absorbed in the second story panel, which is subjected to a lower moment-to-shear ratio than the critical panel of Specimens 3 and 4. For this reason the shear deformations account for relatively more of the internal energy absorption.

The energy absorption characteristics for Specimen 5 are presented in Fig. 5.16(d). When these are compared to Fig. 5.16(a) the much lower energy absorption capacities caused by the lower strength and ductility obtained for the specimen is apparent. The pattern of energy absorption mechanisms is in general similar to that of Specimen 3.

(c) Comparison of Energy Dissipation to that of Ductile Frames

Figure 5.17 shows the energy dissipation normalized as energy dissipated per cycle divided by one half of the maximum displacement variation for each cycle.

The results are compared to those of the ductile bare and infilled frames tested by Klinger and Bertero [50]. These frames were one-third scale models of structural subassemblies of an eleven-story building. It can be observed that the normalized energy dissipation capacity of bare ductile frames is much smaller (by a factor of almost 20) than that of structural walls for a building of similar height. When the results for structural walls are compared to those of ductile infilled frames it is observed that the energy dissipation characteristics of structural walls is relatively better, with the normalized energy dissipation capacity increasing monotonically for an increase in displacement. In the infilled frames the dissipation capacity decreases with the deterioration of the panel.

The comparison of the rectangular and framed structural walls subjected to cyclic loading shows an interesting result: the maximum strength and deformation in the rectangular wall are smaller, but the slope of the normalized energy dissipation capacity is larger. This is probably caused by the lower shear stresses in the thicker panel of the rectangular wall (a maximum of $0.67 \sqrt{f_c}$ MPa compared to $0.876 \sqrt{f_c}$ MPa for the framed wall), because the "pinching" effect in the hysteresis loops is related to the shear stress level. The values observed for the monotonically loaded specimens are in both cases greater than the cyclic ones by a factor of almost two. The normalization procedure (dividing the absorbed energy by one half the displacement variation) is misleading in the case of Specimen 3 which was displaced in only one direction (Fig. 4.2).

5.2. Failure Mechanisms

5.2.1. General

Failure of a properly designed ductile reinforced concrete structure does not take place suddenly. There are usually several stages leading to the collapse of the specimen, and several failure mechanisms developing simultaneously and interacting with each other (i.e. concrete crushing and buckling of the longitudinal reinforcement). The initiation of failure is considered to be the point at which a significant drop in strength can be observed in the overall force-deformation diagram. Failure itself is defined in this report as the condition in which the structure is no longer capable of supporting the service lateral loads, even if it remains standing and holding the vertical dead loads. And finally, collapse of the structure is the inability of the specimen to remain standing holding the vertical dead loads.

The dominant failure mechanism is a function of the specimen's characteristics, and of the type of excitations to which the specimen is subjected. Shear reversals, for example, increase the possibility of flexural shear failure in the panel. Also, several failure mechanisms take place simultaneously and/or trigger one another. For example, buckling of the longitudinal reinforcement and simultaneous rupture of the lateral reinforcement with loss of lateral confinement is commonly observed in axially compressed boundary elements. The observed failure mechanisms are enumerated in Table 4.1 and elaborated upon in the following pages.

5.2.2. Buckling Mechanisms

Specimens 4, 5, and 6 (Sections 4.3.1, 4.3.5 and 4.3.6) had stability problems. This is a mode of failure that is often neglected in reinforced concrete design.

The observed buckling mechanisms can be classified as:

(a) Local Buckling of Longitudinal Reinforcement

The longitudinal reinforcement bars in compression might buckle during the initial portion of a monotonic loading program, as was observed at LP 76 in Specimen 3 (See Figs. 4.2, 4.7 and Section 4.3.1).

This local buckling mechanism is similar to the one observed in reinforced concrete columns loaded monotonically in compression and is elaborated upon in Ref. [9]. As explained in that reference, this type of buckling is caused primarily by the reduction in the modulus of elasticity of the compressive longitudinal reinforcement in the strain hardening range (Fig. 2.13).

The determining parameters involved in this buckling mechanism are: the bar diameter (d), the stirrup spacing (s), the compressive stress strain diagram for the steel, and the effective length factor (K). The length factor is a function of the construction workmanship. In Ref. [9], it is assumed that the longitudinal reinforcement has rotation free and translation fixed support conditions at the points of contact with the lateral reinforcement, resulting in a value of $K=1$.

By using this assumption, in that reference analytical agreement was obtained with the observed values of buckling strain (0.023 to 0.03 m/m) for specimens identical in configuration to the boundary elements in the framed wall specimen (Specimen 3). Figure 5.18 shows that the largest average compressive strain at the base of the north column in Specimen 3 was 0.021 m/m which is slightly under the lower bound of Ref. [9]. The strain distribution along the element's cross-section is not uniform, as was the case in the column specimens [9]. The strains at the extreme compression bars are higher. Gage C1 in Fig. 3.5 was not able to record strains beyond 0.04 m/m, and the maximum strain reached in this bar is not known. The gage in the innermost bar (gage C2 in Fig. 3.5) reached a maximum strain of only 0.0031 m/m (not shown). Assuming a linear distribution of strains along the base of the compression element's cross-section (this is not exact because of the very high shear stresses at that section) the maximum compressive strain can be estimated as 0.047 m/m, which is beyond the local buckling strain. (Note that clip gage C11 is not exactly at the center line of of the column.)

It can also be observed in Fig. 5.18 that the final drop in strength was initiated at LP 75, when the average strain in the column cross-section was 0.01 m/m (which coincides with the strain at which the confined concrete reaches the maximum stress [Fig. 5.2]).

Consequently the failure of Specimen 3 can be interpreted as flexural failure because of excessive compressive strain in the boundary element.

(b) Buckling of Boundary Element After Spalling of the Concrete Cover

This type of failure was observed in Specimens 5 and 6 (Sections 4.3.5 and 4.3.6).

In the case of Specimen 5 (Section 4.3.5) the initiation of failure was caused by an unsymmetric spalling of the concrete cover (Figs. 4.52 and 5.19). At the point spalling initiated (LP 273 in Fig. 4.46) the average strains at the base of the north boundary element were recorded as 0.00298 by gage K11, and 0.0047 by gage C11 (Fig. 3.4). While spalling was observed in the unconfined concrete cover at the top surface of the specimen, the cover on the lower part of the specimen presented no signs of spalling (Fig 5.19). In this slender rectangular boundary element the cover thickness (equivalent to the 38 mm code requirement for the prototype) comprises 28% of the confined core thickness and 52% of the moment of inertia about the weak axis of the column. These percentages are further increased when some arching action penetrates the confinement region (Fig 5.19(a)), an eccentricity was created in the cross-section. This further progressed with an increase in load, causing out of plane bending at the base of the boundary element.

At LP 309 the strains recorded by gages K11 and C11 were respectively 0.0072 and 0.0097. At this point the upper surface completed spalling and a tie ruptured with the capacity of the specimen dropping, and buckling of the longitudinal reinforcement following (Fig. 4.51 and 5.19[c]).

In Specimen 6 failure took place in a similar way (Section 4.3.6), being triggered by the spalling of the concrete cover on only one side of the boundary element (Fig. 5.19[c]). In this case the load reversals caused a deterioration of the unconfined concrete strength.

In order to illustrate this deterioration, the strain histories recorded by clip gages C1 and K1 (Fig 3.4) at the base of the wall during the last three cycles at ductility 4 are shown in Fig 5.20(b). The difference in the strain readings at LP 535 in this figure is caused by the open crack at the interface between the foundation and south boundary element. This difference varies only slightly with the first load reversal (LP's 535-589), but in the next cycle this difference is reduced because of the out of plane deformation of the boundary element, which causes an elongation to be recorded by clip gage K1 (Fig. 5.20[c]). This means that buckling was actually initiated in the second cycle at ductility four even if the load (Fig. 5.20[a]) does not drop a significant amount. At LP 641 when loading the specimen to the north, the tension in the south boundary element is not enough to straighten it, and a residual out of plane curvature remains.

When the specimen was loaded to the south, introducing compression in the south boundary element for the third time at this ductility level, column buckling was observed before reaching the previous load level (Fig. 5.20[a]).

(c) Buckling of Boundary Element with Residual Open Cracks

This buckling mechanism was observed in the south columns of Specimens 3 and 5 (Sections 4.3.1 and 4.3.5) when reversing the load after opening of large tensile cracks in the boundary element.

This mechanism is caused by the reduction in the moment of inertia in the cracked section because of residual tension cracks, and by the reduction in the modulus of elasticity of the longitudinal reinforcement steel because of the Bauschinger effect.

The tensile strains observed along the south column in Specimen 3 are shown in Fig. 5.21. The determining parameters for this type of buckling are the residual crack width and their spacing, the effective EI for the elements' cross-section, and the effective buckling length Kl_{cr} . In order to clarify this mechanism, the results obtained for Specimen 3 are studied in

detail.

1) Crack Width and Spacing

For the first 381 mm gage length at the base of the column, the overall lengthening at LP 76 was 39.1 mm. If the residual tensile strains in the concrete are neglected, the width of all the cracks in this gage span should total 39.1 mm. The strain distribution along the longitudinal steel is not uniform, but in order to simplify this presentation the strain distribution is assumed to be piece-wise linear as shown in Fig. 5.21(c). The crack width can be determined by the strain distribution and the crack spacing.

In order to be able to determine the crack spacing, the cracking mechanism should be understood. The longitudinal steel subjected to tension introduces, through the bond mechanism, tensile stresses in the concrete. When these tensile strains exceed the tensile concrete cracking strain (which can be taken as 0.0002 m/m) [51] tensile cracks occur. The stresses at the crack surface are released and a tensile crack opens in the concrete.

The lateral reinforcement which is tied to the longitudinal reinforcement determines the location of regions of stress concentration (reduced concrete cross-section, Fig. 5.22) and explains the crack spacing in the boundary element being similar to the tie spacing s (Figs. 4.8 and 4.53).

The crack width Δ_c can now be ascertained under the assumptions of the longitudinal strain distribution in the reinforcement being as shown in Fig. 4.20(c) and the crack spacing being equal to the lateral reinforcement spacing s :

$$\Delta_c = s \epsilon_s \quad (5.14)$$

with the widest crack measuring

$$\Delta_c = (33.8)(0.1311) = 4.43 \text{ mm}$$

which is in good agreement with the 4.7 mm observed experimentally (Section 4.3.1) and indicates that the cracks are completely open in the lower part of the south boundary element.

It should be noted that the crack at the base between the column and the foundation is larger (6 mm), because of the bond slip of the reinforcement in the foundation. Also, some 6 mm cracks were open in the panel because the crack spacing is larger than in the column.

Under similar assumptions, the largest crack opening can be approximated at LP 80, the point at which buckling initiated, by taking the average reading from gages C1 and K1, (Fig. 3.4) as shown in Fig. 5.21.

$$\Delta_c = s \epsilon_s = (33.8)(0.1058) = 3.6 \text{ mm}$$

2) Effective EI of Cracked Section

In general the EI of the boundary element's cracked cross-section increases with the height above the foundation (some discontinuities can occur because of the cracking), because of the higher moment of inertia of the cracked concrete cross-section when crack widths are small.

In the case of the longitudinal reinforcement, the moment of inertia of the steel cross-section remains constant, i.e. in Fig. 5.23, the moment of inertia of the steel cross-section with respect to axis 1-1 is:

$$I = 6 \pi (9.52)^2 (101.6)^2 + \frac{\pi (9.52)^4}{4} = 10.765 \times 10^7 \text{ mm}^4$$

On the other hand the modulus of elasticity for the steel reinforcement varies under stress reversals, and can be ascertained if the strain history and the residual strains along the reinforcement are known. This can be achieved by means of the generalized Ramberg-Osgood

formulation developed in Ref. [24]. This procedure considers two possible cases of first stress reversals as shown in Fig. 5.24. One occurs in the elastic plateau range (Point A), the other in the strain hardening range (Point A'). For the latter case, upon unloading the stress is reduced elastically from A' to A''. The σ - ϵ relationship between A and B or A'' and B', is given by the Ramberg-Osgood equation:

$$\bar{\epsilon}_s = \beta \frac{\bar{\sigma}_s}{\sigma_y} (|\bar{\sigma}_s| + \alpha |\bar{\sigma}_s|^n) \quad (5.15)$$

where

$$\bar{\epsilon}_s = (\epsilon_s - \epsilon_{sA}) / 2\epsilon_y \quad (5.16)$$

$$\bar{\sigma}_s = (\sigma_s - \sigma_{sA}) / 2\sigma_y \quad (5.17)$$

in which ϵ_s and σ_s define a point on AE (or A''B'), and ϵ_{sA} and σ_{sA} define a point A (or A''), the parameters α , β and n vary with the residual plastic strain, $\epsilon_{p \max}$, which would develop upon release of the previous loading (distance SO for point A, and SO' for A'). For this investigation α and β were determined using:

$$\alpha = 2.3 \frac{\epsilon_{p \max}}{\epsilon_{sh}} < 2.3 \quad (5.18)$$

$$\beta = [1 + 0.7 \epsilon_p - 0.3 \epsilon_p^{-7/3}] < 1.4 \quad (5.19)$$

where $\epsilon_p = \epsilon_{p \max} / (35 \times 10^{-3})$ and a value $n = 7$ was assumed. With the instrumentation used it was possible to obtain only the average strains for 381 mm gage lengths along the column. The actual strain distribution is not uniform, i.e. in Fig. 5.21 the strains shown along the bar are higher at the sections where concrete cracks are open, and are lower in the portions of the bar in contact with the concrete, because the concrete takes some of the tensile stresses through the bond mechanism. If the average steel strains are used to estimate the average steel stresses along the bar as shown in Fig. 5.24, the modulus of elasticity of the steel is found to vary along the boundary element from 8300 MPa at the base to 50200 MPa at the top of the first floor. (Note that the modulus of elasticity could be even lower at the sections where the cracks are open.) The effective EI of the steel cross section increases from $1.46 \times 10^{11} \text{ N-mm}^2$ at the base to $8.86 \times 10^{11} \text{ N-mm}^2$ at the top.

The concrete cross-section's EI also increases from the base of the element where the cracks remain large, to $7.17 \times 10^{12} \text{ N-mm}^2$ at the top of the boundary element in the third story where the cracks are closed.

The variation of the effective concrete cross-section is related to the crack opening. But it is very difficult to ascertain the portion of concrete cross-section remaining in contact after opening of a crack. This fact is complicated by the shear slippage along the cracks that cause the crack surfaces to contact even in the case of very wide cracks (Fig 5.25). On the basis of experimental results, the axial force carried by the concrete cross-section remaining in contact after opening of a crack can be determined by computing the axial force taken by the steel reinforcement, based on the stress-strain diagram for the steel (Fig. 2.13), and the modified Ramberg-Osgood equation (Eqs. 5.15-5.19). As an example, the steel stresses in region 1 (or their average value along the 381 mm gage length, Fig. 5.21) are determined at LP 80 on the basis of the recorded steel strain history.

At LP 76 the average strain recorded by gages K1 and C1 is 0.1036 m/m. The corresponding stress (from the average experimental curve Fig. 2.13) is 800 MPa. The stress-strain coordinates (σ_{sA} , ϵ_{sA}) of point A'' are determined by unloading elastically to $\sigma_{sA} = \sigma_y = 480 \text{ MPa}$.

$$\epsilon_{sA} = 0.1036 - \frac{(800 - \sigma_y)}{E_s} = 0.101$$

The values of σ_{sA} and σ_y can then be replaced in Eq. 5.17:

$$\bar{\sigma}_s = \frac{(\sigma_s - 480)}{2 \times 480}$$

replacing the values of ϵ_{sA} and ϵ_y in Eq. 5.16 in a similar way:

$$\bar{\epsilon}_s = \frac{(0.075 - 0.101)}{2 \times 0.0023} = -5.74$$

where 0.075 m/m is ϵ_s , the average strain recorded at LP 80 (Figs. 5.21 and 5.24).

Replacing the last two expressions in Eq. 5.15 a function in $\bar{\sigma}_s$ only is obtained. This function is solved numerically to obtain $\bar{\sigma}_s$, the stress value at LP 80.

$$\bar{\sigma}_s = -582 \text{ MPa}$$

By multiplying the stresses by the total longitudinal steel area, the axial force taken by the steel is estimated as :

$$P_{steel} = 8 A_s \sigma_s = 8 \times 285 \times 582 = 1328 \text{ kN}$$

Subtracting this force from the total compressive axial load, it is possible to determine the axial force carried by the concrete, and therefore the portion of the concrete cross-section still in contact. (The contribution of the wall to the section's EI was neglected, which is reasonable because: the neutral axis is very close to the compressive column; only a small portion of the panel is in compression; and the residual open cracks are wider in the panel.)

$$P_{concrete} = 2805/2.133 + 434 - 1328 = 421 \text{ kN}$$

where 2805 kN-m is the moment at the base of the specimen at LP 80, 2.133 m is the center to center distance between the boundary elements, and 434 is half the axial load on the wall.

Figure 5.26 shows the variation of the axial force taken by the steel and by the concrete along the south boundary element and indicates that in the two lower 381 mm spans of the boundary element the cracked concrete is 24% effective in carrying the axial load, and the cracks can be assumed to be almost completely open. In the upper span the concrete carries 69% of the axial load with an average stress in the original gross concrete cross-section of 12.4 MPa or $0.37f'_c$.

It can be gathered from all this that the effective EI for the concrete cross-section along the height of the first story increases from 12.4% to 37% of the original concrete cross-section, at the base and at the top of the boundary element, respectively. (The EI of the original concrete cross-section is $2.6 \times 10^{12} \text{ N-mm}^2$.) The effective EI for the composite steel-concrete cross section (concrete EI + steel EI) varies from $1.02 \times 10^{12} \text{ N-mm}^2$ to $2.24 \times 10^{12} \text{ N-mm}^2$.

3) Effective Buckling Length for Cracked Column

The effective length factor K can be ascertained from Euler's theory as

$$K = \frac{\pi}{l_{cr}} \sqrt{\frac{EI}{P_{cr}}} \quad (5.20)$$

where:

$l_{cr} = 1143 \text{ mm}$, is the height between floors

$EI = 1.02 \times 10^{12} \text{ N-mm}^2$ is the composite section's effective EI at the base of the specimen where the cracks are open (conservative assumption)

$P_{cr} = 1736 \text{ kN}$ is the experimental buckling load

$$K = 2.1$$

This means that the boundary element with residual open cracks has a very large effective

length.

(d) Observations on Predictions of Stability Failure

The possibility of stability failure is often overlooked in the design of reinforced concrete structural walls. Some guidelines appear in Refs. [52,53] and it is of interest to see how they compare to the results obtained.

The Architectural Institute of Japan [52] approaches the problem of buckling of the longitudinal reinforcement by defining a slenderness ratio for reinforcing bars λ :

$$\lambda = \frac{4s}{d} \quad (5.21)$$

where s is the stirrup spacing, and d is the bar diameter.

AIJ states (based on experimental evidence) that buckling is likely for $\lambda \geq 35$, and unlikely for $\lambda \leq 8$. Based on this, and in order to prevent local buckling, the Japanese code limits the stirrup spacing to $s \leq 8d$ ($\lambda \leq 32$).

In the specimens reported in this investigation the ratio of s to d is as follows:

$$s = 2.13d \text{ for the framed walls, and} \\ s = 2.55d \text{ for the rectangular walls}$$

According to the values shown, the specimens tested should not have buckled. But if the values of λ are computed, they are found to be 8.52 for the framed walls and 10.2 for the rectangular walls. That is they are close to the lower bound of the transition range specified by the AIJ. It should be noted that these recommendations are based on results of monotonic tests only.

On the other hand, Paulay [53] recommends that where the combination of flexural and axial load can produce a compression strain of 0.015 m/m or more, the thickness b_w of a rectangular wall should be

$$b_w \geq \frac{h_w}{10} \quad (5.22)$$

where h_w is the free height of the wall (Fig. 2.5).

For the rectangular walls of this investigation the h_w is = 1.14 m, and b_w is = 0.114 m.

$$b_w = \frac{h_w}{10}$$

Then according to both the AIJ and Paulay buckling should not occur. The discrepancy obtained between the results of this investigation and the Japanese Code specifications for local buckling is caused by the high compressive strain levels obtained in the tests. At a strain level of 0.047, such as the one reached in the extreme compression bar in Specimen 3, the modulus of elasticity of the reinforcing steel drops considerably, and the value of the Euler buckling load is decreased.

Paulay's recommendation of acceptable slenderness ratio for rectangular walls would fare better if the value of b_w were to be replaced by the smallest dimension of the confined concrete core cross-section. This would be a reasonable procedure, because in general buckling is reached at strain levels larger than those corresponding to cover spalling.

In conclusion, under monotonic load conditions there are two distinct types of buckling:

1. The possibility of local buckling as determined by the diameter of the longitudinal reinforcement, the spacing of the lateral confinement, the stress-strain characteristics of the steel, the strain levels reached in the longitudinal steel, and the workmanship which affects the effective buckling length. In order to reduce the possibility of local buckling, large diameter bars and small lateral reinforcement spacing with high strength lateral

reinforcement should be used [9]. Good workmanship should provide for good contact between the lateral confinement and the longitudinal reinforcement.

2. The possibility of wall buckling as determined by the ratio of the unsupported height of wall to the thickness of the confined concrete cross-section.

Under load reversals the possibility of buckling increases because of the reduction of the effective EI of the wall cross-section. This reduction is caused by the reduction in the moment of inertia in the cracked concrete section because of residual tensile cracks, and by the reduction in the modulus of elasticity of the longitudinal reinforcement steel because of the Bauschinger effect. Buckling then is determined by the tensile strain reached in the steel and the crack widths.

Paulay's approach does not consider this possibility of opening of large tensile cracks that can leave the steel only as contributing to the out of plane stiffness.

5.2.3. Shear Failure Mechanisms

(a) General

The shear resistance mechanisms can be classified as:

1) Shear resistance offered by the uncracked concrete.

This mechanism is the dominant one for loads below the cracking load level, and can be assumed to take 100% of the shear in the uncracked specimen.

2) Aggregate Interlock and Dowel Action

As long as there is no shearing movement of the crack surfaces, the shear stress parallel to the crack surfaces remains zero. However, if such movement occurs, substantial shear stresses can be developed along open cracks because of the roughness of the crack surfaces (aggregate interlock) and the presence of reinforcing bars crossing the cracks (dowel action).

3) Wall Reinforcement

The horizontal and vertical panel reinforcement crossing the inclined cracks contributes to the shear strength of the wall.

These mechanisms are further elaborated upon in the next chapter.

(b) Monotonic Loading

In Ref. [1], the mode of failure reported for Specimen 1 tested under monotonic conditions was crushing of the wall panel, which is a failure of the shear resisting mechanism. Although some panel crushing was observed on the specimens tested in this investigation, this was not the principal mode of failure under strictly monotonic loading.

There are two reasons for this difference. The most important one is that the "monotonic loading program" used in Ref. [1] was not strictly monotonic (Fig. 5.27) but included a severe load reversal before the crushing of the wall panel. This reversal caused flexural and shear cracking in the panel that contributed to the final failure.

A second reason was the use of cross ties in the critical regions of the panels in the specimens reported in this investigation (Fig. 5.28). These hoops contributed to the improvement of the behavior in this region by providing some confinement and helping to delay the buckling of the panel reinforcement.

Failure of the shear resisting mechanism was observed in Specimen 3R. This specimen failed by crushing of the second floor panel (Section 4.3.4). It should be noted that this was not a virgin panel, and that it was subjected to a different M/V ratio. This failure is elaborated upon in Section 5.2.4.

(c) Cyclic Loading

The failure of the shear resisting mechanisms is more likely under cyclic loading. Specimen 4 (Section 4.3.2) failed by developing a sliding shear mechanism at the base of the first story panel.

The development of the crushed concrete region can be followed in Figs. 4.14 and 5.29. It is also interesting to observe the strain history recorded by gage W31 (Fig. 3.4), during the last 3 cycles at ductility 4 (Fig.5.30).

At LP 80 a compressive strain of 0.0046 m/m was observed. This strain is beyond the crushing strain value for unconfined concrete (Fig.5.2). Some of this strain can be accounted for by shear slippage along a horizontal crack (Fig. 5.29[a]). This shear slippage takes place along some flexural cracks, and follows the location of the horizontal reinforcement. The reason for this is that reinforcement, by disrupting the continuity of the concrete, creates a preferential failure plane.

The residual strain upon release of the load was 0.002 m/m (LP 81). With the application of the next positive cycle, the cracks in the 539 mm length covered by gage W31 opened a total of 13 mm, and when the cracks closed again an increase of diagonal strain with respect to the previous cycle was observed. This increased shear slippage contributed to further deterioration of the concrete in that region by grinding the crack surfaces. This process continued until LP 91A when the recorded average diagonal strain (strain in the uncracked concrete + shear slippage along the horizontal flexural cracks) reached 0.02 m/m, and the panel completely crushed, leaving only the boundary elements as the effective shear resisting elements (Fig. 5.29[c]). The boundary elements then performed as dowels, and the total shear strength of the wall was limited by their shear capacity. According to this at LP 92 the compression and tension boundary element resisted 700 kN. The tension boundary element is not as effective as the compressive one in resisting shear because of the wide open tension cracks. Thus, a $\nu > 0.96\sqrt{f_c}$ (MPa) $\left[11.4\sqrt{f_c}$ (psi) $\right]$ would have been developed in the compression edge.

Specimen 5 developed a flexural shear failure upon only one load reversal (LP 526, Fig. 4.46). As explained previously in Section 4.3.5, the previous buckling of the north boundary element and a portion of the panel had badly damaged the specimen. Because of this, after reversing the load, the wall was able to develop a strength of only $0.656\sqrt{f_c}$ MPa ($7.8\sqrt{f_c}$ psi).

5.2.4. Failure of Repaired Specimens

As elaborated upon in Section 2.6 the repaired specimens were intended to fail in the second story. In this way excessive ductility demands were not to be placed in the previously damaged first story panel. Although Specimen 3R failed by crushing the second story panel, in general the experimental results showed weaknesses in the repair procedure. Shear sliding in the construction joints and brittle rupture of the longitudinal reinforcement interfered with the development of a good hysteretic response.

(a) Rupture of Tension Reinforcement

In the case of repaired specimens, the failure of the tension reinforcement was of the brittle rather than ductile type. There are two reasons for this brittle failure: a) the steel had previously been strain hardened, and b) welding of the steel during the repair procedure had an "embrittlement" effect that further reduced the allowable ductility.

Specimens 4R, 5R, and 6R developed rupture of the main longitudinal reinforcement (see Table 4.1). The strains at which rupture occurred were obtained on the basis of the average readings for the 419 mm gage length at the base of the second story (Fig. 3.4), and were, respectively, 0.035 m/m at LP 332 for Specimen 4R, 0.01 m/m at LP 219 for Specimen 5R, and 0.02 m/m at LP 151 for Specimen 6R. If these strains are compared to the ultimate strains for the virgin #5 and #6 bars (Figs 2.9 and 2.10), a significant ductility reduction can be observed. (It should be noted that since the gage lengths used to obtain the curves shown in Figs 2.9 and 2.10 were different, the comparison is not exact. It should also be remembered that there were residual strains in the bars after testing the virgin specimens, straightening, and repairing them).

The curvature distribution diagrams for the repaired walls at selected load points are shown in Figs. 5.31 and their general shape shows the effect of another significant aspect of the repaired walls' behavior. Since the plastic hinge has been displaced away from the fixed end,

the rotation of the plastic hinge required to cause a unit displacement at the top of the specimen is larger than in the case of virgin walls, where the plastic hinge develops at the base of the specimen (Fig 5.32).

The longitudinal reinforcement ruptured one bar at a time, and the testing was carried on as far as possible before the complete collapse of the specimen.

In conclusion, the repair procedure was effective in restoring the specimen's strength (actually the shear strength was increased nearly 20%, considerably above the allowed $10\sqrt{f'_c}$ psi) and to a large extent in restoring the stiffness. But for the repair to be fully satisfactory, ways to restore the ductility of the longitudinal reinforcement and better ways of restoring the energy absorption and dissipation capacities of the specimen should be pursued.

(b) Crushing of Upper Floor Panel

Specimen 3R failed by crushing of the second floor panel. This failure took place after the specimen reached a shear strength of $1.12\sqrt{f'_c}$ MPa ($13.43\sqrt{f'_c}$ psi). The flexural mode of failure observed in the original Specimen 3 was delayed because the moment at this section is 72% of the moment at the base. The cross-section of the virgin specimen was uniform throughout the height, and this cross-section was proportioned and designed so that the likely mode of failure would be flexural. When the first story was strengthened, the moment capacity of the specimen in the lower story was increased, and consequently the shear forces that could be applied to the specimen were increased. Under these conditions, and also with the second story panel already cracked and its shear capacity weakened by the previous load reversals, a shear failure mode could be anticipated.

Since crushing of the second story panel was initiated out of the gage length covered by the clip gages, there are no data for the concrete crushing strain.

(c) Shear Sliding Along Construction Joint

The horizontal crack along the interface of the old and the new concrete had a poor performance in Specimens 5R and 6R. This was not the case in Specimens 3R and 4R. One of the reasons for this difference is that in Specimens 3R and 4R dowels were left around the panel in order to facilitate the repair procedure (Fig. 2.17). These dowels were not strain hardened as was the rest of the reinforcement in the virgin specimens, and the extra web reinforcement was welded to them in the repair procedure. The old web reinforcement was straightened and left in place, improving the stress transfer across the construction joint (Figs. 2.19 and 2.20). Specimens 5R and 6R, in turn, had no dowels, and the new panel reinforcement was welded to the old, previously strain hardened reinforcement (Fig. 2.20). In general it has been observed that the interface between the old and the new concrete is a critical section, and better procedures should be employed to insure a proper stress transfer. Some ways to achieve that are: providing a roughened concrete surface (or concrete keys whenever possible) to improve the shear transfer; and welding the new reinforcement further up out of the critical plane of contact between the old concrete in the slab and the new concrete in the panel.

5.3. Effect of Test Parameters on Overall Behavior

The practical implications of the results obtained with regards to the different test parameters are reviewed. The test parameters were: wall cross-section (framed wall vs. rectangular wall), confinement of the boundary elements, type of loading, repair procedure and V/M ratio.

5.3.1. Wall Cross-Section

The following observations can be made with respect to the effect of the wall cross-section:

(c) Construction Procedure

Supposedly the ease of construction is the main reason for using a rectangular wall cross-section. The form work is simple and the same forms can be used for walls of different thickness. But there are some construction details that are better resolved in a framed wall.

For example the placement of the horizontal wall steel which should have its ends embedded in a confined concrete region presents problems in the case of rectangular walls. While in a framed wall, the ends of the horizontal wall panel reinforcement can be anchored into the confined concrete region in a practical way (Fig. 2.4a), in a rectangular wall it becomes necessary to either leave a considerably thicker concrete cover in the wall panel, or to bend the ends of the bars to anchor them in the confined concrete of the boundary element.

While the minimum concrete cover required in the walls [30] is 17.8 mm, the cover thickness that results when placing the horizontal reinforcement far inside the wall, so as to allow embedding its ends in the confined concrete region of the boundary element, is equal to the thickness of the concrete cover in the boundary elements plus the diameter of the longitudinal reinforcement in these elements.

This can result in a considerable thickness of the concrete cover in the panel. According to the UBC requirement 2614(d), this cover thickness should be less than one third the wall thickness. A thicker wall cover has the inconvenience of increasing the possibility of temperature and shrinkage cracks showing in the cracked surface.

(b) Strength and Ductility

The rectangular walls studied had a theoretical ultimate moment capacity equal to 89% of that corresponding to the framed walls. However the maximum moments reached in the rectangular walls tested were only 73% and 80% of the ultimate moments reached in the framed walls with similar monotonic and cyclic loading history. Consequently proportional loads could not be reached in the rectangular walls (see Fig. 5.34).

There are several reasons for obtaining a lower ductility and strength in the rectangular wall. Some of these reasons are a consequence of the particular characteristics of the specimens tested, but some others are typical of rectangular walls in general. The main reasons have already been elaborated upon in Section 5.1.1.(e) and Section 5.2.2.(c) and will be briefly summarized here.

1. The slenderness of the wall causes the thickness of the cover (limited by the code to a minimum of 38 mm) to comprise 28% of the column thickness and results in a 48% decrease in the out of plane stiffness (Section 5.2.2[b]). Because of this, when cover crushing is initiated in one face of the wall, a significant eccentricity is created in the boundary element's cross-section.
2. Higher steel ratio ρ in the boundary elements of the rectangular wall (0.0557 compared to 0.0353 for the framed wall), which reduces the overall specimen ductility (this alone is not so important because $\rho = \rho$ and good confinement is used).
3. Smaller diameter longitudinal bars which (if the stirrup spacing is kept constant because of practical considerations which limit the minimum spacing, i.e. concrete pouring) have a lower buckling stress, and for this reason cannot develop a high ultimate strain.

5.3.2. Confinement of Boundary Element

Figure 5.35 shows the confinement characteristics for the boundary elements investigated in Ref. [1], and those of the present investigation. The different confinement arrangements affect the behavior of the boundary element, and consequently, the wall behavior in the following ways:

(a) Concrete Cover Area and Confinement Effectiveness

The UBC Code's [30] minimum cover thickness requirement is the same for hoop or spiral confinement. The unconfined concrete area for the specimens tested with rectangular hoop confinement comprised 19% of the total cross-sectional area. In the boundary elements of Ref. [1], which had the same dimensional cross-section but spiral confinement instead, the unconfined concrete area comprised 36.4% of the total cross-sectional area. In the boundary elements of the rectangular wall, the unconfined concrete comprised 29.3% of the total cross-sectional area. These values give an indication of the loss in strength that can be expected

because of concrete cover spalling, and may appear to indicate that the rectangular confinement in the boundary elements of the rectangular wall are better than the spiral confinement.

But we cannot compare just the concrete cover. One important confinement effect is the increase in concrete strength. In Ref. [9] it is shown that the maximum concrete strength for the confined concrete in the boundary elements of the framed walls is reached at strain levels beyond 0.004 m/m. This means that the maximum concrete strength is reached after the unconfined concrete cover spalls.

The increase in strength that can be obtained is a function of the effectiveness of the confinement arrangement. While for the case of the spiral confinement used in the specimens of Ref. [1] this increase reached 38.7% of f'_c [54], for the tied boundary elements of Specimen 3 the increase in strength under uniform strain (or stress) is 23% f'_c [9]. In both cases the increase in concrete strength is within 4% of that required to make up for the loss of concrete caused by the cover spalling computed on the basis of the concrete area outside of the confining steel.

In the case of the boundary elements corresponding to Specimen 5, the increase in strength corresponding to the confinement arrangement used is not known. It can be inferred that because of its aspect ratio and tie spacing it is probably less than the one corresponding to the previous confinement arrangements. In order to provide a further comparison of the confinement arrangements accounting for the tie spacing and geometry, the volume of spalled concrete was computed, accounting for arching action. To do this it was assumed that the concrete within a wedge at $\pi/4$ radians from the confining steel (lateral and longitudinal) spalls (Fig. 5.35). This computation is not intended to be exact, but can give an idea of the relative advantages of the different confinement arrangements. The volumes obtained, and normalized by dividing them by the original column volume, resulted in a "spalled volume ratio". This ratio was 31% for the boundary elements with square ties, 42% for the ones with spiral confinement, and 46% for the ones corresponding to Specimen 5. According to these observations, the boundary elements with square ties and with spiral confinement are superior to the rectangular ones.

(b) Ultimate Compressive Strain

As explained in Ref. [9], the ultimate compressive strain that can be reached in a monotonically loaded compression element is limited by the buckling of the longitudinal reinforcement. In the case of spirals, the lateral reinforcement spacing is smaller than the one used for the hoop reinforcement, and the longitudinal bars are better restrained against buckling. The #5 bars in the boundary elements of the rectangular walls are likely to buckle earlier than the #6 bars in the framed wall specimens.

(c) Crack Spacing and Crack Width

It is a common experimental observation that the crack spacing in an element subjected to very high tensile strains is the same as the spacing of the lateral reinforcement (Fig. 5.22). Consequently, the crack width (Eq. 5.14) will be higher for the boundary element with hoop confinement ($s= 33.9$ mm) than for the element with spiral confinement ($s= 21.2$ mm). This has an effect on the stability of the boundary element under load reversals, after large tensile strains are reached (Section 5.2.2[c]).

5.3.3. Loading Histories

Monotonic and cyclic loading programs were used in the experiments. In the previous sections, results concerning the effect of the loading programs were presented. These are summarized in the present section, and additional observations are made. Tables 4.1 and 5.8 show comparisons of the results.

Figures 5.27, 5.33 and 5.36 show comparisons of the hysteresis diagrams.

(a) Effect on Deformation Capacity Figure 5.27 shows the effect that even only one load reversal can have. Specimen 1 [1] reached a maximum deformation of 108 mm which is only 58% of that obtained in Specimen 3. And even if the overall cyclic deformation of Specimen 1 is

computed, it is found to be only 85% of that corresponding to Specimen 3.

The load reversal into the inelastic range weakened the wall panel of Specimen 1 and precipitated the crushing failure observed. This damaging effect of load reversals can also be observed in Figs. 5.33 and 5.36. The overall deformation capacity under cyclic loading with respect to that under monotonic loading was 88% for the framed walls, and 84% for the rectangular walls.

(b) Effect on Strength

The maximum strength of the specimens tested under load reversals was 92% and 95% of those tested under monotonic loading for the case of the framed and the rectangular specimens respectively. When the load was cycled at each ductility level a reduction in strength was observed in each consecutive cycle, with the reduction being largest from the first to the second cycles, and becoming smaller in the following cycles. This was observed at all ductility levels except the maximum. At the maximum ductility level the strength would not stabilize after a few cycles, but it would continue to drop.

(c) Effect on Displacement Components

The displacement component diagrams are shown in Figs. 4.12, 4.22, 4.32, 4.44, 4.54, 4.63, 4.72, and 4.81. It can be readily observed that with repeated cycling the relative magnitude of the shear deformation component with respect to the total specimen displacement increases. This indicates that the deterioration of the shear resisting mechanisms with repeated cycling is in general greater than the deterioration of the other deformation mechanisms.

(d) Effect on Energy Absorption and Energy Dissipation

The energy absorption diagrams are shown in Figs. 5.16. Comparing Figs. 5.16 (a) and (b) it can be concluded that the energy absorption capacity decreases significantly when the specimen is subjected to repeated cycling. When the specimen has open cracks, its energy absorption capacity is very poor. It becomes necessary to deform the specimen until the open cracks start closing before any significant amount of energy can be absorbed.

Figure 5.17 shows the normalized energy dissipated per cycle for Specimens 3 and 4. The pinching effect observed in the hysteresis diagrams under load reversals causes this significant drop in energy dissipation capacity.

(e) Effect on Failure Mechanisms

It was observed that under strictly monotonic loading, specimens adequately designed against shear are likely to have stability failures. In order to obtain the rupture of the tensile reinforcement, lower tensile steel ratios and larger diameter bars with closer spacing of the lateral confinement are necessary. The failure of the shear resisting mechanism is more likely under cyclic loading. This is because load reversals contribute to the deterioration of the concrete in the wall panel, and the development of a crushed concrete region along the base of the specimen as shown in Figs. 4.14 and 5.29.

5.3.4. Repair Procedure

The performance of Specimens 3 to 6, before and after the repair and strengthening procedure, is compared in Figs. 5.37 to 5.42, and in Table 5.8. From these data and from the experimental results described in Chapter 4, the following observations are presented:

(a) Stiffness

The repaired framed wall specimens had a stiffness (gathered from the free vibration data in Table 4.2, 2.8 and 2.2 times smaller than that corresponding to the virgin specimens 3 and 4 respectively. The stiffness of the repaired framed specimens was closer to the cracked stiffness of the original specimens. On the other hand, the repaired rectangular specimens had an initial stiffness similar to that of the uncracked walls. In other words the effectiveness of the repair procedure in restoring the original specimen stiffness was higher for the rectangular walls, and was also higher for the monotonically tested framed walls than for the walls subjected

to cyclic loading.

The reason for these differences lies mainly in the level of damage reached in the second panel of the virgin specimens. This panel was not repaired. The difference in the distribution of forces to which the specimens were subjected contributes to the difference in the damage to the second story panel. The rectangular walls had a lower moment-to-shear ratio with the moments in the second story being 69% of the moments in the first story, compared with 73% for the framed walls. For the rectangular walls which correspond to a 7 story prototype building, the shear in the second story was 90% of the shear at the first story, while in the framed walls the shear was constant.

As a consequence of the above facts, damage in the rectangular walls was concentrated in the first story, while in the framed walls it spread further into the upper stories. Repairing the first story was sufficient to restore the original stiffness in the rectangular walls, while in the framed walls the upper stories remained damaged after the repair procedure (Fig. 2.20).

(b) Strength and Deformation

The results obtained for the different specimens are listed in Tables 5.7 and 5.8 and shown in Figs. 5.37 to 5.42. The lateral load strength of the repaired specimens was always higher than the corresponding one of the original virgin specimens. The ratio of the tangential story drift index for the critical panel in the repaired specimens with respect to that in the virgin specimens was 54% and 63% for the monotonically and cyclically loaded framed walls respectively, while the same ratio was 60% and 36% for the rectangular walls. The reduction in the deformation capacity of the framed wall specimens seems logical in view of: the higher rotational ductility demands in the region of inelastic deformation (Fig. 5.32); the reduction in ductility of longitudinal steel (Section 5.2.4.[a]); and the lower moment to shear ratio for the critical section (Table 5.8).

The reduction in deformation capacity is larger for repaired walls than for corresponding virgin specimens loading monotonically or cyclically. This is because a large slippage took place in the repaired rectangular walls at the horizontal crack between the old and new concrete. This slippage is not efficient in dissipating energy. It is necessary to point out that the large deformations in the repaired rectangular specimens were obtained with a very severe drop in strength (in some cases over 50% of the maximum strength).

It should also be noted that the failure of the original specimens was caused by the instability of the compression boundary elements. This type of failure was caused by the large flexural moments at the base of the specimen. Since in the second panel the M/V ratio is lower, the moments in the critical section did not reach the levels obtained at the base of the virgin specimens, and this type of failure was prevented.

6. ANALYTICAL MODELING OF WALL BEHAVIOR

6.1. General

Analytical models that have been proposed to predict wall behavior can be classified into two broad groups: models to predict a specific overall behavior (macroscopic approach); and models derived using basic approach of mechanics of solids (microscopic approach).

The macroscopic equivalent structures attempt to model the global behavior (i.e. the force deformation characteristics for the complete panel) by means of an analogous structural idealization such as an equivalent beam or truss. The main advantage of macroscopic models is economic; they require significantly less computational effort than detailed analytical mechanical models. However, they have several limitations, the main one being that usually the results obtained are valid only for the results on which the derivations are based. Furthermore the equivalent structures' topology and element properties have to be determined a priori. This is difficult to do for the general case. For an accurate modeling, the change in topology because of cracks opening and closing, and in material properties because of change in stress-strain states of the original structure, should be taken into account. This is hard to implement in a simplified model.

On the other hand, the microscopic approach or the detailed analytical mechanical models attempt to model the global deformations using the general approach of mechanics of solids, i.e. starting from a detailed interpretation of the localized behavior, that is by modeling: the steel, the concrete cracked and uncracked, the bond interaction between concrete and steel, the crack opening, the interface shear transfer (aggregate interlocking and dowel action) and the effect of reversals, the region, the member, and eventually the whole structure. While this approach is the logical and most desirable one, it cannot be fully implemented yet because of lack of knowledge of the basic models (in particular of the bond slippage and the interface shear transfer), and the complexities involved in a detailed solution.

A third choice, in-between these two extreme cases, can often be the most reasonable alternative. All these possibilities are further pursued in this chapter.

6.2. Tip Displacement Component Because of Flexural Deformations

6.2.1. Introduction

In order to estimate the flexural deformation component of the specimen's displacement at any level, particularly the component of interstory displacement, it is necessary to ascertain the moment curvature relation for the specimens' cross-section, and the curvature distribution along the specimen.

The moment curvature relation for the specimen cross-section can be determined (Section 5.1.1[b]) on the basis of the axial stress-strain relation for the materials (vertical steel, confined concrete, and unconfined concrete), and using the assumption that plane sections remain plane. As elaborated upon in Section 5.1.2.(d), the moment-curvature relation obtained in this way is in better agreement with the experimental results at the base of the specimen where the foundation restrains the opening of the diagonal cracks. (Strictly speaking this moment-curvature relation is not valid at the base because when cracking takes place plane sections can not remain plane.) In the sections above the foundation, the moment curvature diagrams are affected by the stress redistribution caused by the diagonal cracking (Fig. 5.11). Figures 5.12 and 5.13 show the curvature distribution for specimens at different stages of crack propagation. In general, for sections away from the fixed end, the stresses along the boundary elements are higher than predicted by simple beam theory, and tend to approach those corresponding to a truss analogy [55].

Different approaches can be used to determine the curvature distribution along the specimen. The first, and a rather economical one, would be to estimate the curvature distribution according to an "equivalent truss" model. The main difficulty with this approach is the

uncertainty in the equivalent structure's geometry. This is further complicated by the crack propagation that changes the structure's topology at every load step.

A second approach, much more costly but more reliable, involves keeping track of, and taking into account the stress redistribution because of cracking. This last approach is pursued in this investigation, using a finite element solution.

6.2.2. Solution Approach

(a) General

ANSR-I [56], a general purpose computer program for the analysis of nonlinear structures, was chosen for the finite element solution. The steel reinforcement was modeled using one dimensional elements with kinematic strain hardening. The concrete was modeled using two-dimensional plane stress elements. Both materials are elaborated upon in the following sections. The finite element mesh is shown in Fig. 6.1.

The third floor slab in the models tested had an additional thickness and reinforcement to help distribute the forces applied at that level; also, two pairs of 10x15.3 channels were prestressed to the slab at that level (Figs. 2.4 and 3.3). For this reason the third floor slab was modeled analytically as a very stiff truss.

(b) Modeling of Structural Wall

1) Steel

The idealized cyclic stress-strain curve for the longitudinal reinforcement and the panel reinforcement are shown in Fig. 6.2.

In the idealized curve the following simplifications are made with respect to the realistic axial cyclic steel behavior:

- a) The post yielding behavior is assumed to be linear with an E_{sth} of $0.0077 E_s$ obtained by linearizing the stress-strain relation (Fig. 6.2). This linearization was selected so as to model with a bilinear relation the experimentally determined yielding stress and maximum stress values, and the corresponding strain values (Section 2.4).
- b) The behavior is assumed to be identical in tension and in compression. As shown in Fig. 2.13 and elaborated upon in Section 2.4, this is not rigorously correct. The yielding stress and strain hardening modulus are higher in compression than in tension.
- c) Kinematic hardening is assumed (under load reversals the compressive yielding stress decreases).

The idealized stress-strain curve for the hoop confinement reinforcement is shown in Fig. 6.3.

2) Concrete

The "endochronic theory", introduced originally by Valanis [11] in 1971 for analysis of the behavior of metals, was extended to concrete by Bazant and Bhat [10].

A plane stress concrete element based on this work was developed and incorporated into ANSR-I by de Villiers [37]. This was the element chosen for this investigation.

This material model has the major limitation that it does not account for shear slippage along cracks. This slippage can be a very significant source of shear deformation in walls subjected to high shear conditions. For this reason, this finite element model cannot adequately account for shear deformations under high shear conditions. But as long as the effect of tensile stress redistribution after flexural, and especially diagonal cracking, and the axial stress-strain characteristics of materials are modeled properly, the flexural deformations under high shear can be adequately accounted for.

The concrete in the boundary elements was modeled as confined, while the concrete in the panel and the slabs was modeled as unconfined concrete.

Figure 6.4 shows the experimental stress-strain curve for concrete confined with hoop reinforcement taken from Ref. [9], and its comparison with the stress-strain curve obtained by using the ANSR-I program with de Villiers' model. It can be observed that the stress-strain relation obtained with the "endochronic theory", using a value of the confining steel ratio equal to the one used in the experiment; confining steel properties matching the experimental material properties as shown in Fig. 6.3; and a concrete strength equal to the cylinder strength at the time of testing, results in an overestimation of the strength of the confined concrete. The main reason for this difference is that the endochronic theory was adapted to concrete by Bazant and Bhat [10] on the basis of experimental results for concrete cylinders confined by spiral reinforcement. Since spiral confinement is more efficient than the hoop confinement used in the boundary elements of the wall specimens, an input concrete strength reduced by 28% was necessary to analytically obtain a stress-strain relation in agreement with the experimental results of Ref. [9]. The analytical stress-strain curve as used in the analysis and its comparison with the experimental stress-strain curve is shown in Fig. 6.5. Similarly, the stress-strain curve for the unconfined concrete calculated with the plane stress element of Ref. [37] overestimates the concrete strength. The modified curve is shown in Fig. 6.6.

It should be noted that while not all of the concrete in the boundary element is confined (in the boundary elements of the framed walls there is a 19% area of unconfined concrete cover), the average curve for the whole concrete cross-section, based on the results of Ref. [9], was used (Fig. 6.5). This was done instead of modeling separately the confined concrete core and the unconfined concrete cover. In this way, a reduction in the number of elements was obtained.

3) Bond Between Concrete and Steel

The reinforcing elements are assumed to be rigidly connected to the concrete elements at the nodes. In other words, there is the intrinsic assumption that points of zero bond slippage exist at the nodes between elements.

Since in the boundary elements, the crack spacing was on the average equal to the stirrup spacing ($s=33.88$ mm), the points of zero bond slippage are also on the average a distance $s=33.8$ mm apart (Fig. 5.22). This distance is much smaller than the 285.75 mm used in the analytical model. This simplified modeling of the bond interaction affects the analytically predicted crack width and "tensile softening", and results in larger crack spacing and crack widths.

The tensile softening (Fig. 6.7) is described by Scanlon and Lin [57,58], and is explained as the existence in a reinforced concrete member of concrete tensile stresses after the formation of tension cracks. Figure 6.7(b) shows how, after the crack formation, the stresses in the crack surface drop to zero, but an average tension stress remains in the concrete mass. This is caused by the bond interaction which transfers some of the steel tensile stresses to the concrete.

Neglecting the tensile softening in the analytical model may lead to a slight underestimation of the flexural strength.

4) Flexural Strength of the Specimen's Cross Section

As shown in the finite element idealization (Fig. 6.1), the column reinforcement was lumped at the edges of the columns. The wall reinforcement was also lumped at discrete locations corresponding to the boundaries of the concrete elements in the finite element mesh. Furthermore, the stress-strain relation for the steel was simplified as shown in Fig. 6.2. In order to ascertain the adequacy of this kind of modeling in representing the flexural behavior of the wall, the moment curvature for the specimens' cross-section at the base of the specimen is compared to that calculated using the steel distribution and material properties shown in Figs. 6.1 and 6.2. The results in Fig. 6.8 show that the simplified model represents well the section's moment curvature characteristics.

5) Floor Slabs

The floor slabs are effective in restraining the crack opening and in that way significantly affect the curvature distribution along the specimen. In the analytical model the slabs were modeled by including the steel and the concrete corresponding to a slab width of 1.524m. This is 3/4 of the total slab width. The reason for choosing that effective slab width was the experimental observation of the crack propagation in the slab.

6.2.3. Analytical Results

The force- displacement curves for the experimental and analytical results are shown in Figs. 6.9 to 6.11

The computed results were obtained using a Newton-Raphson iteration solution scheme. In the state determination calculations, the Euler integration method was used. The analysis was carried out by applying the loads in three increments. In the first increment the axial loads (868 kN, Fig. 6.1) were applied at the top of the columns in three equal load steps in order to linearize the behavior at each step.

In the second increment a lateral load of 800 kN was applied distributed along the upper part of the specimen (the stiff truss), together with the corresponding moment as a function of the lateral load as shown in Fig. 6.1. This load increment was applied in load steps of 22.24 kN. The program was halted when reaching the 13-th load step of this increment because the allocated computing time was exceeded. A convergence tolerance of 1 kN was specified, and the number of iterations required for convergence varied from one in the very first load step to 21 in the last one with an average of 10 iterations per load step. The total central processor time required for the run in the CDC 7600 of the Lawrence Berkeley Laboratory was 372 seconds.

Since the purpose of this analysis was to determine the flexural deformations in the specimen, and the computer program as written cannot account for the shear slippage across cracks, which makes up most of the shear deformation in the cracked specimen, the computed displacements were broken down into its flexural and shear components. To facilitate the comparison of the different components, the tip displacement because of the flexural deformations was calculated by computing the average curvature at each line of elements (based on the axial deformations of the boundary elements) and from this curvature distribution by simple geometric transformations the flexural displacement component of the third floor displacement was calculated.

In this way the procedure for the analytical determination of the flexural deformations is similar to the procedure used for their experimental determination. The experimental and the analytical force displacement curves with the breakdown into the different displacement components are shown in Fig. 6.9, while a direct comparison of the experimental and analytical flexural displacement components only is shown in Fig. 6.10.

It can be observed by comparing Figs. 6.9(a) and (b) that the analytical solution does not include the fixed end deformation component, and that it underestimates the shear deformation component. The fixed end deformation is not included because the analytical model was attached to a rigid fixed end, neglecting the slippage of the longitudinal reinforcement in the foundation. As expected, the shear deformation components are underestimated in the analytical solution.

Figure 6.10 shows the direct comparison of the experimental and the analytical flexural displacement curves, and the agreement is excellent. The analytically predicted crack pattern is shown in Fig. 6.11 and shows a good agreement with the experimentally obtained crack pattern shown in Figs. 4.7, 4.8, and 4.11, and reproduced in Fig. 6.11(b).

6.2.4. Cyclic Loading

The possibility of applying the procedure developed in this section to the determination of flexural deformations under high shear and cyclic loading conditions was also investigated. The finite element model used for this load case was basically the same as that shown in Fig. 6.1. Some modification was necessary in order to introduce a displacement control type of excitation. This was complicated by the fact that the model was subjected not only to lateral loads but also to a moment applied at the third floor level and proportional to the lateral load. Figure 6.12 shows the solution scheme adopted. By introducing an arrangement of "relatively rigid" elements at the top of the specimen, the combined effect of shear and moment at the third floor could be reproduced by applying only one horizontal load with a fixed moment arm with respect to the top of the model.

The displacement program chosen for this example was that corresponding to the cycles at ductility two in Specimen 4 (Fig. 4.14). In order to obtain the ± 20 mm flexural displacements at the third floor level, a total displacement of

$$\delta_{3 \text{ shear}} + \delta_{3 \text{ flexural}} + \theta_3(h_v - h_3)$$

was applied at the top of the analytical model set up. The rotation of the third floor, θ_3 when a 20mm flexural displacement is reached in that story, was obtained from the monotonic loading analysis. The desired displacements were obtained by applying a very high horizontal load in a very stiff horizontal element at the top of the set up. The stiffness of this element was of the order of 10^6 times the stiffness of the wall.

The force-flexural displacement curves for the experimental and analytical results are shown in Fig. 6.13. As in the case of monotonic loading, a Newton-Raphson iteration solution scheme was used. The vertical dead loads in the specimen were introduced in three equal load steps. The initial part of the lateral load to the north was introduced in an increment of nine equal load steps, reaching 850 kN at a flexural displacement of 8 mm. The second north load increment was introduced in 8 equal load steps, reaching the desired 20 mm flexural displacement. To reverse the load direction, a very small south load increment was applied (1/100 of the normal load step) in order to improve the accuracy of the direction vectors, and maintain numerical stability. The total south displacement was obtained in a load increment of 17 equal load steps, reaching a flexural displacement of -20 mm. The load was reversed one more time, applying a small load increment, and a north load increment was applied in 25 load increments. This last stage was not completed because the allocated computer time was exceeded. The total number of CP seconds required for the run was 565 seconds.

Comparison of the flexural deformations in Fig. 6.13 shows some discrepancy in the initial loading range. The experimental curve is softer because the specimen had been subjected to three previous cycles at ductility one, that had introduced extensive cracking in the specimen. Once the cracks close the agreement is very good. The unloading stiffness was reproduced very well up to the point of zero load. Beyond this point there is some discrepancy because of the increasing Bauschinger effect on the steel which was not accounted for properly in the analytical model (Fig. 6.2). A Clough degrading model, or even better, a Ramberg Osgood steel model (Fig. 5.24) would have yielded more accurate results. The difference in the peak south load reached is caused by the previous cycling of the experimental model. When removing the south load an excellent agreement can be observed again in the unloading stiffnesses, and when applying a load to the north for the second time it can be observed that the stiffness deterioration is captured in the analytical model.

As shown in Figure 6.13 and Table 6.1, the results are very good, because they were obtained exclusively on the basis of the experimental material properties, and show the potential of the finite element method for the solution of the reinforced concrete problem.

6.3. Tip Displacement Component Because of Shear Deformations

6.3.1. Introduction

The contribution of the shear deformation to the tip displacement is significant for the specimens tested (i.e., Figs. 4.12, 4.22, 4.54, etc.). For that reason it is necessary to investigate the shear strength and shear deformation characteristics of the wall. The shear resisting mechanisms in a reinforced concrete wall can be classified as follows:

(a) Uncracked Concrete.

The lateral force taken by the uncracked concrete V_c makes up for most of the total lateral force in the uncracked specimen. After cracking, there is a reduction in the originally uncracked area, and the magnitude V_c decreases. At a higher lateral load, the axial force in the concrete of the boundary element causes the cover to spall and a reduction of the concrete area takes place. If there is good confinement, a compressive triaxial state of stresses is induced. As shown in Fig. 6.14, the maximum shear stress the concrete can resist increases under triaxial compressive stress [37] (the shear strength is proportional to \sqrt{PQ}). After a certain point, this increase can make up for the loss in concrete area, and the magnitude of V_c increases, as long as concrete crushing does not take place.

(b) Aggregate Interlock and Dowel Action.

Kupfer, et al. [59] confirmed that concrete which fails in tension does so by formation of a crack perpendicular to the principal tensile stress. Immediately before formation of a crack, the shear stress parallel to the crack is zero, because the crack is perpendicular to the principal stress. As long as there is no shearing movement of the crack surfaces, the shear stress parallel to the crack remains zero. However, if such movement occurs, substantial shear stresses can be developed because of the roughness of the crack surfaces (aggregate interlock) and the presence of reinforcing bars crossing the cracks. This phenomenon is called interface shear transfer, and has been investigated by a number of researchers [60 to 68].

The most important observations regarding the lateral force resistance of the aggregate interlock V_a can be summarized as:

1. The larger the crack width Δc , the larger the shear displacement necessary to develop the shear resistance.
2. The larger the crack width, the smaller the maximum attainable shear transfer resistance.
3. As the shear displacement increases, the concrete masses on either side of the crack will be pushed apart, and the crack width will tend to increase. Unless the opening tendency is restrained by an effective restraining force, very little shear can be transmitted.

The bars crossing the shear plane at right angles will be subjected to shear displacement; hence a certain amount of additional shear V_d can be transmitted by dowel action. To develop dowel resistance of some significance, large displacements along the shear plane are necessary.

(c) Panel Reinforcement

The horizontal and vertical panel reinforcement crossing the inclined cracks contribute significantly to the shear resistance of the wall. The horizontal reinforcement can resist shear forces axially V_s , and the vertical reinforcement undergoes a kinking action (Fig. 6.15) so that it also contributes to the horizontal shear resistance.

Figure 6.16 shows a breakdown of the internal resisting shear along plane 2 - 2. The distribution of the internal resisting shear mechanisms is different for the case of an uncracked wall and a previously cracked wall, in that in the latter, there is no uncracked concrete contribution V_c , and at low load levels the dowel (V_d) and to a greater extent aggregate interlock action (V_a) take all the lateral shear. The percentage of the total lateral shear that each shear resisting mechanism takes varies with the load and damage level in a way that is very difficult to quantify.

6.3.2. Analytical Solution for Monotonic Loading Based on a Simplified Model

The uncertainties and complexities involved in the development of a detailed generalized shear deformation model made necessary the development of a simplified model.

The topology (geometric properties) of the specimen and the shear resisting mechanisms change with the load and deformation level. A step-by-step solution is then required.

(a) Uncracked Wall

Before the formation of flexural or diagonal cracks, the wall can be assumed to be elastic. The shear displacements can be computed as

$$\Delta\delta_i^e_{shear} = \frac{6}{5} \frac{\Delta V h_i}{G A_v} = \text{elastic shear displacement at } i^{\text{th}} \text{ floor} \quad (6.1)$$

where h_i is the height of the level considered, A_v is the effective shear area which can be taken as the area of the web, and

$$G = \frac{E_c}{2(1+\nu)} \quad (6.2)$$

taking the value of ν as 0.2 [9], and for the case of Specimen 3 where $E_c = 21300$ MPa, the shear modulus can be computed as:

$$G = \frac{21300}{2(1+0.2)} = 8875 \text{ MPa}$$

and the shear displacement at the third floor level as:

$$\delta_3^e_{shear} = \frac{6}{5} \frac{(3001) V}{(8875)(243000)} = 1.66 \text{ mm/MN}$$

Hence, the elastic shear stiffness at the third floor level is:

$$K_3^e_{shear} = 1 / \delta_3^e_{shear} \\ K_3^e_{shear} = 0.600 \text{ MN/mm}$$

Similarly, the values at the first floor level can be obtained as

$$\delta_1^e_{shear} = 0.652 \text{ mm/MN} \\ K_1^e_{shear} = 1.530 \text{ MN/mm}$$

The $K_3^e_{shear}$ value is shown in Fig. 6.17 together with the experimentally obtained curve. Note that the experimental shear displacement values appear erratic for very small displacement values ($\delta_3 \leq 1 \text{ mm}$). The reason is the limited resolution of the linear potentiometers used to monitor the shear deformations (Fig. 3.4).

In order to check the initial shear stiffness value, an indirect procedure is used: The initial flexural stiffness was found experimentally to be $K_3^e_{flex} = 0.340 \text{ MN/mm}$. Using this value, together with the overall experimental stiffness value $K_3^e = 0.216 \text{ MN/mm}$ (Table 5.4), and assuming the fixed end deformation stiffness to be very high, $K_3^e_{fixed\ end} \gg K_3^e$, the initial shear stiffness can be determined as being:

$$\frac{1}{K_3^e_{shear}} = \frac{1}{K_3^e} - \frac{1}{K_3^e_{flexural}} \quad (6.3) \\ K_3^e_{shear} = 0.592 \text{ MN/mm}$$

which is very similar to the computed value of 0.600 MN/mm.

(b) Cracked Specimens

Concrete cracking must be expected even during service conditions. Most of the cracks in a wall specimen can be broadly classified as either flexural or shear cracks.

In the specimens tested, the average flexural crack width when the longitudinal reinforcement in the boundary element reaches yielding can be computed as $\Delta y = s \epsilon_y = 0.07 \text{ mm}$.

This average computed value is very small and the shear slippage along the cracks will also be small. For this reason the effect of the flexural cracks in the shear deformation before yielding of the longitudinal reinforcement will be neglected.

Diagonal cracks can considerably reduce the shear stiffness of the wall (because the concrete effectiveness is lost), and consequently cause increased shear deformations. In the wall with diagonal cracks, the greater portion of the lateral load is likely to be carried by diagonal concrete strut action, and by the horizontal panel reinforcement in tension (there is also a contribution of the floor slabs). The deformation characteristics of this mechanism are examined next.

A simplified truss analogy is introduced to represent the shear resistance of the diagonally cracked wall:

1) Crack Pattern

A good correlation was obtained between the crack pattern obtained experimentally, and that determined analytically (Section 6.2 and Fig. 6.11). On basis of the previous results, and for a simplified model of shear deformation, the crack pattern is idealized to that shown in Fig. 6.18.

The crack inclination in the upper two panels is uniform and approximately parallel to CH. In the case of pure shear stresses acting in a plain concrete element, the crack angle is $\pi/4$ radians. As the finite element results show in Fig. 6.11, the presence of flexural stresses and floor slabs causes this angle to change. In the lower panel the crack inclination is taken as parallel to AD. It should be noted that under monotonic loading the diagonal cracks propagate gradually, and do not penetrate as much in the upper panels as this idealization shows.

2) Idealized Truss

The idealized truss is shown in Fig. 6.18. Chords AG and BH are assumed to be infinitely rigid, as their deformations at this stage, in which they have moderate crack widths and the reinforcement has not yielded, contribute only to flexural deformations which have been accounted for separately (Section 6.2). The inclination of the diagonal elements in this idealized truss then, matches approximately the orientation of the diagonal concrete struts observed experimentally. Since the crack pattern can be approximated analytically (Figs. 6.11[a] and [b]) accounting for the effect of the panel reinforcement and the floor slabs, it is theoretically possible to predict the topology of this equivalent truss.

The horizontal panel reinforcement and the slab reinforcement are lumped at the slab level. Under a lateral load increment ΔV , chord CD elongates ΔCD . The concrete struts in the lower and upper panels shorten ΔDA and ΔHC respectively, and the third floor undergoes an overall shear displacement $\Delta \delta_3^c$ (Fig 6.18[b])

The shear displacement can be obtained by applying Williot's principles as shown in Fig. 6.18(c) where a negative sign indicates compression:

$$\Delta \delta_3^c = \Delta CD - \Delta DA \sec \theta_1 - \Delta HC \sec \theta_2 \quad (6.4)$$

3) Element Properties

a) Chord CD: The horizontal steel lumped in CD includes half the horizontal steel in the first floor panel, the horizontal steel in the second panel, all of the steel included in the effective first floor slab width, and half of the steel included in the effective second floor slab width. The effective slab width was taken as 1.52 m (Section 6.2). The vertical steel was accounted for in the flexural deformation model.

The cross-sectional area of chord CD is

$$A_{CD} = 3200 \text{ mm}^2$$

and the elongation of chord CD can be computed as

$$\Delta CD = \frac{\Delta f_s}{E_s} l_c = \frac{\Delta V}{A_{CD} E_s} l_c \quad (6.5)$$

b) Concrete Struts: Many formulas are available for calculating equivalent strut widths. The width of the equivalent struts has been determined by many investigators to depend principally on the panel aspect ratio and the ratio of panel stiffness to frame stiffness. Widths typically vary from about one third to one eighth of the length of the panel diagonal. The equivalent strut widths used herein are calculated using empirical formulas developed by Mainstone for cracked concrete infill panels [69,70].

$$\lambda_{h_i} = h_i \left[\frac{E_t \sin 2\theta_i}{4 E I_h h_i} \right]^{1/4} \quad (6.6)$$

and

$$\frac{W_{eti}}{w_i} = .288 \left(\lambda_{h_i} \right)^{-0.1} \quad (6.7)$$

where

h_i, h'_i, θ_i and w'_i refer to Fig. 6.18(a),

w_{eti} is the effective strut width for stiffness of cracked concrete infilled panel.

E' is the panel modulus

E is the frame modulus

I_h is the column moment of inertia and

t is the panel thickness

In the case considered:

$$\begin{aligned} h_1 &= 1.18 \text{ m} & h_2 &= 1.83 \text{ m} \\ h'_1 &= 1.14 \text{ m} & h'_2 &= 1.71 \text{ m} \\ t &= 0.102 \text{ m} \\ \theta_1 &= 31^\circ & \theta_2 &= 42^\circ \\ E' &= E = E_c \\ I_h &= 3.47 \left(10^{-4} \right) m^4 \\ w'_1 &= 2.44 \text{ m} & w'_2 &= 2.81 \text{ m} \end{aligned}$$

Hence (from Eq. 6.5)

$$\begin{aligned} \lambda_{h1} &= 3.348 \\ \lambda_{h2} &= 5.803 \\ w_{et1} &= 0.255 \text{ m} \\ w_{et2} &= 0.242 \text{ m} \end{aligned}$$

The force in the diagonal struts can be calculated from equilibrium

$$\Delta Ci = -\Delta V \sec \theta_i \quad (6.8)$$

The compressive stresses are

$$\Delta f_{c_i} = \frac{-\Delta Ci}{t w_{eti}} \quad (6.9)$$

and the shortening of the compressive struts is:

$$\Delta DA_i = \frac{-\Delta f_{c_i} w'_i}{E_c} = \frac{-\Delta V w'_i}{t w_{eti} E_c \cos \theta_i} \quad (6.10)$$

4) Tangent Stiffness

Equation 6.4 can be expressed in a more general form substituting the expression for the steel deformations (see Eq. 6.5):

$$\Delta CD \text{ for } \frac{\Delta V l_c}{E_s A_s}$$

and the diagonal concrete strut deformations

$$\Delta DA \ \& \ \Delta HC \text{ for } \frac{\Delta V_i w'_i}{b_w w'_{eq \ i} E_c \cos \theta_i}$$

where i refers to the panel, one obtains:

$$\Delta \delta_n^c \text{ shear} = \frac{\Delta V l'_c}{E_s A_s} + \sum_{i=1}^n \frac{\Delta V_i w'_i}{b_w w'_{eq \ i} E_c \cos^2 \theta_i} \quad (6.11)$$

substituting numerical values in this equation, one obtains:

$$\Delta \delta_3^c \text{ shear} = (0.015 \text{ mm/kN}) \Delta V$$

for the shear displacement at the third floor level, and

$$\Delta \delta_1^c \text{ shear} = (0.00536 \text{ mm/kN}) \Delta V$$

for the first floor.

The tangent stiffness of the diagonally cracked wall then becomes:

$$K_3^c \text{ shear} = 66.6 \text{ kN/mm}$$

and

$$K_1^c \text{ shear} = 186.3 \text{ kN/mm}$$

In Fig. 6.17(a) it can be seen that the experimentally obtained third floor tangent shear stiffness for the cracked wall is $\approx 60 \text{ kN/mm}$.

In general an approximate model such as the one presented here should not be expected to be that accurate. In this case the agreement for the experimental and computed values is very good.

5) Transition Point

Having determined the initial stiffness and the cracked tangent stiffness for Specimen 3 it is necessary to determine the transition point, or the point at which the shear resisting mechanism changes from an elastic shear beam to an "equivalent truss". Evidently the change is gradual. The load at which diagonal cracking appears $V = 311 \text{ kN}$ (Section 5.3.1) can be considered to be the point at which the transition starts. The point at which the transition is completed is not well defined. From experimental observation of the diagonal cracking and the results obtained in Section 6.2 (Fig. 6.11), the transition load is considered to be the one at which a diagonal crack completes opening all the way along the height of the panel [$V = 445 \text{ kN}$ from the analytical results shown in Fig. 6.11(a)]. The transition point thus determined is shown in Fig. 6.17 (point A).

(c) Yielding Specimen

1) Experimental Observations

The experimental observations for Specimen 3 (Figs. 6.19[a] and 6.20) show simultaneous yielding of the shear and flexural deformation mechanisms at LP 49. Comparison of Figs. 6.19(a) and 6.19(b) shows that shear yielding in the second story took place at a higher load (LP 51). In other words, even if the shear stresses were the same in all panels, shear yielding is observed only if the flexural mechanism in that panel yields. Being the first panel subjected

to the highest flexural moment, it will have "shear yielding" first, and the upper panels will not show "shear yielding" until higher lateral load levels are reached.

2) Mechanisms of Shear Yielding

In order to understand the observed "shear yielding" and its interaction with the flexural yielding consider Fig. 6.21.

If after flexural yielding is reached in panel ACDB, a small load increment ΔV is applied, the following deformation increments can be visualized in a hypothetical truss (Fig. 6.21 [b])

- a) Chord DB elongates a large amount ΔDB , because the longitudinal reinforcement has reached the plastic plateau.
- b) Chord CA in compression does not shorten a large amount because the concrete in the boundary element is effective in compression $|\Delta CA| \ll |\Delta DB|$.
- c) While the vertical chords are the main flexural resisting mechanism, the shear resisting mechanism is made up of the horizontal and diagonal chords. Chords CD and DA shorten small amounts $-\Delta CD$ and $-\Delta DA$ under load increment ΔV [Fig. 6.18(b)].
- d) Chord CB, that has practically no tensile axial stiffness after diagonal cracking of the wall panel, elongates a large amount ΔCB to accomodate the other chord deformations. The resulting deformed configuration is shown in Fig. 6.21(b) and is analogous to the deformed configuration obtained from the photogrammetric reading (Fig. 4.82).

3) Calculation of Shear Stiffness After Yielding

The device used for measurement of the shear distortions is shown in Fig. 3.4. The value of the shear distortion is computed from the changes in diagonal distance as measured by the linear potentiometers (Fig. 6.21):

$$\Delta \gamma_{av} = \frac{\Delta CB - \Delta DA}{2} \frac{w'}{l_c h} \quad (6.12)$$

a discussion of the reliability of this shear measurement procedure was presented by Ma, et al. [24].

In Eq. 6.12 there is an implicit assumption that large deformations take place in the diagonal elements only. As has just been explained, the tensile boundary element also undergoes large deformations. To accomodate this the diagonal element CB undergoes additional tensile deformation. Therefore Eq. 6.12 is revised in light of this observation.

From Fig. 6.21(b) ΔCB can be expressed as a function of the deformations of the other chord elements:

$$\begin{aligned} \Delta CB = & \Delta DB \frac{h}{w'} + \Delta CD \frac{l_c}{w'} - \Delta DA \\ & - \Delta CA \frac{h}{w'} + \Delta AB \frac{l_c}{w'} \end{aligned} \quad (6.13)$$

substituting this expression into Eq. 6.12, one obtains:

$$\begin{aligned} \Delta \gamma_{av} = & \frac{\Delta DB}{2 l_c} - \frac{\Delta CA}{2 l_c} + \frac{\Delta CD}{2 h} \\ & + \frac{\Delta AB}{2 h} - \Delta DA \frac{w'}{l_c h} \end{aligned} \quad (6.14)$$

The first two terms in this expression give the effect of the axial deformation of the boundary elements in the observed shear deformations. Since the axial deformations in the boundary elements are related to the flexural moments, the first two terms can be considered to be the effect of the interaction with the flexural mechanism.

From Eq. 6.14 the increase in the shear deformation at the i -th floor level can be expressed as

$$\Delta \delta_{i, shear} = \sum_{j=1}^i h_j \Delta \gamma_{av j} \quad (6.15)$$

where j refers to the panel level (Fig. 6.18).

The shear distortion in the first floor panel can be obtained substituting the corresponding values in Eq. 6.14.

$$\left(\frac{\Delta CD}{2 h} \right) h = \left(\frac{\Delta V l'_c}{2 h E_s A_s} \right) h \quad (6.5[a])$$

$$= 2.083 (10^{-6}) \Delta V \text{ mm/N}$$

$$\left(\Delta DA \frac{w'}{l_c h} \right) h = - \frac{\Delta V w'}{t w'_{et} E_c \cos \theta} \frac{w'}{l_c} \quad (6.10[a])$$

$$= -5.373 (10^{-6}) \Delta V \text{ mm/N}$$

to calculate ΔDB and ΔCA two procedures are available:

- a) A very accurate procedure would be to calculate the values of $\Delta DB / \Delta V$ and $\Delta CA / \Delta V$ from the mathematical model for flexural deformation developed in Section 6.2. This procedure would take into account the effect of diagonal cracking in spreading the yielding of the reinforcement along the boundary element.
- b) A simplified procedure would be to assume that the strain along the boundary elements is constant, that only steel takes tension in the tension boundary element, that the steel is already yielded, and that steel and concrete take compression in the compression boundary element. These are all reasonable assumptions.

For the sake of simplicity, the second procedure is pursued here. From the specimen's geometry and making the simplifying assumption that only the boundary elements take the flexural moment:

$$\frac{\Delta DB}{2 l_c} h = \frac{\Delta V h_v}{2 l_c^2 A_s E_{sth}} h \quad (6.16)$$

$$= 193.75 (10^{-6}) \text{ mm/N } \Delta V$$

where h_v is the effective moment arm of the forces acting on the wall (Fig. 6.12), and

$$\frac{\Delta CA}{2 l_c} h = - \frac{\Delta V h_v h^2}{2 l_c^2 A_{cc} E_c} \quad (6.17)$$

where (from Ref. [9]):

$$E_c = 21300 \text{ N/mm}^2$$

and A_{cc} = composite column area =

$$A_c + \left(\frac{E_s}{E_c} - 1 \right) A_s = 572000 \text{ mm}^2$$

$$\frac{\Delta CA}{2 l_c} h = -0.0063 (10^{-6}) \text{ mm/N } \Delta V$$

Hence from Eq. 6.15

$$\Delta \delta_{i, shear}^y = 199 (10^{-6}) \text{ mm/N } \Delta V$$

$$K_{shear}^y = 5.02 \text{ kN/mm}$$

In Fig. 6.17(b) it can be observed that this is a reasonable average value for the shear yielding

stiffness.

The upper panels will not develop shear yielding until the flexural moment reaches a high enough value so that those panels present flexural yielding. Right after the lower panel yields, the overall shear displacement increment at the third floor level will be

$$\begin{aligned}\Delta\delta_{3\ shear}^y &= \Delta_{1\ shear}^y + \Delta_{2\ shear}^y \\ &= 207 (10^{-6}) \text{ mm}/N \Delta V\end{aligned}\quad (6.18)$$

and the overall tangent shear stiffness according to the simplified analysis is:

$$K_{3\ shear}^y = 4.82 \text{ kN}/\text{mm}$$

This stiffness, together with the more accurately determined stiffness BCC' (that was determined on the basis of the results obtained from the analytical flexural deformation model for $\frac{\Delta DB}{\Delta V}$, and $\frac{\Delta CA}{\Delta V}$) are shown in Figure 6.17(a).

6.3.3. Analytical Solution for Monotonic Loading of Rectangular Wall

In order to provide another example and test the validity of the assumptions inherent in the development of the shear deformation model, the stiffnesses for the monotonic shear force-shear deformation curve for Specimen 5 (rectangular wall specimen) were calculated. Following step-by-step the procedure developed in Section 6.3.2 three stages of behavior are recognized.

(a) Uncracked Wall

On the basis of Eq. 6.1:

$$\delta_{3\ shear}^e = \frac{6}{5} \frac{1}{GA_v} \left[\sum_{i=1}^3 (h_i - h_{i-1}) \Delta V_i \right] \quad (6.1[a])$$

where i refers to each individual panel.

This equation is similar to Eq. 6.1 but takes into account the fact that the shear force is different in each panel. One obtains:

$$\delta_{3\ shear}^e = 0.00135 \text{ mm}/\text{KN} \Delta V$$

and

$$K_{3\ shear}^e = 743 \text{ KN}/\text{mm}$$

(b) Cracked Specimen

1) Crack Pattern

The idealized crack pattern for this specimen is similar to that shown in Fig. 6.18.

2) Idealized Truss

The geometry of the idealized truss is shown in Fig. 6.18.

3) Element Properties

a) Chord CD: Including the horizontal reinforcement in the panel and the slabs as explained in Section 6.3.2 the cross-sectional area of chord CD is

$$A_{CD} = 2370 \text{ mm}^2$$

b) Concrete Struts: Applying Eqs. 6.6 and 6.7 in this case

$$\begin{aligned}
 h_1 &= 1.18 \text{ m} & h_2 &= 1.83 \text{ m} \\
 h_1' &= 1.14 \text{ m} & h_2' &= 1.71 \text{ m} \\
 t &= 0.114 \text{ m} \\
 \theta_1 &= 31^\circ & \theta_2 &= 42^\circ \\
 E &= E \\
 I_h &= 2.08 \left(10^{-4}\right) \text{ m}^4 \\
 w_1 &= 2.44 \text{ m} & w_2 &= 2.81
 \end{aligned}$$

Hence (from Eq. 6.6)

$$\lambda h_1 = 3.79 \text{ m}$$

$$\lambda h_2 = 5.37 \text{ m}$$

and (from Eq. 6.7)

$$w_{et_1} = 0.614 \text{ m}$$

$$w_{et_2} = 0.730 \text{ m}$$

4) Tangent Stiffness

Replacing values in Eq. 6.11

$$\begin{aligned}
 \Delta \delta_3^c \text{ shear} &= \frac{1880 \Delta V}{0.19 (10^6) (2370)} \\
 &+ \frac{1}{114 (0.026) (10^6)} \left[\frac{2438 \Delta V}{614 (0.857)} + \frac{2810 (0.85 \Delta V)}{730(0.743)} \right]
 \end{aligned}$$

(note that for the second panel the average shear force is 0.85 of the base shear)

$$\Delta \delta_3^c \text{ shear} = 7.22 \times 10^{-6} \text{ mm/N}$$

$$\Delta \delta_3^c \text{ shear} = 3.5 \times 10^{-6} \text{ mm/N}$$

and

$$K_3^c \text{ shear} = 138 \text{ kN/mm}$$

$$K_1^c \text{ shear} = 285 \text{ kN/mm}$$

(c) Yielding Specimen

Following the procedure used for the case of the framed walls, the element properties corresponding to the first floor of Specimen 5 are:

$$A_s = 1783 \text{ mm}^2 \quad (9\#5 \text{ bars})$$

$$A_{cc} = A_c + \left(\frac{E_s}{E_c} - 1\right) A_s = 46057 \text{ mm}^2$$

$$E_s = 0.19 (10^6) \text{ MPa}$$

$$E_c = 0.021 (10^6) \text{ MPa}$$

these, together with the values in Section 6.3.3.(b) are used to determine the values of the terms in Eqs.6.15 and 6.14.

From Eq. 6.5(a):

$$\frac{\Delta CD}{2} = \frac{1880 \Delta V}{2 (0.19 \times 10^6) (2370)} = 2.1 (10^{-6}) \text{ mm/N}$$

From Eq. 6.10(a):

$$\frac{\Delta DA w'}{l_c} = - \frac{2440^2 \Delta V}{114 (614) (21300) (0.857) (2370)} = - 2.0 (10^{-6}) \text{ mm/N}$$

From Eq. 6.16:

$$\frac{\Delta DB h}{2 l_c} = \frac{4720 (1180^2) \Delta V}{2 (2134^2) (1783) (1485)} = 273 (10^{-6}) \text{ mm/N}$$

From Eq. 6.17

$$\frac{\Delta CA}{2 l_c} = - \frac{4720 (1180^2) \Delta V}{2 (2134^2) (46057) (21300)} = -0.74 (10^{-6}) \text{ mm/N}$$

replacing these values in Eq. 6.15 one obtains:

$$\begin{aligned} \Delta \delta_{shear}^y &= 277.5 (10^{-6}) \text{ mm/N} \\ K_{shear}^y &= 3.6 \text{ kN/mm} \end{aligned}$$

and from Eq. 6.18

$$\begin{aligned} \Delta \delta_{shear}^y &= 277.5 (10^{-6}) + 3.59 (10^{-6}) = 281 (10^{-6}) \text{ mm/kN} \\ K_{shear} &= 3.56 \text{ kN/mm} \end{aligned}$$

The results obtained are shown in Fig. 6.22. This result is shown in Fig. 6.22. It can be observed that the stiffness values obtained using this simplified procedure are in reasonable agreement with the experimental observations.

6.3.4. Shear Deformations Under Cyclic Loading

A complete solution for shear deformations under generalized loading is beyond the scope of this work. Nevertheless the possibility of extending the results obtained so far, for explaining the results obtained, is explored in this section.

A simplified procedure to determine the shear deformations under cyclic loading is presented. This procedure is based on the shear mechanism developed in the previous section. The monotonic shear deformation relationship is used as an envelope for the cyclic shear deformation curve. The following description refers to the tangent stiffness of the cyclic shear deformation curve. (Fig 6.23)

(a) Elastic Loading (path OAA') (Fig. 6.23[a])

The virgin wall with no diagonal cracks responds as an elastic shear beam (Eq. 6.1). Points A and A' are symmetric, and were defined in the monotonic shear deformation model as the load at which a diagonal crack opens all the way along the height of the panel. At this point it can be assumed that the shear resisting mechanism changes from an elastic shear beam to an "equivalent truss mechanism".

(b) Diagonally Cracked Wall (Path AB) (Fig. 6.23[b])

When the diagonal cracking load is exceeded (point A), the wall follows the monotonic curve until either the load is reversed or the yielding point B is reached (point B was determined in the previous section in basis of the flexural yielding, and its interaction with the shear deformations). If the load is reversed at point B, or before B is reached, the return path is a straight line with elastic stiffness. This hypothesis is based on the phenomenon that upon unloading, the materials used (steel and concrete) rebound almost elastically. Because of the actual constitutive relation for materials (Figs. 5.24 and 6.5), the real unloading stiffness will be slightly lower than that proposed by this model.

As shown in Fig. 6.23(b), when the load is removed after reaching diagonal cracking load, there is a residual shear deformation because the cracks do not close completely.

(c) Yielding Wall (Path BC) (Fig. 6.23[c])

When the yielding load is exceeded the response will coincide with the monotonic curve until the load is reversed. Upon load reversal the wall will unload elastically (C1 D2).

(d) Negative Loading. (Path D1 E' or D2 E') (Fig. 6.23[d])

If after reaching either D1 or D2 a negative load increment is applied, the open cracks along the compression diagonal (CB in Fig. 6.24 [a] and [b]) have to close before the diagonal concrete strut becomes effective and the stiffness picks up again. Before that happens, the shear resistance is provided by the dowel action and the aggregate interlock along the open cracks. If the wall has been loaded up to cracking in only one direction, a portion of the shear resistance is also provided by the uncracked concrete cross-section.

The development of a microscopic model in which the panel with open cracks is modeled requires a tremendous computational effort, and the results from such complex models have been generally disappointing [71 to 73], although Ma et al. [24] were able to clarify the mechanisms. This is due principally to the present lack of knowledge regarding the mechanical behavior of cracked reinforced concrete, in particular in regards to bond slippage and interface shear transfer.

Therefore it was decided at this point to develop guidelines based on the careful observation of the experimental results obtained in the present investigation (i.e. Figs. 4.3, 6.19[a] and [b], 4.15, 4.47, and 4.57) and those obtained by other researchers [1,24,74,75]. The following conclusions were gathered:

1. The deformation level at which the shear stiffness picks up after a load reversal corresponds approximately to the zero shear deformation. This is because at zero shear deformation the diagonal cracks along the compression diagonal (CB in Fig. 6.24) close, and the diagonal concrete strut becomes effective. (This can be clearly observed in the photogrammetric readings of Figs. 4.82(a) and (d), and the schematic representation of the deformed configuration in Figs. 6.24(a) and (b). They show that at load point 83T in Fig. 6.25 for Specimen 4, the diagonal cracks close and the stiffness changes drastically). However due to bond-slippage and deterioration at the crack surfaces it would require the deformation to go beyond zero shear deformation.
2. There is a maximum lateral shear resistance that can be developed while the diagonal cracks in the panel are open (Figs. 6.25, 4.57, etc.), (also Refs. [1,74,75]). While this maximum shear resistance is affected by a number of different parameters such as the type of boundary elements, the amount and distribution of longitudinal reinforcement, the concrete strength, etc., it seems to be mainly a function of the axial stress on the specimen's cross section. Referring to this maximum strength as the "friction shear strength" V_f , a simple expression is assumed:

$$V_f = [\alpha_1 + \alpha_2 f_a] A_c \quad (6.19)$$

Where f_a is the average axial stress on the specimen's cross-sectional area A_c , and α_1 and α_2 are constants determined on the basis of experimental results of this investigation and that of Refs. [1,74,75] as:

$$\alpha_1 = 0.104 \text{ MPa} \quad (6.20)$$

$$\alpha_2 = 0.169 \quad (6.21)$$

Table 6.2 shows the comparison of predicted and observed V_f values. On basis of these observations, points E and E' on Figs. 6.23(d) and (e) are determined to be at the intersection of the monotonic shear deformation curve with the friction shear strength level V_f . The shear stiffness of the wall diagonally cracked in both directions will change at these points. Note that if the wall is not diagonally cracked in both directions (i.e. if point A' in Fig. 6.23 has not been reached previously) the shear resisting mechanism in this direction is still an elastic shear beam. A way to take this into account is to define the reloading stiffness as D1 A' or D2 A'

instead (Fig. 6.23[e]).

(e) Further Negative Loading for the First Time

In the first excursion into the negative loading region (Path A'B' Fig. 6.23[f]) the wall follows the monotonic envelope until the load is reversed again. Upon load reversal the behavior is initially elastic.

(f) Reloading After Cycling (Path EC2 Fig. 6.23[g])

If the wall has previously reached both diagonal cracking points A and A', and is loaded beyond the friction shear strength load level V_f (Eq. 6.19), it will follow path E C2, where C2 corresponds to the largest deformation previously reached in that direction, and to a degraded strength. If the load is reduced before reaching C2, the behavior is elastic (point H). If the specimen has not previously been loaded beyond yield in this direction, C2 matches point B the corresponding yielding point in this direction.

At present there is not insufficient data to quantify in a general form the amount of strength degradation with shear cycling. If this degradation is neglected, and the cyclic shear behavior at ductility two is computed, the results shown in Fig. 6.26 are obtained.

Path A-B-C1 The monotonic curve (Fig. 6.17[a]) is followed (hysteresis rules [a], [b], and [c] up to a load of 984 kN which is the load determined analytically to correspond to a displacement ductility of 2 (point C in Fig. 6.13). It can be observed that the shear deformation determined experimentally is very close to the one determined analytically (point C1 in Fig. 6.26).

Path C1-D2 Unloading is performed elastically to zero load (hysteresis rule [c]). It can be observed that the experimental unloading stiffness initially matches the elastic stiffness, but decreases gradually before reaching zero load and good agreement is not obtained.

Path D2-E' Point E' is determined at the intersection of the zero shear deformation with the "friction shear strength V_f " (empirical Eqs. 6.19 to 6.21) (hysteresis rule [d]):

$$V_f = [0.104 + 0.169 \frac{0.868}{0.32}] 0.32 (MN)$$
$$V_f = 180 \text{ kN}$$

where 0.868 MN is the axial load in the specimen, and 0.32 m^2 is the cross-sectional area. It can be observed that point E' agrees with the experimental results.

Path E'-F The loading path follows line E'-F, where F matches point B' the mirror yield point of the monotonic envelope (hysteretic rule [f]). It can be observed that the stiffness is in reasonable agreement with the experimentally observed one.

Path F-G1 Loading is continued along the monotonic envelope to a load of -991 kN. This load was determined analytically to be the load at which a nominal ductility of -2 is reached (Fig. 6.13 and Table 6.1). The agreement with the experimental curve at this point is reasonably good.

Path G1-G2-E The procedure followed and the results are similar to those of path C1-C2-E'. Point E is the mirror point of point E' (hysteresis rule [d]).

Path E-C1 Reloading after having reached yielding in this direction is done following the hysteresis rule (f). C1 corresponds to the largest deformation reached previously in this direction. It can be observed that while the deformations differ from those of the experimental results, the stiffnesses are in good agreement. This means that the location of point E is not quite correct.

6.4. Tip Displacement Component Because of Fixed End Deformations

6.4.1. Introduction

As explained in Section 5.1.3, in the particular case of the specimens pertaining to this investigation, the fixed end deformations caused by the slippage of the longitudinal reinforcement along its embedment in the foundation (Fig. 6.27) contribute only a minor portion of the total tip displacement (see Figs. 4.2, 4.5, and 4.12). There are several reasons that explain this situation: 1) the geometry of the Specimen (Fig. 5.15); 2) the extremely good embedment length and confinement provided to the longitudinal reinforcement in the foundation; 3) the existence of either a pull or push action only, on the longitudinal bars at a given time; 4) the existence of distributed vertical panel reinforcement of small diameter which has more area to transfer bond stresses than that of one large bar of equivalent steel area; and finally 5) the confining effect that the steel plates used for bearing the prestressing rods attaching the specimen to the foundation (Fig. 6.28) have on the concrete they bear against. These steel plates help prevent the spalling of the foundation's unconfined concrete cover.

6.4.2. Solution Procedure

(a) General

The general approach to the solution of the fixed end deformation problem is summarized in Fig. 6.29.

In order to predict the displacement $\delta_{3 \text{ fixed end}}$ under generalized loading conditions, the specimen is assumed to be properly designed against shear effects, so that the dowel action (because of the shear in the longitudinal reinforcement at the base of the specimen) has only a negligible effect in the longitudinal steel strain at that level. In this way the external action relevant to $\theta_{\text{fixed end}}$ is only the moment at the base M_o .

As elaborated in Section 6.2, if the axial stress-strain relations for the materials used are known, it is possible to determine the curvature (ϕ_o) and the position of the neutral axis at the base of the specimen as a function of a generalized moment at the base M_o (see Fig. 5.3). The steel stresses and strains at the base of the specimen ϵ_s^o and σ_s^o are determined in this process.

Having ascertained the longitudinal strains at the base of the specimen, it is necessary to determine the strain distribution along the length of the embedded bar. This strain distribution will allow determination of the bond slip (δ_s^A) at the base of the specimen (Fig. 6.27).

The criteria for the determination of the strain distribution will be elaborated upon later in this section.

(b) Analytical Expressions for Bond Slippage

In Fig. 6.27 the base of the foundation CC' is the axis relative to which the displacements are measured. The displacement of the steel section at the base of the wall δ_s^A can be computed as follows:

$$\delta_s^A = \int_0^{x_c} \epsilon_s^x dx \quad (6.22)$$

This expression is based on Bertero, et al. [22], and assumes that the straight boundary CC' of the foundation remains rigid.

The strain distribution along the embedment length ϵ_s^x is in general unknown, and it is convenient to express it as a function of the bond stress distribution in the following way, using:

$$\epsilon_s^x = \epsilon_s^o - (\epsilon_s^o - \epsilon_s^x) \quad (6.23)$$

where $(\epsilon_s^o - \epsilon_s^x)$ is the decrease in steel strain from $x=0$ to $x=x$ due to stress transfer

$$\text{stress transfer} = \int_0^x \frac{\delta\sigma_s^x}{E_{tx}} \quad (6.24)$$

where E_{tx} is the tangential modulus of elasticity corresponding to σ_s^x , and

$$\delta\sigma_s^x = \frac{\mu_x \phi dx}{A_s} \quad (6.25)$$

where μ_x is the bond stress, ϕ is the perimeter of the bar, and A_s is the steel cross-sectional area.

Therefore:

$$\epsilon_s^x = \epsilon_s^o - \int_0^x \frac{\mu_x \phi}{A_s E_{tx}} dx \quad (6.26)$$

$$= \epsilon_s^o - \frac{\phi}{A_s} \int_0^x \frac{\mu_x}{E_{tx}} dx \quad (6.27)$$

using this last equation δ_s^A can be computed as follows:

$$\begin{aligned} \delta_s^A &= \int_0^{x_c} \epsilon_s^x dx \\ &= \epsilon_s^o x_c - \int_0^{x_c} \int_0^x \frac{\mu_x \phi}{A_s E_{tx}} dx dx \end{aligned} \quad (6.28)$$

by using this expression the determination of δ_s^A is reduced to predicting the bond stress distribution along the bar. The bond stress distribution is highly complex, and varies as a function of σ_s^o , ϵ_s^o , f'_c , the degree of confinement, the deformations in the reinforcement bar, the degradation with the variation of ϵ_s^o , the axial force in the specimen, etc. [20,22].

Since the tip displacement caused by fixed end deformations is rather small (about 10% of the total tip displacement as shown in Section 4.3), a simplified mechanical model is considered to be adequate. The model gives an estimate of the peak value of bond resistance, and an approximate bond stress distribution along the embedment length. More refined models (warranted in beam column connections, where the fixed end deformation is rather significant) are shown in Refs. [20,22].

(c) Experimental Data

The instrumentation pertinent to the fixed end deformation measurements are clip gages K11, C11, K1, and C1 shown in Fig. 3.4. This clip gage set up is used to determine the bond slip δ_s^o at the base of the wall. It can be observed that clip gages C1 and C11 are attached to the foundation ($x=0$ in Fig. 6.27) while gages K1 and K11 are attached to the base of the column. Consequently the difference in the readings of K1 and C1, and K11 and C11 gives the opening of the crack at the base of the specimen. It should be noted that for a true δ_s^o reading, C1 and C11 should be attached to the base of the foundation (plane C-C' in Fig. 6.27), but since the foundation is very rigid, it is assumed that the point at which the clip gages were attached to (Fig.3.4) is far enough from the column to prevent localized distortions, and that this point does not displace with respect to C-C'.

Related data were obtained with strain gages F1, F2, C1-C4, V1, and V2 (Fig. 3.5). It can be observed that only one bar in each column is instrumented with a strain gage below the foundation level. Gages C1-C4 give the maximum steel strains ϵ_s^o at the foundation level O-O', and gages F1 and F2 provide some data regarding the strain distribution along the embedment.

It should be recognized that the data available are not sufficient to formulate an accurate mechanical model. For that reason data obtained by Viwathanatepa [20] was also studied.

Figure 6.30 shows the fixed end deformation component for Specimen 3 presented in Fig. 4.5 after greatly expanding the horizontal axis.

Figure 6.31 compares the strain distribution data obtained in this investigation with that presented by Viwathanatepa. A general agreement can be observed with some minor differences: 1) The strain gradient along the reinforcement is larger in the case of Viwathanatepa's results. This is explained because the simultaneous application of the push and pull action in the #6 bar specimen of Ref. [20] is different from the push only or pull only conditions that the bars embedded in the foundation of the structural walls were subjected to. The higher strain gradient is mostly noticeable in the region where the effect of the tension and compression forces overlap. 2) After a certain strain level, the unconfined concrete cover in the specimens of Ref. [20] spalls. This is not the case in the specimens tested, the reason being that the foundation of the structural wall was attached to the anchor blocks at the test site by means of prestressed rods (Figs. 2.17, 3.3[a], and 6.28). The bearing plates for those rods together with the very good confinement for the column (Fig. 6.28) prevented the spalling of the unconfined concrete cover reported in Refs. [20,22].

According to Viwathanatepa's observations, the region of the concrete disturbed by a # 6 stressed bar, when good confinement is provided, amounts to a cylinder concentric with the bar and with a radius of 50 mm. For this reason no interaction is expected between the different longitudinal reinforcing bars at the base of the walls (Fig. 6.28[a]).

(d) Analytical Prediction of Fixed End Deformation

The general process for deriving the fixed end deformations is summarized in the flow chart of Fig. 6.29. The following assumptions are used in the analytical prediction of the fixed end deformation:

1. The strain distribution in the cross-sectional area of the boundary elements is assumed to be constant.
2. The effect of the panel reinforcement which comprises 25% of the total longitudinal reinforcement is considered in the computation of the moment-curvature relation at the base of the wall. In this way, its effect is taken into account in the evaluation of ϵ_s^A (the tensile steel strain at the base of the wall in Fig. 6.27).
3. The steel stress-strain is idealized as shown in Fig. 6.2. A more elaborate model (i.e. Fig. 5.24) is not warranted in this case.
4. As previously explained, because of the very good confinement provided by the hoops in the column and the prestressing plates, all the concrete along the embedment length is assumed to be confined (there is no spalling of unconfined concrete cone [22]), and no interaction is expected among the longitudinal bars.

(e) Numerical Computations

It is necessary to distinguish different regions in the behavior as a function of the bar straining:

1) Region $\epsilon_s^A \leq \epsilon_s^y$

It should be recognized that the data available from this investigation [Section 5.4.2.(c)] are not sufficient to estimate the bond stress distribution. For this reason data reported by Viwathanatepa [20] were also studied. It is apparent from Figs. 6.31(a) and (b) that a constant bond stress distribution with a peak stress of 10 MPa could approximately represent the bond stress distribution in the reinforcement.

For a strain $\epsilon_s^A = \epsilon_s^y = 2100 \mu\epsilon$ or a stress $\sigma_s = 444 \text{ MPa}$, which is reached at a load (Table 6.1) of 774 kN, and a bar diameter d of 19 mm, the required embedment length l_d is:

$$l_d = \frac{\sigma_s d}{4 \mu_o} = 209 \text{ mm} \quad (6.29)$$

This represents the length required to transfer the required steel stress to the concrete.

While initially (before any cracking takes place) the wall can be considered to behave elastically, and the deformations in the compression region are as large as the ones in the tension region, as soon as cracking initiates, the pull out in the tension side is much greater than the deformation in the compression side. The latter is neglected in this presentation. The effect of this assumption can be derived from inspection of Fig. 6.27. If δ_s^B is zero, the tip displacement $\delta_{3 \text{ fixed end}}$ is slightly underestimated. This can also be expressed as:

$$\delta_{3 \text{ fixed end}} = (\delta_s^B + \delta_s^A) \frac{h_3}{l_c} \approx \delta_s^A \frac{h_3}{l_c} \quad (6.30)$$

The value of δ_s^A can be computed replacing $x = x_c = 209 \text{ mm}$ in Eq. 6.28.

$$\delta_s^A = 0.219 \text{ mm}$$

and the related third floor flexural displacement is (Eq. 6.30):

$$\delta_{3 \text{ fixed end}} = \frac{\delta_s^A h_3}{l_c} = 0.31 \text{ mm}$$

which is shown as point (A) in Fig. 6.30. The initial stiffness of the base shear-fixed end deformation component diagram is then

$$K_s^{\text{fixed end}} = 774/0.31 = 1497 \text{ kN/mm}$$

2) Region $\epsilon_c^A \geq \epsilon_c^y$

Figure 6.32 shows the bond distribution assumption and corresponding stress and strain distributions. These are very simplified relations. More comprehensive models are presented in [20,22].

The embedment length required to transfer the stress at the point when the maximum load was reached in the wall is:

$$l_d = \frac{639 \text{ MPa} \times 18.9 \text{ mm}}{4 \times 10 \text{ MPa}} = 302 \text{ mm}$$

and the value of δ_s^A can be computed as:

$$\delta_s^A = \frac{209 \times 0.0021}{2} + 93 \times 0.0021 + \frac{0.1179 \times 93}{2} = 5.9 \text{ mm}$$

Neglecting the deformation in the compression side, the third floor displacement can be computed from Eq. 6.30.

$$\delta_{3 \text{ fixed end}} = 8.4 \text{ mm}$$

This is shown as point B in Fig. 6.30.

Other intermediate points (C and D) computed in a similar way are presented in Fig. 6.30. In spite of the very crude assumptions regarding bond stress distributions good results were obtained as can be seen in Fig. 6.30.

6.5. Evaluation of Analytical Results for Overall Force Deformation Relations

Experimental and analytical strengths at different stages are compared in Table 6.1. Figure 6.33 shows the curve obtained by superimposing the deformation components (Figs. 6.10, 6.17, and 6.30) and its comparison to the experimentally obtained overall deformation curve.

The force deformation values at a few chosen points are compared to the experimental

results in Table 6.3. The determination of these points is illustrated as follows:

1. At the analytical flexural cracking load of 267 kN, the flexural deformation as obtained from the finite element analysis is 0.9 mm (Table 6.1). The shear deformation model is in the uncracked stage (Fig. 6.17), and is computed as

$$\delta_{3 \text{ shear}} = 267/K_{3 \text{ shear}}^e = 267/592 = 0.45 \text{ mm}$$

The fixed end deformation (Section 6.3.3.[e]) is computed as

$$\delta_{3 \text{ fixed end}} = 267/K_{3 \text{ fixed end}}^e = 267/2497 = 0.11 \text{ mm}$$

The total displacement obtained adding these components is

$$\delta_3 = 1.5 \text{ mm}$$

2. The procedure can be repeated for the following points. At the analytical diagonal cracking load of 356 kN, the deformations are found to be:

$$\delta_{3 \text{ flexural}} = 1.3 \text{ mm}$$

$$\delta_{3 \text{ shear}} = 0.6 \text{ mm}$$

$$\delta_{3 \text{ fixed end}} = 0.14 \text{ mm}$$

$$\delta_3 = 2.1 \text{ mm}$$

3. At 774 kN, when the first yield of steel is analytically determined to take place, the flexural deformation (Table 6.1) is $\delta_{3 \text{ flexural}} = 5.3 \text{ mm}$. The shear deformation is beyond the transition point of 445 kN at which the shear resisting mechanism changes [Section 6.2.3.(b), and Fig. 6.17(a)]

$$\delta_{3 \text{ shear}} = 445/K_{3 \text{ shear}}^e + (774-445)/K_{3 \text{ shear}}^s = 5.69 \text{ mm}$$

The fixed end deformation is computed as

$$\delta_{3 \text{ fixed end}} = 774/2497 = 0.31 \text{ mm}$$

and the overall deformation is

$$\delta_3 = 11.3 \text{ mm}$$

4. At the maximum strength point of 1090 kN:

$$\delta_{3 \text{ flexural}} = 71.9 \text{ mm} \quad (\text{Table 6.1})$$

The shear deformation can be estimated from the overall tangent shear yielding stiffness $K_{3 \text{ shear}}^s = 4.82 \text{ kN/mm}$ [Section 6.3.2.(c)].

$$\delta_{3 \text{ shear}} = 5.69 + (1090 - 774)/K_{3 \text{ shear}}^s = 71.25 \text{ mm}$$

The fixed end deformation was computed in Section 6.4.2.(e) as 8.4 mm and the overall deformation is :

$$\delta_3 = 152 \text{ mm}$$

The agreement obtained is very good. In this way the original objective of developing a physically reasonable model of structural wall behavior under high shear conditions was achieved. Without further study, the idealization should not be applied to walls with openings, nor to walls with special panel reinforcement, (i.e. walls with diagonal panel reinforcement).

7. CONCLUSIONS AND RECOMMENDATIONS

7.1. Conclusions

The conclusions presented herein are based on the limited studies conducted, and should be considered as preliminary findings.

First, conclusions are presented regarding the main parameters controlling seismic behavior and design. These parameters are: strength; stiffness; stability and deformation; and energy absorption and energy dissipation capacities. Next, conclusions are presented regarding different factors that can affect the above parameters. These factors are: loading history; cross section; confinement of edge members; and moment-to-shear ratio. Finally, some conclusions are presented regarding the effectiveness of the repair technique used.

7.1.1. Main Parameters Controlling Seismic Behavior

(a) Strength

1. UBC's Eq. (9-5) underestimates the flexural cracking load capacity of reinforced concrete structural walls. Better results can be obtained by replacing the value of I_g in that equation by the equivalent moment of inertia of the composite reinforced concrete cross section.
2. Ultimate strength, computed according to present code formulas is less than the actual flexural strength capacity. This is primarily due to the fact that the code does not account for steel strain hardening.
3. The strength of properly designed slender walls (i.e. walls in which their lateral load capacity is controlled by their flexural strength) can be accurately estimated at different levels: cracking, working, yield, and maximum. The analysis must be based on realistic material mechanical characteristics and the assumption that plane sections remain plane.
4. The maximum flexural strength of a reinforced concrete structural wall can be estimated in a simple way by:

$$M_{\max} = (A_{s, \text{col}} f_{\max} + D/2) d$$

where

$A_{s, \text{col}}$ = Cross sectional steel area in boundary element.

f_{\max} = Maximum tensile strength of longitudinal reinforcement in the boundary element.

D = Axial dead load in specimen.

d = Effective depth of section, assumed to be the center-to-center distance between boundary elements.

5. Shear strength under monotonic load conditions can not be computed accurately from the UBC code equations, because these equations do not accurately reflect actual physical behavior. The following parameters are neglected in the code: the actual material properties, the contribution of the boundary elements; the strain hardening of the wall steel; and the effect of the floor slabs in restraining the opening of the shear cracks.

When the wall is subjected to very high moment and shear, wide flexural and diagonal cracks open on the tension side of the neutral axis. The interface shear transfer along these wide open cracks is very low; and the only portion of the wall that can effectively resist shear is the well confined concrete and longitudinal steel in the compression boundary element. Under these conditions, shear stresses greater than 0.96 and up to $1.82 \sqrt{f'_c}$ Mpa could be developed in the compression boundary element.

It should be noted that, in the code equations, the effective depth of the wall is considered to be $0.8 l_w$. This depth is used to compute the nominal shear stress. As the investigation reported herein demonstrates, after failure of the panel, only the well confined concrete and longitudinal reinforcement in the compression boundary element should be considered to resist shear effectively, and the maximum allowable shear stress value should be revised.

6. Under cyclic load reversals, the wide cracks due to inelastic deformation of the longitudinal reinforcement do not close immediately following load reversal. There is a range of loading where cracks along the whole cross section of the member remain open. At this point shear resistance is provided only by aggregate interlocking and dowel action. The aggregate interlocking deteriorates with cycling because of the grinding effect that takes place at the surface of the cracks; the only effective dowel action is that of the steel in the boundary member. The code equations are based on results of monotonic tests only and do not account for this deterioration and reduction in shear strength.

7. In the framed walls, nominal shear stresses of $1.116 \sqrt{f'_c}$ MPa ($13.43 \sqrt{f'_c}$ psi) were developed before shear failure took place. In the rectangular walls, the maximum nominal shear stress developed was $0.783 \sqrt{f'_c}$ MPa ($9.43 \sqrt{f'_c}$ psi), without inducing shear failure.

8. In all the tests reported the walls were capable of supporting the axial load due to gravity forces, even after the lateral load carrying capacity was lost.

(b) Stiffness

1. The stiffness of uncracked walls can be accurately estimated using beam theory and including shear deformations.

2. In order to estimate the stiffness of cracked or yielding walls subjected to high shear stresses: (a) realistic mechanical characteristics of materials should be used; and (b) the stress redistribution due to concrete cracking should be accounted for. Suggestions are made in this investigation of ways to estimate the stiffness of walls after cracking and yielding take place.

(c) Stability

1) Monotonic loading

Two distinct modes of buckling should be considered: local buckling and wall buckling.

The possibility of local buckling is determined by the diameter of the longitudinal reinforcement; the spacing of the lateral confinement; the stress-strain characteristics of the steel; the strain levels reached in the longitudinal steel and the workmanship which affects the effective buckling length. In order to reduce the possibility of local buckling large diameter bars and small lateral reinforcement spacing with high strength lateral reinforcement should be used.

The maximum compression strain that can be reached in a boundary element under monotonic loading is limited by the steel strain corresponding to buckling stress in the longitudinal reinforcement $f_{s\ cr}$:

$$f_{s\ cr} = \left(\frac{\pi d}{4 s K} \right)^2 E_{cr}$$

where K is the "effective length factor", a function of the workmanship (good workmanship should provide for good contact between the lateral confinement and the longitudinal reinforcement), d is the bar diameter, s is the tie or hoop spacing, and E_{cr} is the steel modulus corresponding to the buckling strain.

The possibility of wall buckling is determined by the ratio of the unsupported height of wall to the thickness of the confined concrete cross-section, and the compressive strain that can be reached.

2) Cyclic load reversals

Under load reversals the possibility of buckling increases because of the reduction of the effective EI of the wall cross section. This reduction is caused by: a reduction in the modulus of elasticity of the longitudinal reinforcement steel because of the Bauschinger effect, and a lessening in the moment of inertia in the cracked concrete section because of residual tensile cracks. Buckling then is determined by the tensile strain reached in the steel and the crack widths.

(d) Deformation

1. All walls yielded before reaching the UBC allowable story drift index of 0.005 K. Thus, except for cases where poor soil conditions can lead to significant rocking and/or sliding of the wall foundation, walls similar to those studied herein will satisfy the code allowable drift index.
2. The maximum interstory drift values obtained in the tests on the virgin specimens were greater in all cases than 0.015 (the maximum acceptable story drift under nonlinear response, according to the ATC recommendations). The values obtained were 0.0623 and 0.0405 for the monotonic and cyclic tests on framed walls, and 0.0238 and 0.0193 for the monotonic and cyclic tests on rectangular walls. This means that the available maximum deformation capacity of the tested walls exceeded the limit recommended by the ATC document [34].
3. The maximum overall deformation reached in the framed walls was 186.5 mm (corresponding to a nominal ductility value of 9.8). The corresponding value for the rectangular walls was 138 mm.
4. For the specimens tested, the maximum average curvatures observed in the critical cross section and measured over a length of 0.381 m, were 0.032 rad/m for the framed walls and 0.019 rad/m for the rectangular walls. The maximum rotations at the first floor level were 0.0438 and 0.021 rad respectively.
5. For the specimens reported, the contribution of the fixed end deformations to the total third floor displacement is small: 7% to 11%. Under monotonic loading the shear deformations are almost in a constant ratio with the flexural deformations ($\delta_{3\ shear} = 0.46 \delta_{3\ flex}$ for the framed specimen, and $\delta_{3\ shear} = 0.43 \delta_{3\ flex}$ for the rectangular specimen). Under cyclic loading $\delta_{3\ shear}$ increases with the number of load reversals and the intensity of the deformation, reaching 0.87 and 0.85 $\delta_{3\ flex}$ for the framed and the rectangular walls respectively.
6. Using the procedures developed in this investigation, the wall deformations under high shear stress conditions ($v_c \geq 6\sqrt{f'_c}$ psi or $0.5\sqrt{f'_c}$ MPa) can be predicted under monotonic load conditions up to the maximum flexural strength level. Procedures to determine the wall deformation under cyclic loading, are also presented but require further refinement.

(e) Energy Absorption and Dissipation

1. In the virgin framed wall subjected to monotonic loading the energy absorption increases with the lateral deformations (after yield the rate of increase is almost linear). The flexural deformations constitute the main source of energy absorption.

With cyclic loading the relation between energy absorption and lateral deformation is not linear any more, but changes as a function of the crack opening and magnitude of deformation. When cracks are open all across the specimen's cross section, the energy absorption capacity of the specimen is small and the shear deformations are the main energy absorption mechanism. When the specimen is deformed far enough so that cracks close, the stiffness and energy absorption starts to increase, and flexural deformations become the main source of energy absorption.

2. The normalized energy dissipation capacity (energy dissipated by cycle / one half displacement variation per cycle) of the structural walls tested is 20 times greater than that of ductile frames in a building of similar height, and almost 10 times greater than that of infilled frames.
3. The energy dissipation capacity of the framed wall specimens subjected to cyclic loading is 23% higher than that of the rectangular walls. However, for displacement amplitudes smaller than those corresponding to failure of the rectangular wall, the normalized energy dissipation for the rectangular wall is approximately 16% larger than for the framed wall.

7.1.2. Factors Affecting the Parameters that Control Seismic Behavior

(a) Effect of Loading History

1. The hysteretic behavior of the cyclically loaded specimens showed a decrease in strength with respect to the monotonically loaded specimens of 8% for the framed walls and 5% for the rectangular walls.

Under monotonic loading a displacement ductility ratio of 9.8 was reached. However, as soon as the load was reversed to a value of only 35% of the monotonic maximum strength, instability failure of the whole compression boundary element took place. Thus, such a displacement ductility ratio can not be used for seismic design.

3. The overall deformation capacity is the sum of the maximum positive and negative displacements in one cycle. The drop in overall deformation capacity under cyclic loading with respect to that under strictly monotonic loading was 26% for the rectangular walls, and 22% for the framed walls with hoop confinement in the boundary elements.

4. Cyclic loading contributes to the opening of flexural cracks throughout the whole wall cross section and in a region near the base of the specimen. Increased shear deformations took place along these horizontal cracks and shear failure occurred in this region.

5. The natural frequency of the specimens, as determined from the small amplitude free vibration tests, consistently decreases with increases in the maximum ductility level as well as with increases in the number of cycles at certain level of displacement. The reduction was on the order of 50% at a nominal ductility of three indicating a change in stiffness of the order of four.

6. The damping ratio in the virgin specimens ranged from 0.0183 to 0.0261, during small amplitude free vibration tests. After the specimens underwent yield deformations, the damping during small amplitude free vibration tests increased to a maximum of: 0.0452 at a nominal ductility value of $\mu = 2$; 0.029 at $\mu = 3$; and 0.038 at $\mu = 5$.

(b) Effect of Specimen's Cross Section

The specimen's cross section had a considerable effect on the specimen's behavior.

1) Strength

In the framed walls, the maximum analytical flexural strength was reached experimentally. In the rectangular walls, the experimental strength reached 92% of the analytical flexural strength. At this strength, instability failure took place.

2) Deformation

The maximum overall deformation reached in the framed walls was 186.5 mm, 35% higher than the corresponding value for the rectangular walls.

3) Stability and mode of failure

Under monotonic loading the framed wall failed with local buckling of the longitudinal reinforcement. Under cyclic loading, a flexural shear failure developed with a crushed concrete band along the base of the specimen. The rectangular walls, in turn, had instability failures under both monotonic and cyclic load.

The out of plane instability of a structural wall in the region of large inelastic deformations should be considered, especially in thin rectangular walls.

Framed walls have better stability characteristics than rectangular walls with similar panel thickness.

4) Construction

Rectangular walls have architectural advantages over and require simpler formwork construction than framed walls. However, the construction of the spirally confined columns in the framed walls is easier than the construction of columns with hoop confinement in thin rectangular walls.

(c) Effect of Hoop vs. Spiral Confinement

1. For all practical purposes, flexural strength is the same for walls with spiral confinement in the boundary elements and similar walls with hoop confinement in the boundary elements. The greater loss of concrete cover area in the boundary elements with spiral confinement is compensated for by a higher increase in strength of the confined concrete.

2. The closer spacing of the spiral confinement allows the development of larger compression stresses in the boundary element before local buckling of the longitudinal reinforcement takes

place.

7.1.3. Effect of Repair Technique

1. The repair technique that was used was to replace the damaged concrete in the first story panel and to increase its' moment and shear capacity so as to have most of the damage occur in the second story. This repair technique proved to give good results. The repaired specimen was as strong as the previous specimen, its' flexural strength was greater than that of the original specimen. This might not be always desirable, as it might increase the possibility of premature shear failure in the upper stories.
2. The overall deformation capacity of repaired walls was reduced by as much as 17%, compared to the deformation capacity of virgin walls. The overall interstory tangential drift capacity was reduced by as much as 20%, although rupture of welded tension reinforcement in the boundary elements was observed to initiate at an interstory tangential story drift of only 0.007.
3. The stiffness of the repaired specimens was similar to that of the cracked original specimens. But the interstory drift stiffness at the story where failure took place was four times greater for the repaired specimens.

7.1.4. Effect of Moment-to-Shear Ratio

1. No tests were performed in which the moment-to-shear ratio was the only parameter changing. However, testing of the repaired walls in which failure was obtained in the second story indicates that a reduction in the moment-to-shear ratio increases the possibility of shear failure by crushing of the concrete in the compression region of the panel, and reduces the available deformation capacity.

7.2. Implications of Results Obtained in Seismic Resistant Design

7.2.1. Evaluation of Critical Load Condition

1. The UBC code provisions do not consider several factors that can increase the probability of brittle shear failure. Some of these factors tend to increase the actual moment capacity of the wall. Others tend to decrease the moment to shear ratio of the forces acting on the wall; and still others tend to decrease the shear capacity of the wall. In the first group are: the actual yielding strength and strain hardening of the reinforcing steel; the actual strength of the concrete at the time the earthquake excitation takes place; the vertical steel reinforcement in the panel; and the axial force in the wall. In the second group are: the effect of the higher modes of response; the interaction of the wall and frame systems; and the softening of the lower floor panels during nonlinear response. All of the factors in this second group affect the distribution of the lateral forces acting on the wall and the moment-to-shear ratio in the critical section. In the third and most important group is the effect of load cycling, and the effect of axial forces.

In order to compensate for these assumptions, the 1973 UBC code specifies a factor of 2 ($1.4 E/\phi$) for the shear loads. This amounts to a total factor of 3.24 E. However there is no certainty that even such a high load factor will be enough to prevent shear failure. The new 1976 UBC code increases the probability of shear failure by decreasing the factor to $\frac{2E}{\phi}$.

7.2.2. Design Criteria

The code criteria for design of walls against shear is not consistent with that used for ductile moment resisting frames. It is necessary to design against shear according to flexural strength and the largest expected shear-to-moment ratio of the forces acting on the wall.

Realistic material properties should be used to estimate the wall's flexural strength, accounting for the effect of the axial load and panel reinforcement. In determining the critical V/M ratio, the effect of higher modes of vibration, the interaction of wall frame systems, and the nonlinear response of the structure should be accounted for. Finally, it is necessary to

consider the reduction in shear strength under cyclic load reversals and high shear conditions ($v_c \geq 6\sqrt{f'_c}$ psi. or $0.5\sqrt{f'_c}$ MPa).

7.2.3. Selection of Wall Cross Section (Minimum Dimensions)

The slenderness of structural walls should be limited to prevent instability failures. Ideally this limitation should be a function of the ductility desired. It is suggested that Paulay's recommendation [53] be modified and adopted. Paulay has suggested that the wall slenderness should be limited so that: the thickness of any part of a wall where the combination of flexure and axial load can produce a compressive strain of 0.0015 m/m should not be less than $h_w/10$; where h_w is the clear vertical distance between floors or other horizontal lines offering effective lateral support. Ideally, the wall slenderness should be limited not only as suggested by Paulay, but also as a function of the crack opening required to reach the desired ductility. This was demonstrated experimentally in the investigation reported herein.

7.3. Recommendations for Future Research

7.3.1. Experimental

The results of the investigation reported suggest further study of the following areas:

1. To study ways of improving the hysteretic behavior of reinforced concrete walls when these walls are subjected to load reversals under high shear conditions ($\geq 0.5\sqrt{f'_c}$ MPa or $\geq 6\sqrt{f'_c}$ psi) that cause a degradation of the shear strength capacity. A possible way to do this is through the use of diagonal panel reinforcement. In this way the reinforcement would be capable of taking the diagonal tensile stresses more efficiently, and under load reversals could delay the degradation along the flexural shear crack observed in the cyclic tests.
2. To investigate the relative importance of panel steel spacing and panel steel percentage.
3. To search for repair procedures that can restore the original available ductility. In particular, to search for a solution for the problem of brittle longitudinal reinforcement, which is a consequence of previous strain hardening and heat treatment of the reinforcement during welding.
4. To study the effect that a realistic foundation has on the behavior of R/C wall systems. The specimens tested were attached to very stiff concrete blocks which do not represent usual foundation conditions. The flexibility in the foundation can introduce changes in the boundary conditions and dynamic characteristics of the structure. This affects the distribution of the shear forces on the wall (M/V ratios).
5. To study ways of improving seismic design methods. Structural walls should have enough shear strength to withstand the maximum shear that could be developed with the available moment capacity and the largest realistic V/M ratio. The effect of higher modes of vibration and nonlinear structural response should be accounted for in the determination of the maximum V/M ratio.

7.3.2. Analytical

1. To implement a concrete finite element in which the capability of accounting for shear transfer vs shear slippage along the surface of open tensile cracks is available. A force slippage relation that could be used in this model is not yet available. However, a "sawtooth" idealization for the crack surfaces (such as that shown in Fig. 7.1), in which the amount of slippage is limited as a function of the crack opening, would be a significant improvement over presently available methods.
2. To implement a finite element capable of accounting for the effect of the reinforcement crossing the cracks on the interface shear transfer.
3. To improve the mathematical models developed in Chapter 6, or develop a new model to predict the response of structural walls subjected to generalized loading.

4. To carry out analytical studies of nonlinear response of R/C structural wall systems subjected to different ground motions, in order to estimate demands (number of yielding excursions, magnitude of inelastic deformations, maximum value of V/M , etc.). Demands must be estimated in order that walls may be designed and detailed so their available capabilities exceed expected demands.



REFERENCES

1. Wang, T. Y., Bertero, V. V., and Popov, E. P., "Hysteretic Behavior of Reinforced Concrete Framed Walls," Report No. EERC 75-23, Earthquake Engineering Research Center, University of California, Berkeley, 1975.
2. Bertero, V. V. and Collins, R. G., "Investigation of the Failures of the Olive View Stair-towers During the San Fernando Earthquake and their Implications in Seismic Design," Report No. EERC 73-26, Earthquake Engineering Research Center, University of California, Berkeley, 1973.
3. Wiegel, R. L. (ed.), Earthquake Engineering Prentice-Hall, Inc., 1970, 518 pp.
4. Taylor, M. A., "Constitutive Relations for Concrete Under Seismic Conditions," Proceedings, Workshop on Earthquake-Resistant Reinforced Concrete Building Construction, University of California, Berkeley, July 11-15, 1977.
5. Bertero, V. V. and Vallenias, J., "Confined Concrete Research and Development Needs," Proceedings, Workshop on Earthquake-Resistant Reinforced Concrete Building Construction, University of California, Berkeley, July 11-15, 1977.
6. Popov, E. P., "Mechanical Characteristics and Bond of Reinforcing Steel Under Seismic Conditions," Proceedings, Workshop on Earthquake-Resistant Reinforced Concrete Building Construction, University of California, Berkeley, July 11-15, 1977.
7. Kent, D. C. and Park, B., "Flexural Members with Confined Concrete," Proceedings, ASCE, Vol. 97, ST7, July 1971, pp. 1969-1990.
8. Sargin, M., "Stress-Strain Relationship for Concrete and the Analysis of Structural Concrete Sections," University of Waterloo, Ontario, 1971.
9. Vallenias, J. M., Bertero, V. V., and Popov, E. P., "Concrete Confined by Rectangular Hoops Subjected to Axial Loads." Report No. EERC 77-13, Earthquake Engineering Research Center, University of California, Berkeley, 1977.
10. Bazant, Z. P. and Bhat, P. D., "Endochronic Theory of Inelasticity and Failure of Concrete," Journal of the Engineering Mechanics Division, ASCE, Vol. 102, EM4, Proceedings Paper 12360, August 1976.
11. Valanis, K. C., "A Theory of Viscoplasticity Without a Yield Surface," Part I. General Theory. Archives of Mechanics. Stossowanej, 23, 4, Warszawa, 1971, pp. 517-533.
12. Mroz, Z., "An Attempt to Describe the Behavior of Metals Under Cyclic Loads Using a More General Workhardening Model," Acta Mechanica Vol. 7, 1969, pp. 199-212.
13. Martin, J. F., Topper, T. M. and Sinclair, "Computer Based Simulation of Cyclic Stress-Strain Behavior with Applications to Fatigue," Materials Research Standards, Vol II, No. 2, pp. 23-29.

14. Dafalias, Y. F. and Popov, E. P., "Plastic Internal Variables Formalism of Cyclic Plasticity," Journal of Applied Mechanics, Vol. 43, December 1976, pp. 645-651.
15. Petersson, H. and Popov, E. P., "Constitutive Relations for Generalized Loadings", Engineering Mechanics Division Journal, ASCE, In press.
16. Nayak, G. C. and Zimkieurez, O. C., "Elastic Plastic Stress Analysis. A Generalization for Various Constitutive Relations Including Strain Softening," International Journal of Numerical Methods in Engineering, Vol. 5, No. 1, 1972, pp. 113-115.
17. Minor, J. and Jirsa, J. O., "Behavior of Bent Bar Anchorages," ACI Journal, Vol. 72, No. 4, April 1975, pp. 141-149.
18. Morita, S. and Katu, T., "Splitting Bond Failures of Large Deformed Reinforcing Bars," Preprint, ACI 1977 Annual Convention, San Diego, California, March 1977.
19. Hassan, F. M. and Hawkins, N. M., "Effects of Post-Yield Loading Reversals on Bond Between Reinforcing Bars and Concrete," Report SM 73-2, Department of Civil Engineering, University of Washington, Seattle, Washington, March 1973.
20. Viathanatepa, S., "Deterioration of Bond in Reinforced Concrete Under Generalized Loading," Ph.D. dissertation, University of California, Berkeley, California, In preparation.
21. Cobb, J. L., "The Influence of Shock Loading and Axial Compression Upon Bond Deterioration Under Cyclic Loading," Mechanical Engineering Report, Department of Civil Engineering, University of California, Berkeley, June 1977.
22. Bertero, V.V., Popov, E.P., Viathanatepa, S., "Bond of Reinforcing Steel: Experiments and a Mechanical Model," Nonlinear Behavior of Reinforced Concrete Spatial Structures, Contributions to the IASS Symposium, Darmstadt, July 3-7, 1978.
23. Mahin, S. A., and Bertero, V. V., "An Evaluation of Some Methods for Predicting Seismic Behavior of Reinforced Concrete Buildings," Report No. EERC 75-5, Earthquake Engineering Research Center, University of California, Berkeley, February 1975.
24. Ma, S. M., Bertero, V. V. and Popov, E. P., "Experimental and Analytical Studies on the Hysteretic Behavior of Reinforced Concrete Rectangular and T-Beams," Report No. EERC 76-2, Earthquake Engineering Research Center, University of California, Berkeley, 1976.
25. Park, R., Kent, D. C., and Sampson, R. A., "Reinforced Concrete Members With Cyclic Loading," Journal of the Structural Division, ASCE, ST7, July 1972.
26. Bazant, Z. D. and Bhat, P. D., "Prediction of Hysteresis of Reinforced Concrete Members," Journal of the Structural Division, ASCE, Vol. 103, ST1, Proceedings Paper 12662, January 1977, pp. 153-180.
27. Suidan, M. and Schnobrich, W. C., "Finite Element Analysis of Reinforced Concrete," Journal of the Structural Division, ASCE, Vol. 99, No ST10. Proceedings Paper 10081, October 1973.

28. Cervenka, V. and Gerstle, K. H., "Inelastic Analysis of Reinforced Concrete Panels, Part I: Theory," International Association of Bridge and Structural Engineers Publications, Vol. 31-11, 1971, pp. 31-45, "Part II: Experimental Verification and Application," Vol. 32-11, 1972, pp. 25-39.
29. Darwin, D. and Pecknold, "Analysis of Reinforced Concrete Shear Panels under Cyclic Loading," Journal of the Structural Division, ASCE, Vol. 102, ST2, Proceedings Paper 11896, February 1976.
30. Uniform Building Code, International Conference of Building Officials, Pasadena, 1973 edition.
31. SEAOC Seismology Committee, Recommended Lateral Force Requirements and Commentary, Structural Engineers' Association of California, 1959.
32. Uniform Building Code, International Conference of Building Officials, Pasadena, 1976 edition.
33. SEAOC Seismology Committee, Recommended Lateral Force Requirements and Commentary, Structural Engineers' Association of California, 1974.
34. Applied Technology Council, "Tentative Provisions for the Development of Seismic Regulations for Buildings", ATC Publication ATC 3-06, June 1978.
35. Building Code Requirements for Reinforced Concrete (ACI 318-71) and Commentary, American Concrete Institute, 1971.
36. Building Code Requirements for Reinforced Concrete (ACI 318-77) and Commentary, American Concrete Institute, 1977.
37. De Villiers, I. P., "Implementation of Endochronic Theory for Analysis of Concrete Structures," Ph.D. Dissertation, University of California, Berkeley, 1977.
38. Building Code and Commentary for Reinforced Concrete Structures, Architectural Institute of Japan, 1971, (In Japanese).
39. Hatakeyama, H., "Comparative Study of Design of Shear Walls in High-Rise Buildings," CE 299 Report, Department of Civil Engineering, SESM, University of California, Berkeley, 1973.
40. Brown, R. H. and Jirsa, J. O., "Reinforced Concrete Beams under Load Reversals," ACI Journal, Vol. 68, No. 3, May 1971, pp. 380-390.
41. Popov, E. P., Bertero, V. V., and Krawinkler, H., "Cyclic Behavior of Three Reinforced Concrete Flexural Members with High Shear," Report No. EERC 72-5, Earthquake Engineering Research Center, University of California, Berkeley, 1972.

42. Bertero, V. V. and Popov, E. P., "Seismic Behavior of Ductile Moment Resisting Reinforced Concrete Frames," Reinforced Concrete Structures in Seismic Zones, ACI Publication SP-53, 1977.
43. Wilson, E. L. and Dovey, H. H., "Three Dimensional Analysis of Building Systems - TABS," Report No. EERC 72-8, Earthquake Engineering Research Center, University of California, Berkeley, December, 1972.
44. Oesterle, R. G., Fiorato, A. E., and Corley, W. G., "Free Vibration Tests of Structural Walls," Portland Cement Association, 1976.
45. Newmark, N. M. and Hall, W., "Seismic Design Criteria for Nuclear Reactor Facilities," Proceedings of the Fourth World Conference on Earthquake Engineering, Vol. II, Section B4, 1969, pp. 37-50.
46. Blume, J. A., Sharpe, R. L., and Cost, G., "Earthquake Engineering for Nuclear Reactor Facilities," John A. Blume and Associates, JAB-101, 1971, 147 pp.
47. Cardenas, A. E., et al. "Design Provisions for Shear Walls," ACI Journal, Proceedings, Vol. 70, No. 3, March 1973.
48. Leonhardt, F., "Deep Beams - Plane Structures Loaded Parallel to their Mid Plane," Bulletin D'Information No. 65, Comite European du Beton, Paris, France, February 1968, pp. 1-113, (in French).
49. Bertero, V. V., Popov, E. P., and Wang, T. Y., "Hysteretic Behavior of Reinforced Concrete Flexural Members with Special Web Reinforcement," Report No. EERC 74-9, Earthquake Engineering Research Center, University of California, Berkeley, 1974.
50. Klinger, R.E. and Bertero, V.V., "Infill Frames in Earthquake Resistant Construction," Report No. EERC 76-32, Earthquake Engineering Research Center, University of California, Berkeley, 1976.
51. Winter, G. and Nilson, A. H., Design of Concrete Structures, Mc Graw-Hill, 1968.
52. Proceedings of AIJ Annual Conference Architectural Institute of Japan October 1974, (in Japanese).
53. Paulay, T., "Some Considerations of Earthquake Resistant Reinforced Concrete Shear Walls," International Symposium on Earthquake Structural Engineering, St. Louis, Missouri, U.S.A., August 1976.
54. Richard, F.E., Brandtzaeg, A., and Brown, R.L., "The Failure of Plain and Spirally Reinforced Concrete in Compression," University of Illinois Engineering Experiment Station, Bulletin No. 190, Urbana Illinois, April 1929.
55. ASCE-ACI Committee 426, "The Shear Strength of Reinforced Concrete Members," Journal of the Structural Division, ASCE, Vol. 83, No. ST6, June 1973, pp. 1091-1187.

56. Mondkar, D. G. and Powell, G. H., "ANSR-I, General Purpose Program for Analysis of Nonlinear Structural Response," Report No. EERC 75-37, Earthquake Engineering Research Center University of California Berkeley, December, 1975.
57. Scanlon, A., "Time Dependent Deflections of Reinforced Concrete Slabs," University of Alberta, Ph.D. Dissertation, December, 1971.
58. Lin, C. S., "Nonlinear Analysis of Reinforced Concrete Slabs and Shells," Ph.D. Dissertation, University of California, Berkeley, April, 1973.
59. Kupfer, H., Hilsdorf, H. K., and Rusch, H., "Behavior of Concrete Under Biaxial Stresses," A.C.I. Journal, August, 1969.
60. Paulay, T., and Loefer, P. J., "Shear Transfer by Aggregate Interlock," Proceedings of the Shear Symposium, American Concrete Institute, ACI Special Publication SP-42, Vol.1, 1973.
61. Fenwick, R. C. and Paulay, T., "Mechanisms of Shear Resistance in Concrete Beams," Proceedings ASCE, Vol. 94, No. ST-10, October, 1968.
62. Mattock, A. H., Holfbeck, J. F., and Ibrahim, I. O., "Shear Transfer in Reinforced Concrete," ACI Journal Proceedings, Vol. 66, No. 2, February, 1969.
63. Loefer, P. J., "Shear Transfer by Aggregate Interlock," M.E. Thesis, University of Canterbury, Christchurch, New Zealand, 1970.
64. Fenwick, R. C., "The Shear Transfer of Reinforced Concrete Beams," Ph. D. Dissertation, University of Canterbury, Christchurch, New Zealand, 1966.
65. Holfbeck, J. A., Ibrahim, I. O., and Mattock, A. H., "Shear Transfer in Reinforced Concrete - Recent Research," Journal of the Prestressed Concrete Institute, Vol. 17, No. 2, March/April 1972.
66. Dulacska, H., "Dowel Action of Reinforcement Crossing Cracks in Concrete," A.C.I. Journal, Vol 69, No. 12, December, 1972.
67. Mattock, A. H., "The Shear Transfer Behavior of Cracked Monolithic Concrete Subjected to Cyclically Reversing Shear," Structural Mechanics Report, University of Washington, SM 74-4, November, 1974.
68. Jimenez, R., Perdicaris, P., Gergely, P. and White, R. N., "Interface Shear Transfer and Dowel Action in Cracked Reinforced Concrete Subjected to Cyclic Shear," Methods of Structural Analysis, Proceedings of the National Structural Engineering Conference, ASCE, Vol 1, Madison, Wisconsin, 1976.
69. Mainstone, R. J., "On the Stiffness and Strengths of Infilled Frames," Proceedings of the Institution of Civil Engineers, Supplement (iv), Paper 73605, 1971.

70. Mainstone, R. J., "Supplementary Note on the Stiffness and Strengths of Infilled Frames," BRS Current Paper CP 13/74, 1974.
71. Aktan, H. M., "A Method to Analyze the Cyclic Behavior of Slender Reinforced Concrete Shear Walls," Ph.D. Dissertation, University of Michigan, 1977.
72. Moss, P. J. and Carr, A. J., "Aspects of the Analysis of Frame-Panel Interaction", Bulletin of the New Zealand Society for Earthquake Engineering, Vol. 4, No. 1, March, 1971.
73. Franklin, H. A., "Nonlinear Analysis of Reinforced Concrete Frames and Panels", SESM Report No. 70-5, Dept. of Civil Engineering, University of California, Berkeley, March, 1970.
74. Kustu, O. and Bouwkamp, J., "Behavior of Reinforced Concrete Deep Beam-Column Subassemblages under Cyclic Loads," Report No. EERC 73-8, Earthquake Engineering Research Center, University of California, Berkeley, May 1975.
75. Verbic, B., "Test of Panel Joints in "Vranica" Type Large Panel Buildings." Institut Za Materijale I Konstrukcije, Sarajevo, Yugoslavia, April 1977.

T A B L E S

TABLE 2.1
ESTIMATED WEIGHT OF SEVEN-STORY PROTOTYPE BUILDING

Floor Area of Building 1 021 m ²		
Roof Weight (kN)		
Slab	(23.6 kN/m ³)(.203 m)(1 021 m ²)	4 891
Mech. & Rfg.	(.96 kN/m ²)(1 021 m ²)	980
Partitions	(.48 kN/m ²)(1 021 m ²)	490
Columns	(4.38 kN/m)(1.402 m)(28)	172
Shear Walls	(23.6 kN/m ³)(2.485 m ² x 6)(1.402 m)	493
Ext. Walls	(2.92 kN/m)(147 m)	429
Spandrel	(4.38 kN/m)(147 m)	644
Total Roof Weight = 8 105 kN		
Typical Floor Weight (2nd Floor to 6th Floor) (kN)		
Slab	(23.6 kN/m ³)(.203 m)(1 021 m ²)	4 891
Mech. & Flg.	(.48 kN/m ²)(1 021 m ²)	490
Partition	(.96 kN/m ²)(1 021 m ²)	980
Columns	(4.38 kN/m)(2.54 m)(28)	312
Shear Walls	(23.6 kN/m ³)(2.485 m ² x 6)(2.54 m)	894
Ext. Walls	(2.92 kN/m)(147 m)	429
Spandrel	(4.38 kN/m)(147 m)	644
Total Typical Floor Weight = 8 640 kN		
First Floor Weight (kN)		
Slab	(23.6 kN/m ³)(.203 m)(1 021 m ²)	4 891
Mech. & Flg.	(.48 kN/m ²)(1 021 m ²)	490
Partition	(.96 kN/m ²)(1 021 m ²)	980
Columns	(4.38 kN/m)(3.15 m)(28)	387
Shear Walls	(23.6 kN/m ³)(2.206 m ² x 6)(3.15 m)	1 107
Ext. Walls	(2.92 kN/m)(147 m)	429
Spandrel	(4.38 kN/m)(147 m)	644
Total First Floor Weight = 8 928 kN		
Total Building Weight = 8 105 + (5)(8 640) + 8 928 = 60 233 kN		

TABLE 2.2
SPECIMEN TYPES AND THEIR MAIN CHARACTERISTICS

Wall Type	Column Dimensions (m x m)	Panel Dimensions (m x m)	Shear Span ($h_v = \frac{M}{V}$) of forces acting on Wall (m x m)	$\frac{h_v}{l_w}$	ρ_{column}	$\rho_h = \rho_n$	ρ''_{column}
Framed I Section (10 Story Building)	0.254 x 0.254	1.880 x 0.102	4.383	1.836	0.0353	0.0082	0.0154
Rectangular (7 Story Building)	0.114 x 0.279	1.885 x 0.114	3.849	1.595	0.0557	0.0054	0.0184

TABLE 2.3
MECHANICAL CHARACTERISTICS OF MATERIALS

(a) STEEL PROPERTIES (MPa)

	f_y	f_{max}
Col. Transverse Reinf. (gage No. 7 wire)	440	479
Wall Reinf. (#2 Bar)	507	730
Col. Long. Reinf. (#5 Bar)	482	687
(#6 Bar)	444	639
Repaired Col. Long. Reinf. (#8 Bar)	454	668

(b) CONCRETE PROPERTIES AT TIME OF TESTING

		Test No.							
		3	4	4R	3R	5	6	6R	5R
f'_c (MPa) (27.53)*	Footing	33.2	34	34.5	34.5	35.	35	35	35
	1st Fl.	35.2	35.1	50.4	51.7	34.5	34.7	45.8	49
	2nd Fl.	35.4	35.4	36	36	33.5	34.5	37	38
	3rd Fl.	33.8	37.3	38	38	32.4	34.5	36	36
Concrete f'_t (MPa)	Splitting	3.3	3.4	3.6	3.81	3.25	3.2	3.3	3.3
	Flexural	3.7	3.7	4.36	4.46	3.5	3.6	3.7	3.8
Repaired Concrete f'_t (MPa)	Splitting			3.63	3.7			3.4	3.5
	Flexural			4.4	4.5			3.3	3.6

*Specified at 28 days.

TABLE 2.4
CONCRETE MIX PROPORTIONS

(a) ORIGINAL SPECIMENS

Material	Weight for one cubic meter (kN)
Type II Santa Cruz Cement	4.04
Water	2.34
Antioch Fine Sand, FM = 1.54	1.94
Pleasanton Top Coarse Sand	6.91
Pleasanton 6 mm x 3 mm Fine Gravel	7.40
Total	22.63

Slump 125 mm

(b) REPAIRED SPECIMENS

	Weight for one cubic meter (kN)
Cement*	4.79
Water (2/3 Crushed Ice)	2.0
Olympian No. 1-1/2 Coarse Sand, FM = 2.3	8.73
Watsonville 6 mm Crushed Granite	7.54
Total	23.06

Slump 50 mm

*Type II Santa Cruz for framed wall specimens; Chem. Comp. for rectangular specimens.

TABLE 4.1
SHEAR WALL TESTS

	Specimen	Load Program	Max.+ Load (kN)	Max.- Load (kN)	Max.+ Displ. (mm)	Max.- Displ. (mm)	Max. Nominal Shear Stress† (MPa)	Failure Mechanism
FRAMED WALLS	3	monotonic	1090	-381.6	185	-1.4	5.566 $.936\sqrt{f'_c}$ ($11.27\sqrt{f'_c}$)*	Local buckling during first branch of monotonic loading; instability upon load reversal
	4	cyclic	1008	-987	72	-73 (-09.7 at -205 kN)	5.195 $.876\sqrt{f'_c}$ ($10.55\sqrt{f'_c}$)*	flexural shear cracking and crushing of first story panel
	4R	monotonic	1297	-914	128	-26.7	6.685 $1.114\sqrt{f'_c}$ ($13.41\sqrt{f'_c}$)*	rupture of tension reinforcement and buckling of compression reinforcement in second story; crushing of third story panel and tearing of third floor slab
	3R	cyclic	1300	-1089	83.5	-45 (-74 at -251 kN)	6.7 $1.116\sqrt{f'_c}$ ($13.43\sqrt{f'_c}$)*	crushing of second story panel; tearing of third floor slab
RECTANGULAR WALLS	5	monotonic	916.3	-847.4	80.7	-57.12	4.164 $.71\sqrt{f'_c}$ ($8.54\sqrt{f'_c}$)*	instability during first branch of monotonic loading; instability upon load reversal; flexural shear failure at first story
	6	cyclic	856.2	-870.5	50.2	-52.2	3.956 $.67\sqrt{f'_c}$ ($8.11\sqrt{f'_c}$)*	instability
	6R	monotonic	1162.2	-1158	63.45	-59 (-126.09 at -588kN)	4.76 $.783\sqrt{f'_c}$ ($9.43\sqrt{f'_c}$)*	rupture of tension reinforcement and buckling of compression reinforcement in second story
	5R	cyclic	1065	-1027	50.57	-50.16	4.35 $.707\sqrt{f'_c}$ ($8.51\sqrt{f'_c}$)*	rupture of tension reinforcement and buckling of compression reinforcement in second story

† computed as $(V/.8bw)_{max}$

* psi

TABLE 4.2

EXPERIMENTAL FREQUENCIES AND DAMPING VALUES FOR STRUCTURAL WALL MODELS

Excitation	Original Specimens					Repaired Specimens								
	Specimen	Damage State				Specimen	μ (Prev. No. of Cycles for Original Specimen)	Damage State						
		Virgin		$\mu=3$				Virgin		$\mu=3$		$\mu=5$		
		ω (Hz)	$\xi \left(\frac{c}{c_c}\right)$	ω (Hz)	$\xi \left(\frac{c}{c_c}\right)$			ω (Hz)	$\xi \left(\frac{c}{c_c}\right)$	ω (Hz)	$\xi \left(\frac{c}{c_c}\right)$	ω (Hz)	$\xi \left(\frac{c}{c_c}\right)$	
Ambient	Framed	20				3R	+ 10.4	27.1						
Hammer Impact	Wall 3	45	.0181			(cyclic loading)	(1)	27.25	.0207					
Sudden Release	(monotonic loading)	45	.0261					23.5	.0397					
				$\Delta = .08$ mm						$\Delta = .28$ mm				
Ambient	Framed	41				4R	+4	31.0		23.6				
Hammer Impact	Wall 4	41.5	.0173			(monotonic loading)	(12)	28.5	.0151	23.2	.0127	12.2	.0157	
Sudden Release	(cyclic loading)	41	.0217					27.5	.0452	21.8	.0241	9.8	.0380	
				$\Delta = .10$ mm						$\Delta = .25$ mm				
Ambient	Rectangular	40		29.6		5R	+3	36						
Hammer Impact	Wall 5	39.5	.0056	22.7	.0109	(cyclic loading)	(12)	39.875	.0081					
Sudden Release	(monotonic loading)	39.2	.0183	22.1	.0229			39.375	.0146					
				$\Delta = .09$ mm						$\Delta = .127$ mm				
Ambient	Rectangular	37.8		17.6		6R	+ 5.88	29.7						
Hammer Impact	Wall 6	38.6	.0134	17.0	.0222	(monotonic loading)	- 3.62	37.0	.0105					
Sudden Release	(cyclic loading)	37.2	.0232	16.1	.0291		(1)	36.1	.0227					
				$\Delta = .09$ mm						$\Delta = .102$ mm				

TABLE 5.1
STRENGTHS OF SPECIMENS (KN)

Specimen	Flexural Crack Load			Diagonal Cracking Load	
	Measured	Computed		Measured	Computed
		Based on A_g	Based on equivalent composite area		
3	222	162.0	175.4	311	352.6
4	222	162.0	175.4	355	352.6
5	110	100.5	129.8	278	227.0
6	123	100.5	129.8	278	227.0
	Working Load ($f_s \leq 165.5$ MPa)			Initial Yielding	
	Measured	Computed		Measured	Computed
3	453	400		761.2	706
4	480	400			706
5	265	292		624.0	624
6	290	292		624.0	624

TABLE 5.2
COMPARISON OF SPECIMEN STRENGTHS

Specimen	Specimen Strengths kN (kN-m)				
	Flexural				Shear
	Measured	Code [†]	Approximate Analysis	Refined Analysis	UBC Code*
3	1090 (4777)	876 (3841)	931 (4083)	1095 (4799)	826
4		876 (3841)			826
5	916 (3525)	510 (1962)	844 (3249)	979 (3768)	684
6		510 (1962)			684
3R	1300 (4113)	1213 (3841)			826
4R	1297 (4103)	1213 (3841)	1289 (4083)	1516 (4799)	826
5R	1162 (3056)	746 (1962)			684
6R	1065 (2801)	746 (1962)	1234 (3249)	1432 (3768)	684

[†]Code values are on the basis of specified material properties. The force values are computed on the basis of the moment values and the M/V ratio used in the experiments (not the M/V ratio specified by the code). ϕ factors are not included.

*Values are on the basis of specified material properties. ϕ factors are not included.

TABLE 5.3
CURVATURES

Maximum Curvature at Maximum Strength Level (rad.m)

Specimen	Experimental	Analytical
3	0.032	0.035
5	0.019	0.031

TABLE 5.4
SECANT STIFFNESS (MN/mm)

Specimen	Initial		Cracked		At First Yield	
	Measured	Computed	Measured	Computed	Measured	Computed
3	.216	.220	.161	.151	.0603	.0871
4	.179	.220	.157	.151	.0664	.0871
5	.241	.230	.121	.156	.059	.096
6	.238	.230	.124	.156	.058	.096

TABLE 5.5
SECANT STIFFNESS COMPONENTS AT FIRST YIELD (MN/mm)

SECANT STIFFNESS COMPONENTS AT FIRST YIELD (MN/mm)									
Specimen	Fixed-End Stiffness		Shear Stiffness		Flexural Stiffness		Total Stiffness		
	Measured	Computed	Measured	Computed	Measured	Computed	Measured Sum of Components	Measured From Overall Displ.	Computed
3	.757	∞	.150	.213	.149	.147	.0678	.0603	.0871
4	3.192	∞	.151	.213	.149	.147	.0732	.0664	.0871
5	.762	∞	.193	.226	.118	.150	.0668	.059	.096
6	.626	∞	.192	.226	.112	.150	.0636	.058	.096

TABLE 5.6
CONTRIBUTION OF DIFFERENT SOURCES OF LATERAL DEFORMATION AT THIRD-FLOOR LEVEL

Specimen	Level of Behavior																	
	$\mu = 1$					$\mu = 3$					$\mu = \mu_{max}$							
	Fixed End		Shear	Flex.	Meas.	Error %	Fixed End		Shear	Flex.	Meas.	Error %	Fixed End		Shear	Flex.	Meas.	Error %
	mm	mm	mm	mm	mm	mm	mm	mm	mm	mm	mm	mm	mm	mm	mm	mm	mm	mm
%	%	%	%	%	%	%	%	%	%	%	%	%	%	%	%	%	%	
3	1.7	7.3	6.9	17.6	9	3.8	16.2	32.0	54.9	5	16.3	45.8	97.0	184.9	14			
	10	41	39	100		7	29	58	100		8	25	52	100				
4	2.7	8.8	7.5	18.5	2	4.2	18.6	28.0	54.4	7	6.8	28.8	33.0	72.0	5			
	14	48	40	100		8	34	51	100		9	40	46	100				
5	0.9	3.9	7.2	12.9	7	1.6	10.5	25.8	37.2	-2	7.6	25.0	59.9	80.4	10			
	7	30	56	100		4	28	69	100		9	31	74	100				
6	1.2	3.9	6.7	12.7	7	2.4	12.1	22.1	38.8	6	5.5	17.1	20.2	49.3	13			
	9	31	53	100		6	31	57	100		11	35	41	100				

TABLE 5.7
STORY DRIFT INDEX R_i

Specimen (Load Pt.)	Stage	1st Story	2nd Story	3rd Story	Overall Drift*
3 monotonic (75) (76)	1st yield	.0039	.0046	.0048	.0044
	max. str.	.0550	.0569	.0600	.0574
	max. displ.	.0623 ⁽¹⁾	.0589	.0628	.0614
4 cyclic (82) (84) (92) (94)	1st yield	.0036	.0043	.0041	.0040
	max. + str.** & displ.	.0257	.0223	.0230	.0238
	max. - str.	.0261	.0213	.0224	.0235
	max. - displ.	.0405 ⁽²⁾	.0140	.0127	.0249
(94)	max. + str. in last cyc.	.0383 ⁽²⁾	.0076	.0088	.0200
5 monotonic (309) (339) (527) (566)	1st yield	.0035	.0040	.0046	.0040
	max. + str.	.0238 ⁽³⁾	.0248	.0249	.0244
	max. + displ.	.0254 ⁽⁴⁾	.0250	.0253	.0252
	max. - str.	.0161 ^(1,5)	.00967	.0101	.0123
	max. - displ.	.0335 ⁽⁶⁾	.0098	.0093	.0189
6 cyclic (535)	1st yield	.00361	.00405	.0046	.0040
	max. + str.	.0188	.0144	.0150	.0163
	max. + displ.	.0193	.0151	.0152	.0167
	max. - displ.	.0193 ⁽⁷⁾	.0152	.0161	.0171

**max. + str. & displ. = maximum positive strength and displacement

Specimen (Load Pt.)	Stage	1st Story	2nd Story	3rd Story	Overall Drift*
4R monotonic (322)	max. + displ. before failure	.0241	.0508	.0582	.0426
		$R_\theta=0$ $R_T=.0241$	$R_\theta=.0619$ $R_T=.0338^{(8)}$	$R_\theta=.0352$ $R_T=.0230^{(9)}$	
3R cyclic (650)	max. + displ. before failure	.0143	.0313	.0425	.0280
		$R_\theta=0$ $R_T=.0241$	$R_\theta=.0055$ $R_T=.0258^{(10)}$	$R_\theta=.0125$ $R_T=.0299^{(11)}$	
6R monotonic (151)	max. + load	.0096	.0275	.0205	.018
		$R_\theta=0$ $R_T=.0096$	$R_\theta=.00717$ $R_T=.0203^{(12)}$	$R_\theta=.0205$ $R_T=0$	
5R cyclic (219)	max. - load	.0042	.0104	.0106	.0083
		$R_\theta=0$ $R_T=.0042$	$R_\theta=.00336$ $R_T=.00704^{(13)}$	$R_\theta=.00925$ $R_T=.00135$	

*at third floor level

(1) local buckling ; (2) flexural shear failure ; (3) buckling ; (4) after buckling ; (5) under reversal ; (6) after failure ; (7) buckling of compression column ; (8) rupture of welded tension reinforcement ; (9) crushing of concrete ; (10) crushing of story panel ; (11) third floor slab damaged ; (12) just before failure of welded tension reinforcement ; (13) rupture of tension reinforcement

TABLE 5.8

STRENGTH AND DEFORMATION COMPARISON FOR VIRGIN AND REPAIRED WALLS

Specimen	Loading	Specimen Strength (kN)	Overall Displacement $\pm \delta_3$ (mm)	Critical Panel	M/V in. Critical Panel (mm)	Maximum Shear in Critical Panel (kN)	Maximum Moment in Critical Panel (kN-m)
3	monotonic	1090	186.5	1	4383	1090	4777.8
4R	monotonic	1297	154.7	2	3202	1297	4153.0
4	cyclic	1008	145	1	4383	1008	4418.3
3R	cyclic	1300	128.5	2	3202	1300	4167.6
5	monotonic	916.3	137.85	1	3849	916.3	3526.8
6R	monotonic	1162.2	122.45 (189.54)*	2	2668	1048.9	2798.5
6	cyclic	870.5	102.4	1	3849	870.5	3350.5
5R	cyclic	1065	100.73	2	2668	961.2	2564.4

*At a load of -588 kN

TABLE 6.1
 COMPARISON OF EXPERIMENTAL AND ANALYTICAL
 RESULTS FOR FLEXURAL DEFORMATION MODELS (SPECIMEN 3)

Loading Stage	Analytical		Experimental	
	Flexural Deformation (mm)	Strength (mm)	Flexural Deformation (mm)	Strength (mm)
Flexural Cracking	0.9	267	0.9	222* 222†
Diagonal Cracking	1.4	356	1.5	311* 355†
First Yield of Tension Steel	5.3	774	5.2	800
Normal Ductility +2	19.4	984	20.3	979†
Normal Ductility -2	-20.8	-991	-20.	-940†
Maximum Strength	71.9	1090	78	1090*

* Specimen 3

† Specimen 4

TABLE 6.2
COMPARISON OF PREDICTED AND OBSERVED V_f VALUES

$$V_f = [.104 \text{ MPa} + .169 f_a] A_c$$

Specimen	Observed V_f (KN)	Computed V_f (KN)
1[1]	180	180
3	180	180
5	130	130
R-3[24]	110	119
4	44	32
2[74]	80	75
1[74]	80	117

TABLE 6.3
COMPARISON OF EXPERIMENTAL AND ANALYTICAL RESULTS FOR OVERALL DEFORMATIONS
(SPECIMEN 3)

Stage	Load from Analysis (kN)	Deformations (mm)				
		Analytical				Experimental
		Flexural	Shear	Fixed End	Total	Total
Flexural Cracking	267	0.9	0.45	0.11	1.5	1.8
Diagonal Cracking	356	1.4	0.60	0.14	2.1	2.7
First Yield of Tension Steel	774	5.3	5.7	0.3.	11.3	12.
Maximum Strength	1090	71.9	71.25	8.4	152.	160.

FIGURES

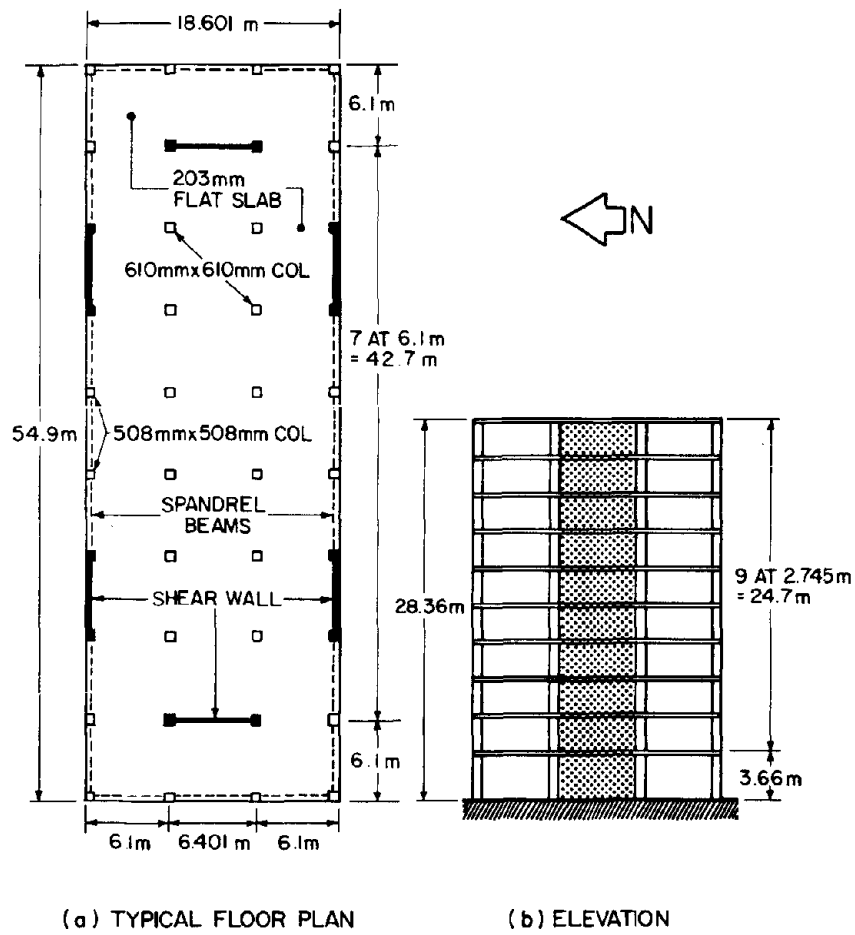


Fig. 2.1 Ten-Story Prototype Building

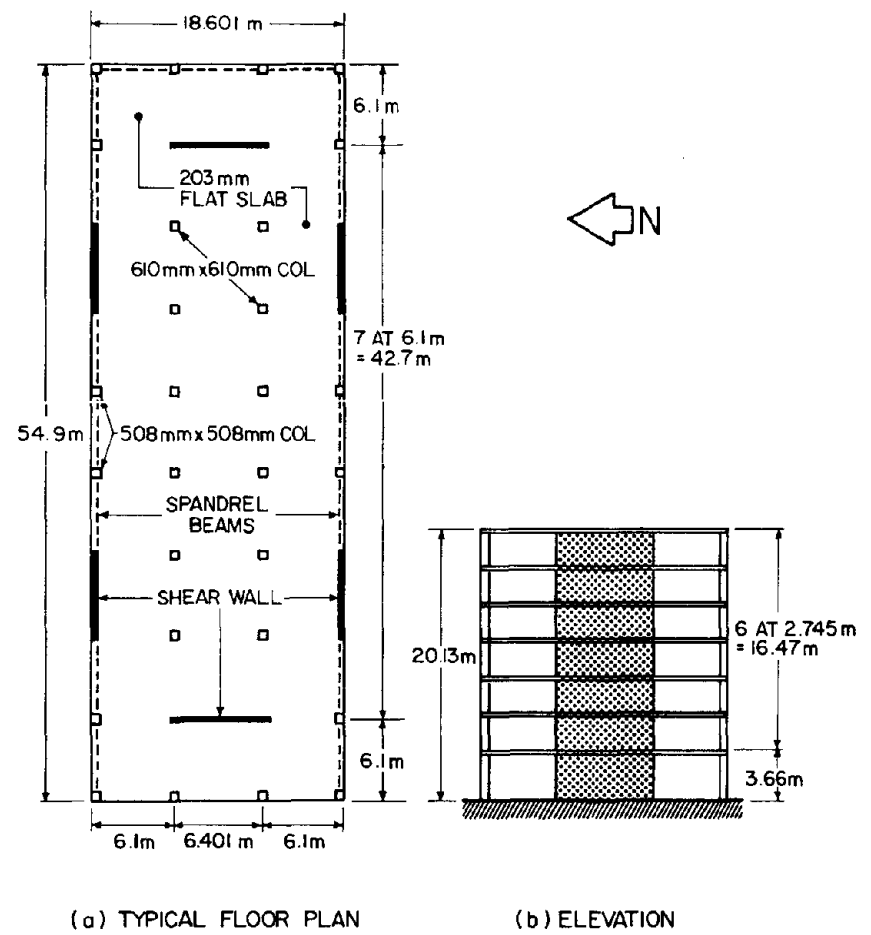


Fig. 2.2 Seven-Story Prototype Building

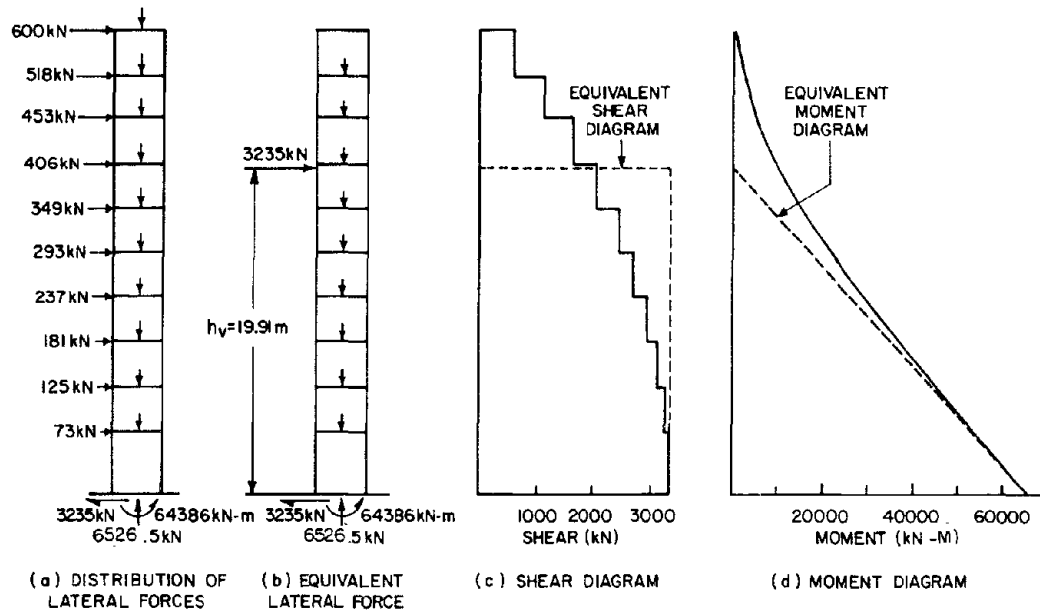


Fig. 2.3 Shear and Moment Diagram of Single N-S Wall of Ten-Story Building When Subjected to half of 1.4E and to 1.4 (Torsion) Code Forces

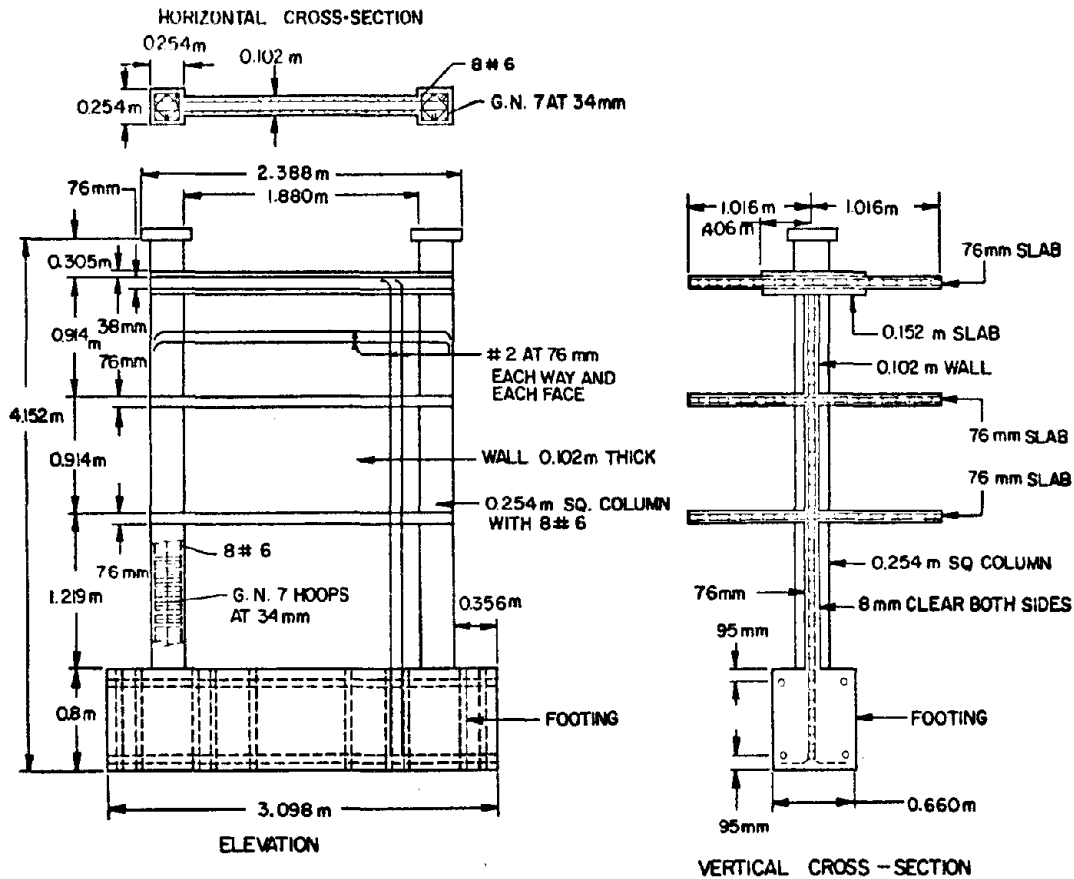


Fig. 2.4a Dimensions and Details of Framed-Wall Specimens

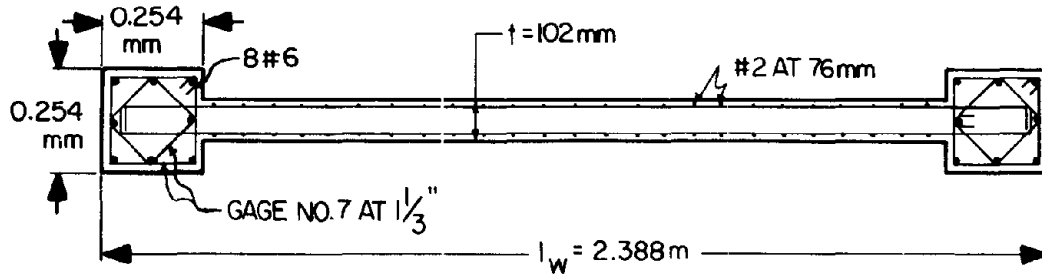


Fig. 2.4b Detailed Cross-Section of Framed Wall

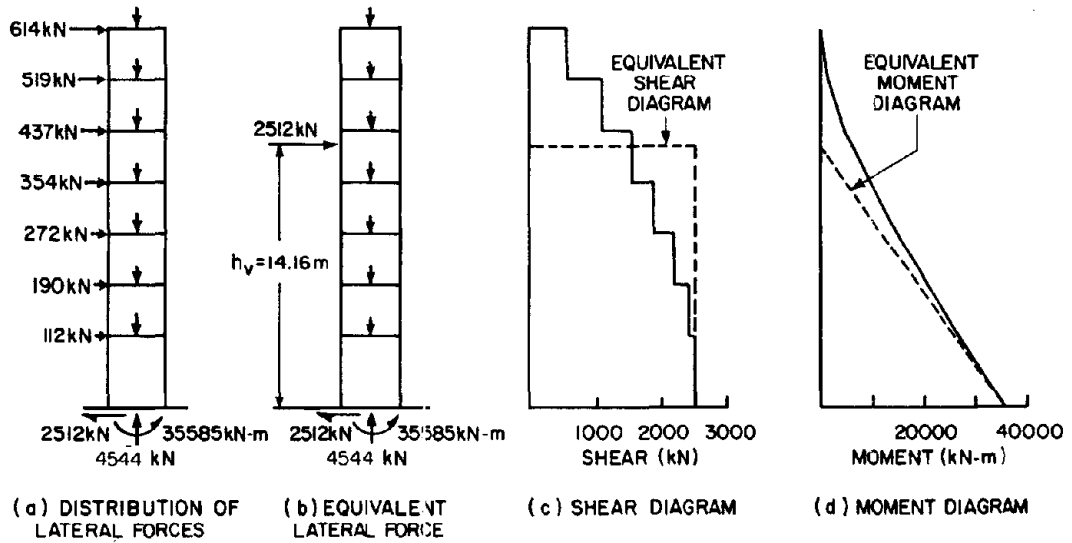


Fig. 2.5 Shear and Moment Diagrams of a Single N-S Wall of Seven-Story Building When Subjected to half of 1.4E and to 1.4 (Torsion) Code Forces

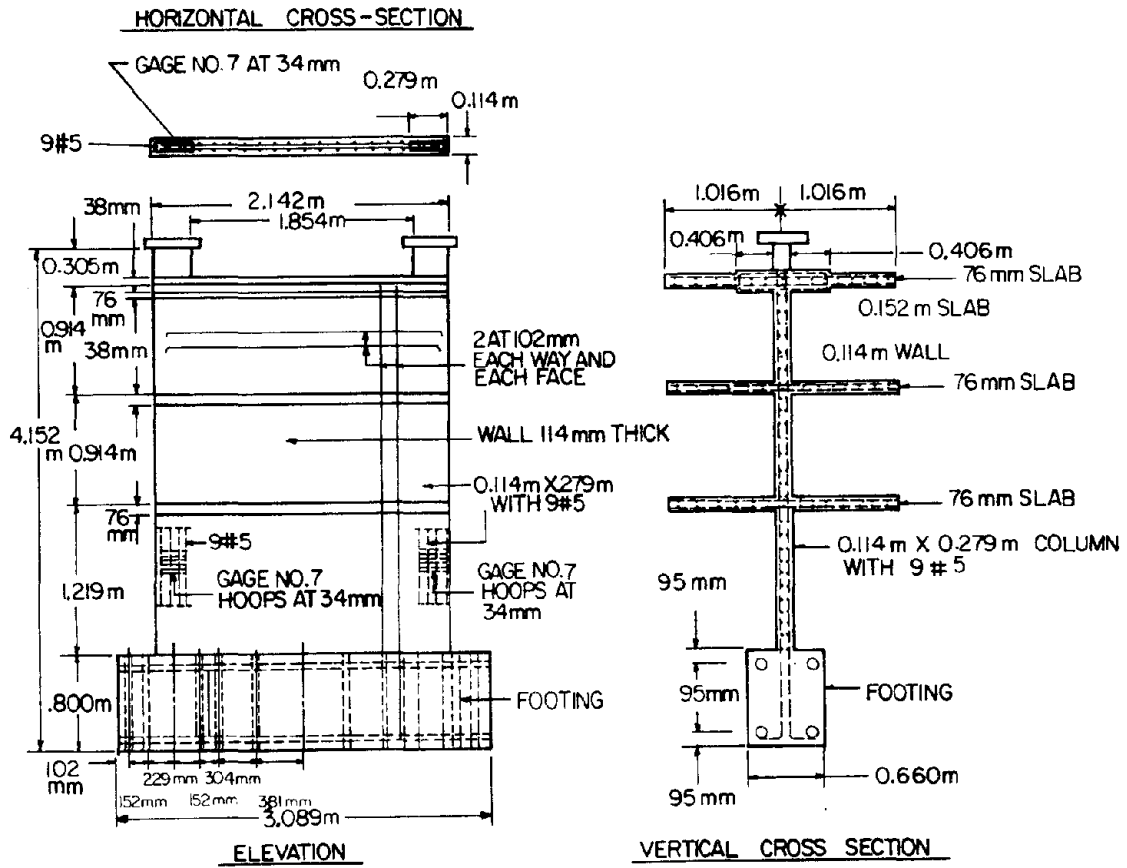


Fig. 2.6a Dimensions and Details of Rectangular Specimens

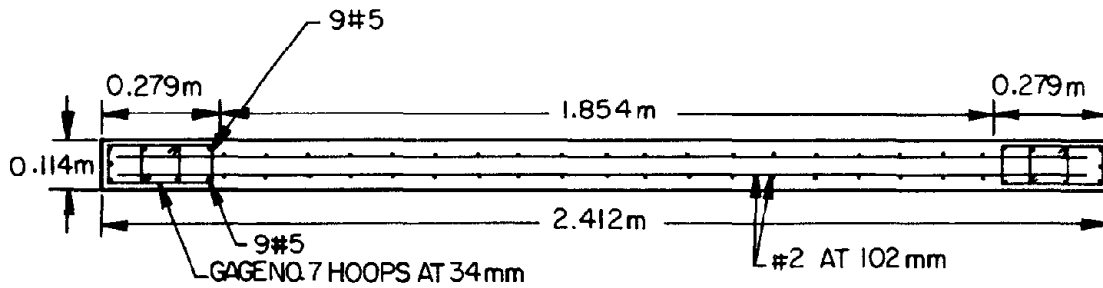


Fig. 2.6b Detailed Cross-Section of Rectangular Wall

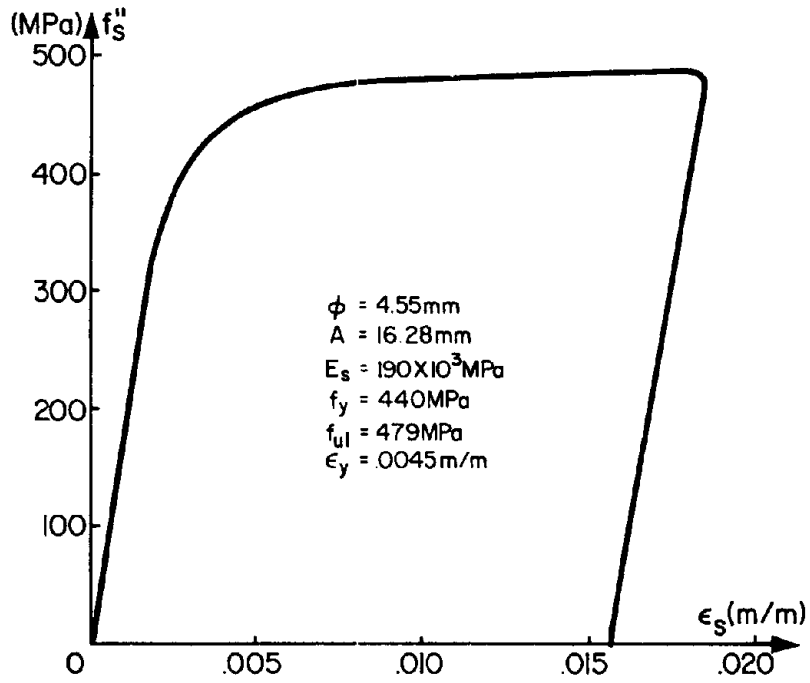


Fig. 2.7 Tensile Stress-Strain Diagram for Gage No. 7 Wire

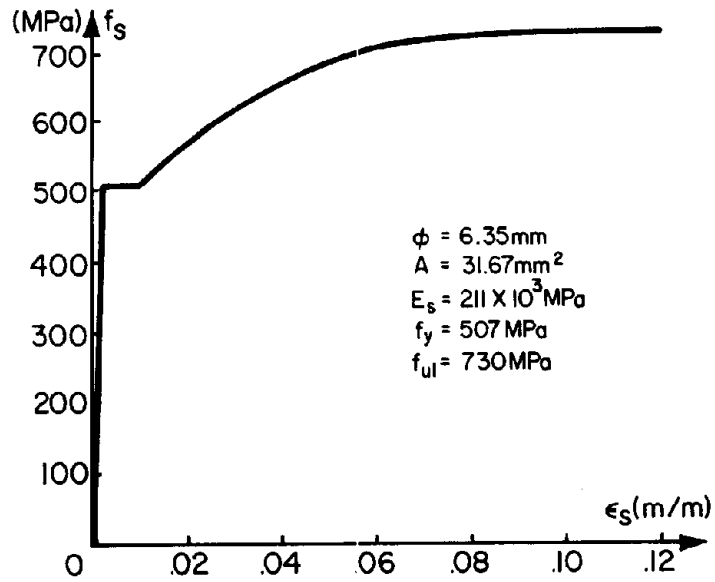


Fig. 2.8 Tensile Stress-Strain Diagram for No. 2 Reinforcing Bar

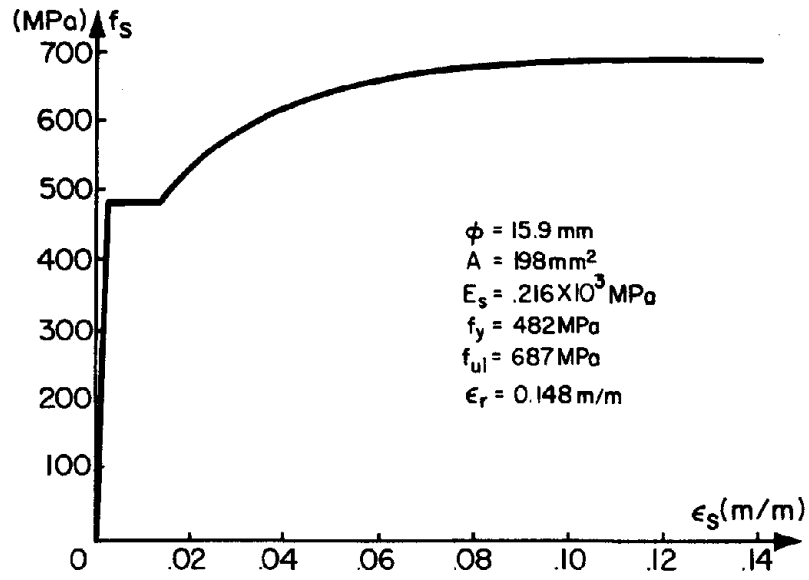


Fig. 2.9 Tensile Stress-Strain Diagram for No. 5 Reinforcing Bar

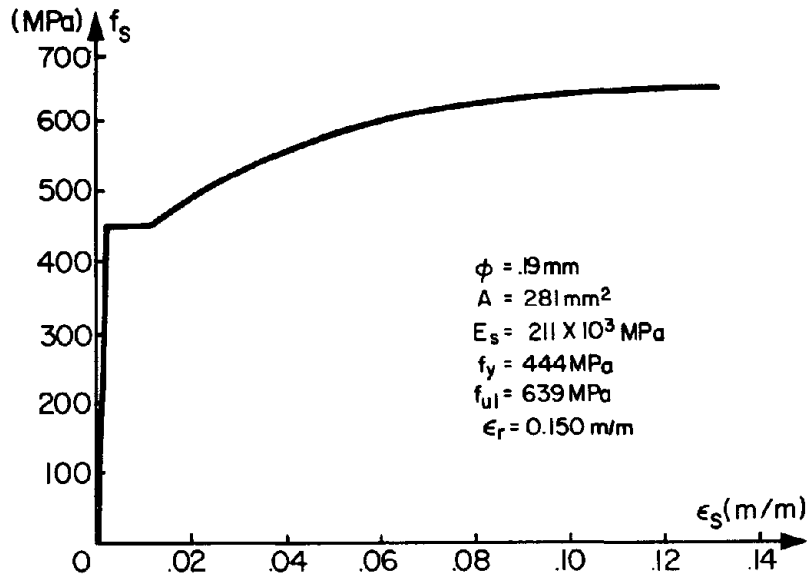


Fig. 2.10 Tensile Stress-Strain Diagram for No. 6 Reinforcing Bar

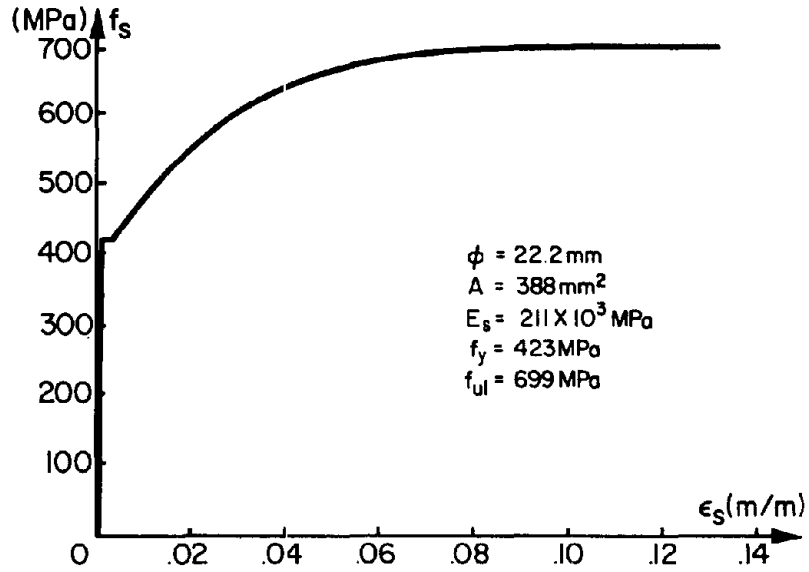


Fig. 2.11 Tensile Stress-Strain Diagram for No. 7 Reinforcing Bar

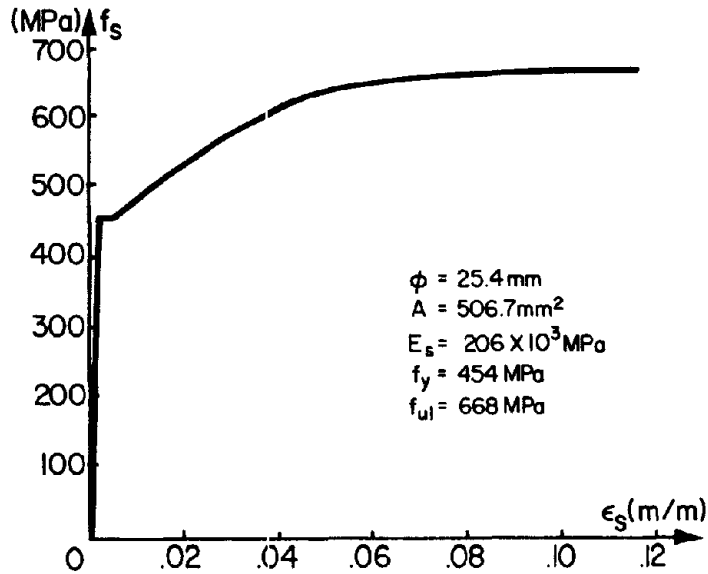


Fig. 2.12 Tensile Stress-Strain Diagram for No. 8 Reinforcing

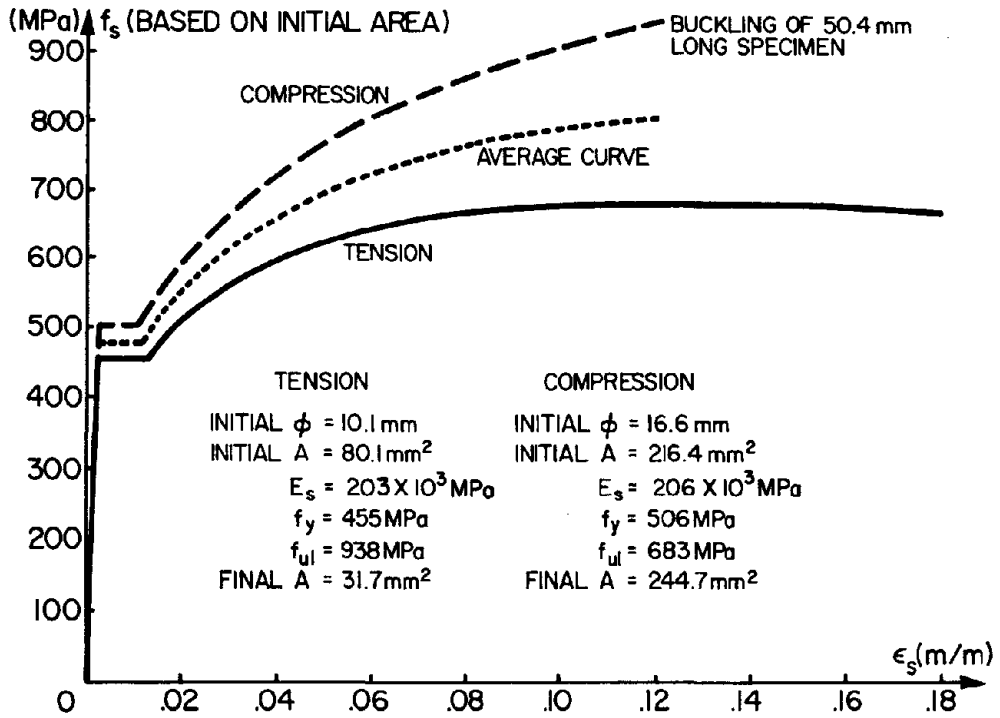


Fig. 2.13 Tensile and Compressive Stress-Strain Diagrams for Machined No. 6 Reinforcing Bars

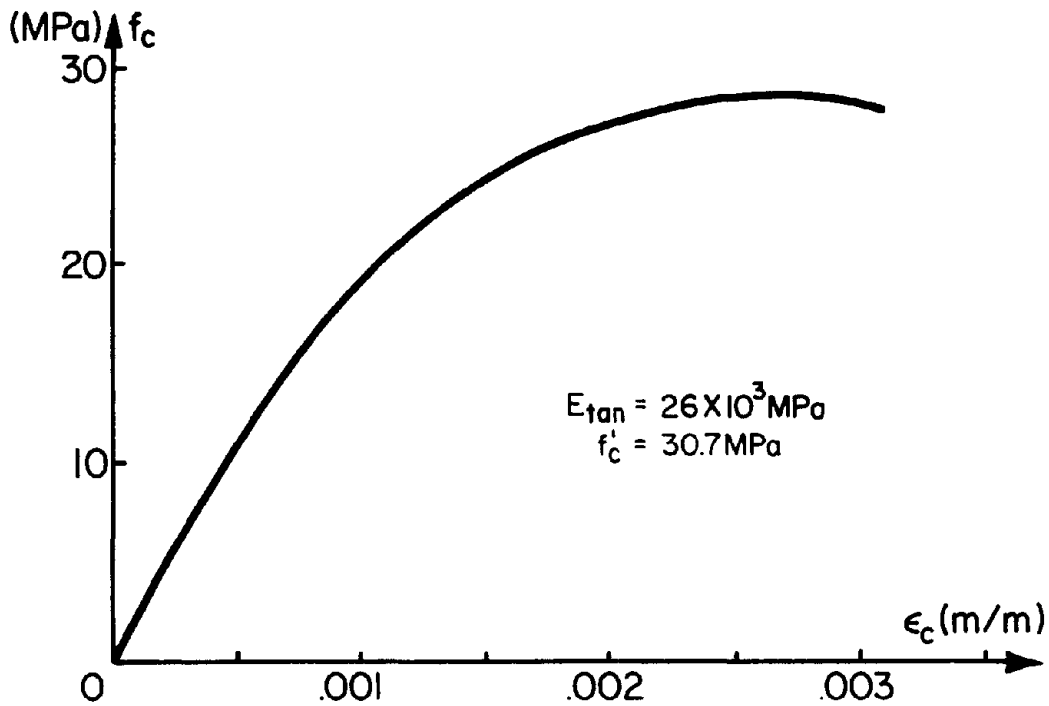


Fig. 2.14 Typical Compressive Stress-Strain Diagram for Concrete Test Cylinders

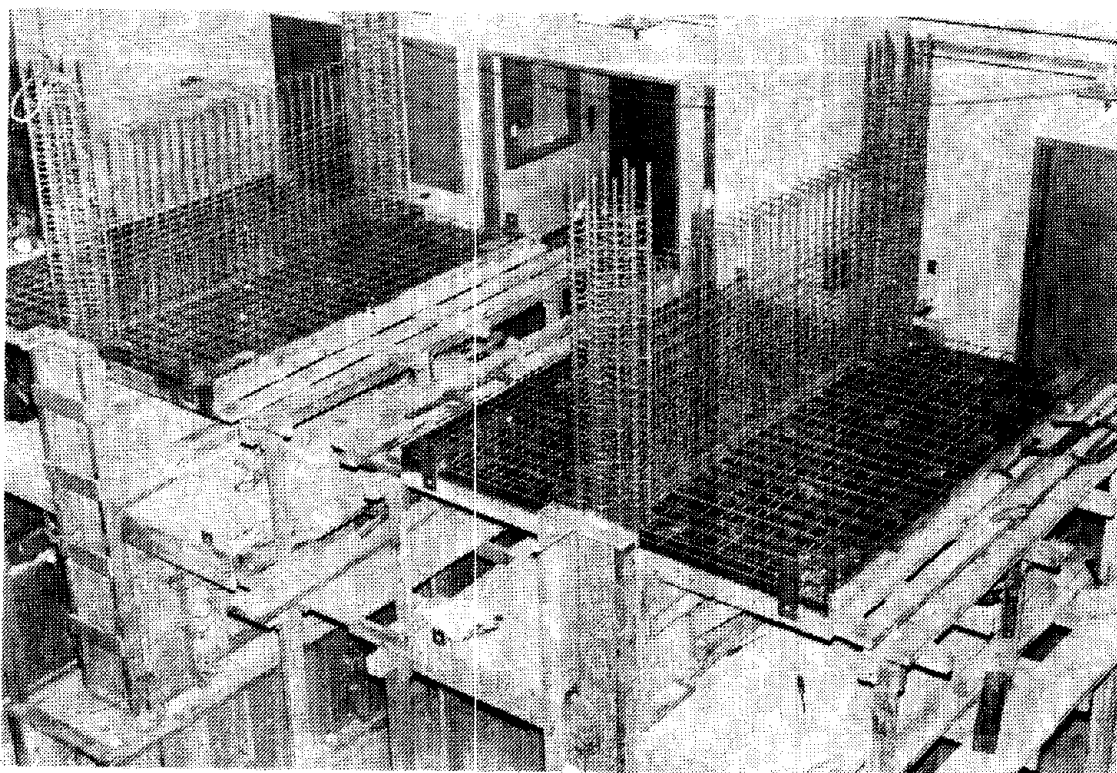


Fig. 2.15 Framed Walls During Construction

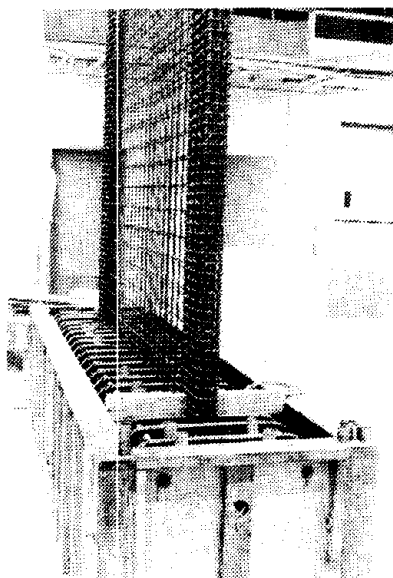


Fig. 2.16 Reinforcement for Panel and Boundary Elements of Rectangular Wall

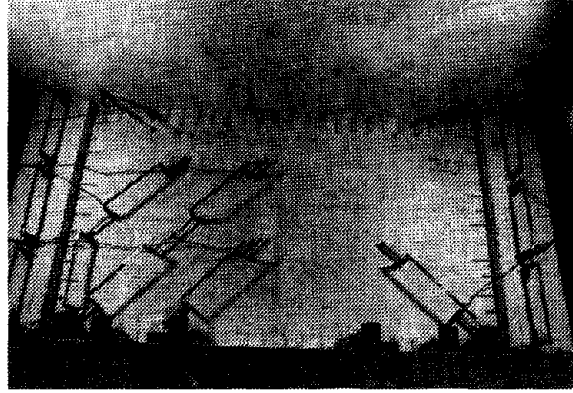


Fig. 2.17 Dowels for Repair of First-Story Panel in Framed Wall Specimen

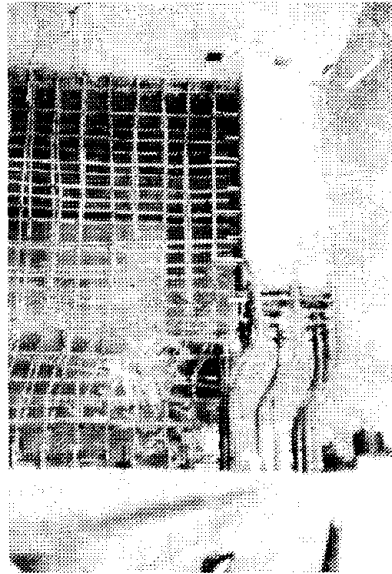


Fig. 2.18 Buckled Wall Reinforcement During Repair Procedure

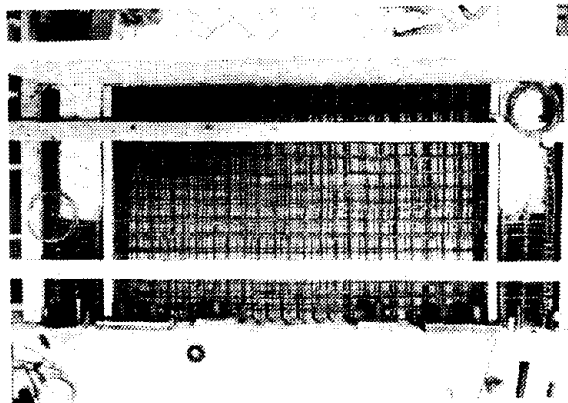


Fig. 2.19 Framed Wall After Removal of Damaged Concrete and Placement of New Steel Reinforcement

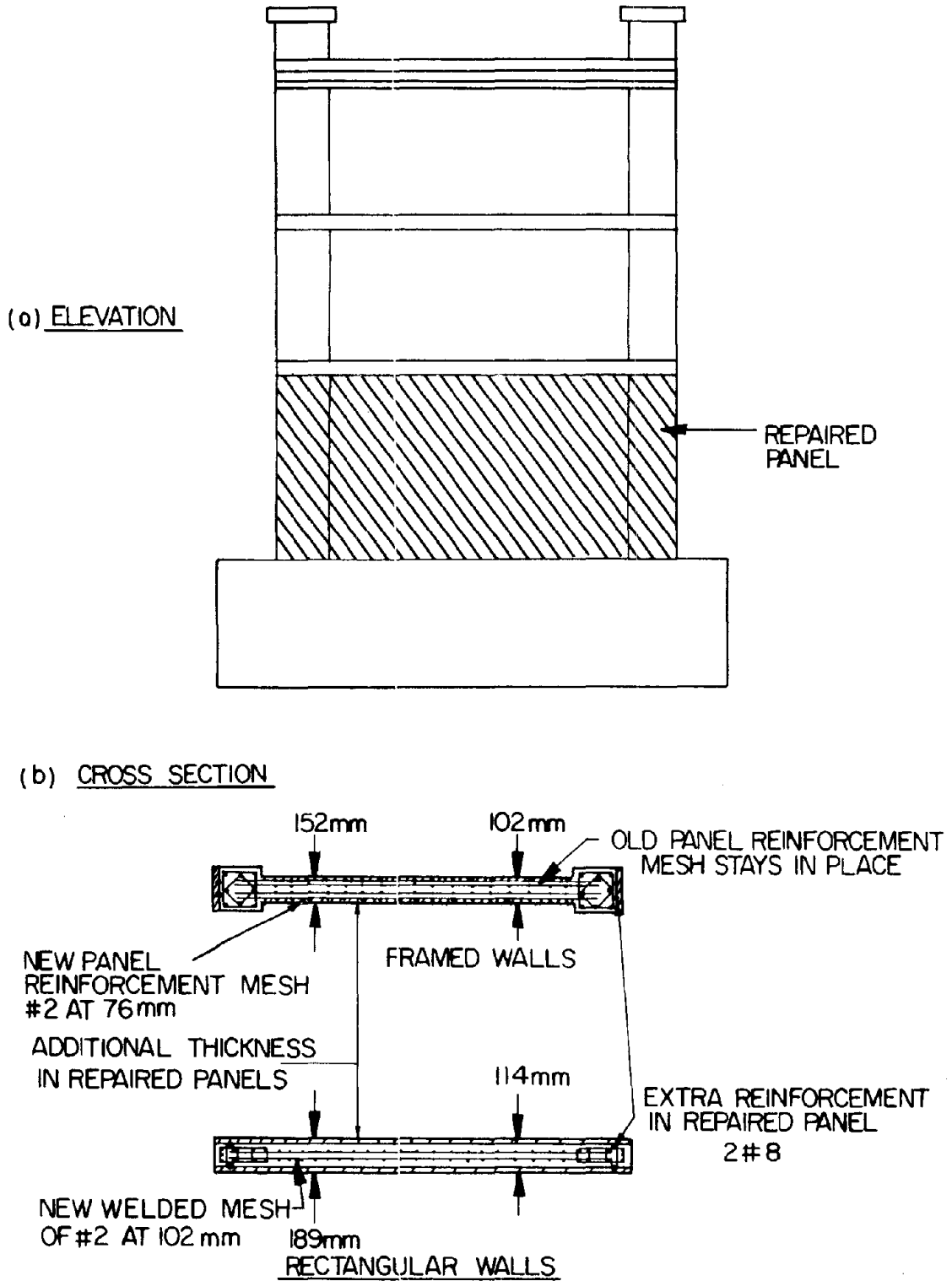
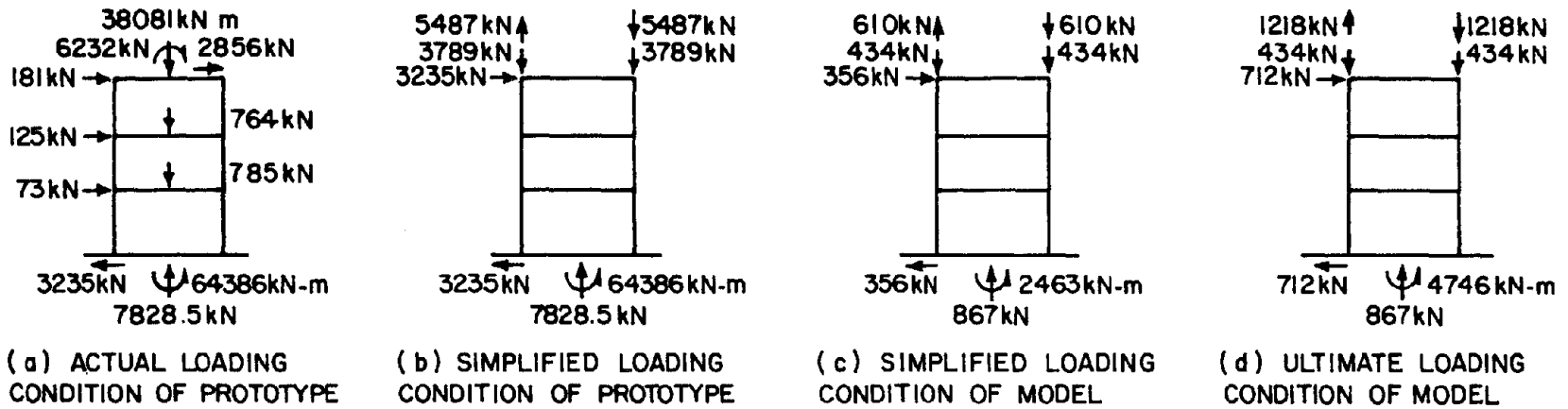
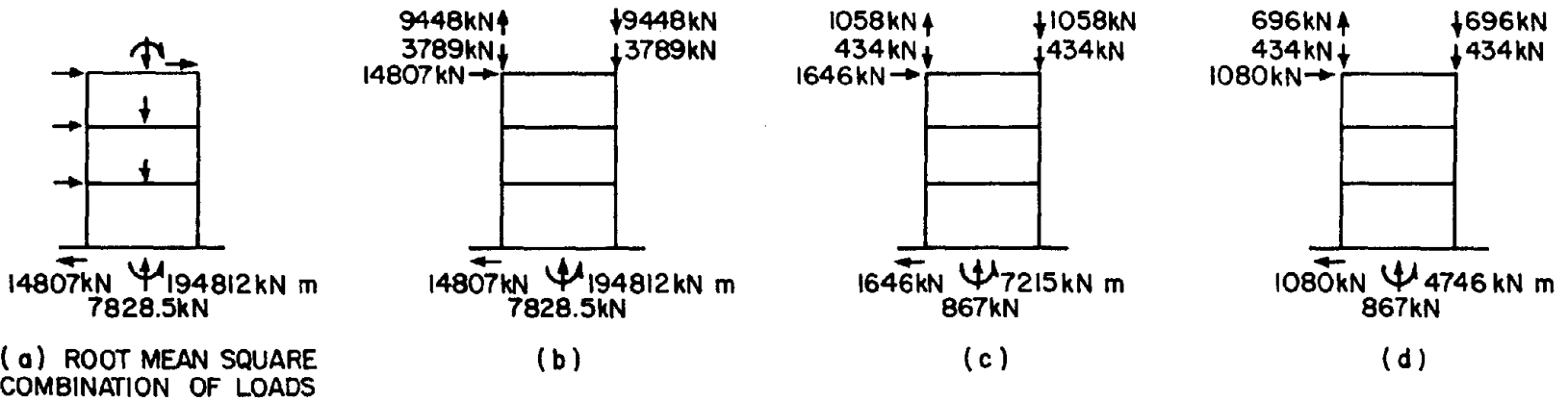


Fig. 2.20 Repaired Walls

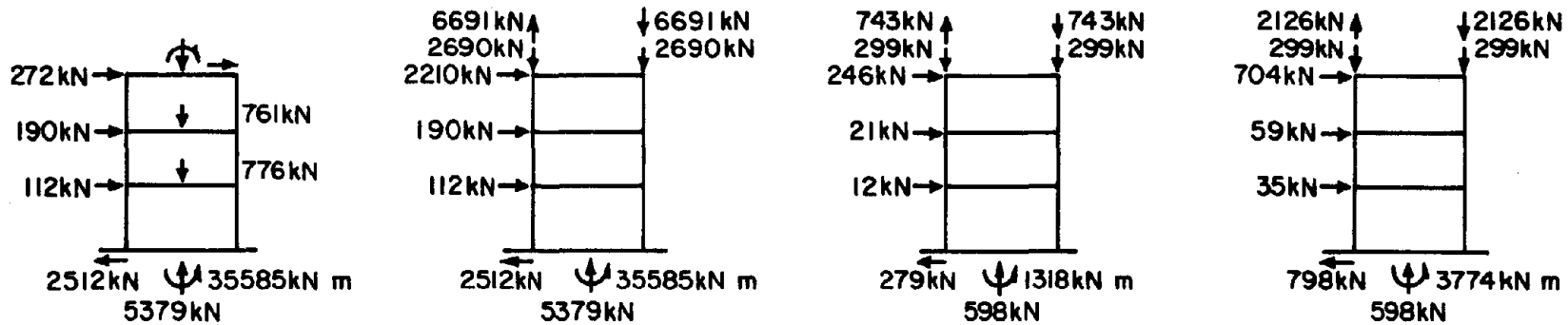


(i) Two Walls Resist Total Load and Torsion Specified by the UBC.



(ii) El Centro Earthquake Response Spectrum Analysis of Entire Building (3 Modes, 5% Damping)

Fig. 3.1 Loading Conditions of Prototype and Model of Framed Wall for Ten-Story Building



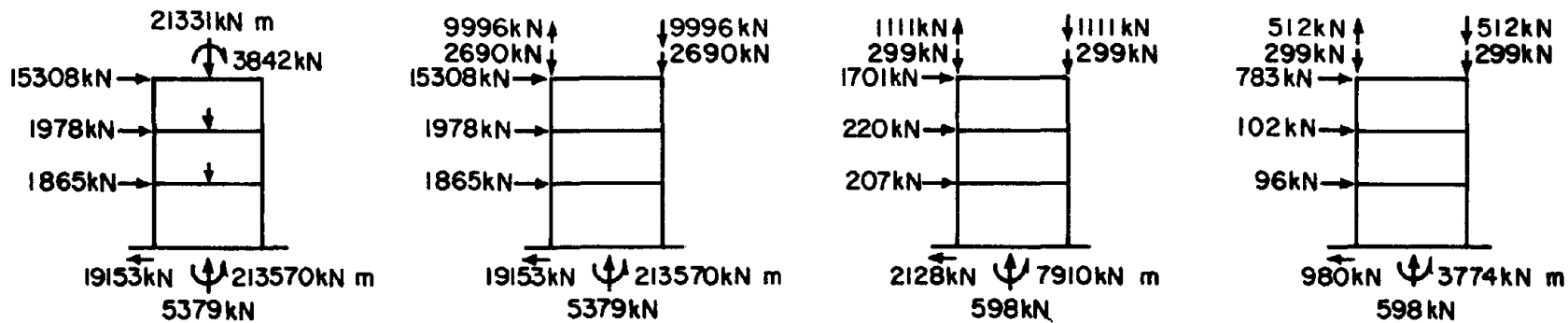
(a) ACTUAL LOADING
CONDITION OF PROTOTYPE

(b) SIMPLIFIED LOADING
CONDITION OF PROTOTYPE

(c) SIMPLIFIED LOADING
CONDITION OF MODEL

(d) ULTIMATE LOADING
CONDITION OF MODEL

(i) Two Walls Resist Total Earthquake Load and Torsion Specified by the UBC.



(a) ROOT MEAN SQUARE
COMBINATION OF LOADS

(b) SIMPLIFIED LOADING
CONDITION OF PROTOTYPE

(c) SIMPLIFIED LOADING
CONDITION OF MODEL

(d) ULTIMATE LOADING
CONDITION OF MODEL

(ii) San Fernando Earthquake Response Spectrum Analysis of Entire Building (3 Modes, 5% Damping)

Fig. 3.2 Loading Conditions of Prototype and Model of Rectangular Wall for Seven-Story Building

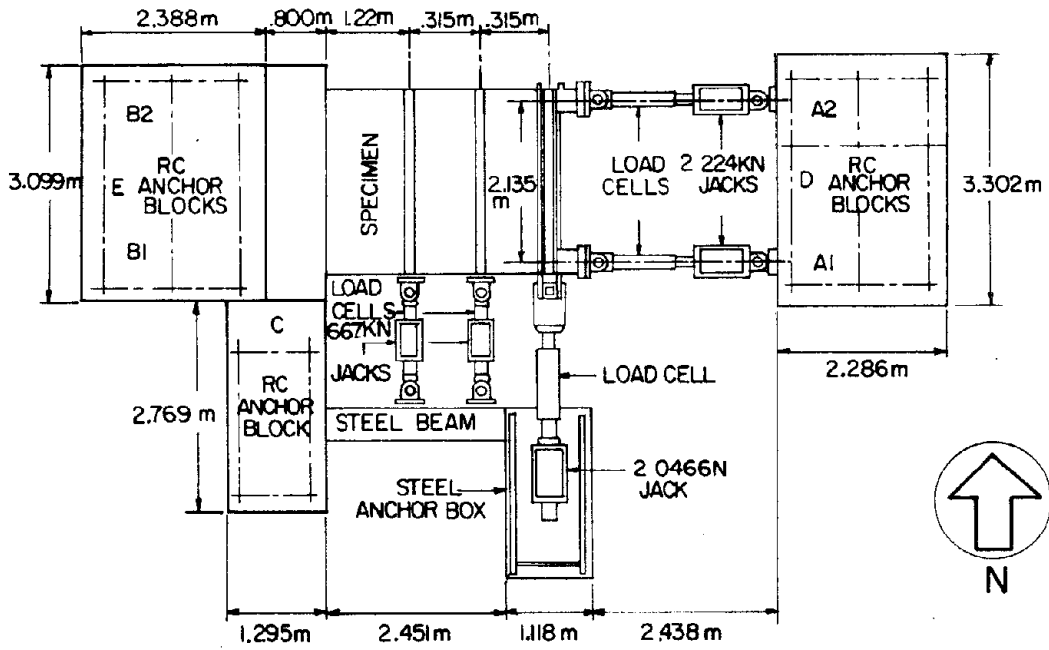


Fig. 3.3a Plan

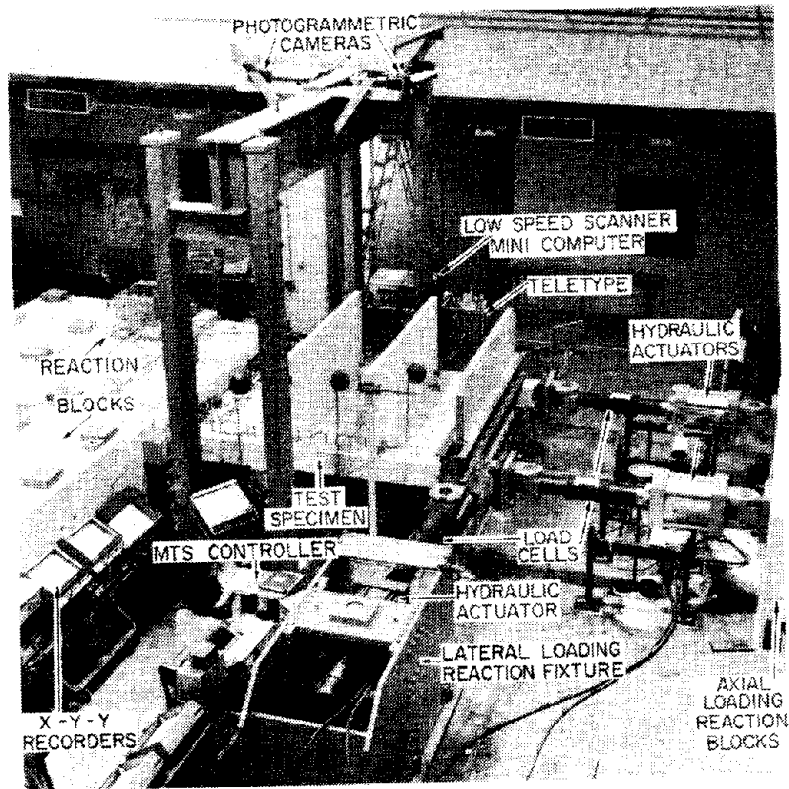


Fig. 3.3 Plan and General View of Testing Facility

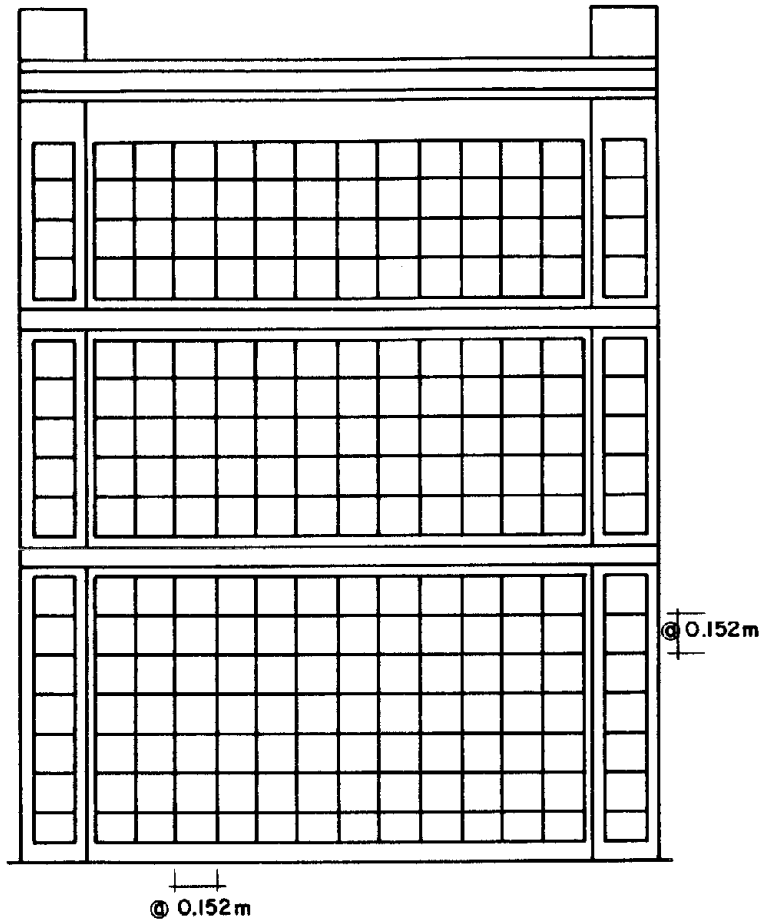


Fig. 3.6 Photogrammetric Reference Grid for Framed Walls

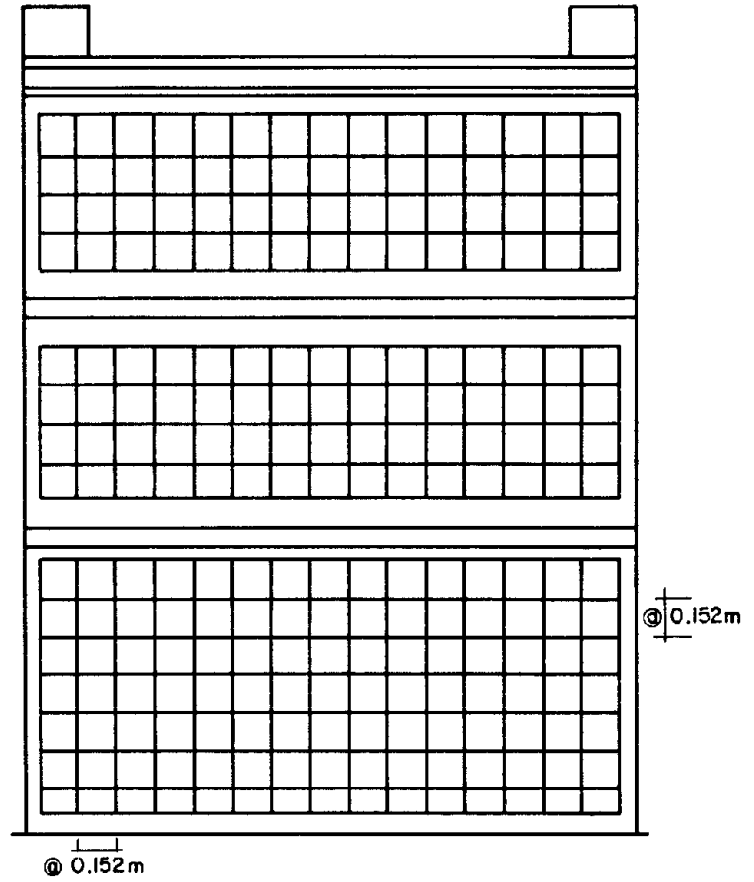


Fig. 3.7 Photogrammetric Reference Grid for Rectangular Walls

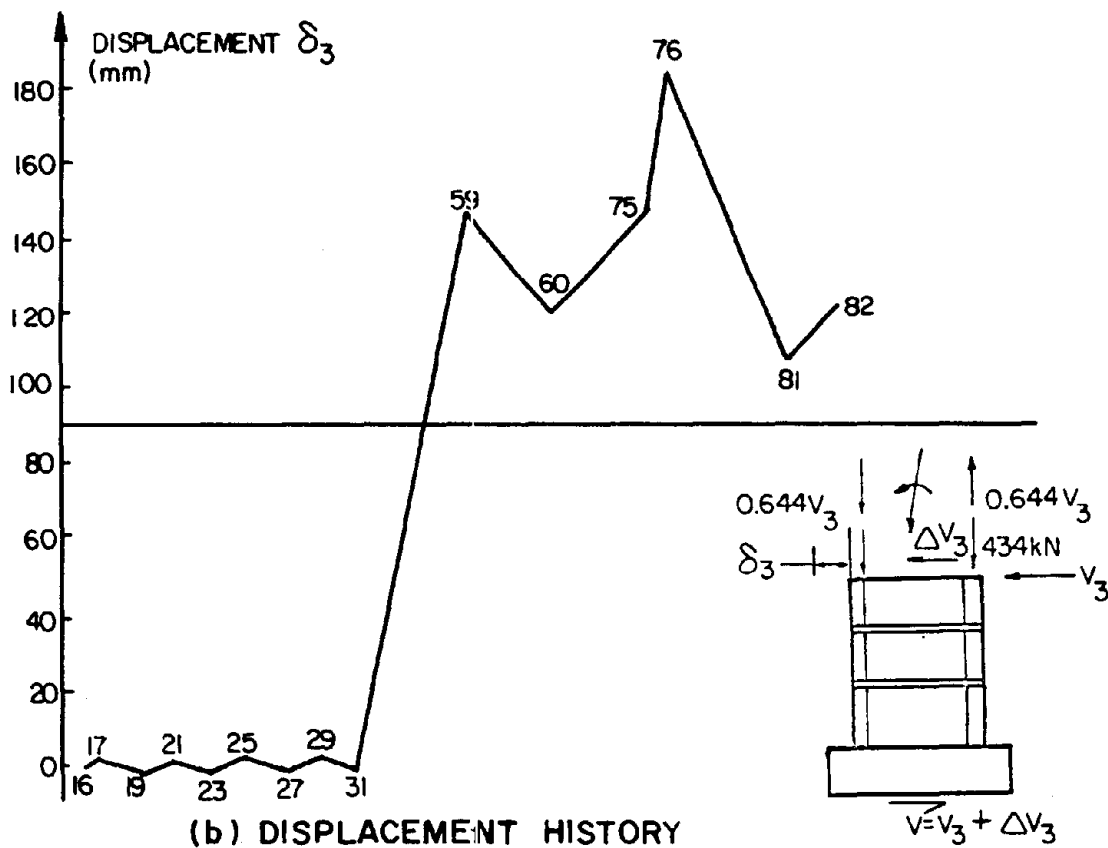
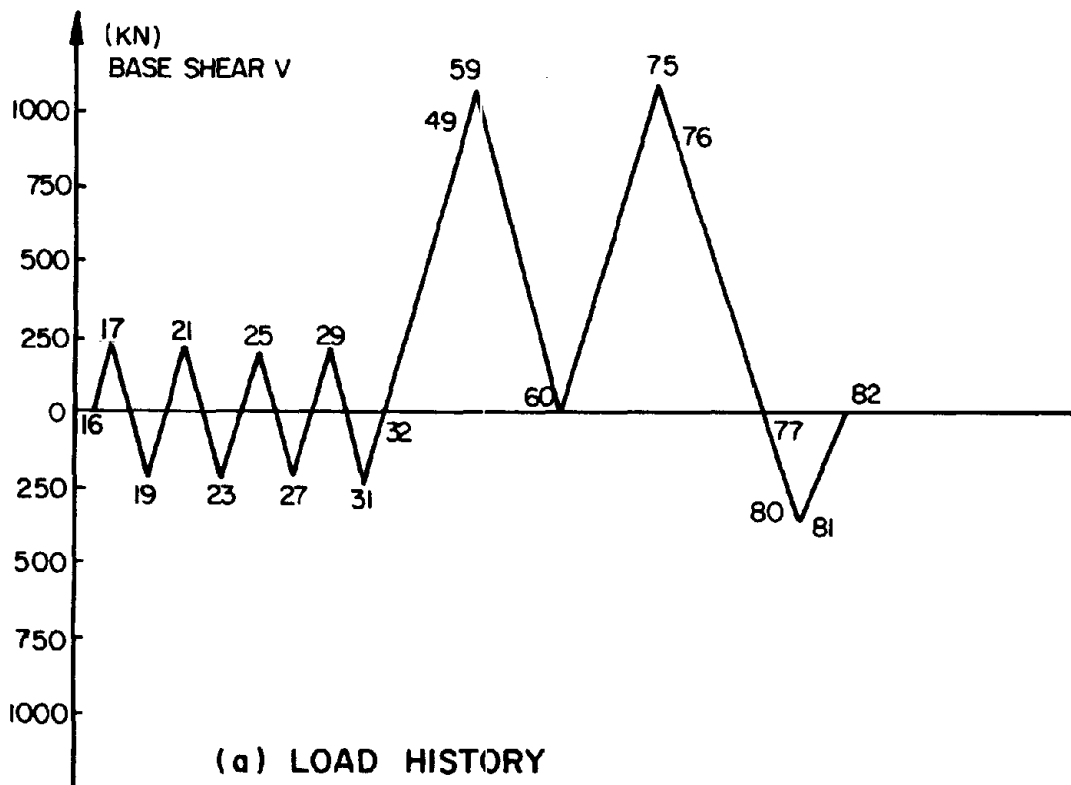


Fig. 4.1 Load Program for Framed Wall (Monotonic Loading) Specimen 3

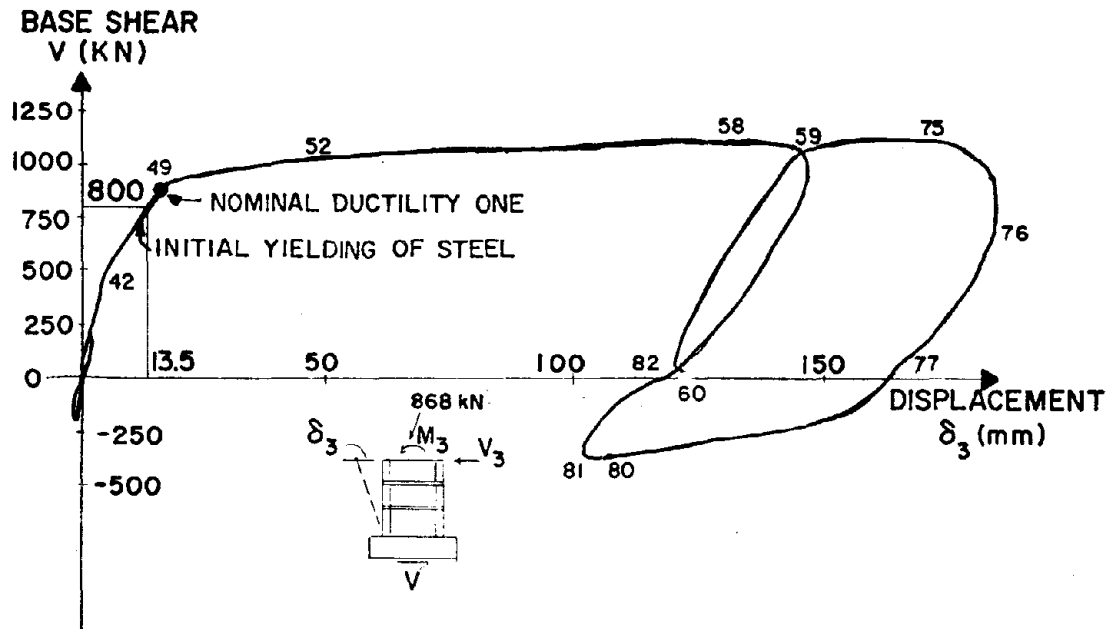


Fig. 4.2 Displacement at Third Floor of Framed Wall (Monotonic Loading) Specimen 3

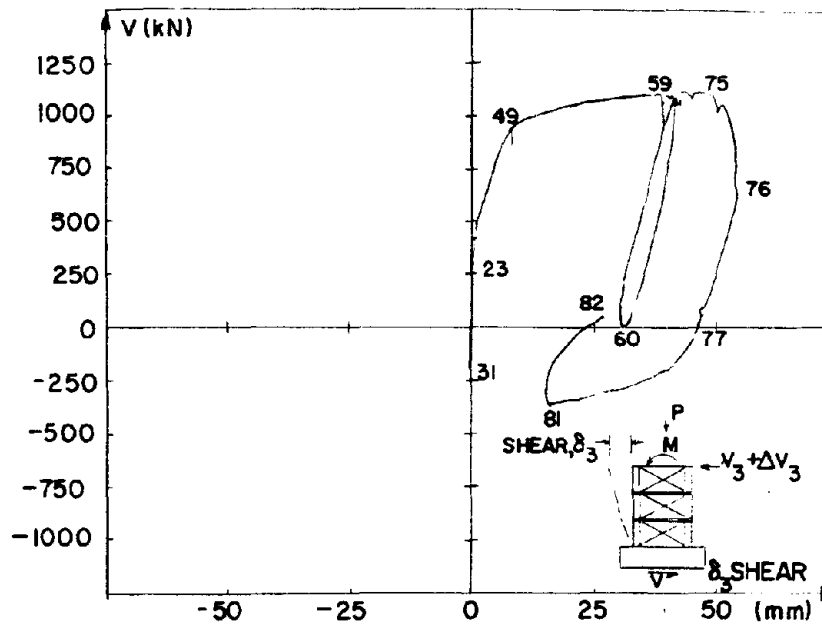


Fig. 4.3 Displacement at Third Floor of Framed Wall (Monotonic Loading) Due to Shear Deformation, Specimen 3

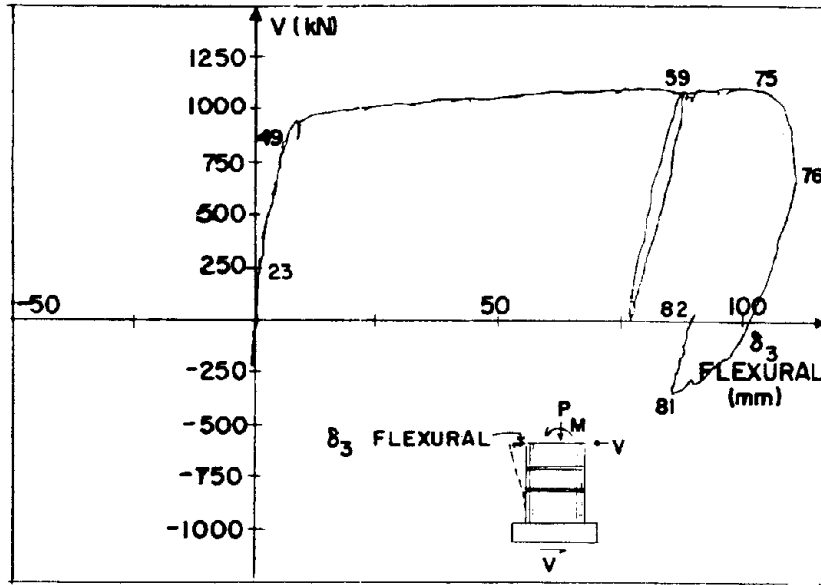


Fig. 4.4 Displacement at Third Floor of Framed Wall (Monotonic Loading) Due to Flexural Deformation, Specimen 3

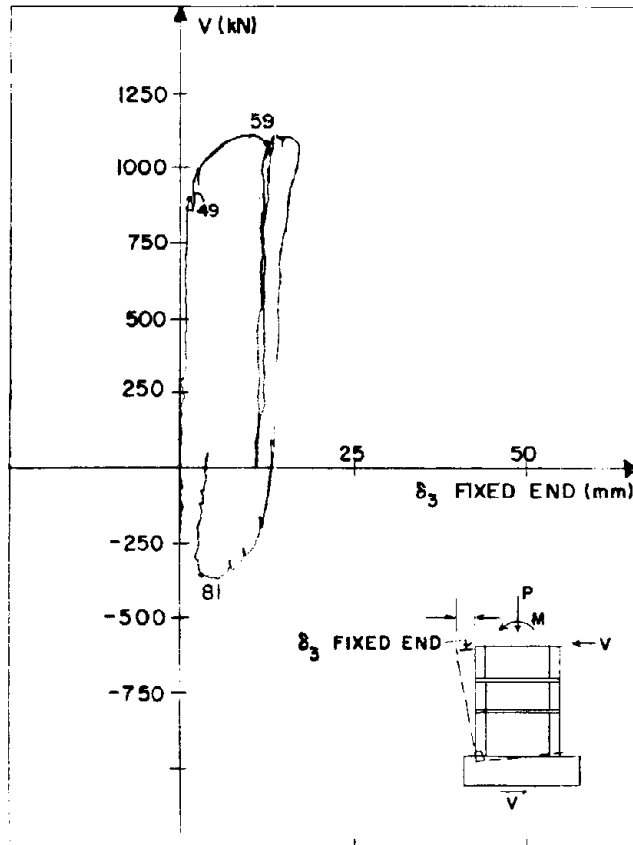


Fig. 4.5 Displacement at Third Floor of Framed Wall (Monotonic Loading) Due to Fixed-End Deformation, Specimen 3

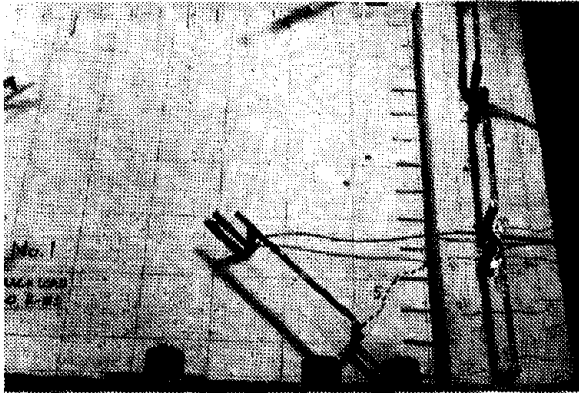


Fig. 4.6a

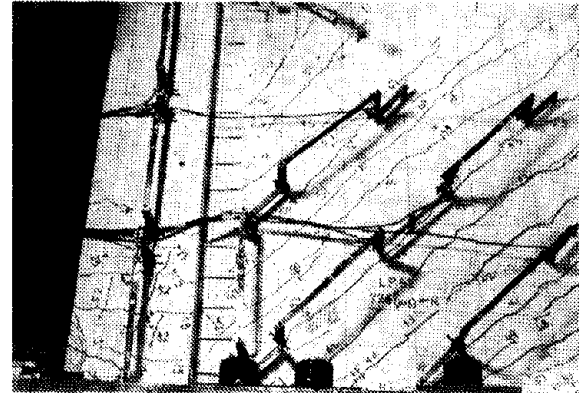


Fig. 4.7a

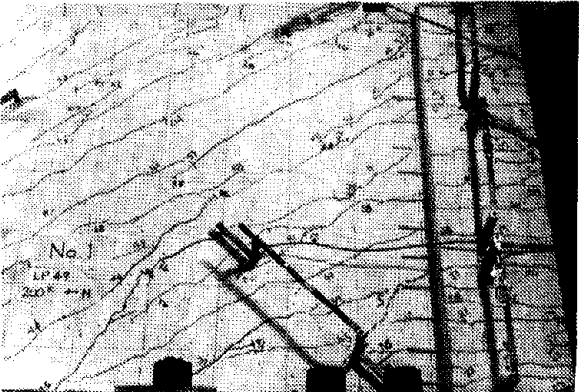


Fig. 4.6b

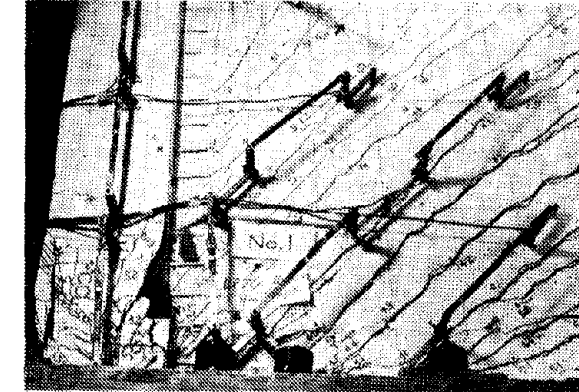


Fig. 4.7b

Fig. 4.6 Sequence of Crack Formation up to $\mu = 1$, Specimen 3

Fig. 4.7 Concrete Cover Spalling and Buckling in North Column, Specimen 3

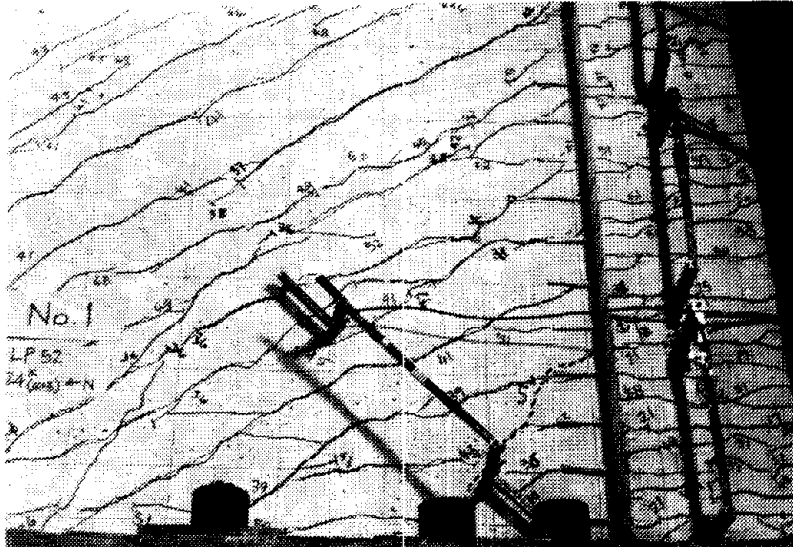


Fig. 4.8a



Fig. 4.8b



Fig. 4.8c

Fig. 4.8 Tension Cracks in South Panel and Column, Specimen 3

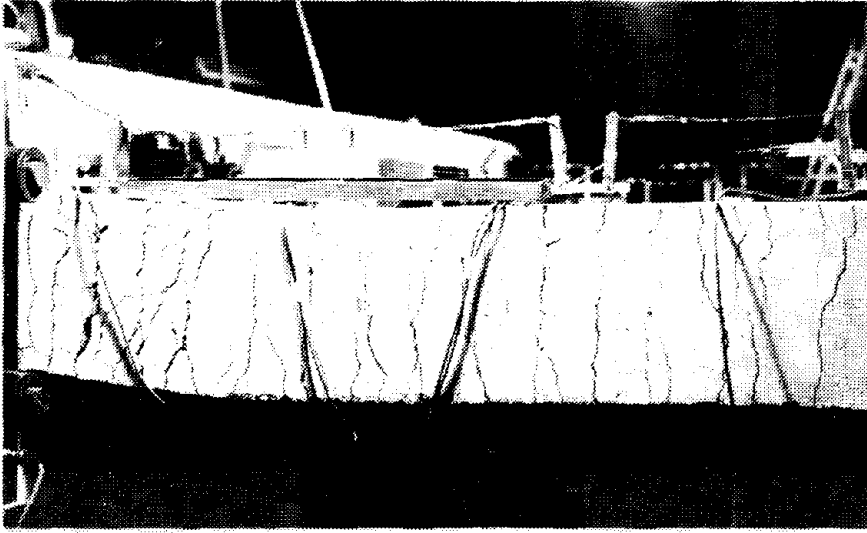


Fig. 4.9a
LP80

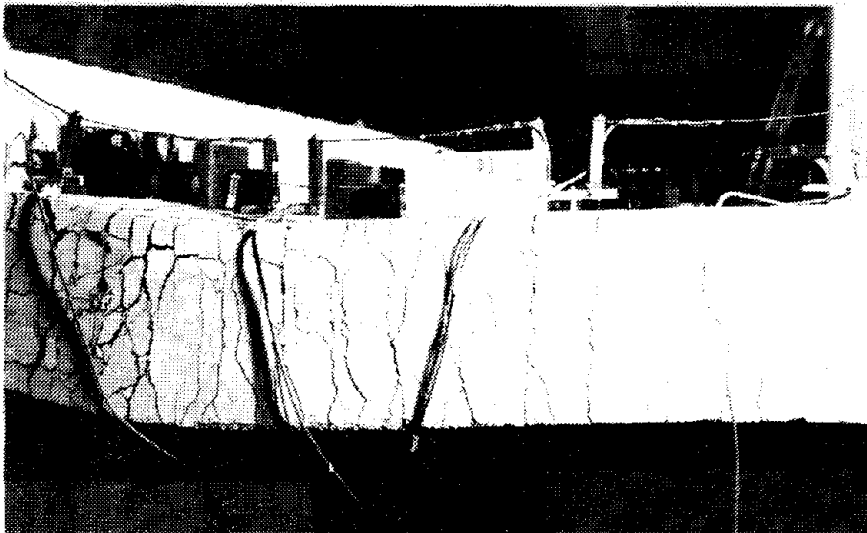


Fig. 4.9b
LP81

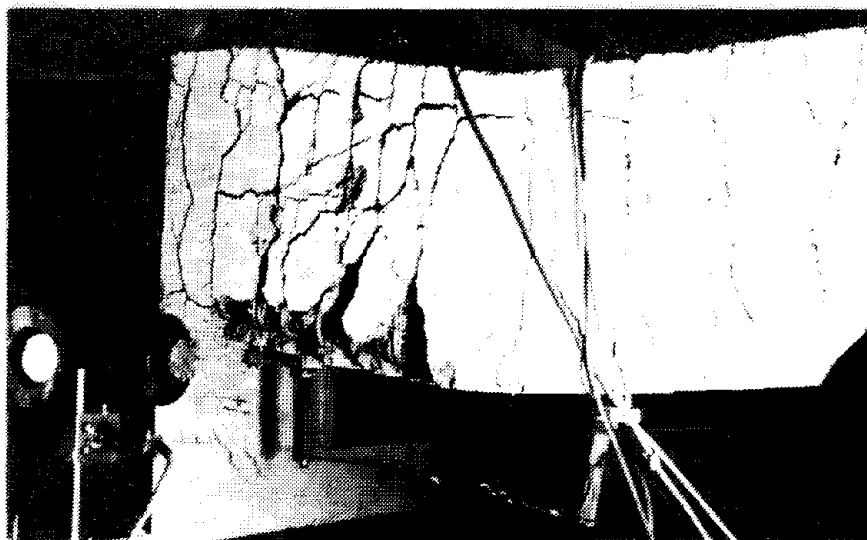


Fig. 4.9c
LP82

Fig. 4.9 Buckling of South Column, Specimen 3

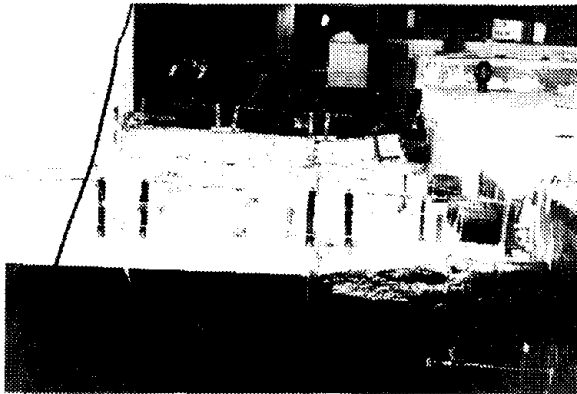


Fig. 4.10a Buckled Column and Panel



Fig. 4.10b Buckled Column

Fig. 4.10 Views of Buckled South Column, Specimen 3

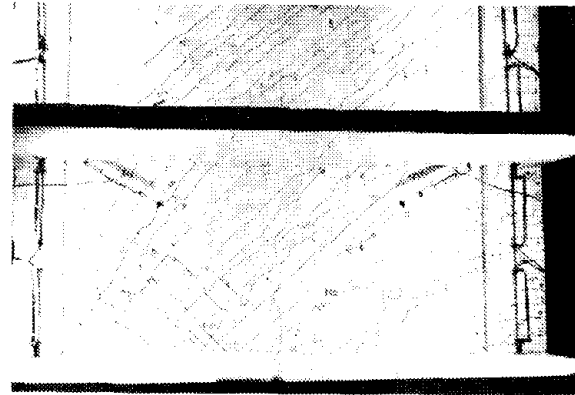


Fig. 4.11a Top View

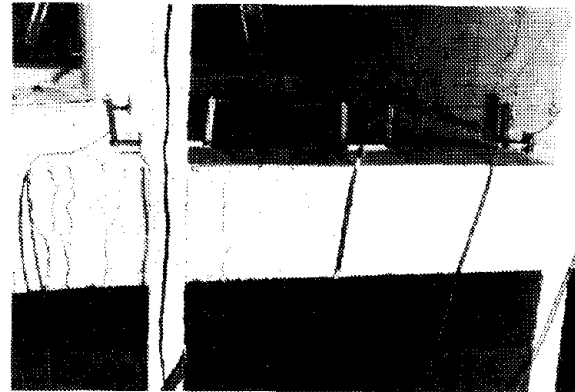


Fig. 4.11b Side View

Fig. 4.11 Second Panel at Conclusion of Test, Specimen 3

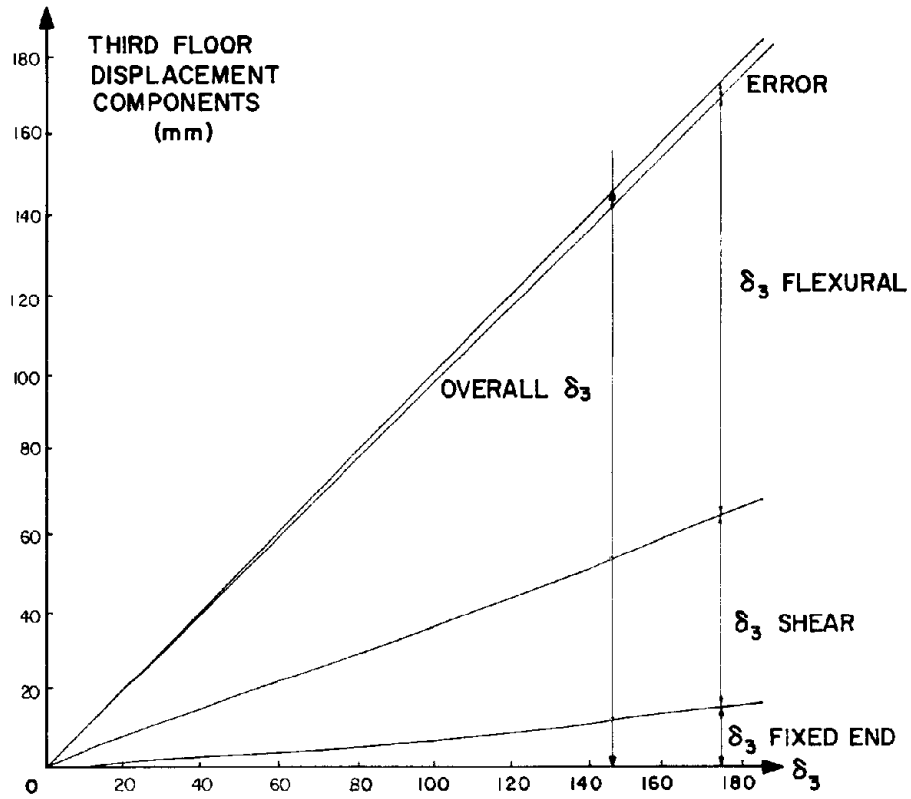


Fig. 4.12a At Third Floor Level

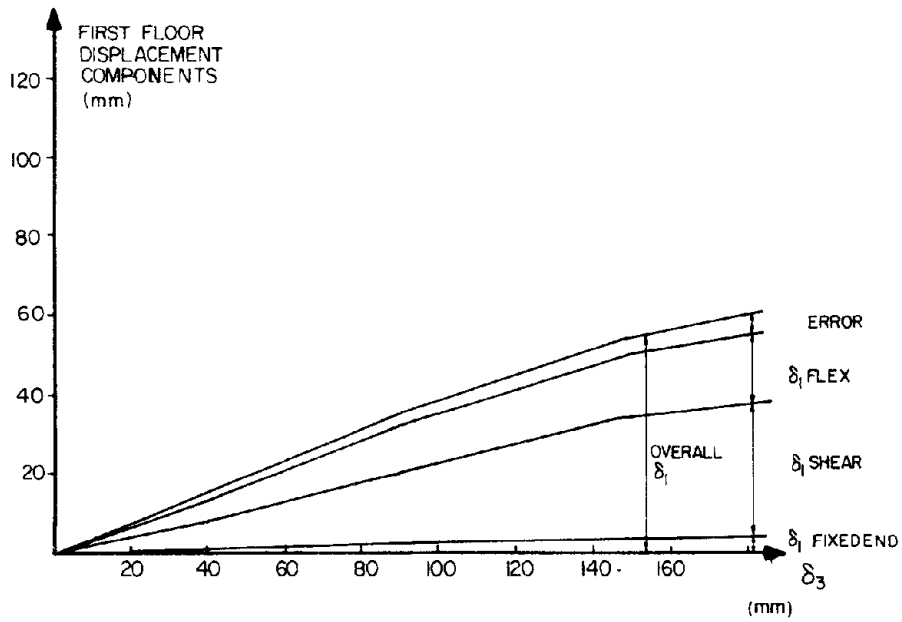


Fig. 4.12b At First Floor Level

Fig. 4.12 Displacement Component Diagrams

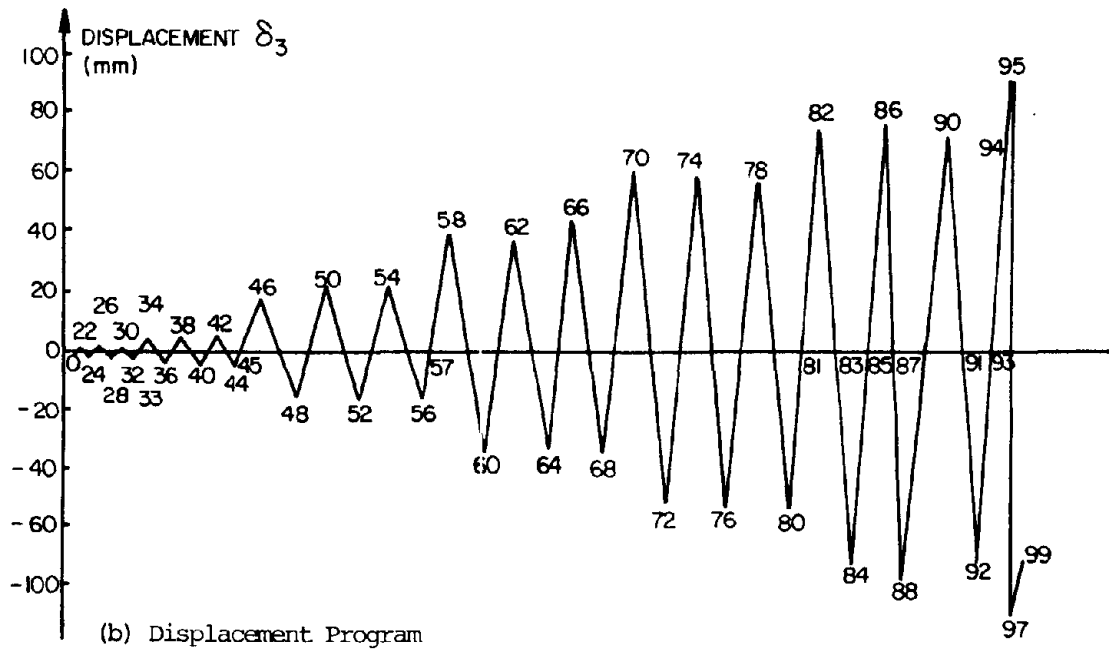
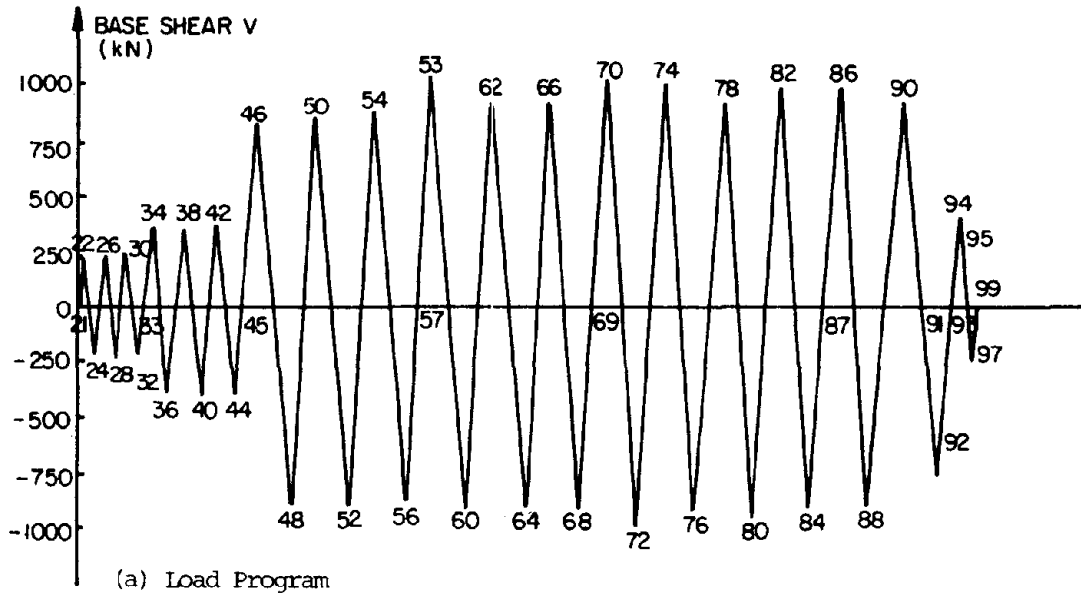


Fig. 4.13 Load Program for Framed Wall (Cyclic Loading), Specimen 4

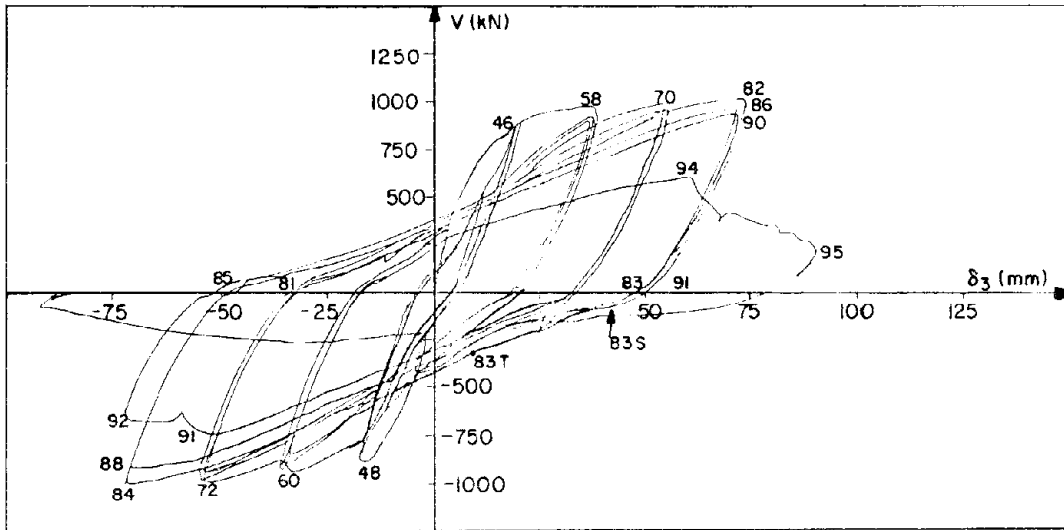


Fig. 4.14 Displacement at Third Floor of Framed Wall (Cyclic Loading), Specimen 4

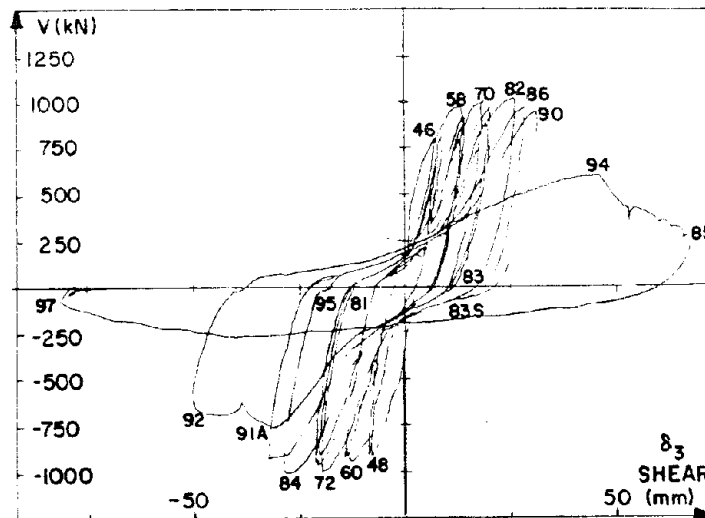


Fig. 4.15 Displacement at Third Floor of Framed Wall (Cyclic Loading) Due to Shear Deformation, Specimen 4

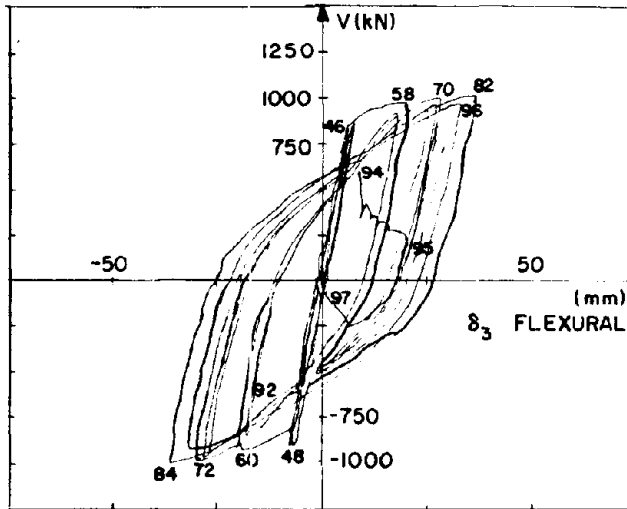


Fig. 4.16 Displacement at Third Floor of Framed Wall (Cyclic Loading) Due to Flexural Deformation, Specimen 4

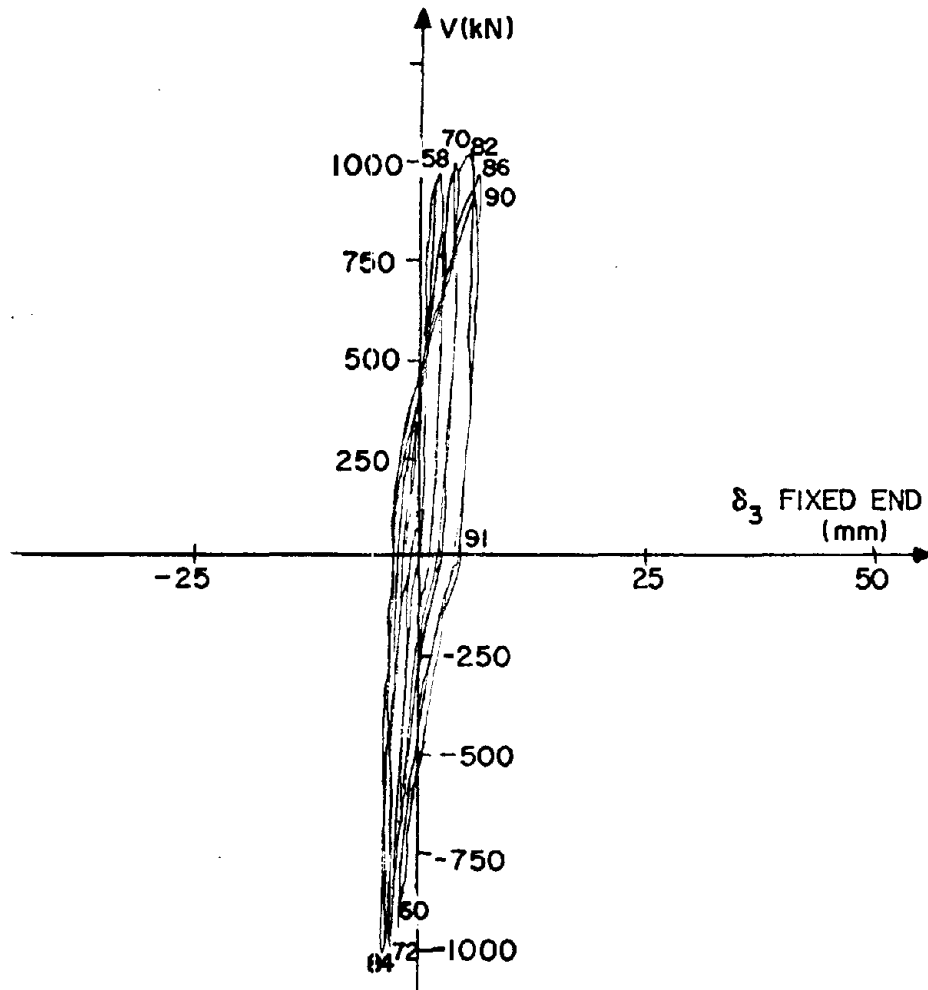


Fig. 4.17 Displacement at Third Floor of Framed Wall (Cyclic Loading) Due to Fixed-End Deformation, Specimen 4

Fig. 4.18a
Cracking load

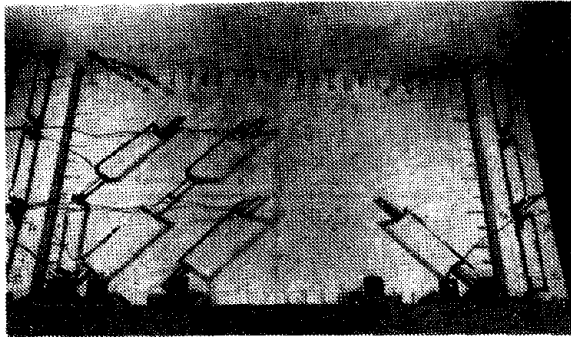


Fig. 4.18b
Service load

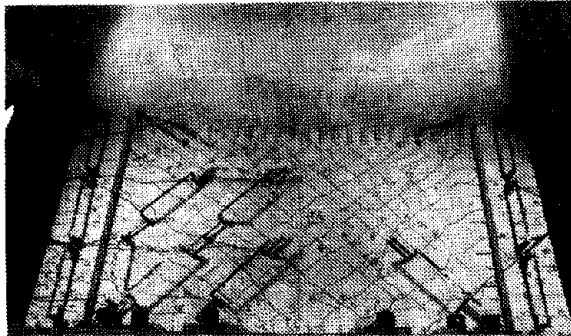


Fig. 4.18c
 $\mu = 1$



Fig. 4.18 Sequence of Crack Propagation, Specimen 4

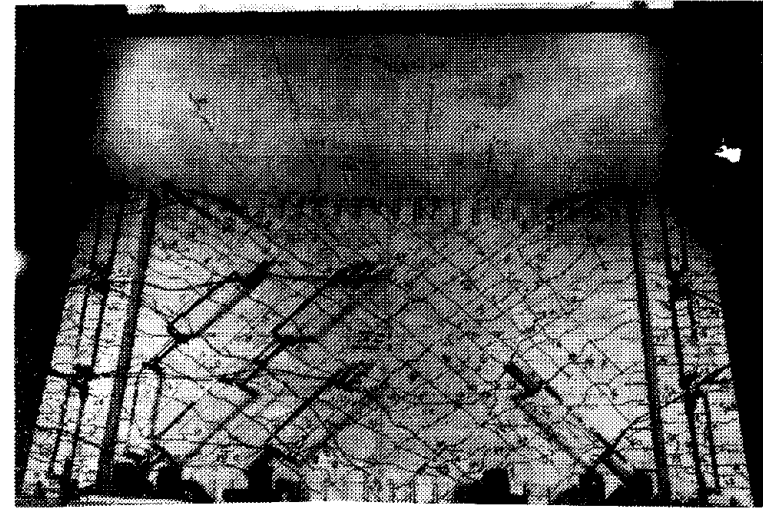


Fig. 4.19a First panel

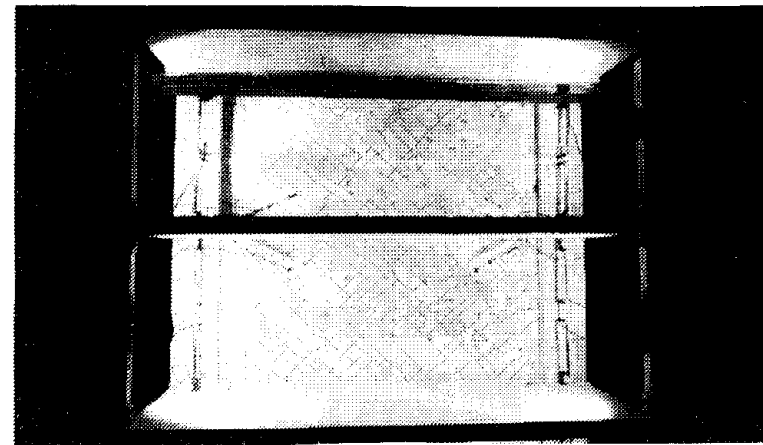


Fig. 4.19b Upper panels

Fig. 4.19 Cracking at $\mu = 2$, Specimen 4

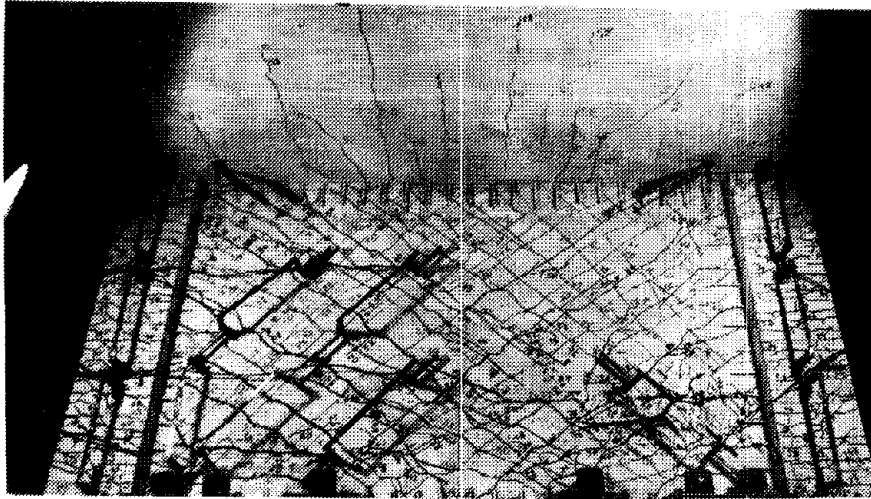


Fig. 4.20a
Initial
crushing

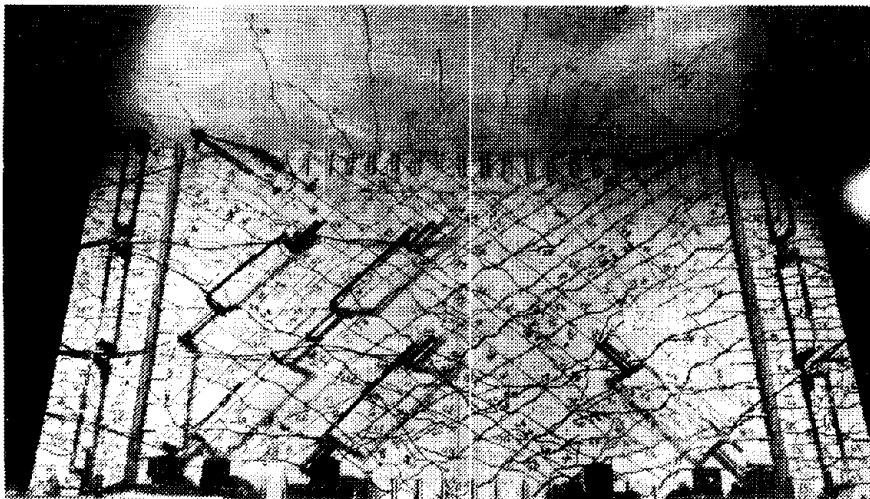


Fig. 4.20b
Horizontal panel
reinforcement
buckling

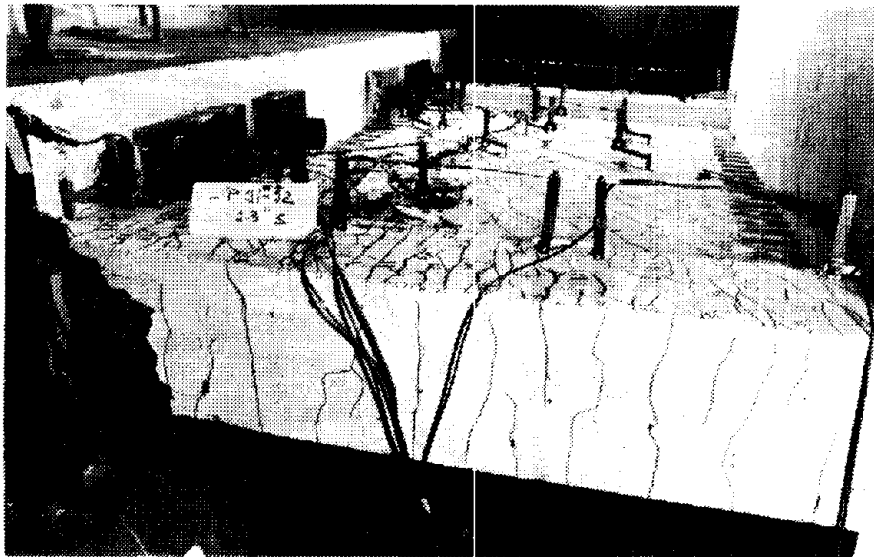


Fig. 4.20c
Flexural shear
failure

Fig. 4.20 Development of Failure Mechanism, Specimen 4

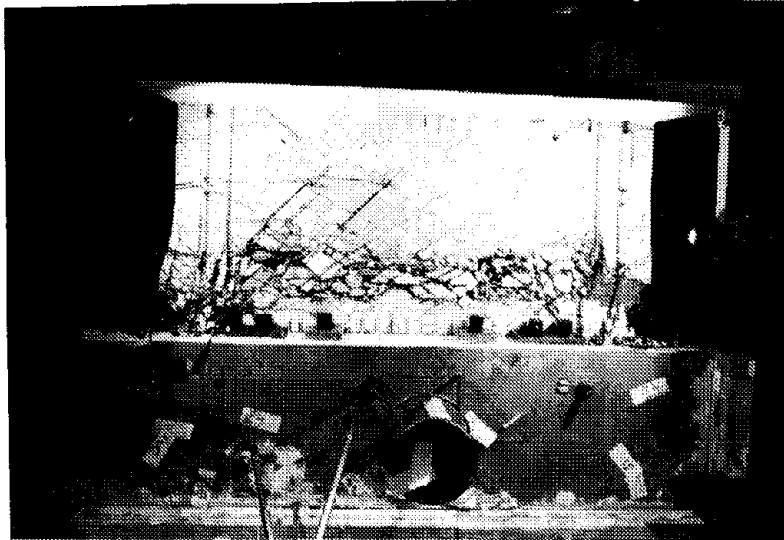


Fig. 4.21 Specimen 4 After Failure

THIRD FLOOR DISPLACEMENT COMPONENTS (mm)

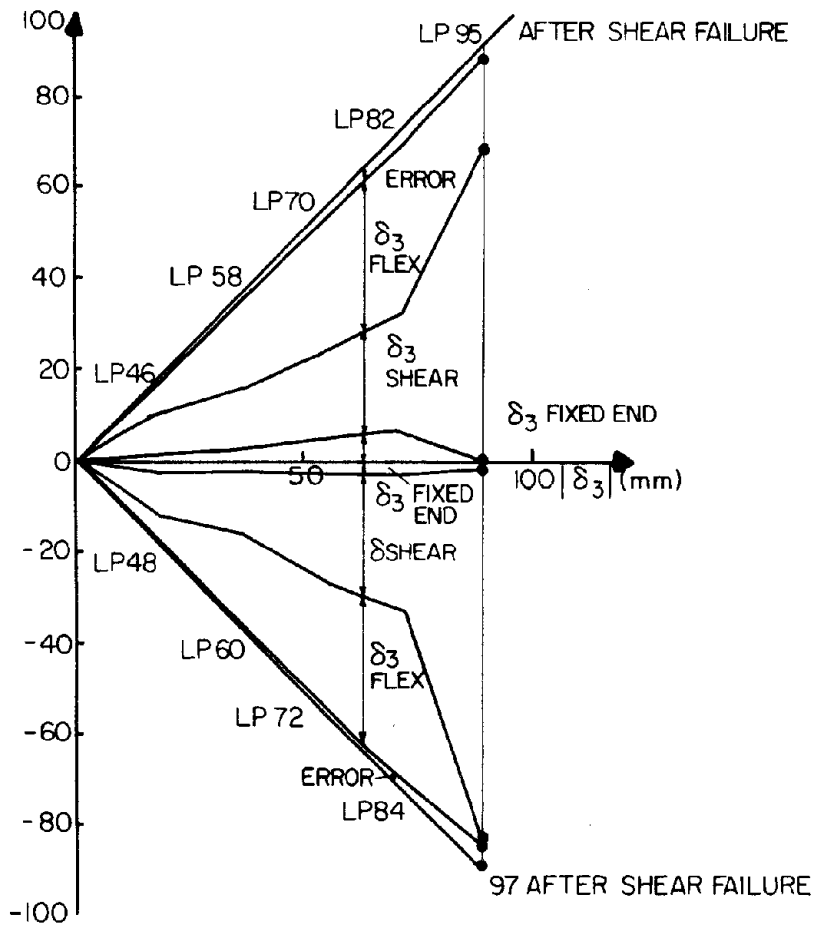
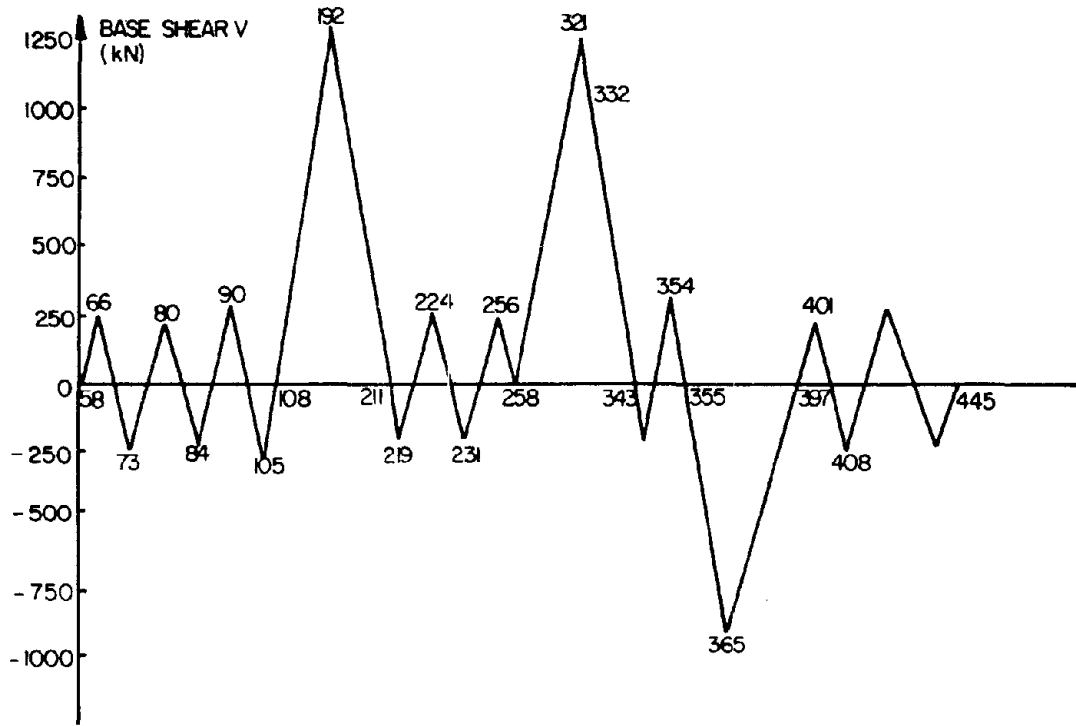
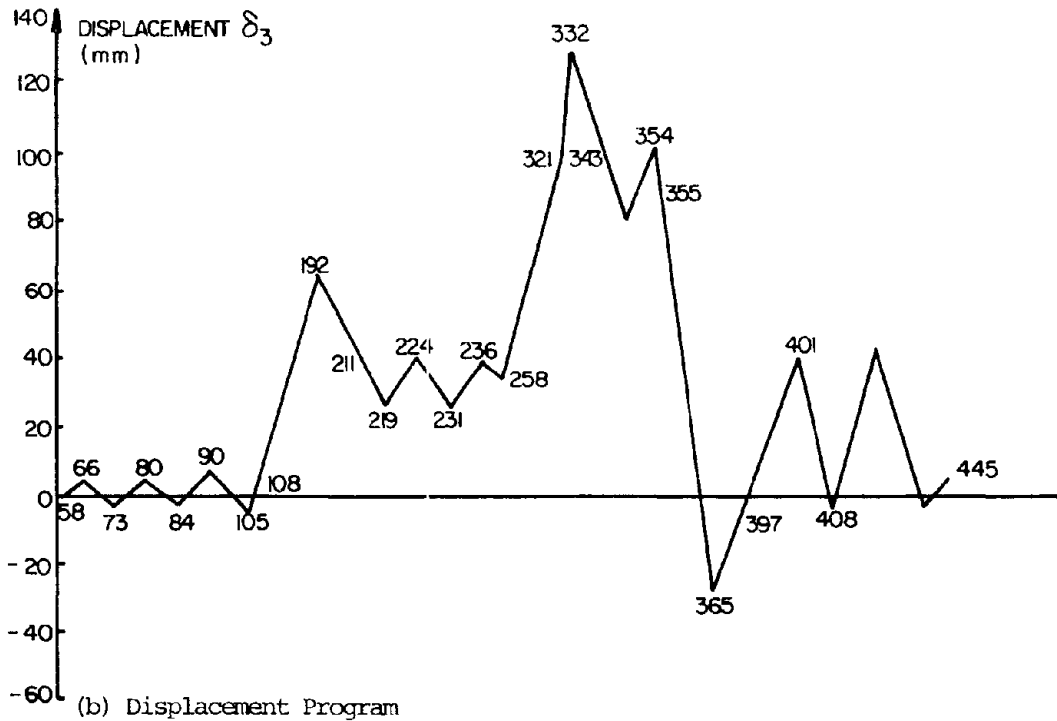


Fig. 4.22 Displacement Components Diagram, Specimen 4



(a) Load Program



(b) Displacement Program

Fig. 4.23 Load Program for Repaired Framed Wall (Monotonic Loading), Specimen 4R

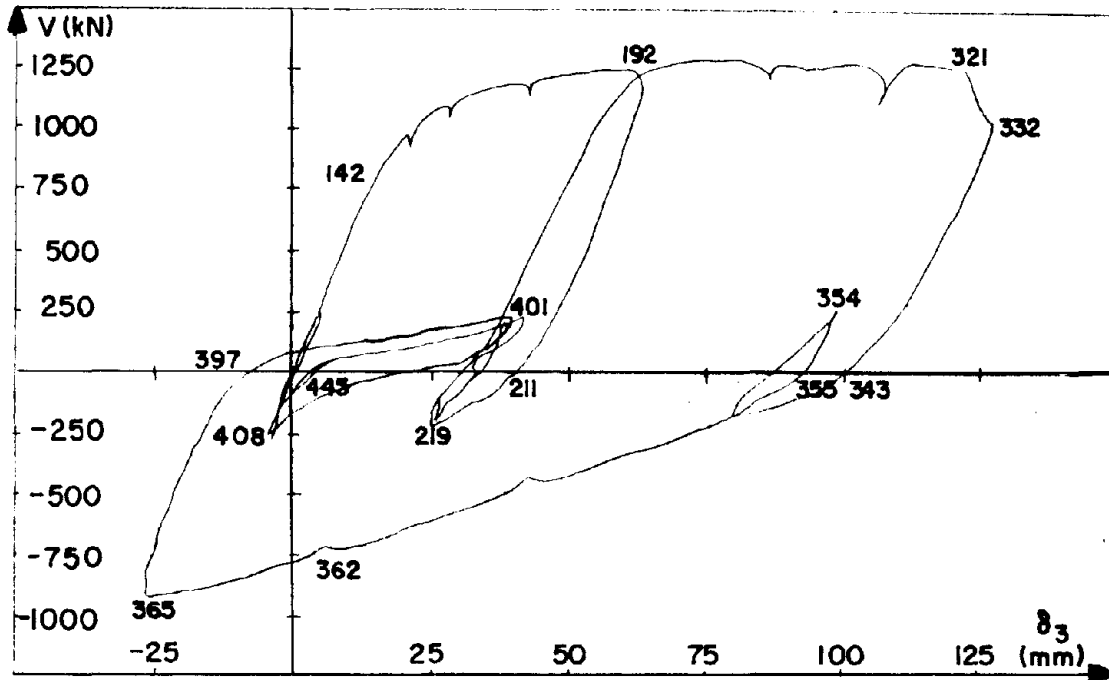


Fig. 4.24 Displacement at Third Floor of Repaired Framed Wall (Monotonic Loading), Specimen 4R

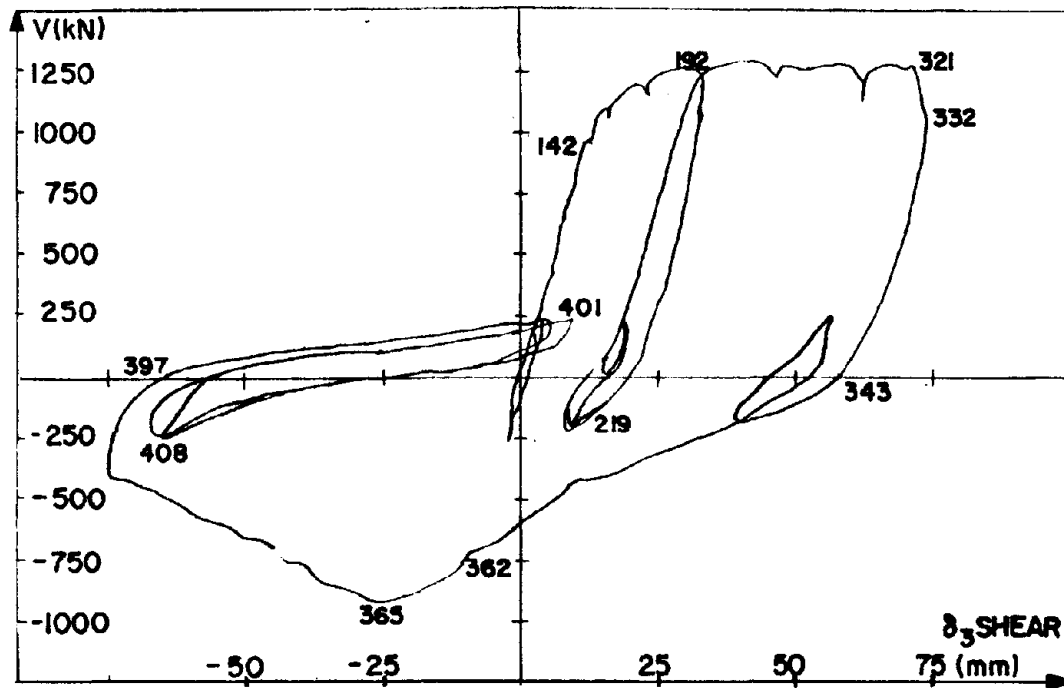


Fig. 4.25 Displacement at Third Floor of Repaired Framed Wall (Monotonic Loading) Due to Shear Deformation, Specimen 4R

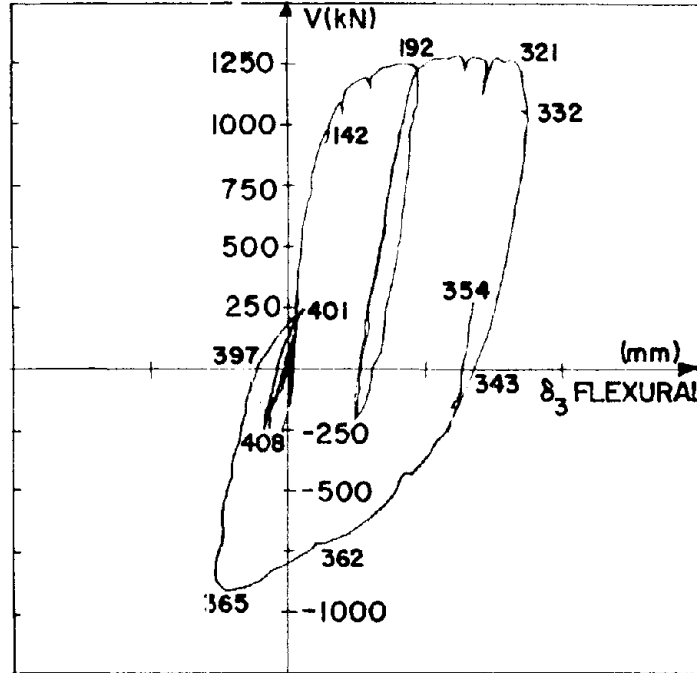


Fig. 4.26 Displacement at Third Floor of Repaired Framed Wall (Monotonic Loading) Due to Flexural Deformation, Specimen 4R

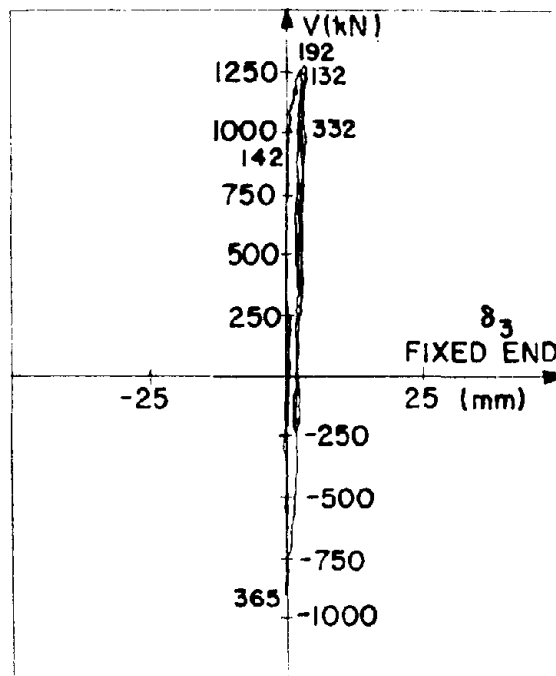


Fig. 4.27 Displacement at Third Floor of Repaired Framed Wall (Monotonic Loading) Due to Fixed-End Deformation, Specimen 4R

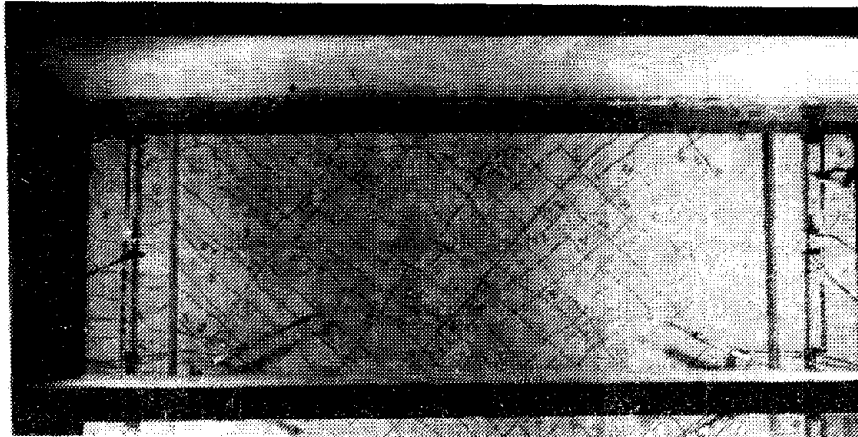


Fig. 4.28a
Third floor
panel

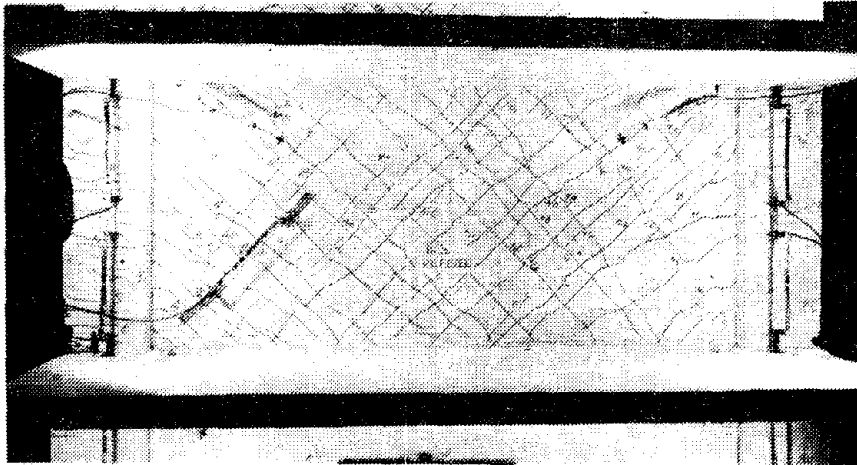


Fig. 4.28b
Second-floor
panel

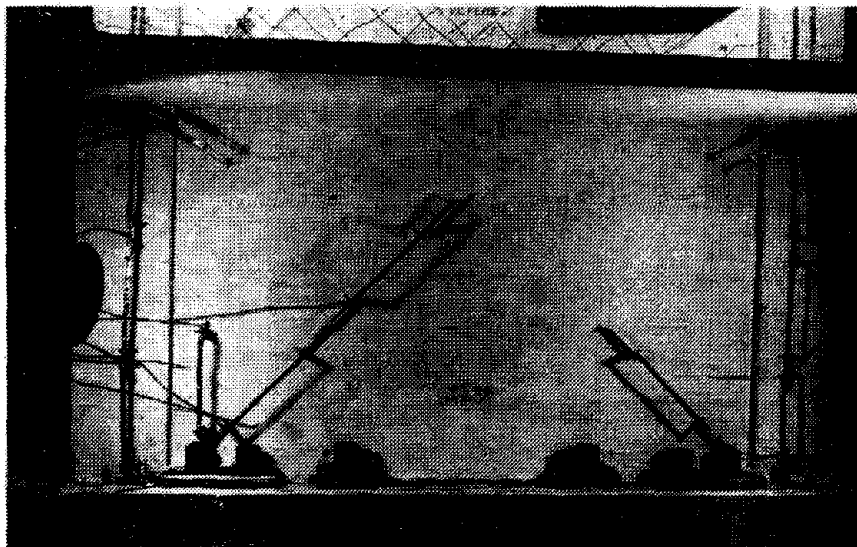


Fig. 4.28c
First-floor
panel

Fig. 4.28 Specimen 4R at Initiation of Test

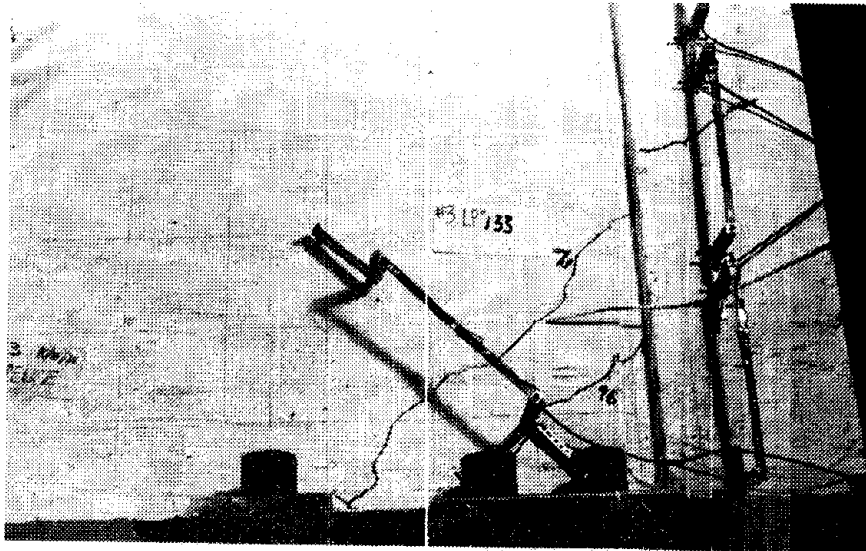


Fig. 4.29a

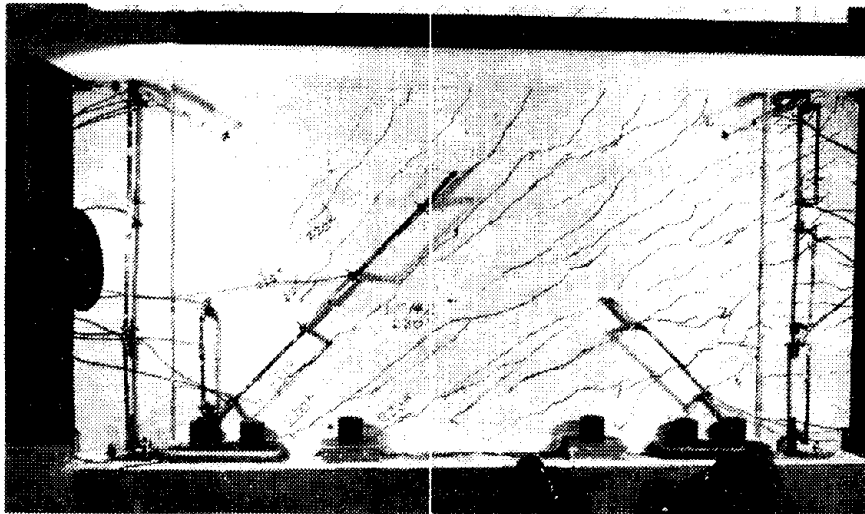


Fig. 4.29b
 $\mu = 1$

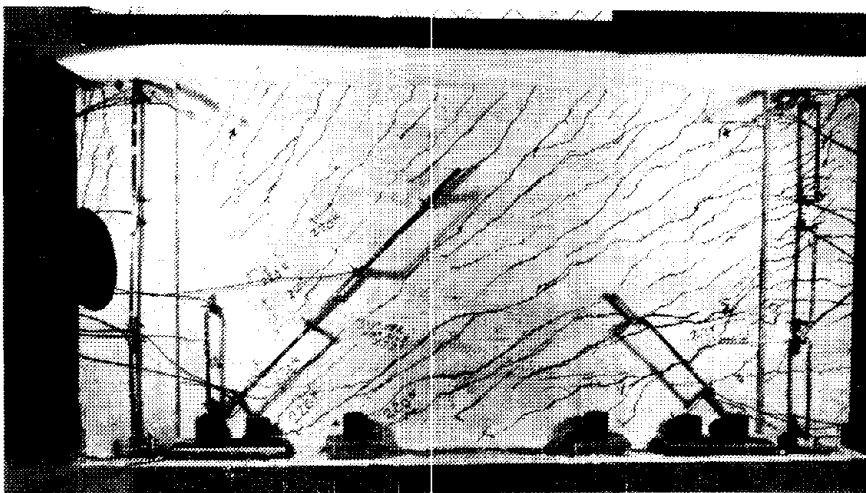


Fig. 4.29c
 $\mu = 3$

4.29 Sequence of Crack Propagation for First-Floor Panel, Specimen 4R



Fig. 4.30 Rupture of Tension Reinforcement at Top of First-Floor Columns, Specimen 4R



Fig. 4.31a Third-story panel, crushed

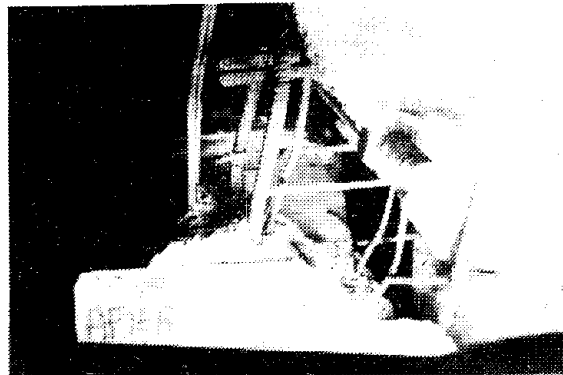


Fig. 4.31b Cracks between columns and slab at third-floor level

Fig. 4.31 Specimen 4R After Failure

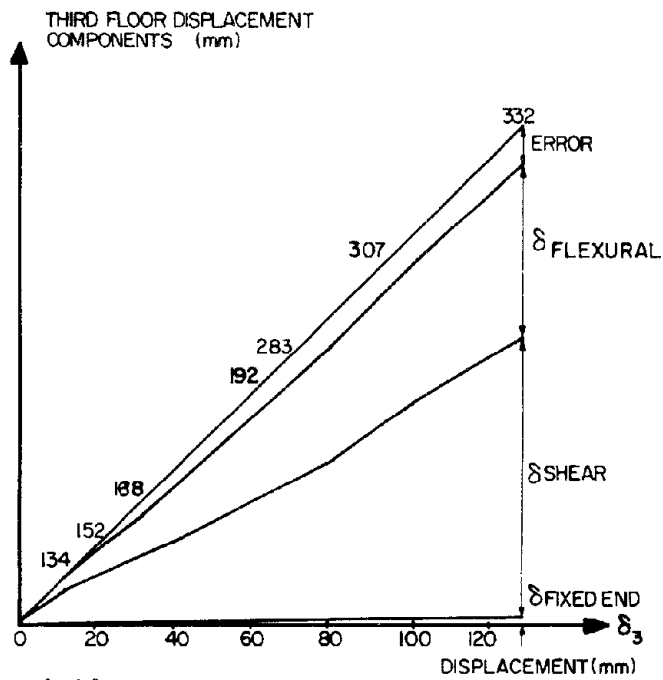


Fig. 4.32 Displacement Components Diagram at Third-Floor, Specimen 4R

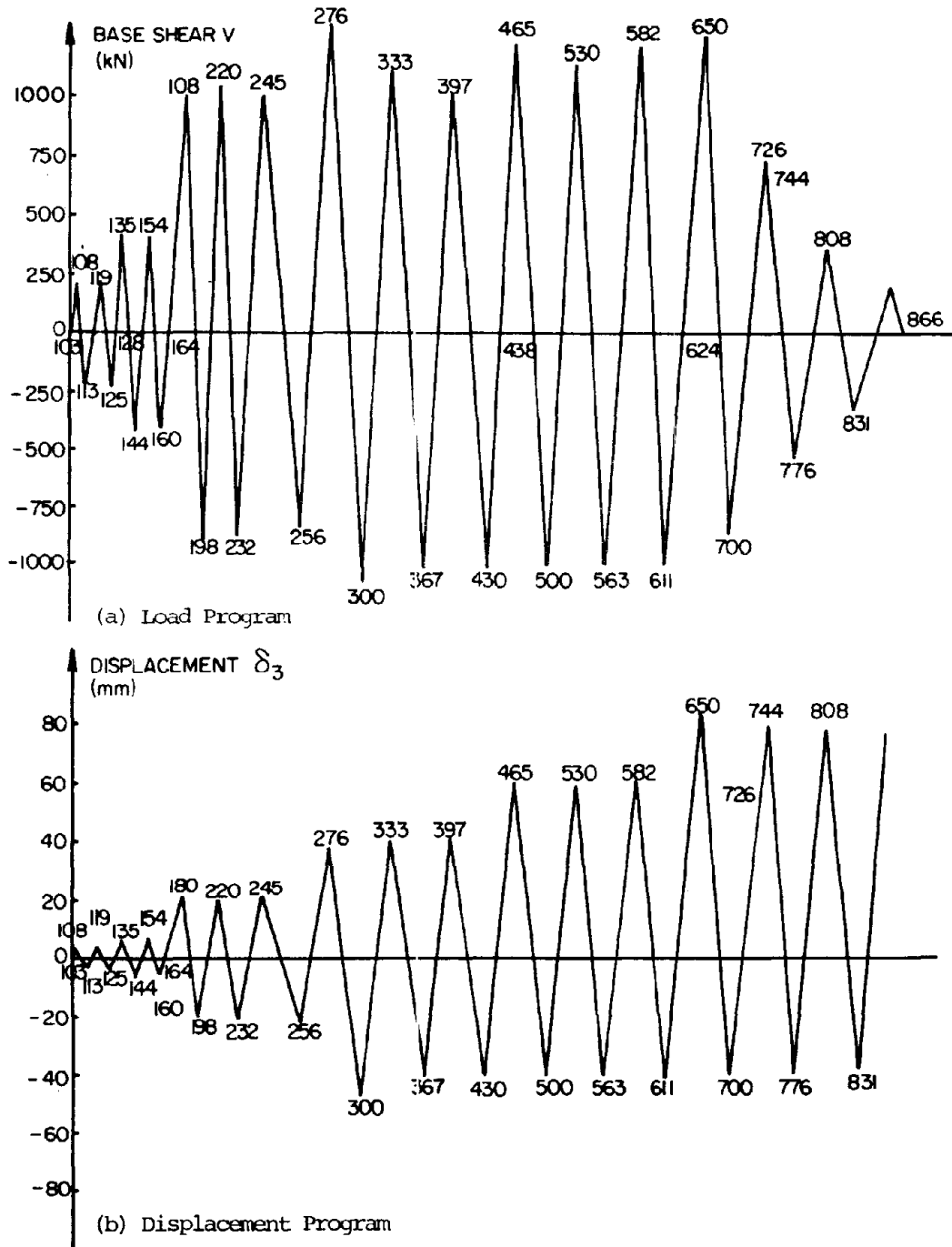


Fig. 4.33 Load Diagram for Repaired Framed Wall (Cyclic Loading), Specimen 3R

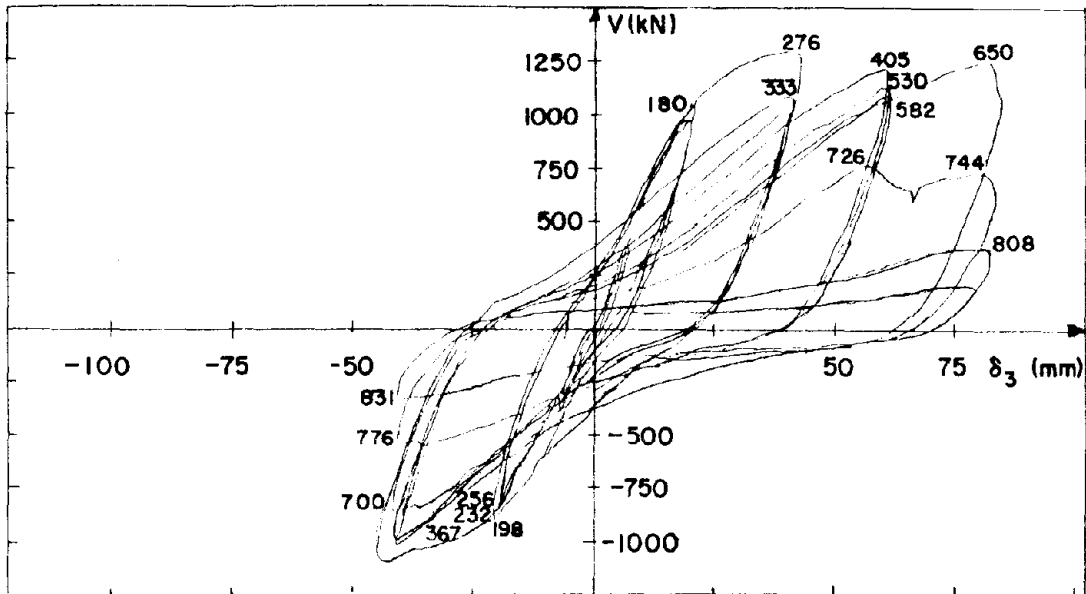


Fig. 4.34 Displacement at Third Floor of Repaired Framed Wall (Cyclic Loading), Specimen 3R

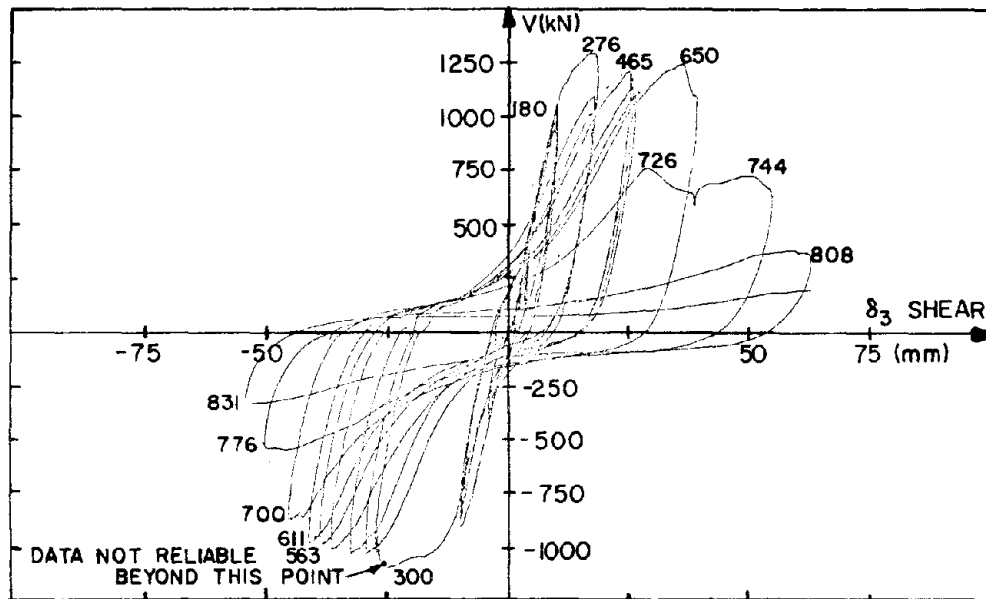


Fig. 4.35 Displacement at Third Floor of Repaired Framed Wall (Cyclic Loading) Due to Shear Deformation, Specimen 3R

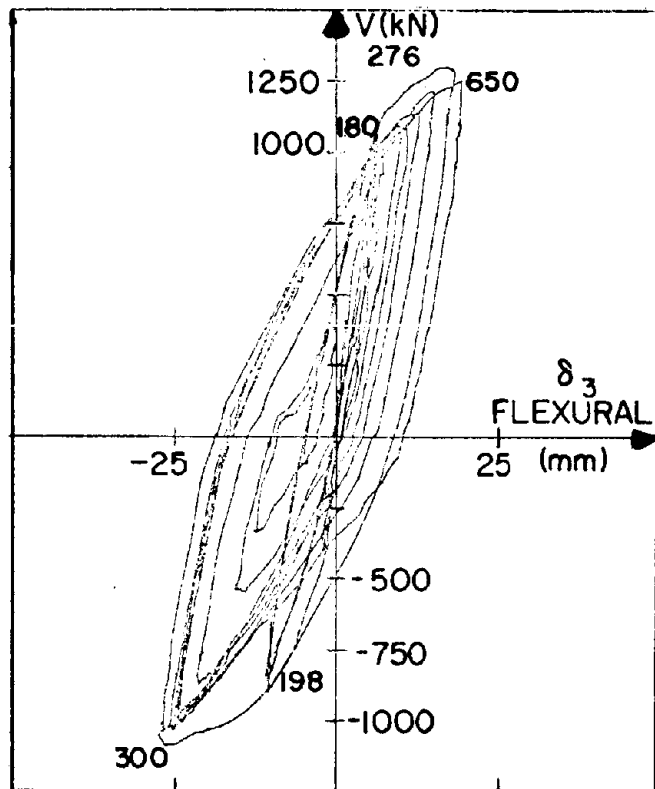


Fig. 4.36 Displacement at Third Floor of Repaired Framed Wall (Cyclic Loading) Due to Flexural Deformation, Specimen 3R

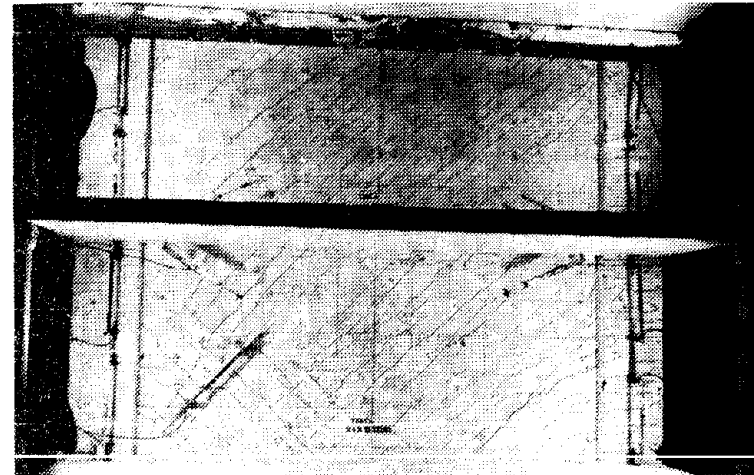


Fig. 4.37a Upper panels

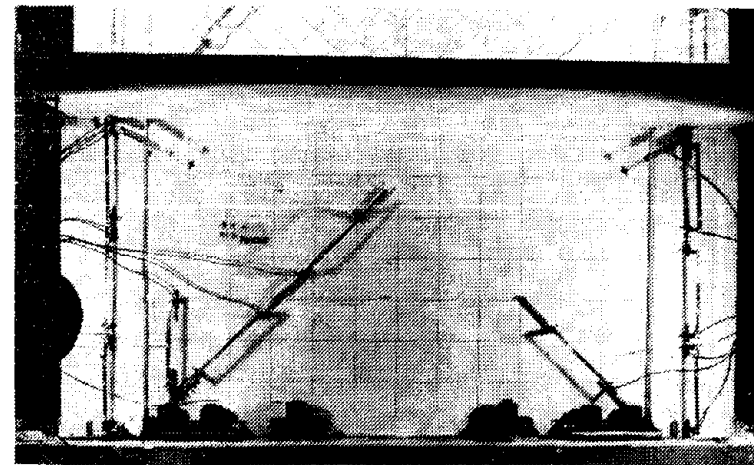


Fig. 4.37b Repaired panel

Fig. 4.37 Specimen 3R at Initiation of Test

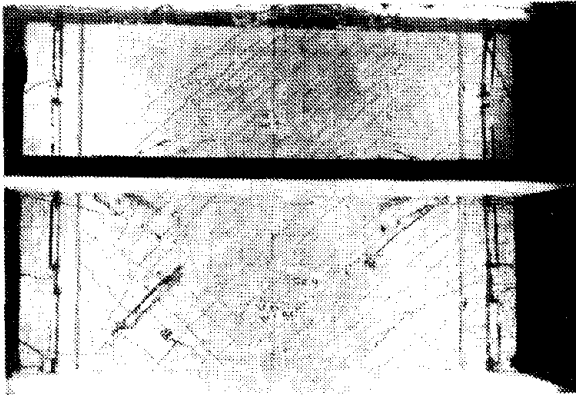


Fig. 4.38a Upper panels

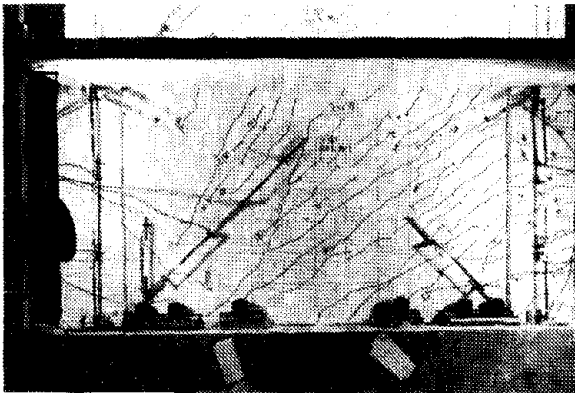


Fig. 4.38b Lower panel

Fig. 4.38 Cracking at $\mu = 1$, Specimen 3R

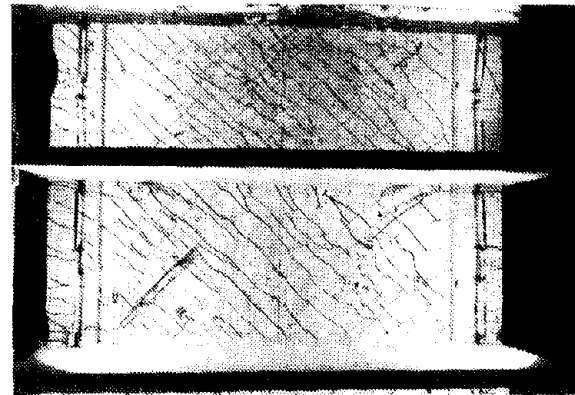


Fig. 4.39a Upper panels

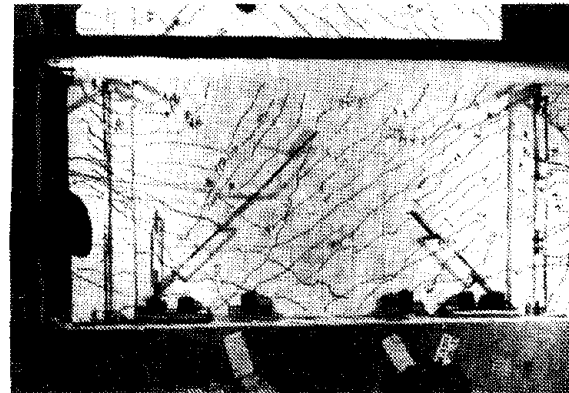


Fig. 4.39b Lower panel

Fig. 4.39 Cracking at $\mu = 1$, Specimen 3R

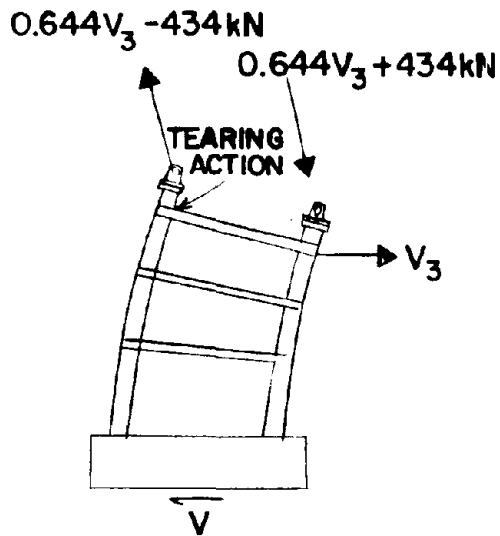


Fig. 4.40a Tearing action at column-slab connection



Fig. 4.40b Top view

Fig. 4.40 Crack Between Third Floor Slab and Top of North Column, Specimen 3R

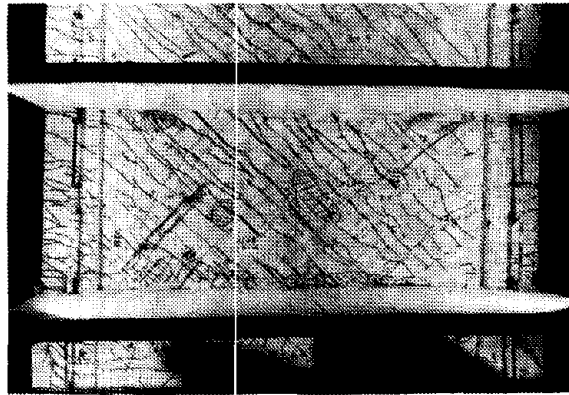


Fig. 4.41a LP 611 Initiation of concrete crushing at second story

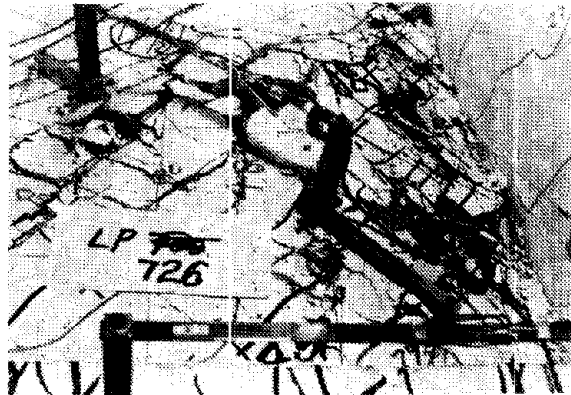


Fig. 4.41b LP 726 crushing at second story

Fig. 4.41 Cracking of Second Story Panel, Specimen 3R

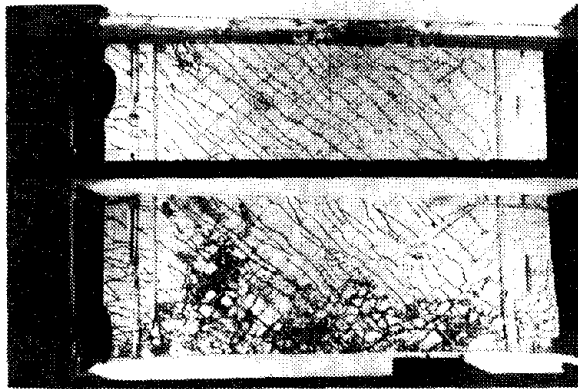


Fig. 4.42a Second-story failure



Fig. 4.43a Top view

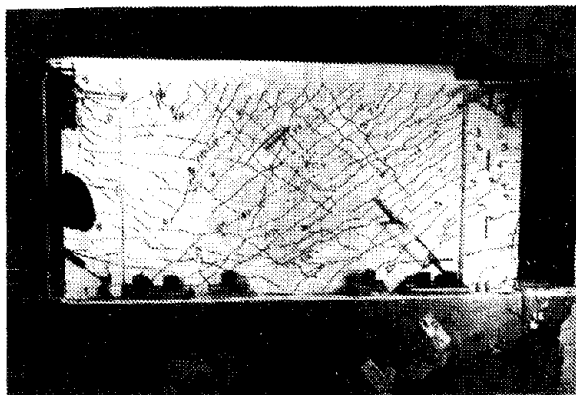


Fig. 4.42 View of first story at failure

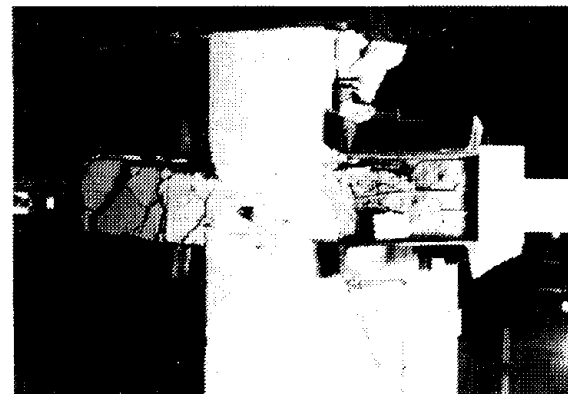


Fig. 4.43b Side view

Fig. 4.42 Failure of Specimen 3R

Fig. 4.43 Views of Failure at North Column Slab Connection

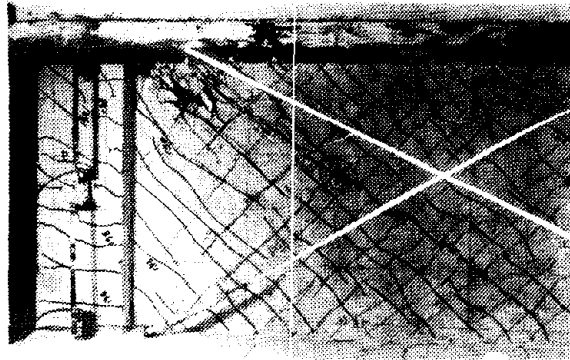


Fig. 4.43c
Wire for measurement
of shear deformation

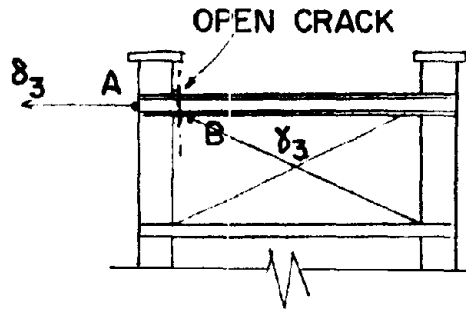


Fig. 4.43d
Instrumentation

Fig. 4.43 Views of Failure at North Column-Slab Connection

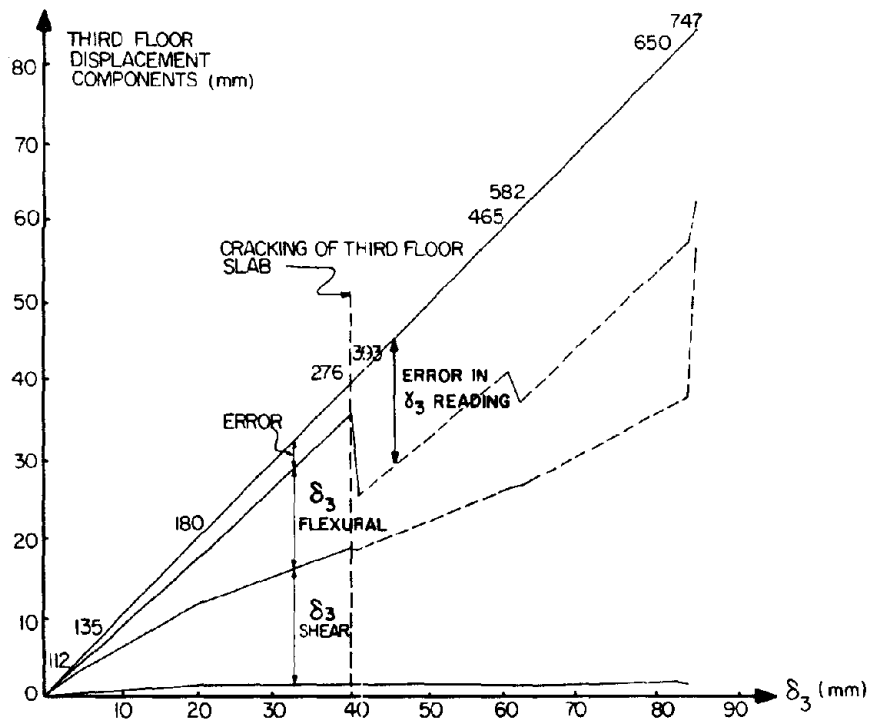


Fig. 4.44 Displacement Components Diagram, Specimen 3R

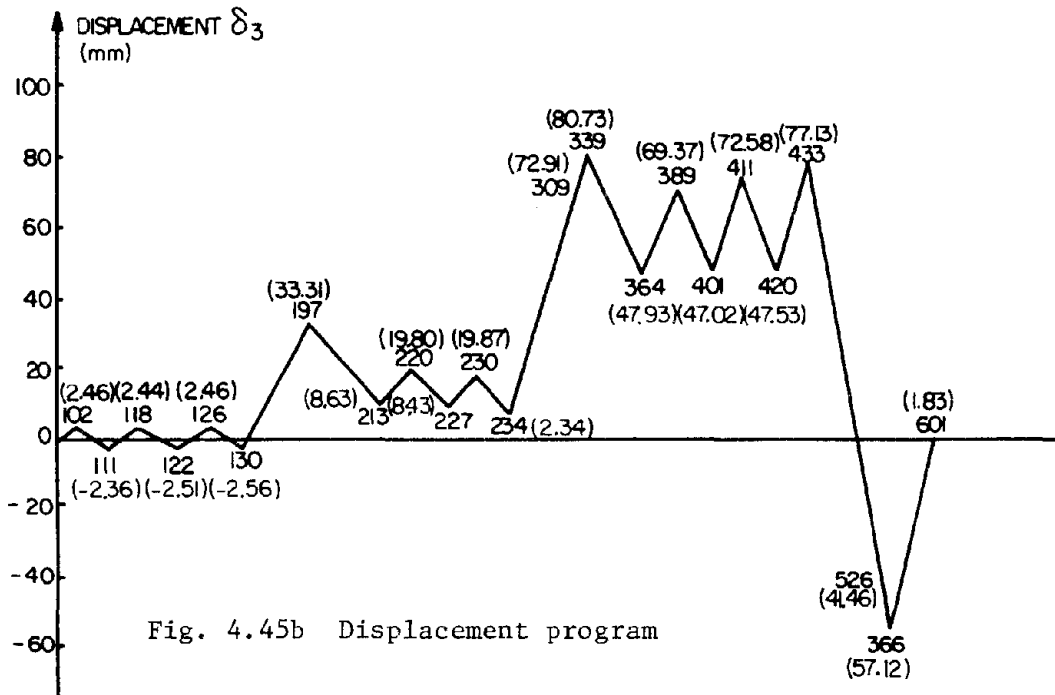
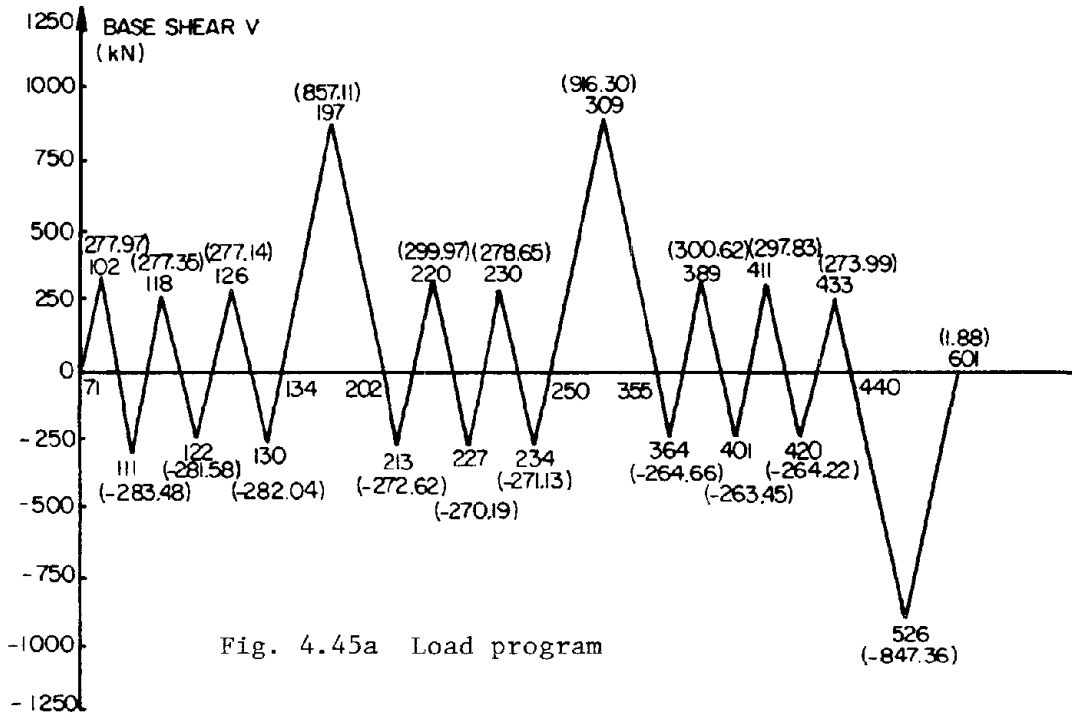


Fig. 4.45 Load Program for Rectangular Wall (Monotonic Loading), Specimen 5

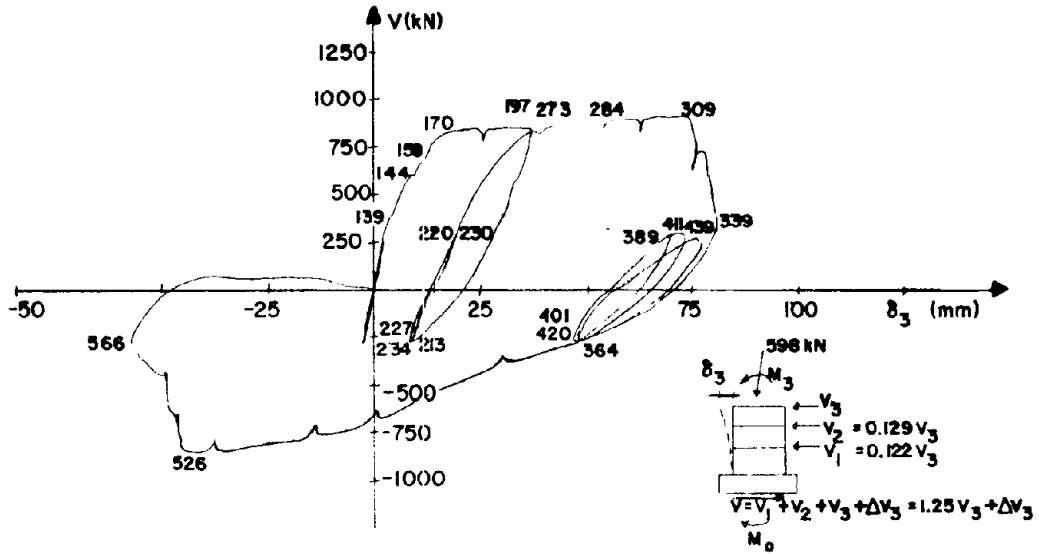


Fig. 4.46 Displacement at Third Floor of Rectangular Wall (Monotonic Loading), Specimen 5

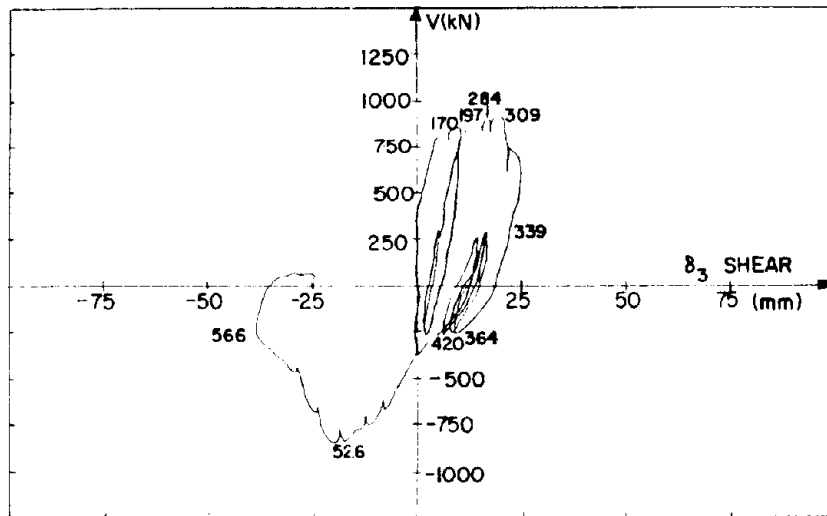


Fig. 4.47 Displacement at Third Floor of Rectangular Wall (Monotonic Loading) Due to Shear Deformation, Specimen 5

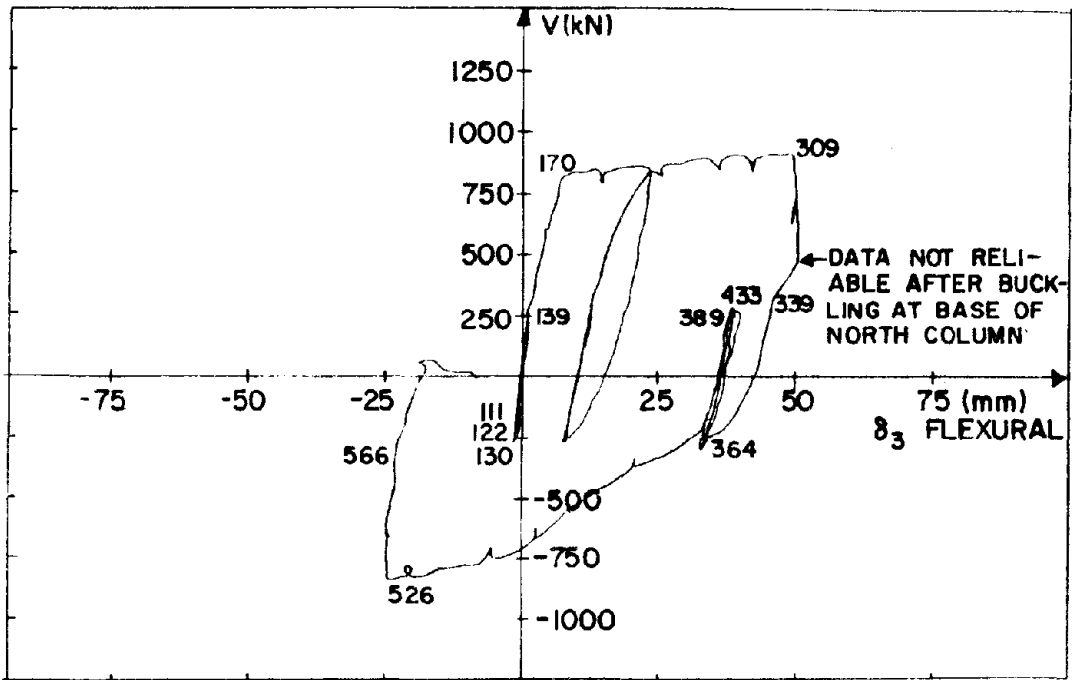


Fig. 4.48 Displacement at Third Floor of Rectangular Wall (Monotonic Loading) Due to Flexural Deformation, Specimen 5

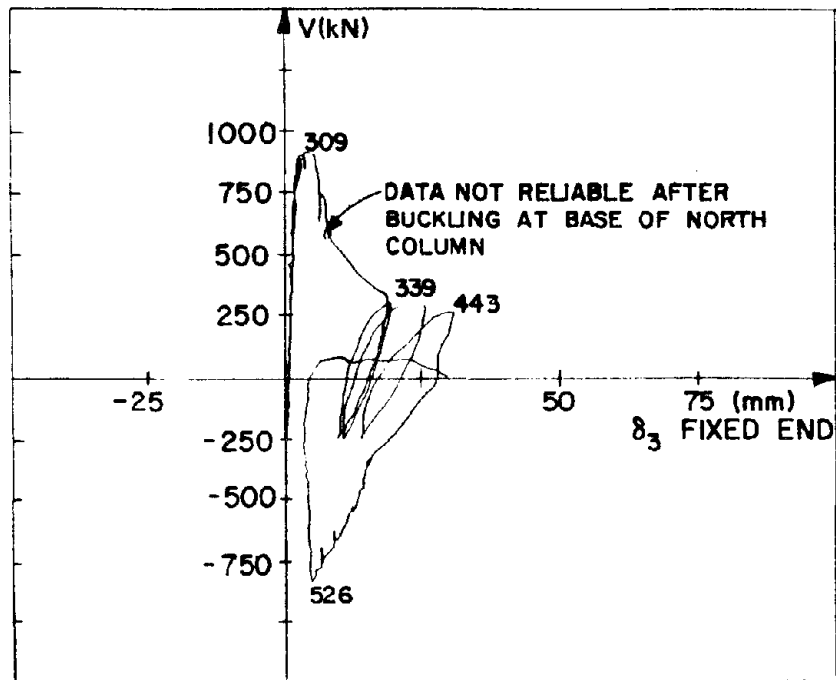


Fig. 4.49 Displacement at Third Floor of Rectangular Wall (Monotonic Loading) Due to Fixed-End Deformation, Specimen 5



Fig. 4.450a Tension side

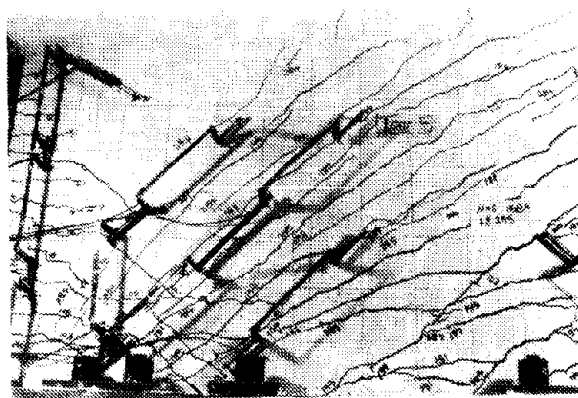


Fig. 4.50b Compression side

Fig. 4.50 Sequence of Crack Propagation, Specimen 5

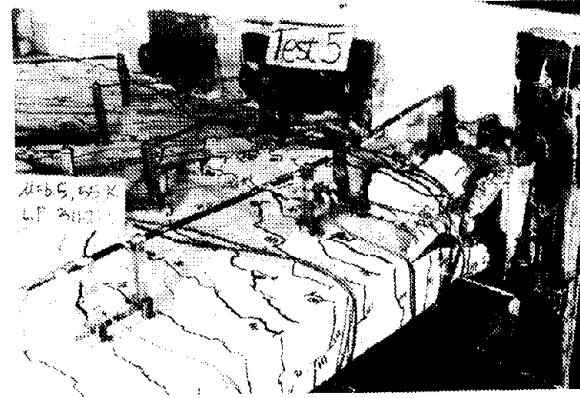


Fig. 4.51 Buckling of Longitudinal Reinforcement at Base of North Column, Specimen 5

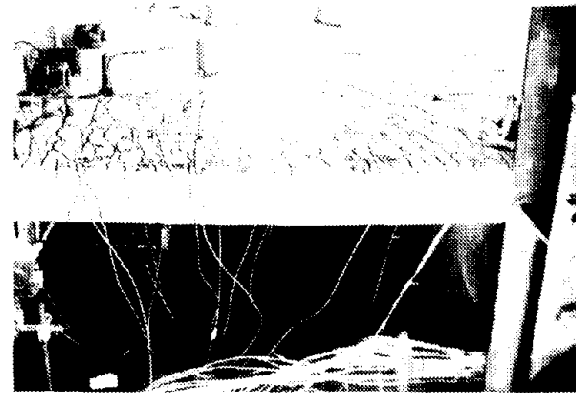


Fig. 4.52 South Column Initiation of Buckling, Specimen 5



Fig. 4.53a At LP 521

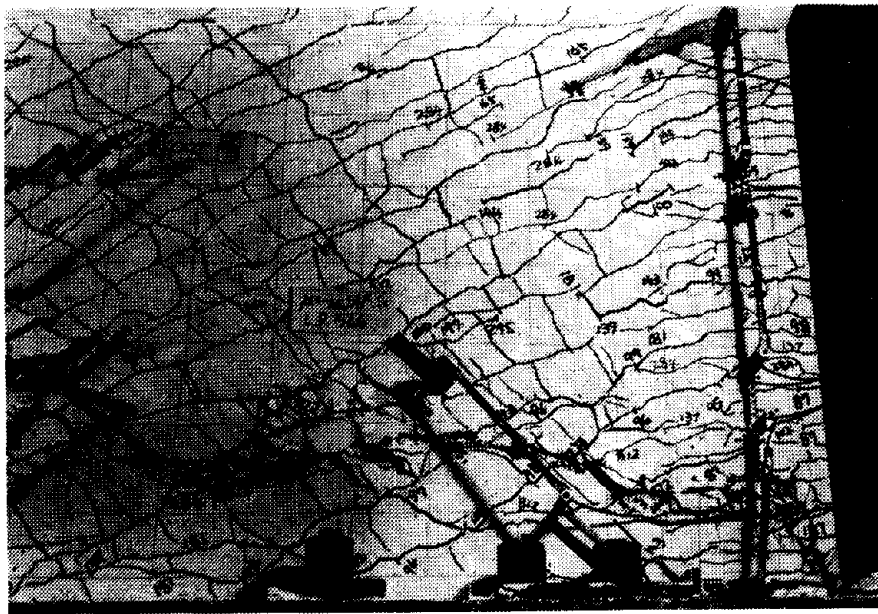


Fig. 4.53b At LP 566

Fig. 4.53 Flexural Shear Crack, Specimen 5

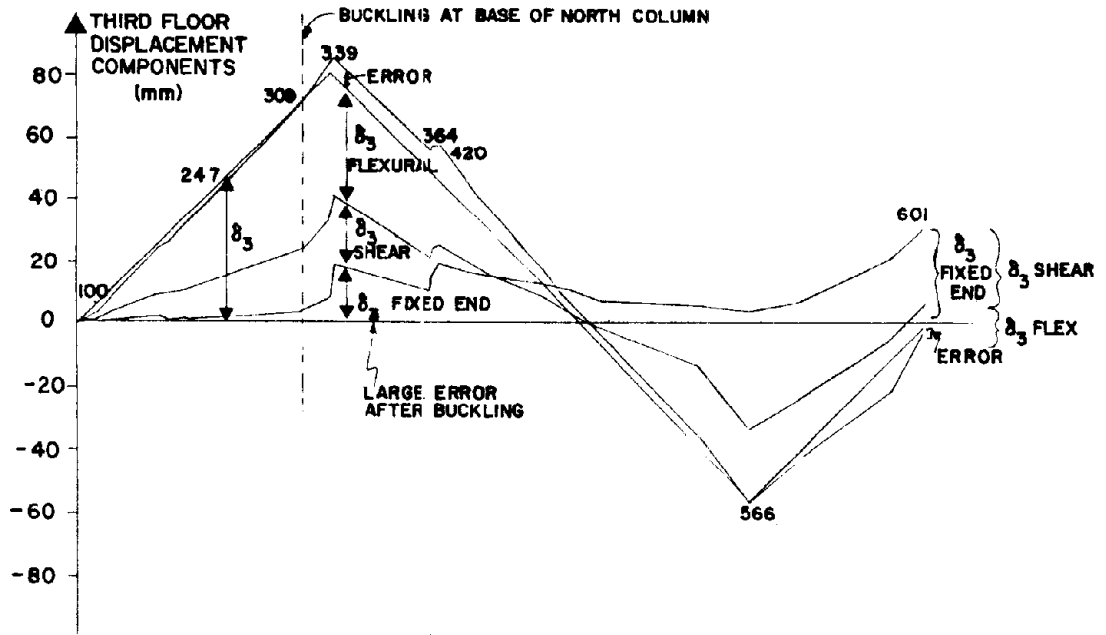


Fig. 4.54a At third-floor level

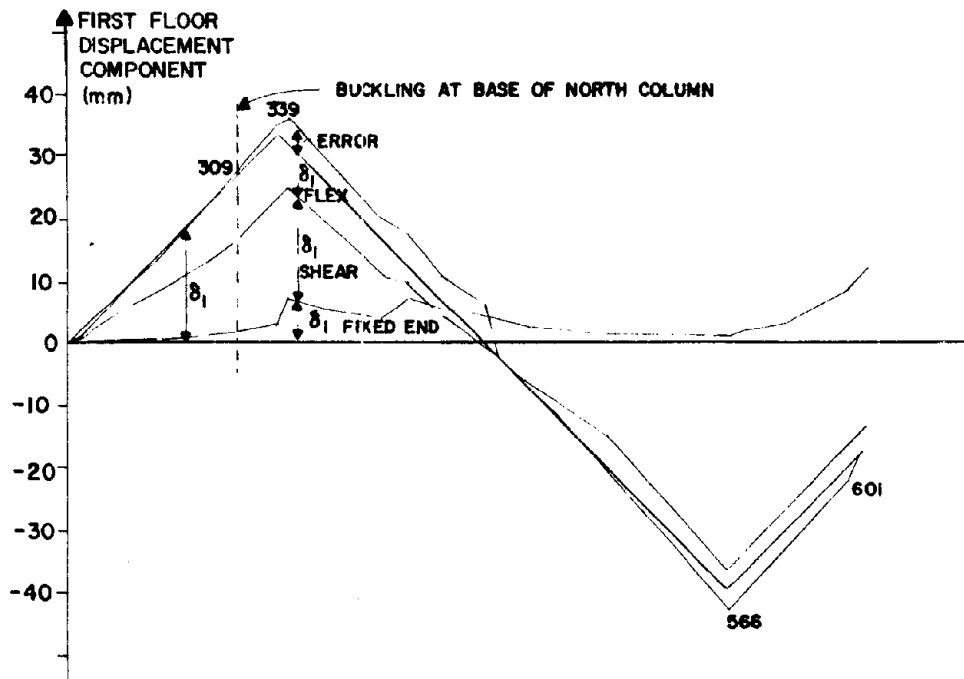


Fig. 4.54b At first-floor level

Fig. 4.54 Displacement Components Diagram, Specimen 5

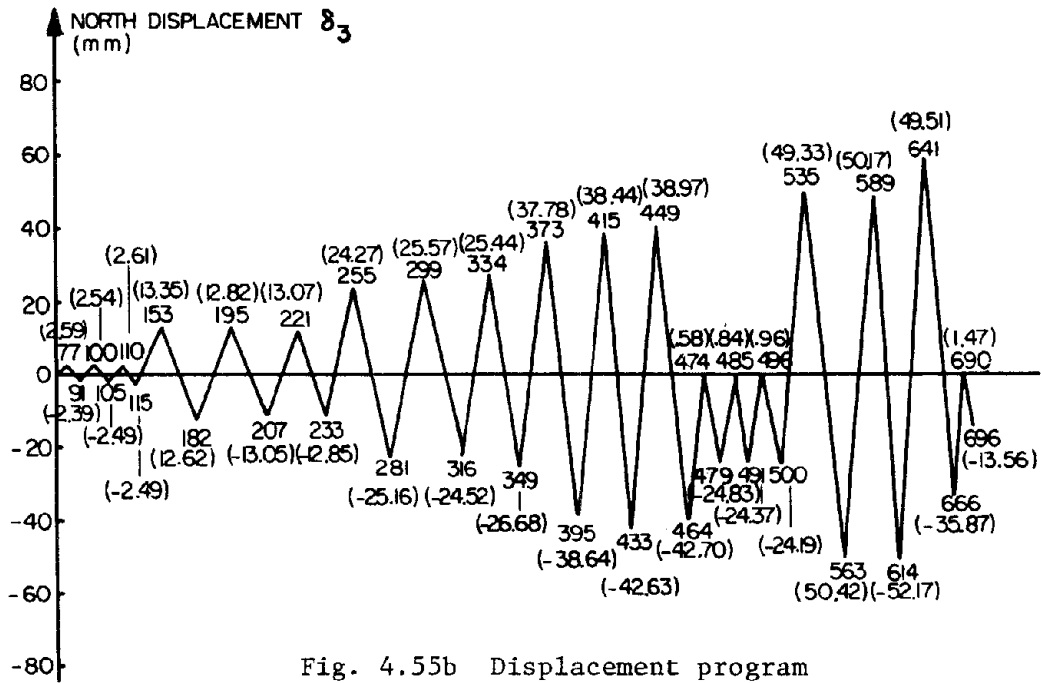
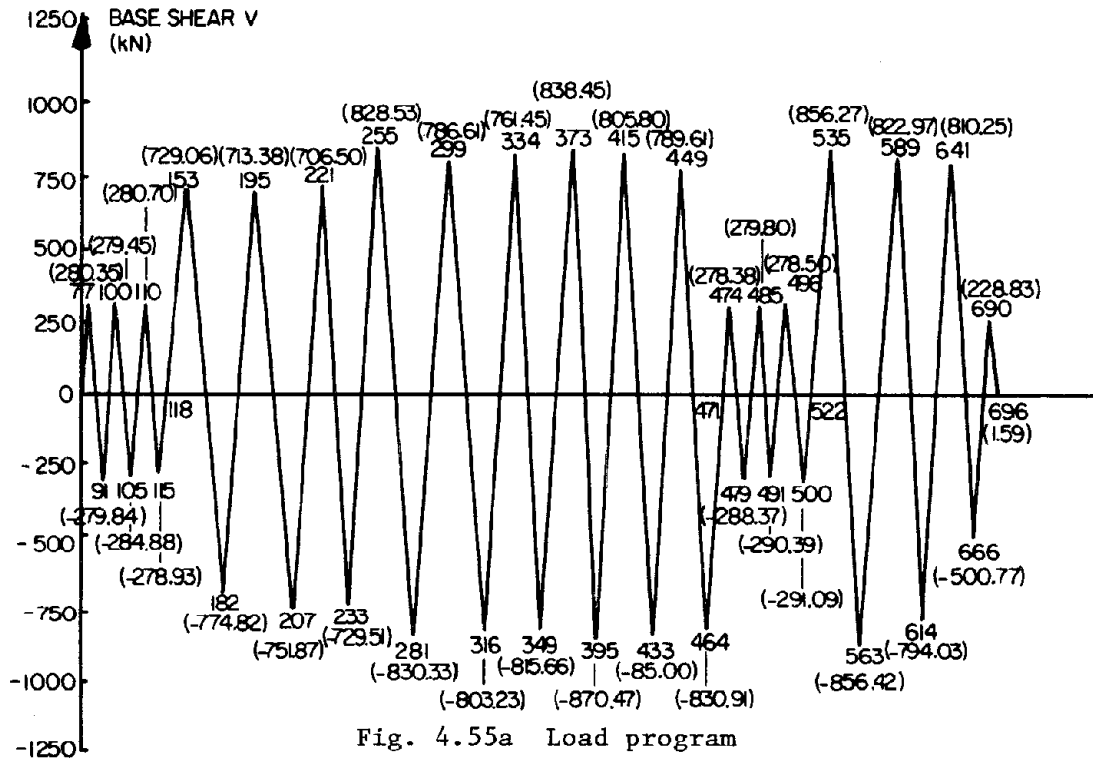


Fig. 4.55 Load Program for Rectangular Wall (Cyclic Loading), Specimen 6

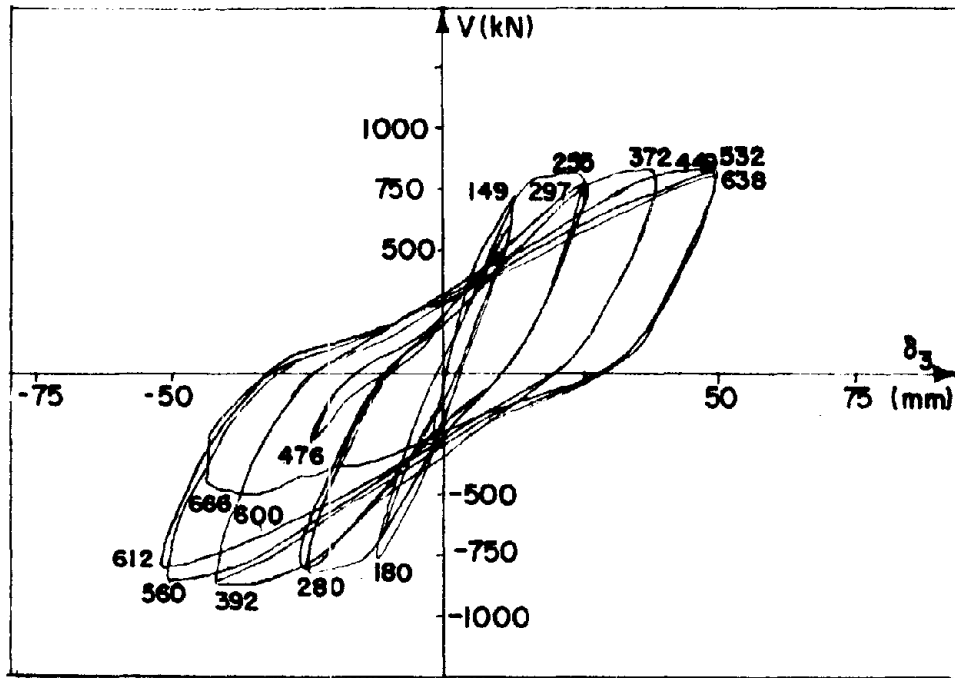


Fig. 4.56 Displacement at Third Floor of Rectangular Wall (Cyclic Loading), Specimen 6

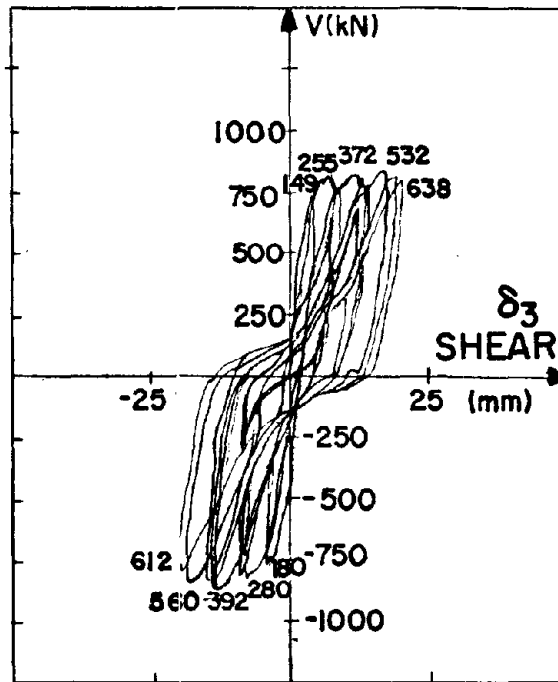


Fig. 4.57 Displacement at Third Floor of Rectangular Wall (Cyclic Loading) Due to Shear Deformation, Specimen 6

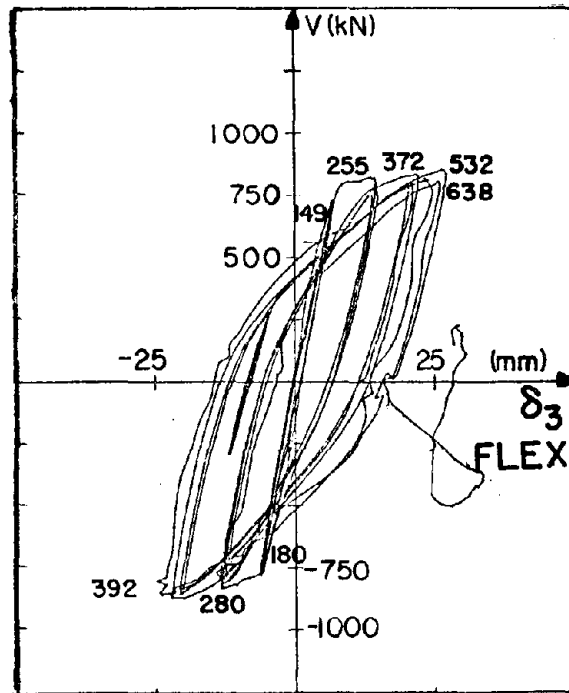


Fig. 4.58 Displacement at Third Floor of Rectangular Wall (Cyclic Loading) Due to Flexural Deformation, Specimen 6

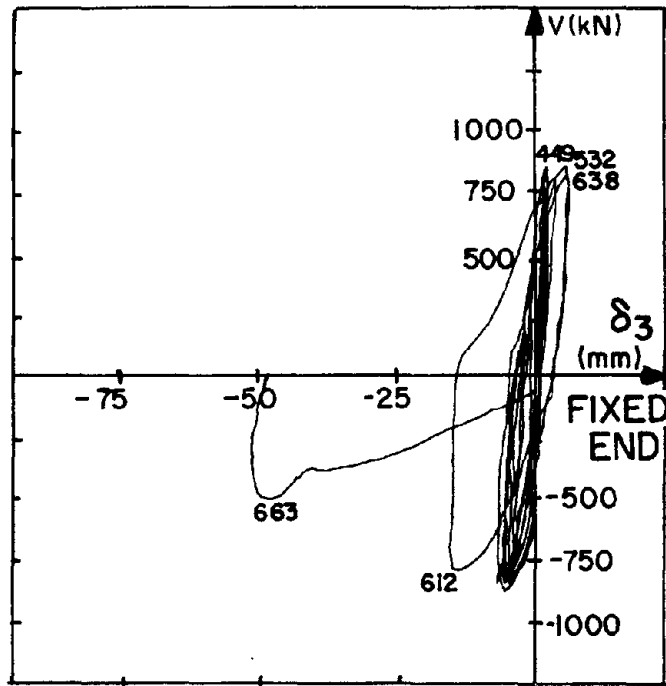


Fig. 4.59 Displacement at Third Floor of Rectangular Wall (Cyclic Loading) Due to Fixed-End Deformation, Specimen 6

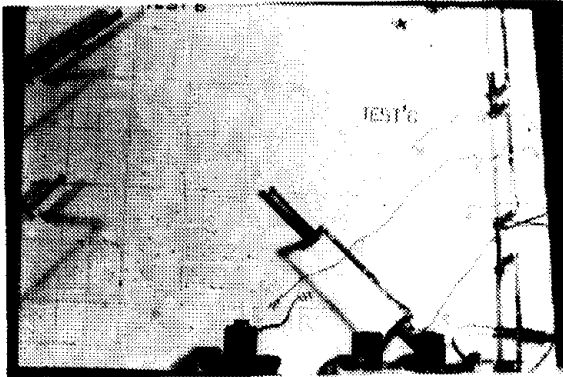


Fig. 4.60 Initial Cracking of Rectangular Wall (Cyclic Loading), Specimen 6



Fig. 4.62a

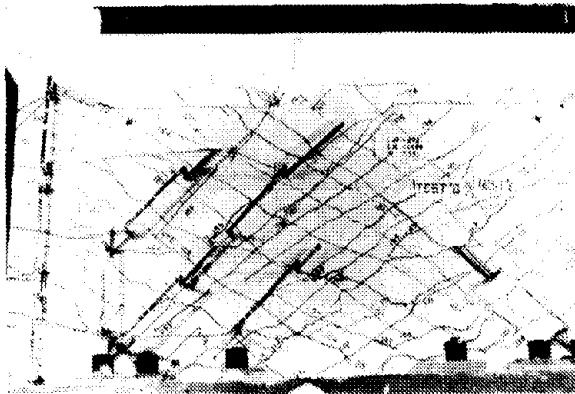


Fig. 4.61 Crack Pattern at $\mu = 3$ for Rectangular Wall (Cyclic Loading), Specimen 6

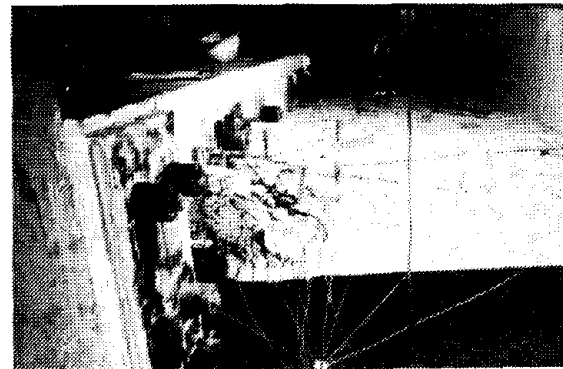


Fig. 4.62b

Fig. 4.62 Buckling at Base of North Column, Specimen 6

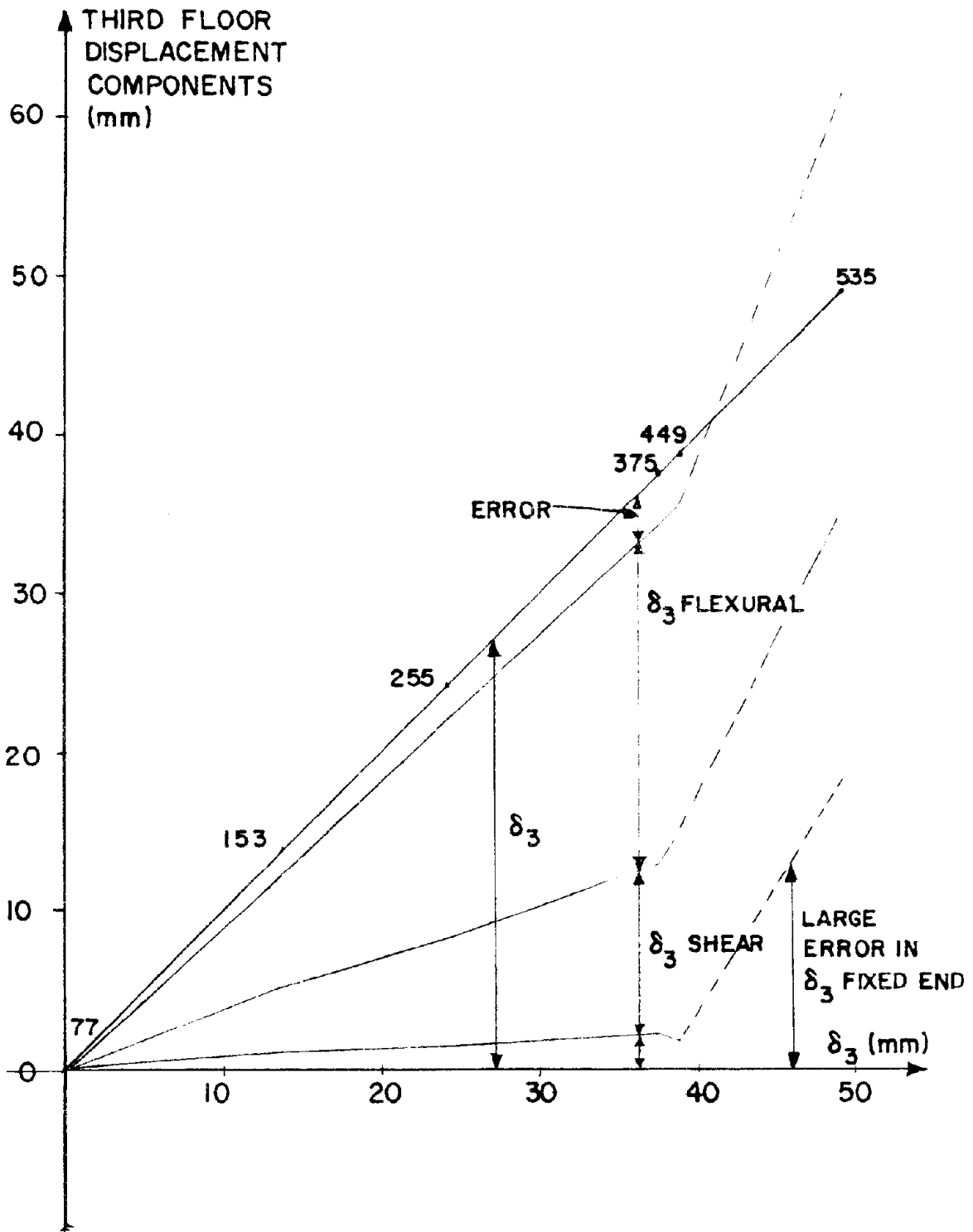


Fig. 4.63 Displacement Components Diagram, Specimen 6

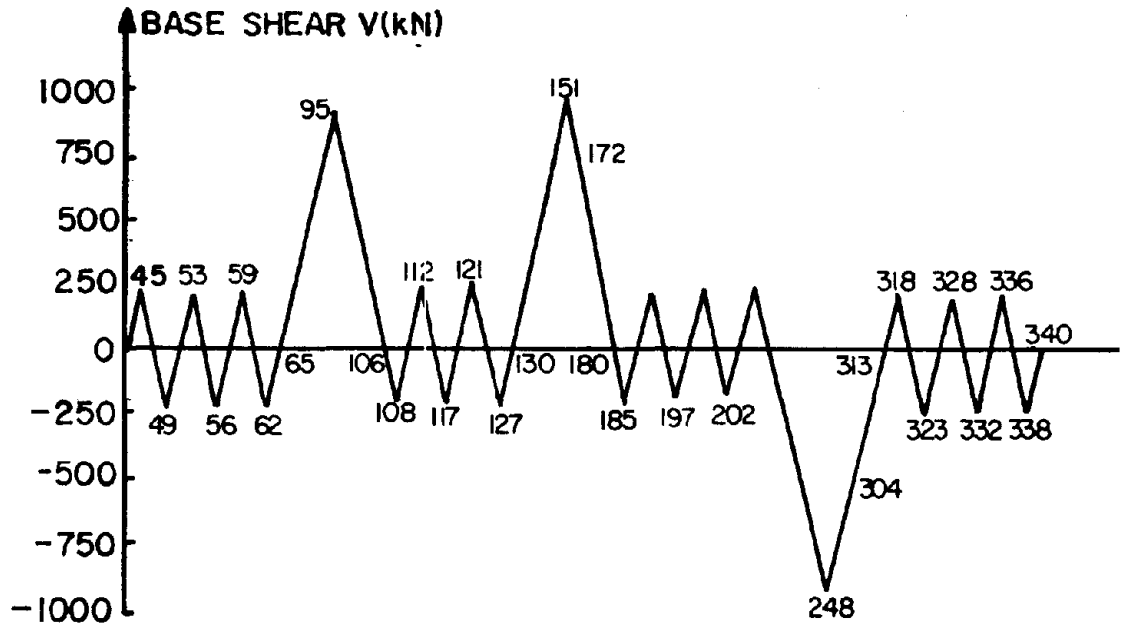


Fig. 4.64a Load program

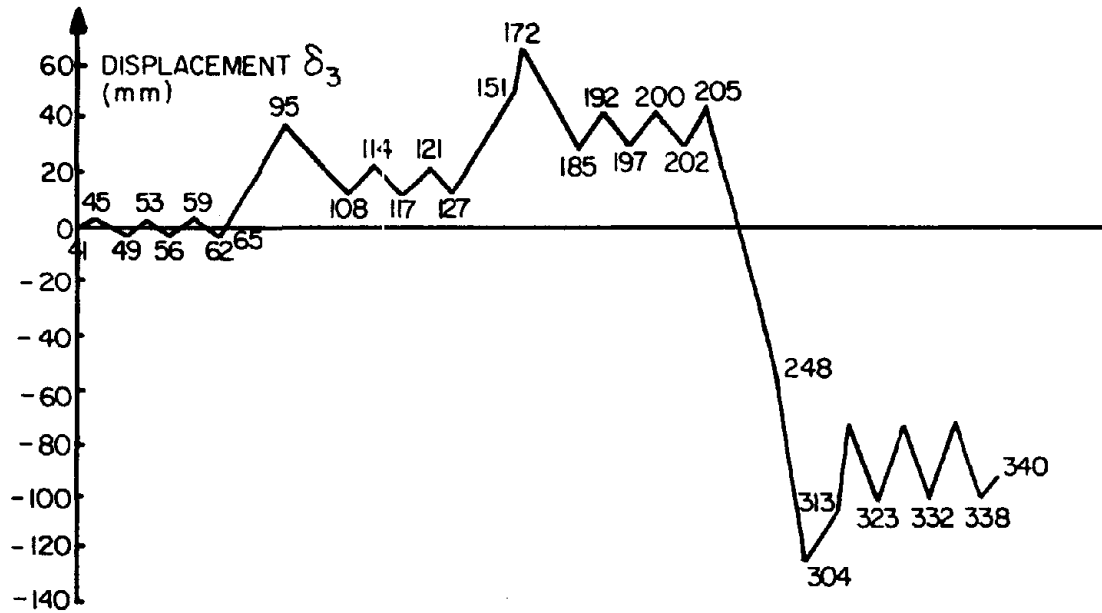


Fig. 4.64b Displacement program

Fig. 4.64 Load Program for Repaired Rectangular Wall (Monotonic Loading), Specimen 6R

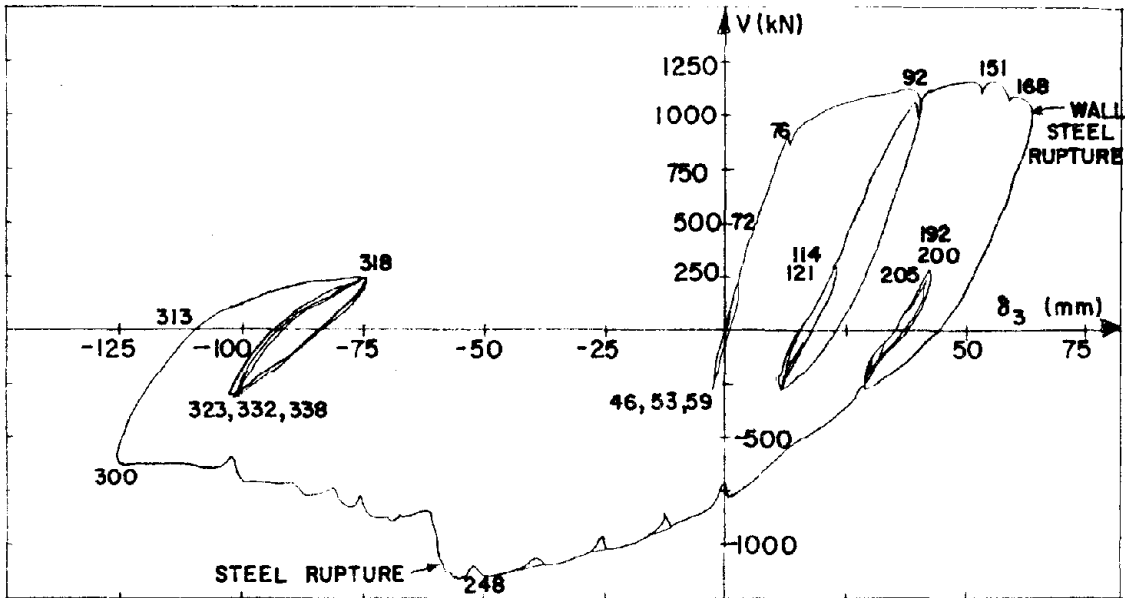


Fig. 4.65 Displacement at Third Floor of Repaired Rectangular Wall (Monotonic Loading), Specimen 6R

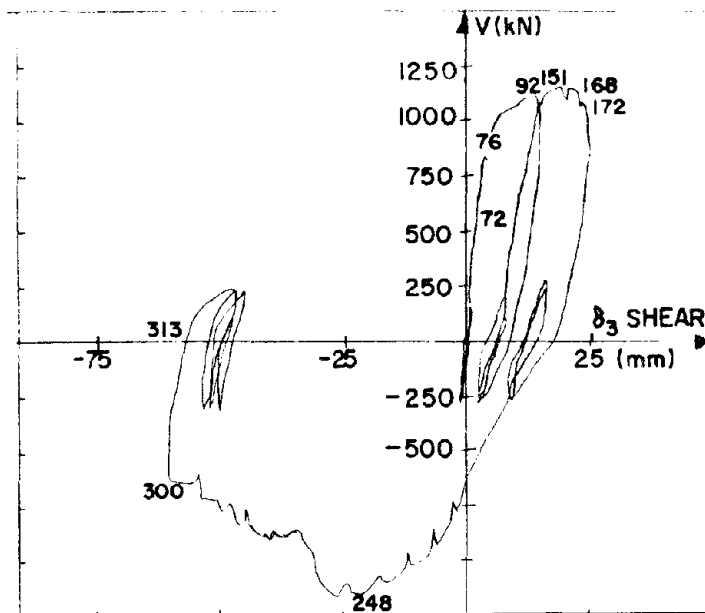


Fig. 4.66 Displacement at Third Floor of Repaired Rectangular Wall (Monotonic Loading) Due to Shear Deformation, Specimen 6R

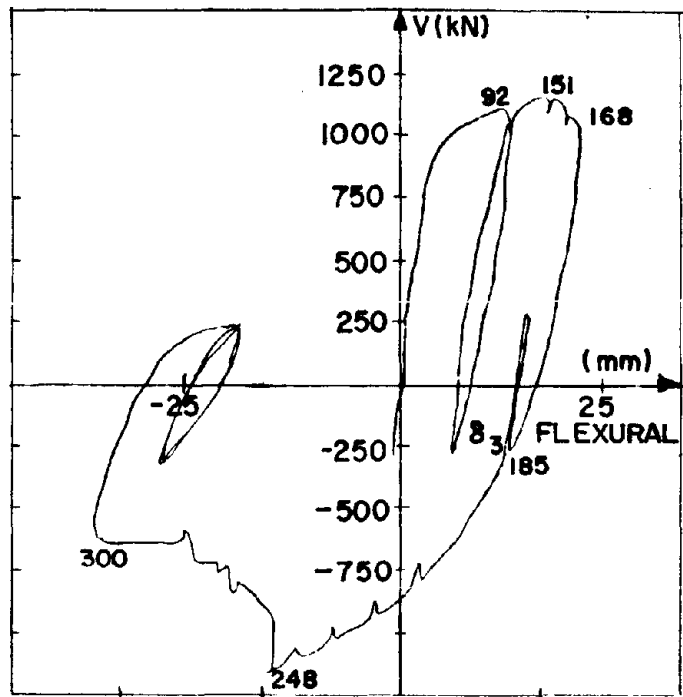


Fig. 4.67 Displacement at Third Floor of Repaired Rectangular Wall (Monotonic Loading) Due to Flexural Deformation, Specimen 6

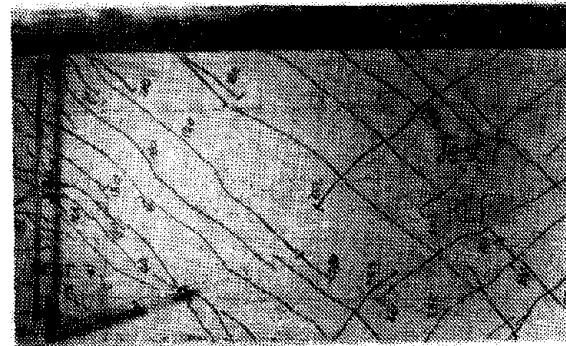


Fig. 4.68a
Third story

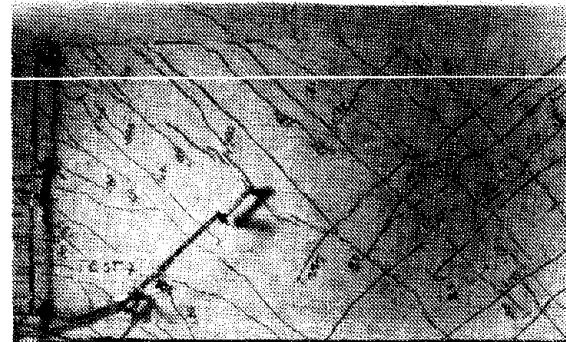


Fig. 4.68b
Second story

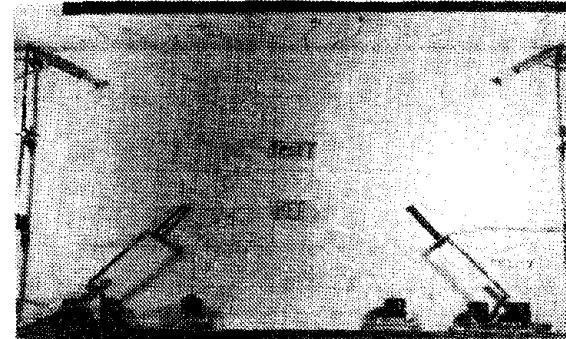


Fig. 4.68c
Third story

Fig. 4.68 Specimen 6R at Initiation of Test



Fig. 4.69a
 $\mu = s$

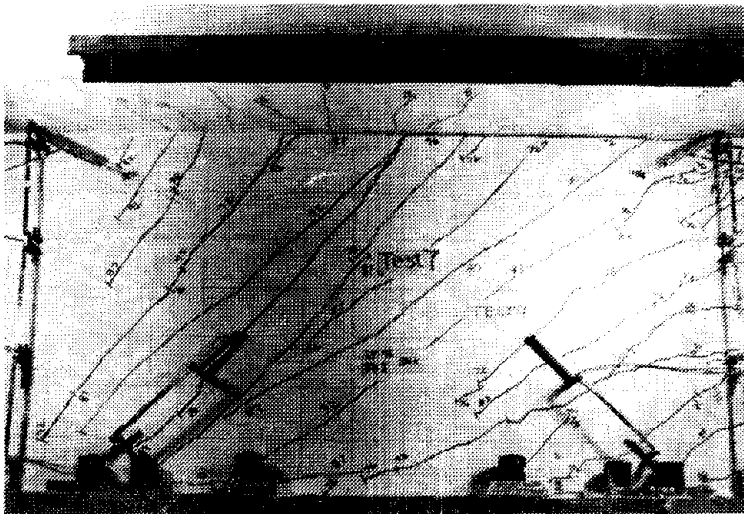


Fig. 4.69b
 $\mu = 3$

Fig. 4.69 Crack Sequence for First-Floor Panel, Specimen 6R

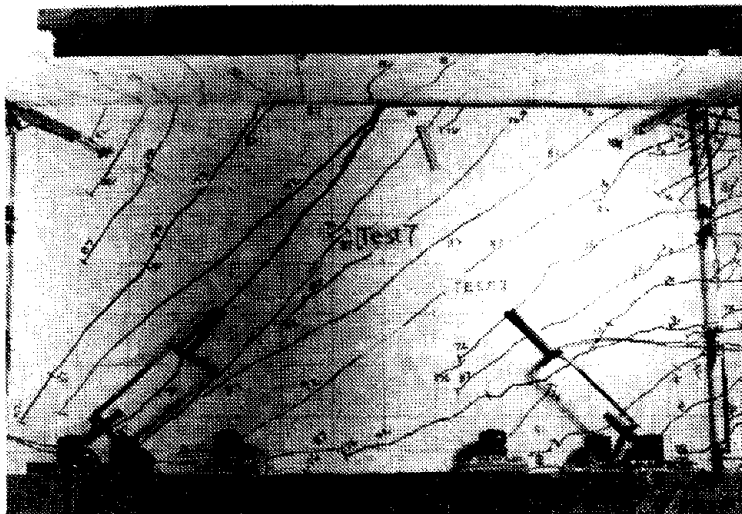


Fig. 4.70 Main Crack in First Floor Panel, Specimen 6R

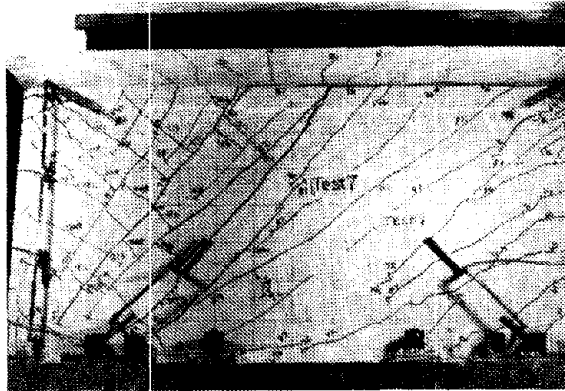


Fig. 4.71a
LP 213

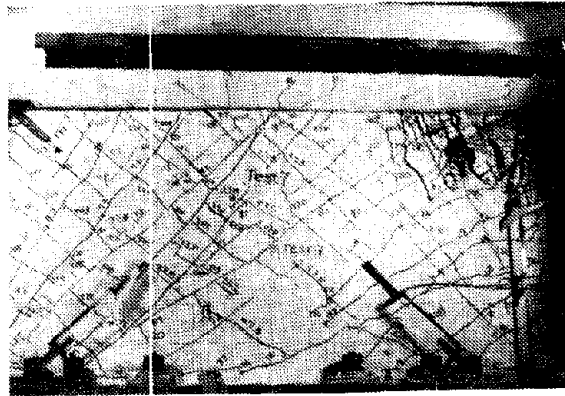


Fig. 4.71b
LP 300

Fig. 4.71 Crack Sequence for First Floor Panel When Loaded to the North, Specimen 6R

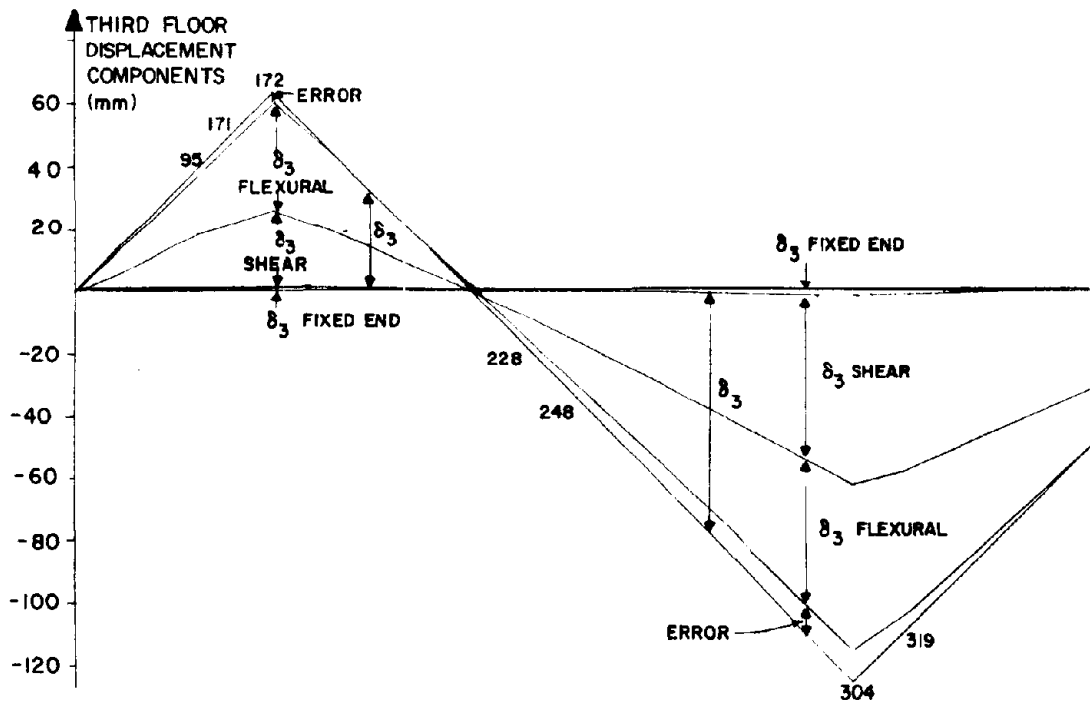


Fig. 4.72 Displacement Component Diagram, Specimen 6R

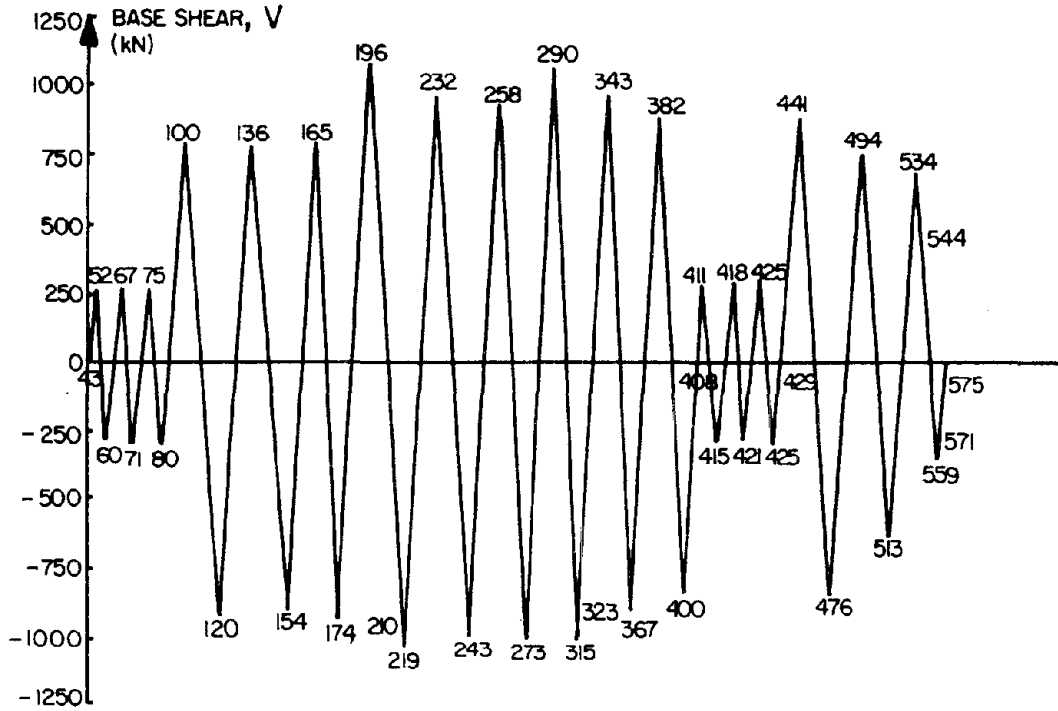


Fig. 4.73a Load program

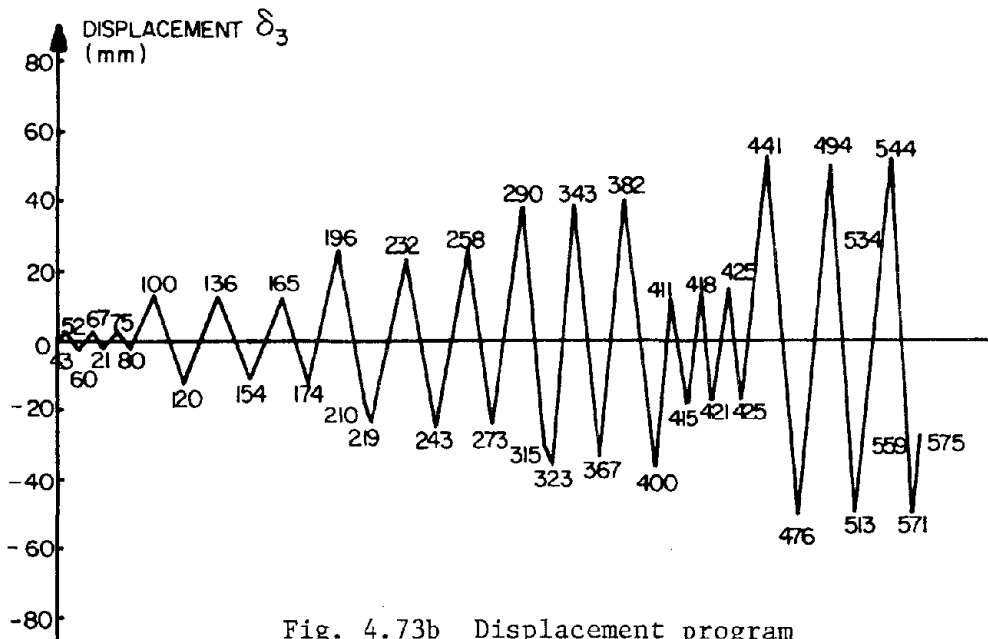


Fig. 4.73b Displacement program

Fig. 4.73 Load Program for Repaired Rectangular Wall (Cyclic Loading), Specimen 5R

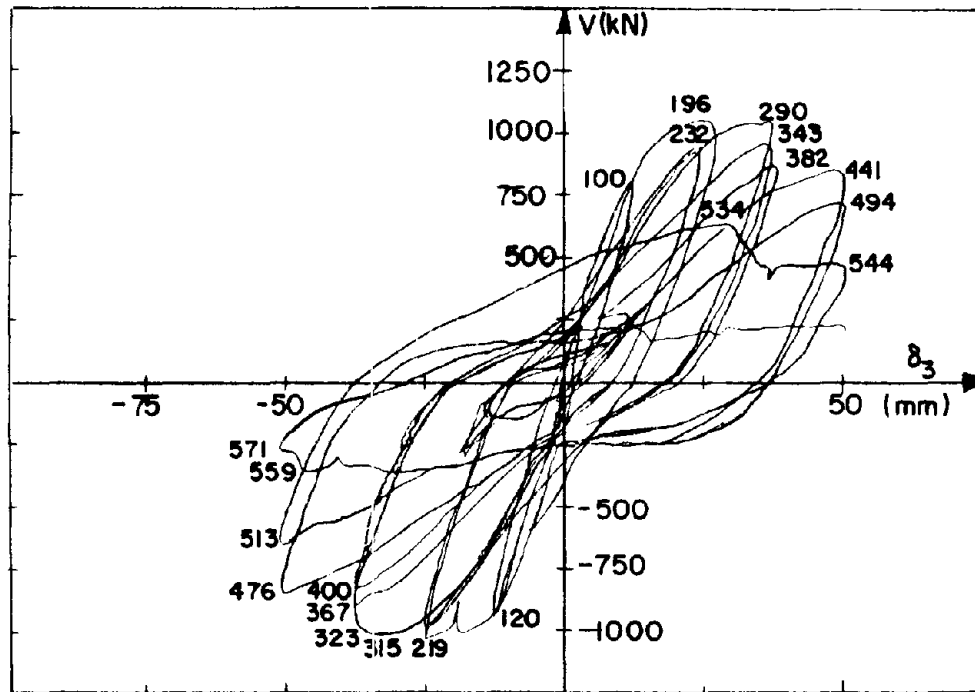


Fig. 4.74 Displacement at Third Floor of Repaired Rectangular Wall (Cyclic Loading), Specimen 5R

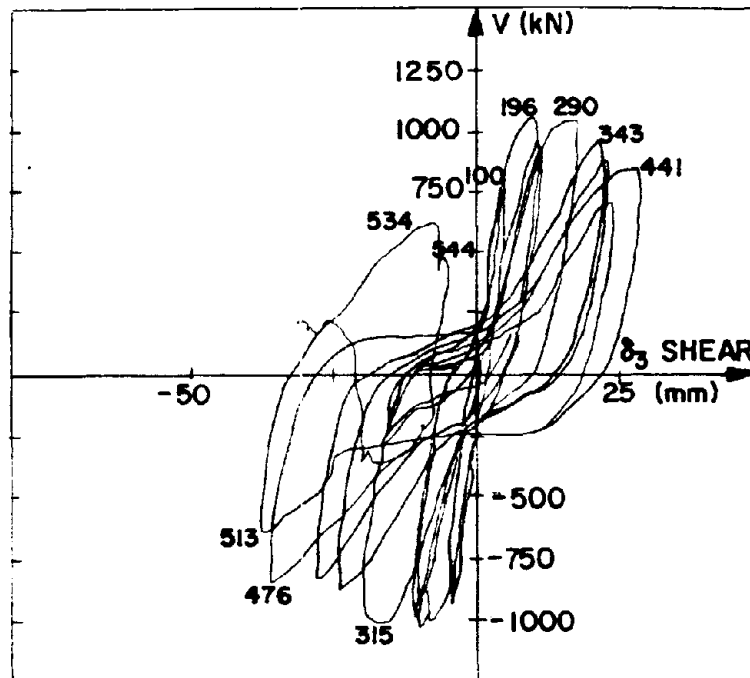


Fig. 4.75 Displacement at Third Floor of Repaired Rectangular Wall (Cyclic Loading) Due to Shear Deformation, Specimen 5R

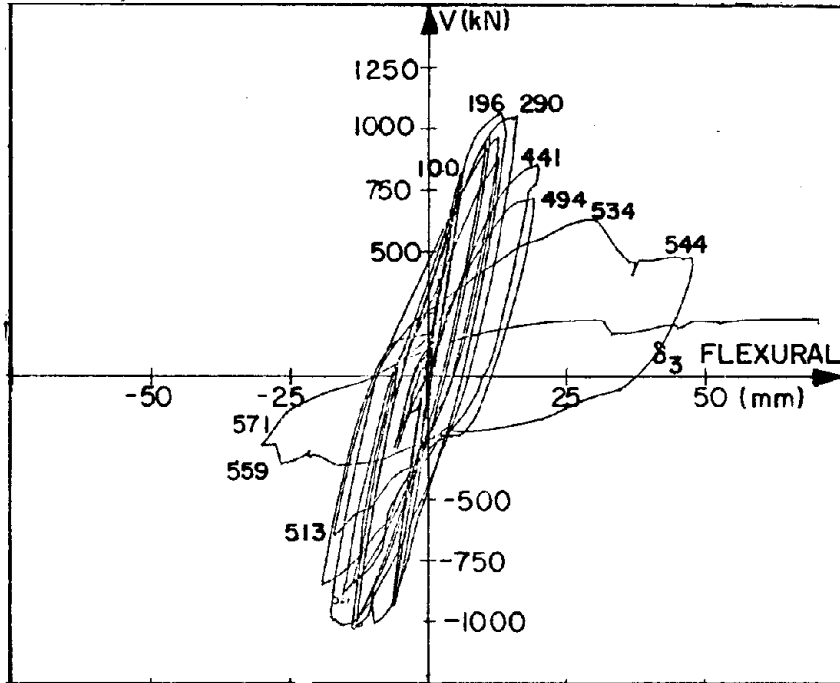


Fig. 4.76 Displacement at Third Floor of Repaired Rectangular Wall (Cyclic Loading) Due to Flexural Deformation, Specimen 5R

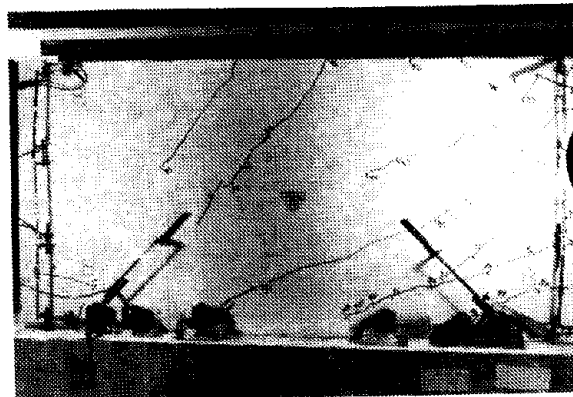


Fig. 4.77a
 $\mu = 1$

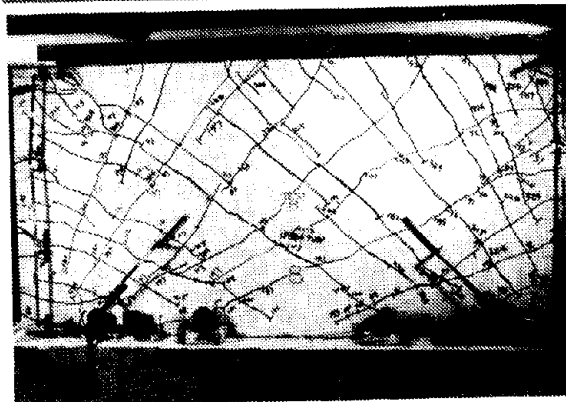


Fig. 4.77b
 $\mu = 3$

Fig. 4.77 Crack Formation Sequence, Specimen 5R

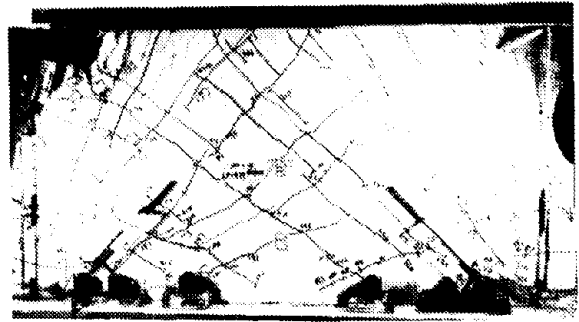
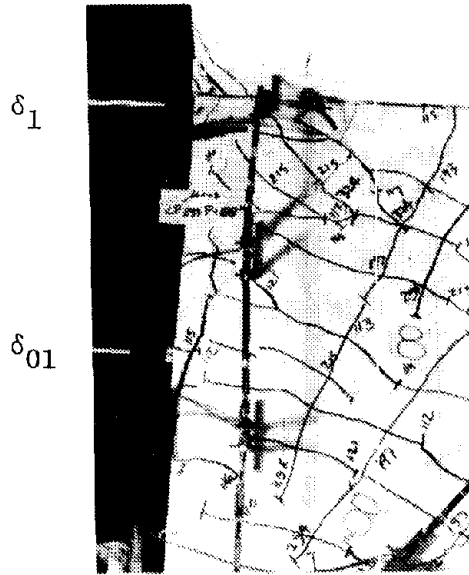


Fig. 4.79 Failure of Specimen 5R

Fig. 4.78 Crack Formation Interfering with Reading of Linear Potentiometers, Specimen 5R

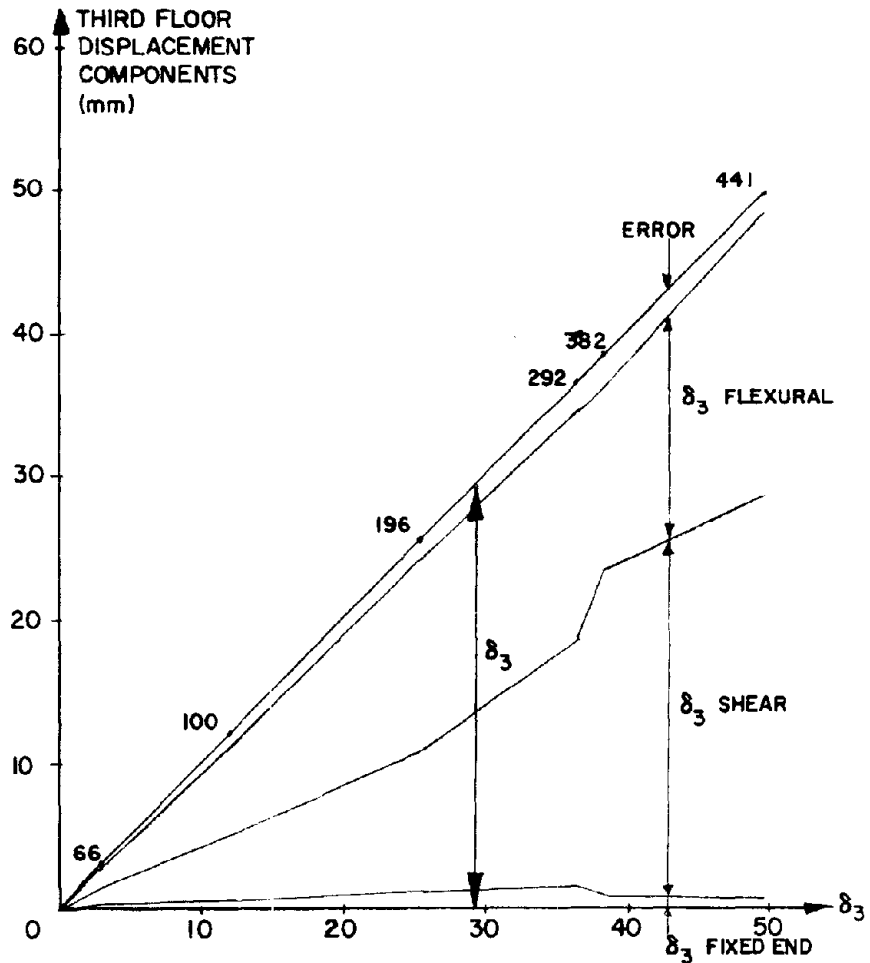
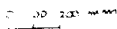
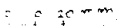


Fig. 4.80 Displacement Components Diagram, Specimen 5R

SCALE FOR FIGURES
4.81 TO 4.87

SPECIMEN 
DISPLACEMENT 

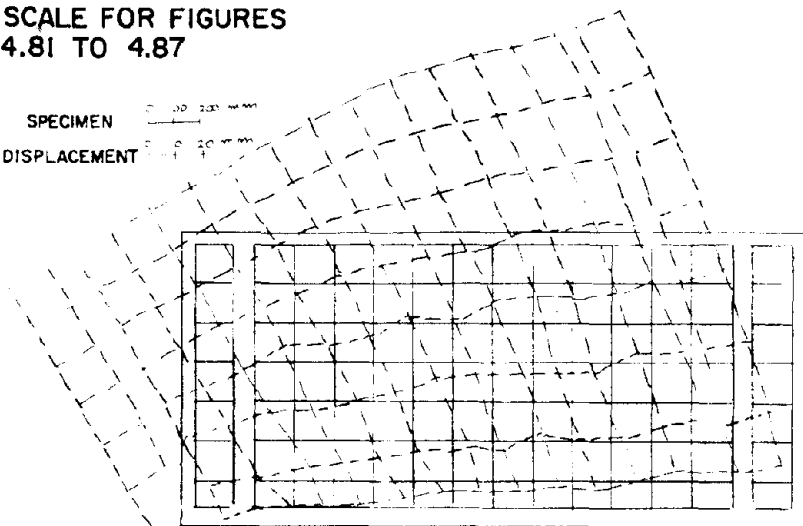


Fig. 4.81a LP 76, $V = 676$ KN

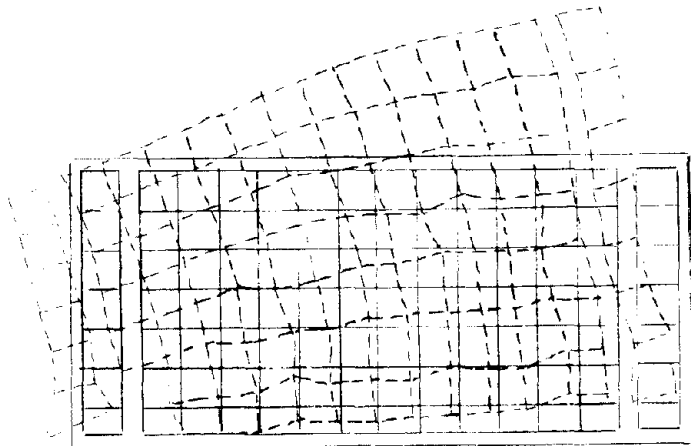


Fig. 4.81b LP 81, $V = 365$ KN

Fig. 4.81 Deformation Pattern of First Story,
Specimen 3

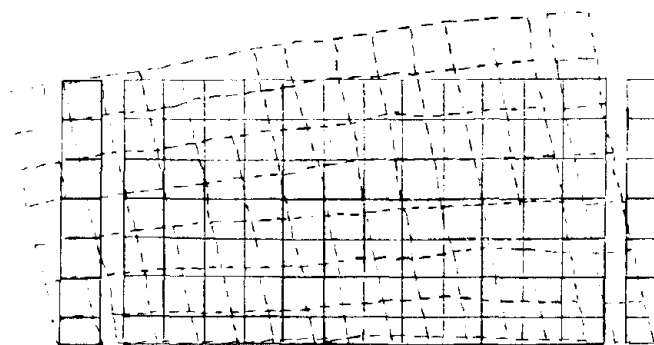


Fig. 4.82a LP 82, $V = 1023$ KN

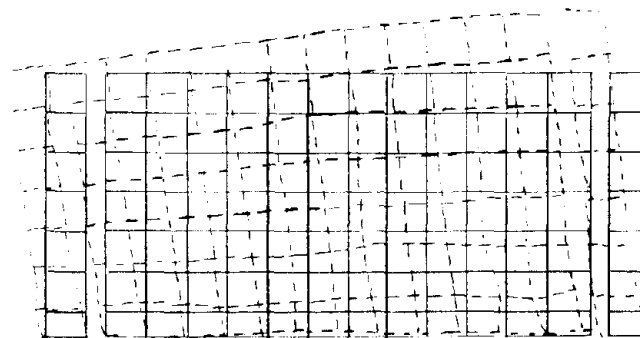


Fig. 4.82b LP 83, $V = 1$ KN

Fig. 4.82 Deformation Pattern of First Story,
Specimen 4

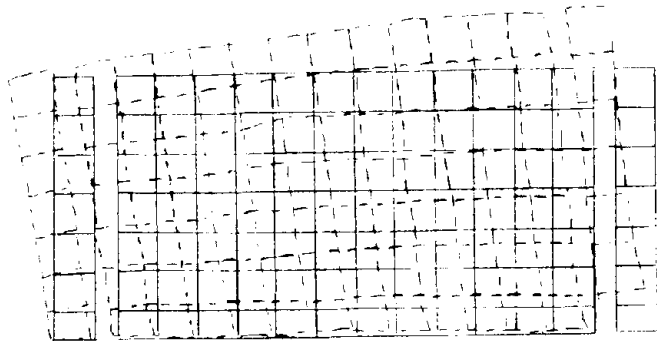


Fig. 4.82c LP 83S, $V = -20$ KN

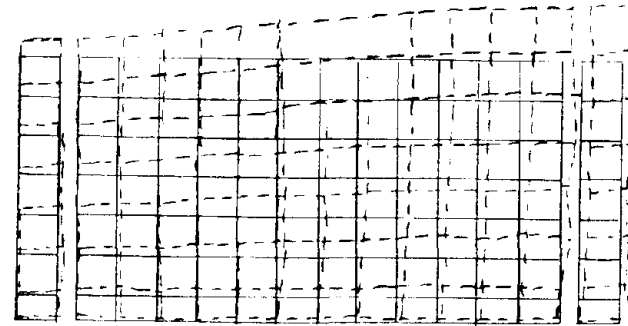


Fig. 4.82d 83T, $V = 294$ KN

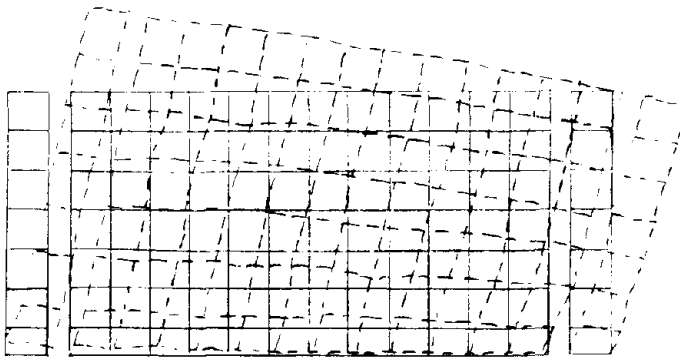


Fig. 4.82e LP 84, $V = 1003$ KN

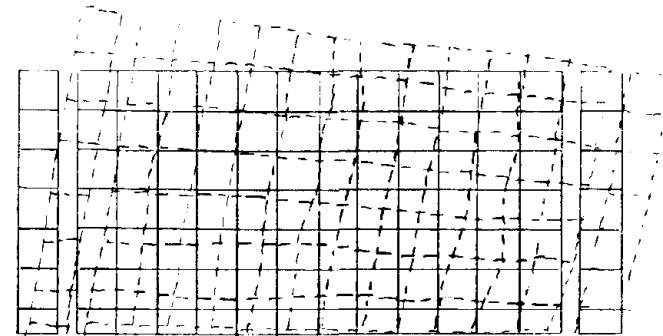


Fig. 4.82f LP 85, $V = 3$ KN

Fig. 4.82 Deformation Pattern of First Story, Specimen 4

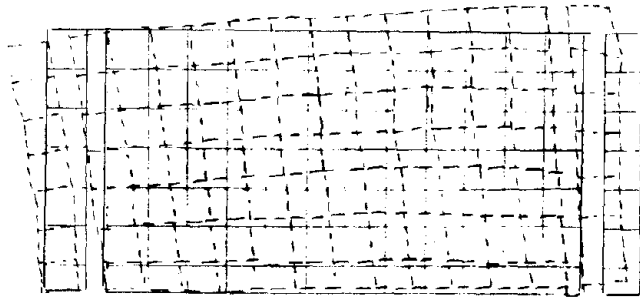


Fig. 4.83a LP 192, $V = 1262$ KN

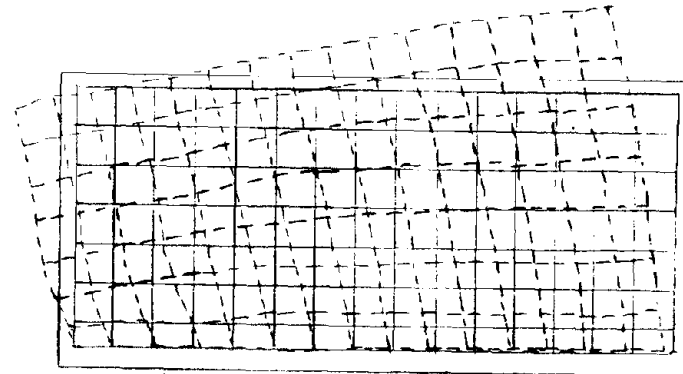


Fig. 4.84a LP 312, $V = 616$ KN

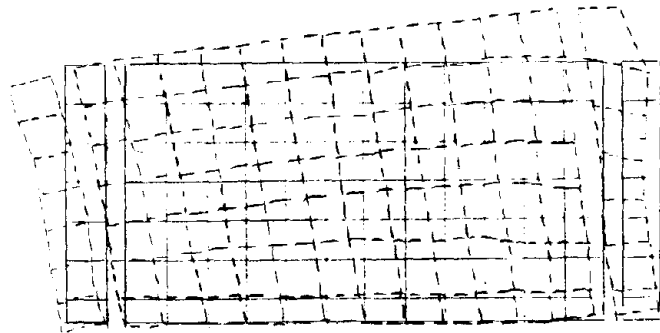


Fig. 4.83b LP 15, $V = 114$ KN

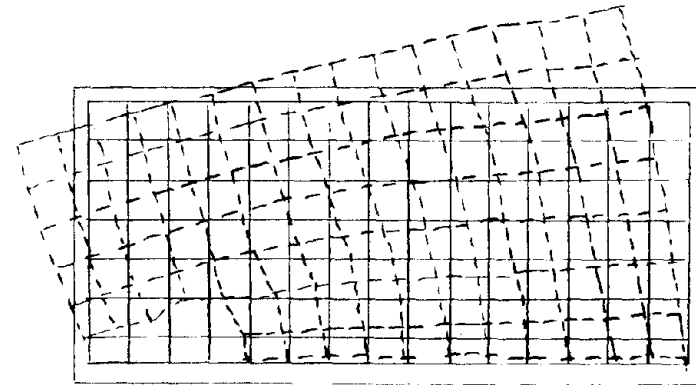


Fig. 4.84b LP 342, $V = 296$ KN

Fig. 4.83 Deformation Pattern of First Story,
Specimen 4R

Fig. 4.84 Deformation Pattern of First Story,
Specimen 5

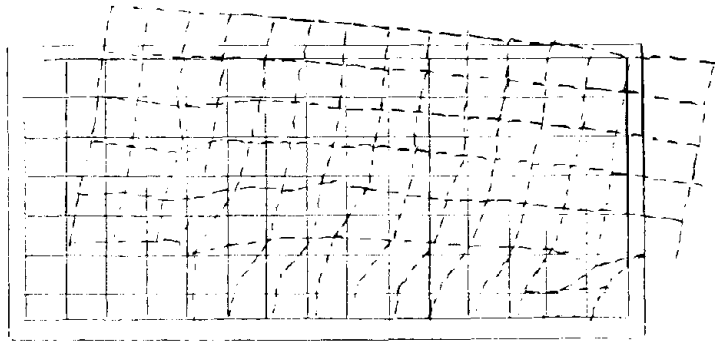


Fig. 4.84c LP 547, V = 251 KN

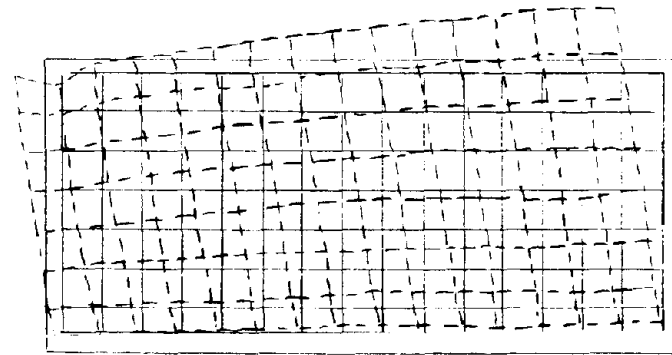


Fig. 4.85b LP 532, V = 856 KN

Fig. 4.84 Deformation Pattern of First Story, Specimen 5

x

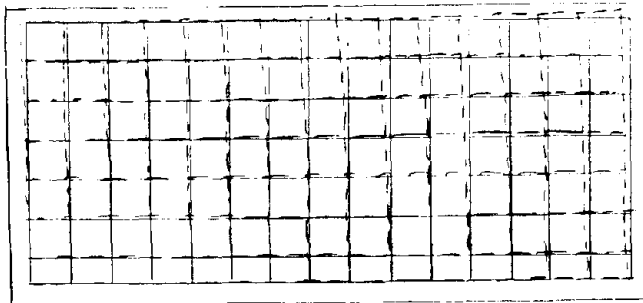


Fig. 4.85a LP 149, V = 729 KN

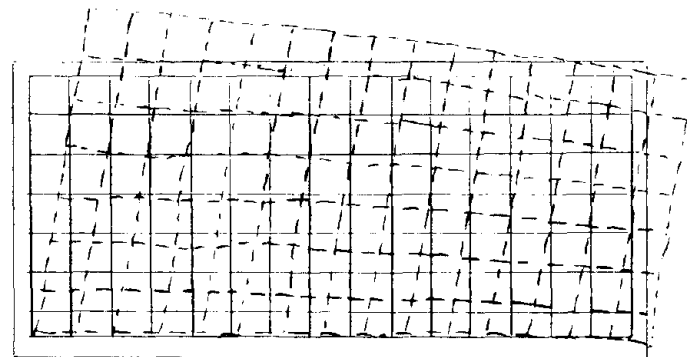


Fig. 4.85c LP 561, V = 856 KN

Fig. 4.85 Deformation Pattern of First Story Specimen 6

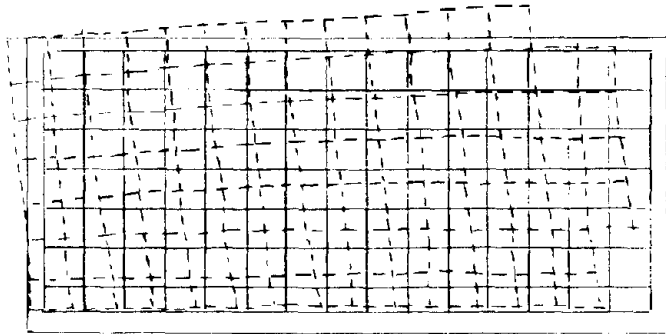


Fig. 4.85d LP 638, $V = 810$ KN

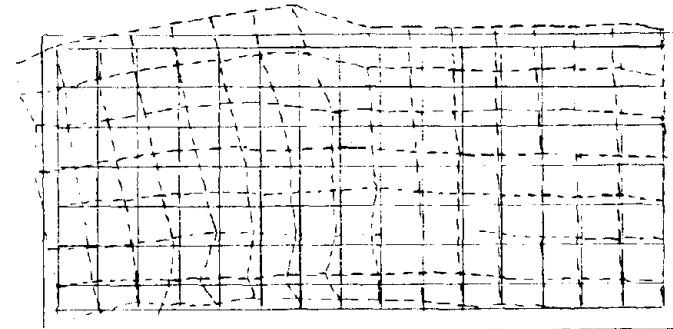


Fig. 4.86a LP 168, $V = 1162$ KN

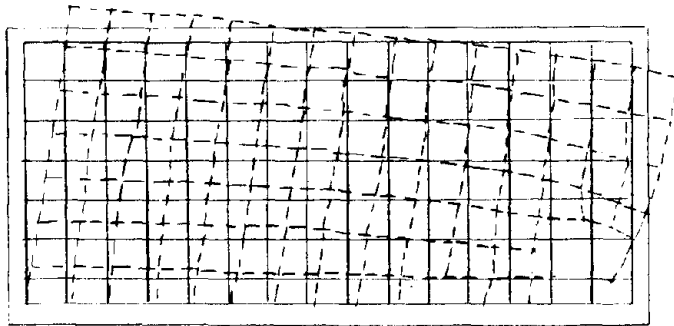


Fig. 4.85e LP 670, $V = 670$ KN

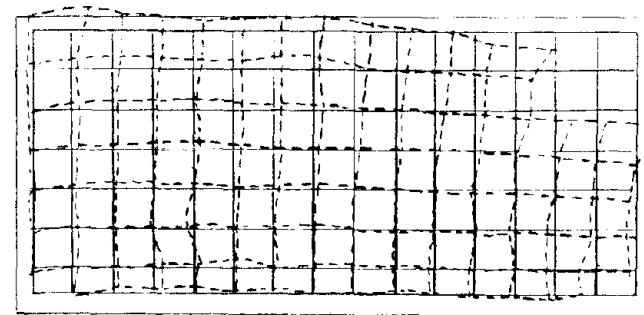


Fig. 4.86b LP 300, $V = 588$ KN

Fig. 4.85 Deformation Pattern of First Story,
Specimen 6

Fig. 4.86 Deformation Pattern of First Story,
Specimen 6R

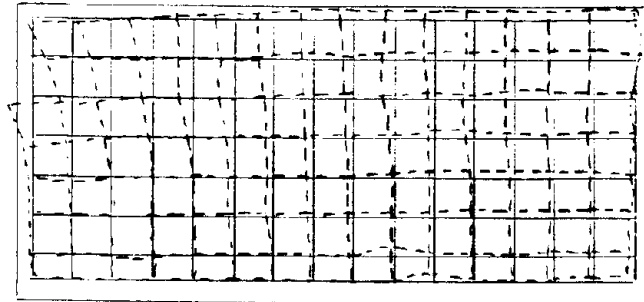


Fig. 4.87a LP 442, $V = 774$ KN

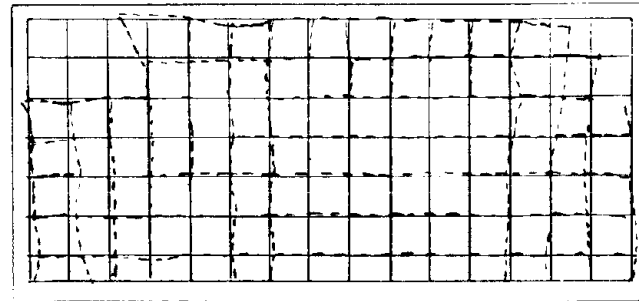


Fig. 4.87b LP 571, $V = -227$ KN

Fig. 4.87 Deformation Pattern of First Story,
Specimen 5R

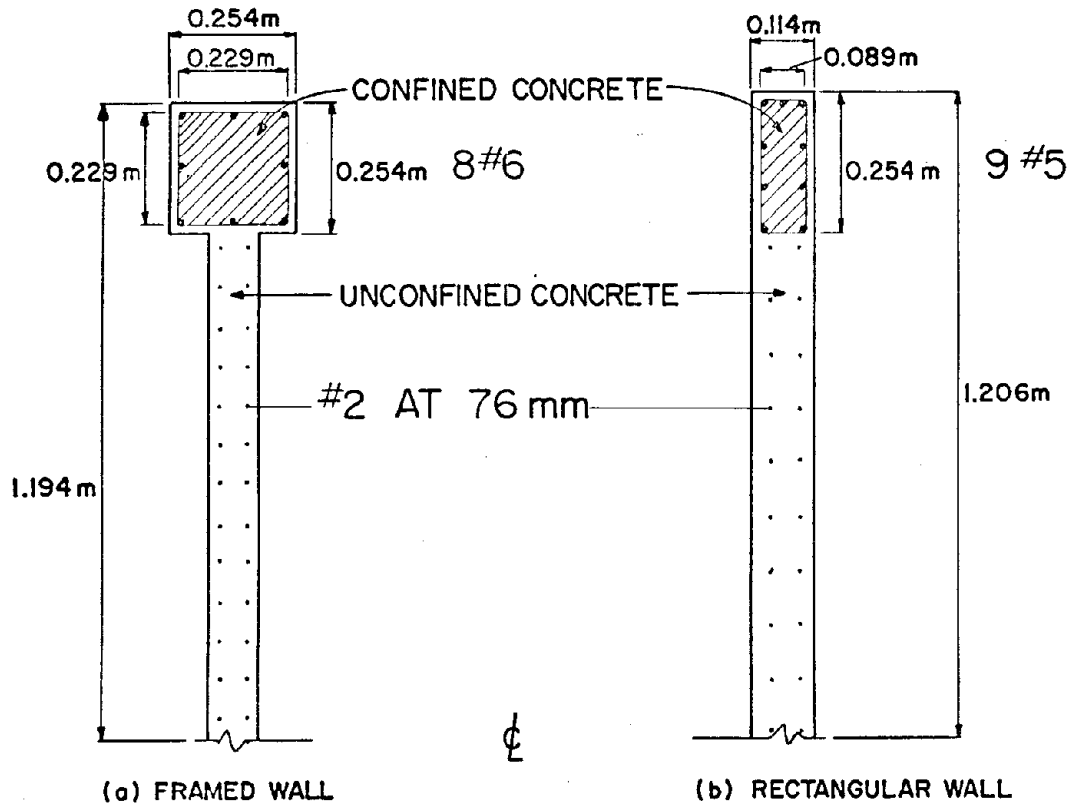


Fig. 5.1 Cross Section of Walls Considered for Analytical Prediction of M- ϕ Relationship

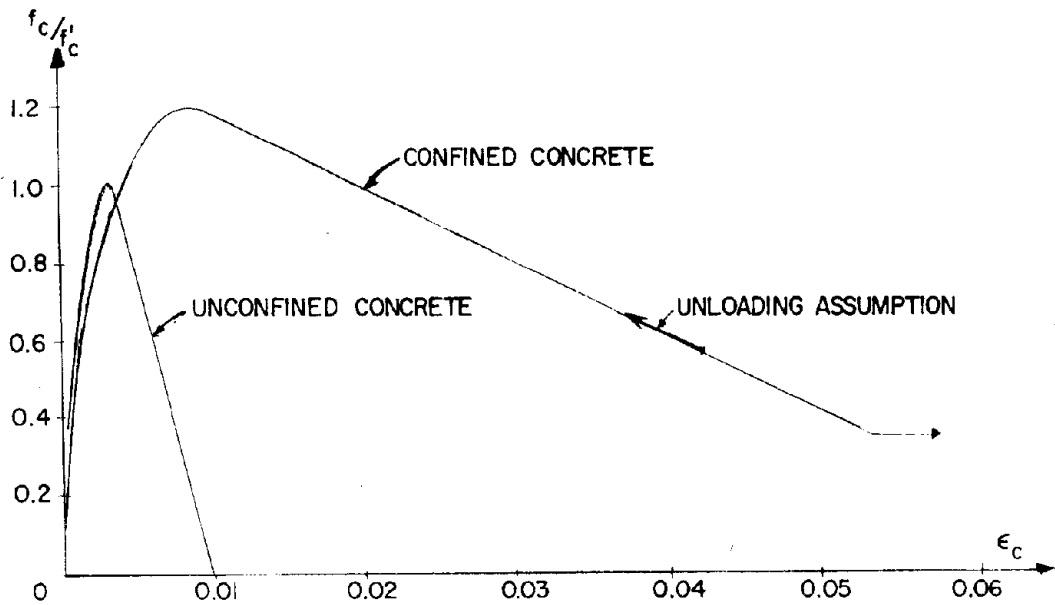


Fig. 5.2 Concrete Stress-Strain Relationship Considered for Analytical Prediction of M- ϕ Relationship

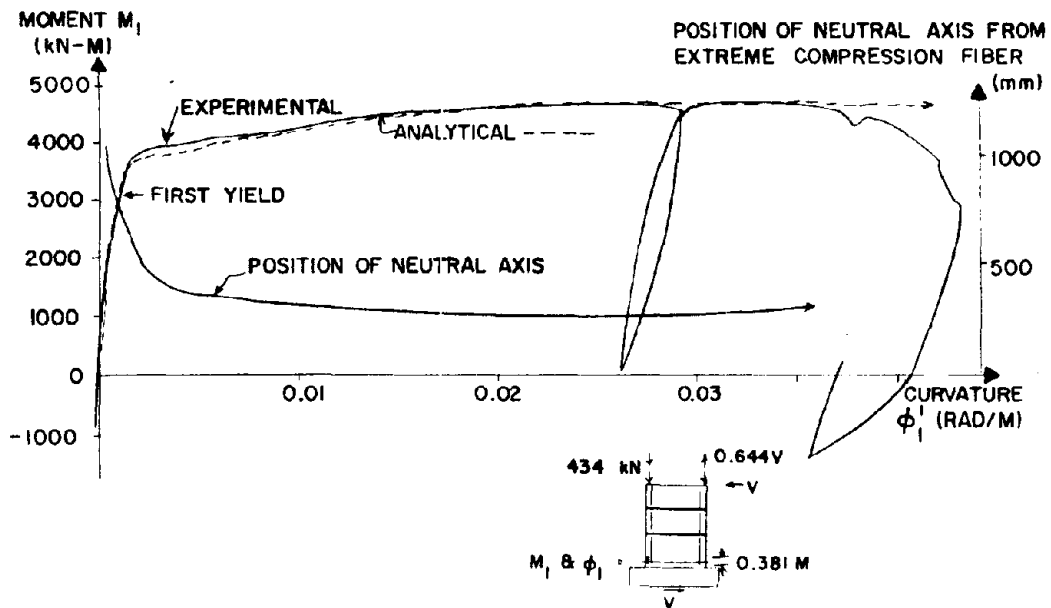


Fig. 5.3 Comparison of Experimental and Analytical Curves for Specimen 3

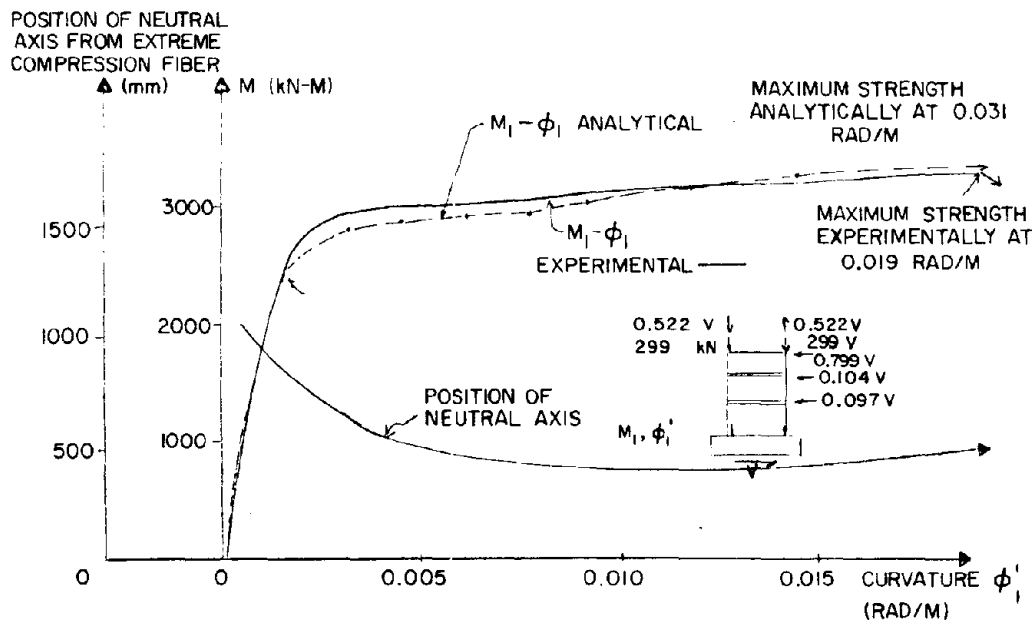


Fig. 5.4 Comparison of Experimental and Analytical Curves for Specimen 5

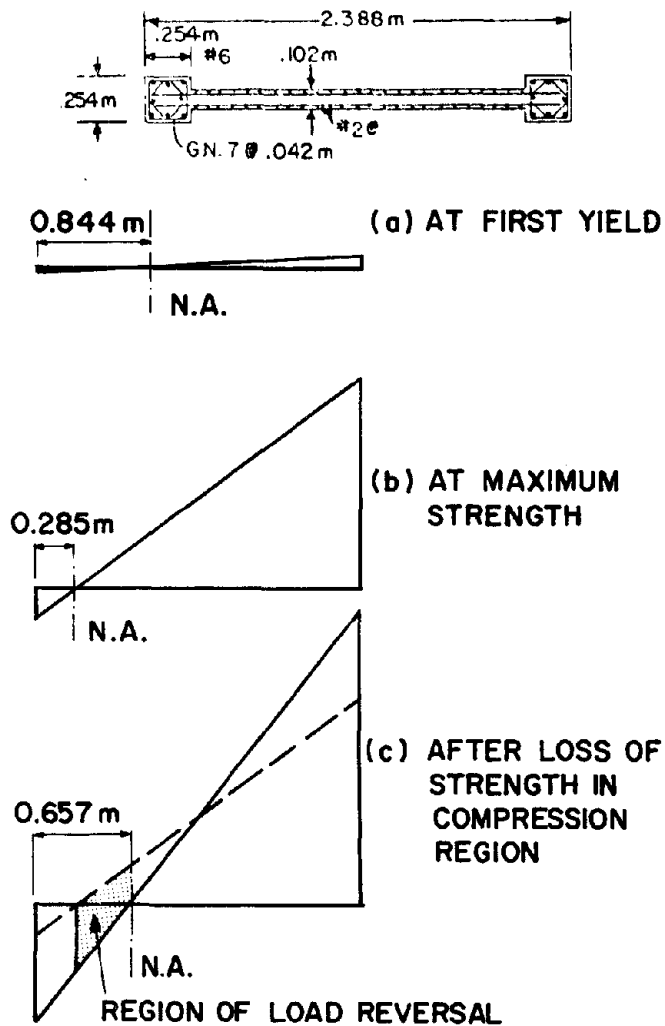


Fig. 5.5 Position of Neutral Axis Under Monotonic Loading, Specimen 3

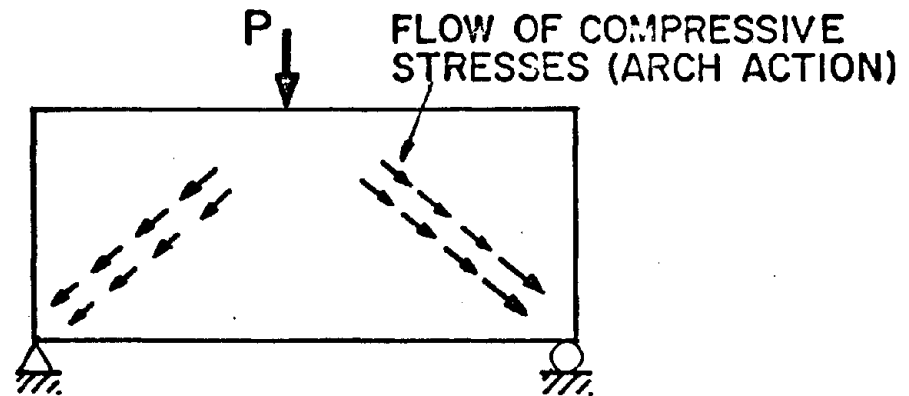


Fig. 5.6a Arch action

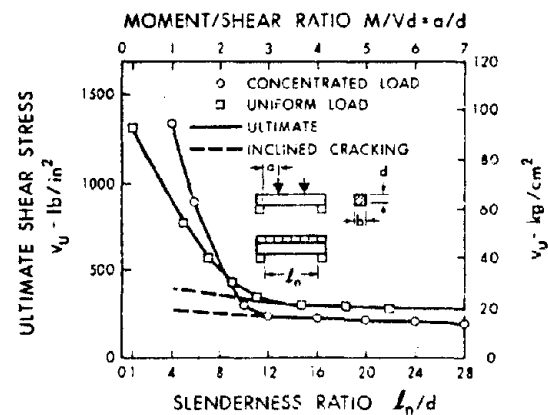
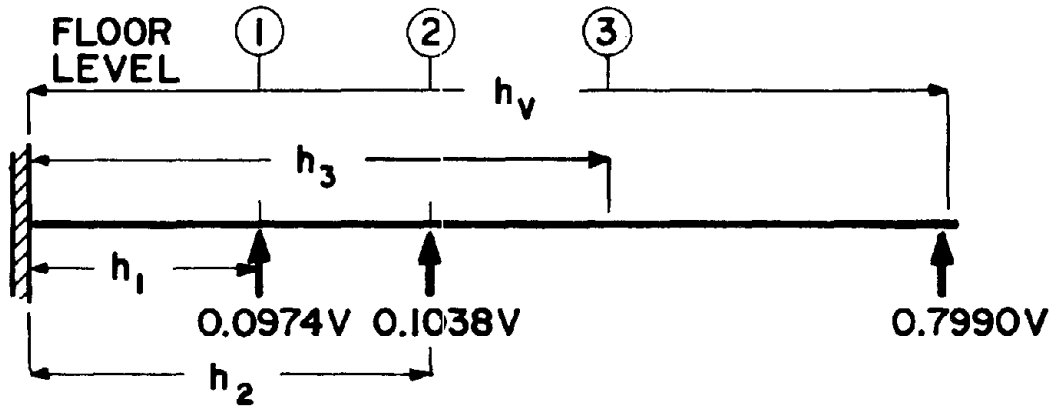
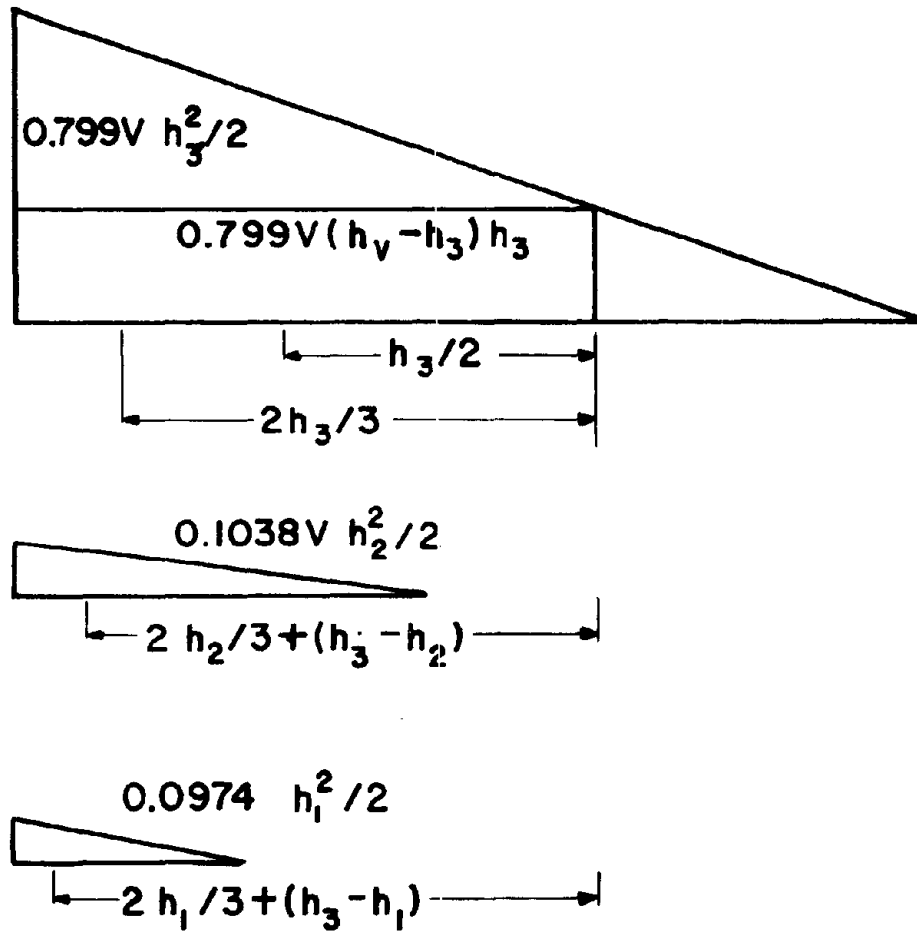


Fig. 5.6b Experimental shear capacity

Fig. 5.6 Reserve Shear Capacity of Deep Beams



(a) LOAD DISTRIBUTION ON RECTANGULAR WALL



(b) MOMENT AREAS

Fig. 5.7 Load Distribution on Rectangular Wall

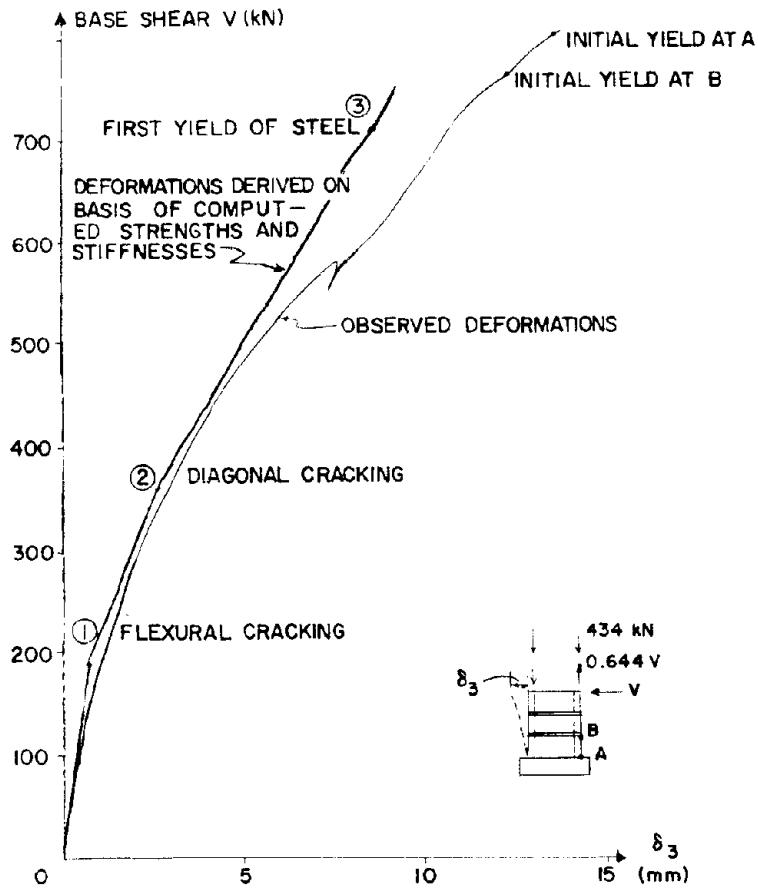


Fig. 5.8 Initial Stiffness, Specimen 3

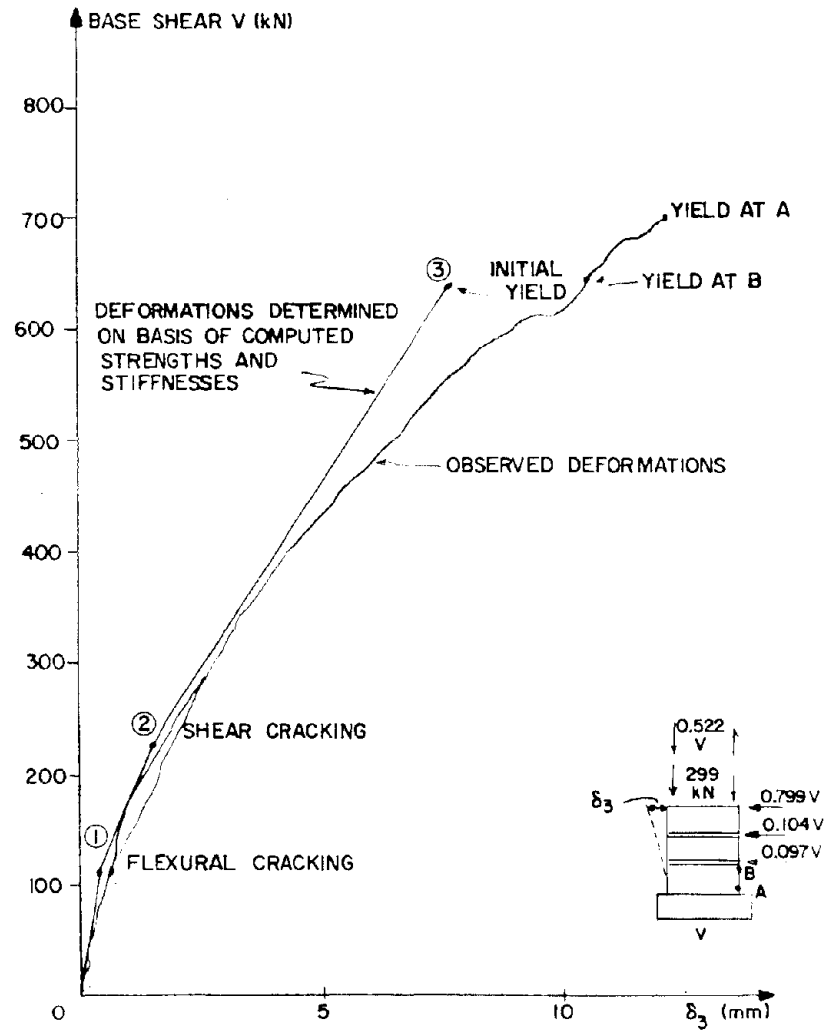


Fig. 5.9 Initial Stiffness, Specimen 5

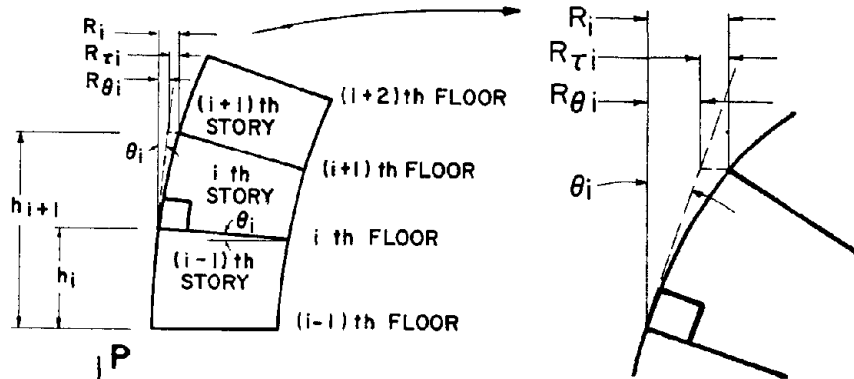


Fig. 5.10 Story Drift Geometry

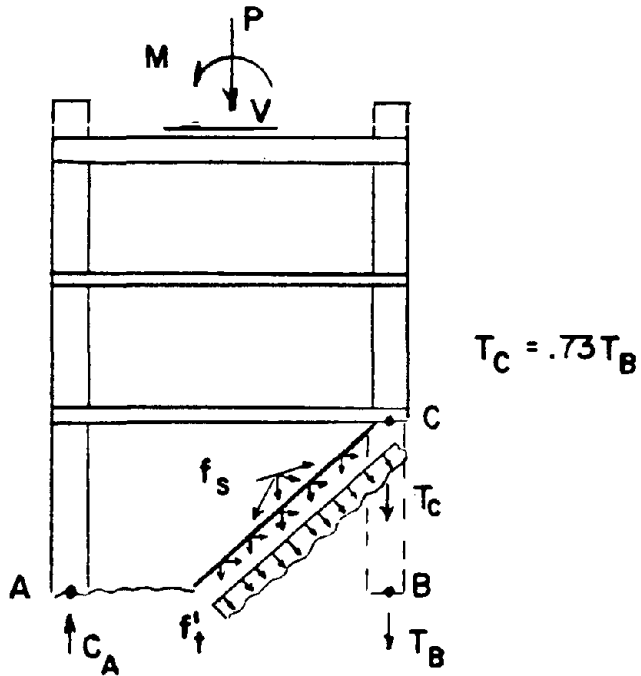


Fig. 5.11a Free-body diagram at onset of diagonal cracking

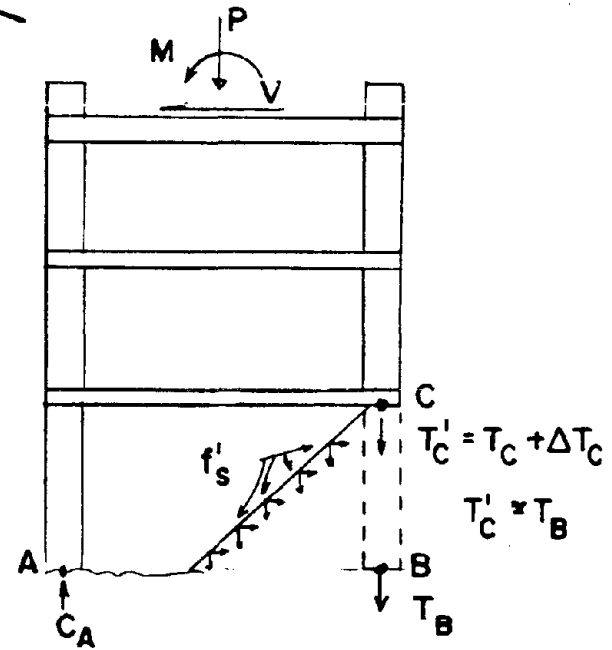


Fig. 5.11b Free-body diagram after diagonal cracking

Fig. 5.11 Effect of Diagonal Crack

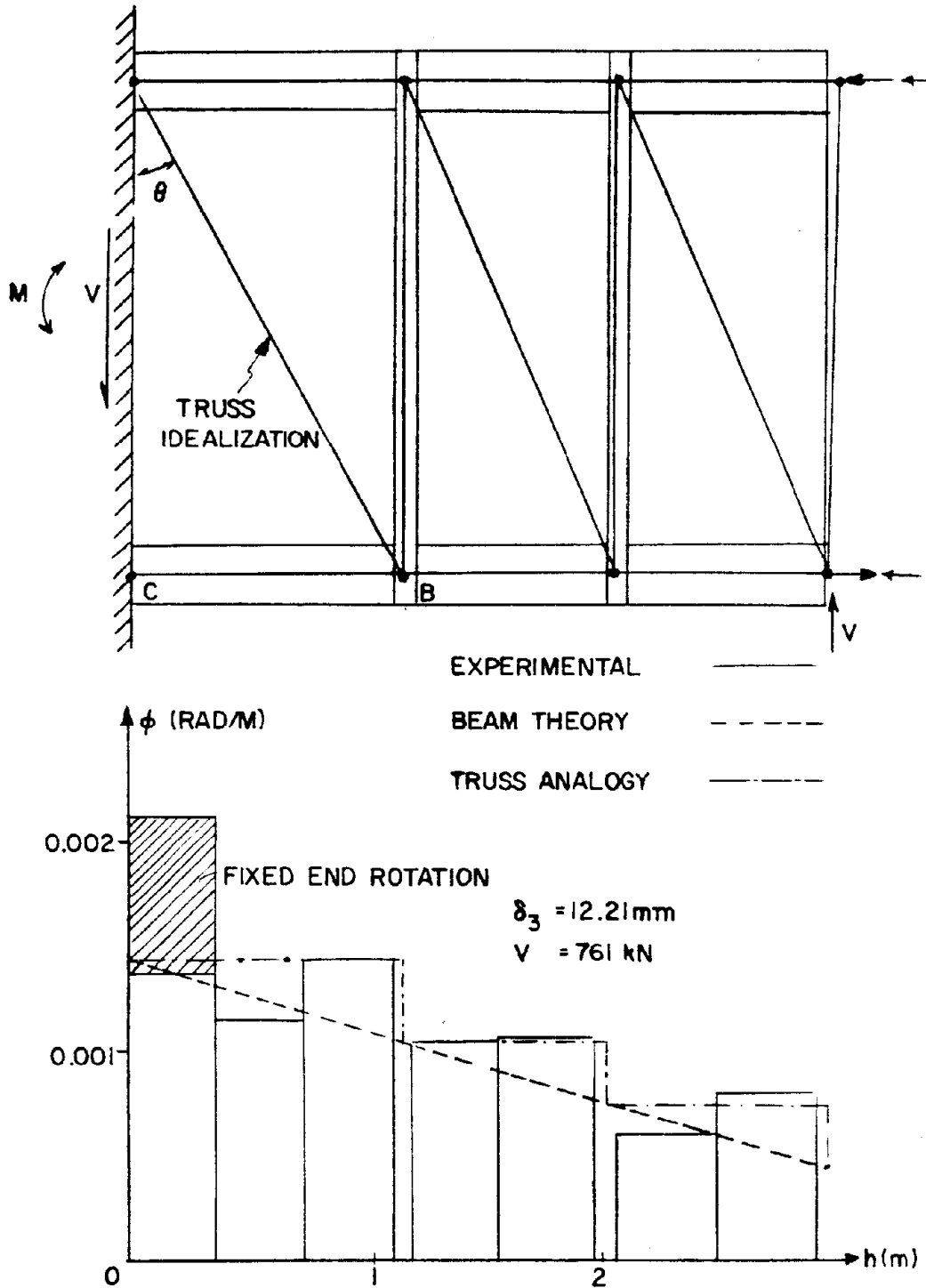


Fig. 5.12 Curvature Distribution at Initiation of Yielding, Specimen 3

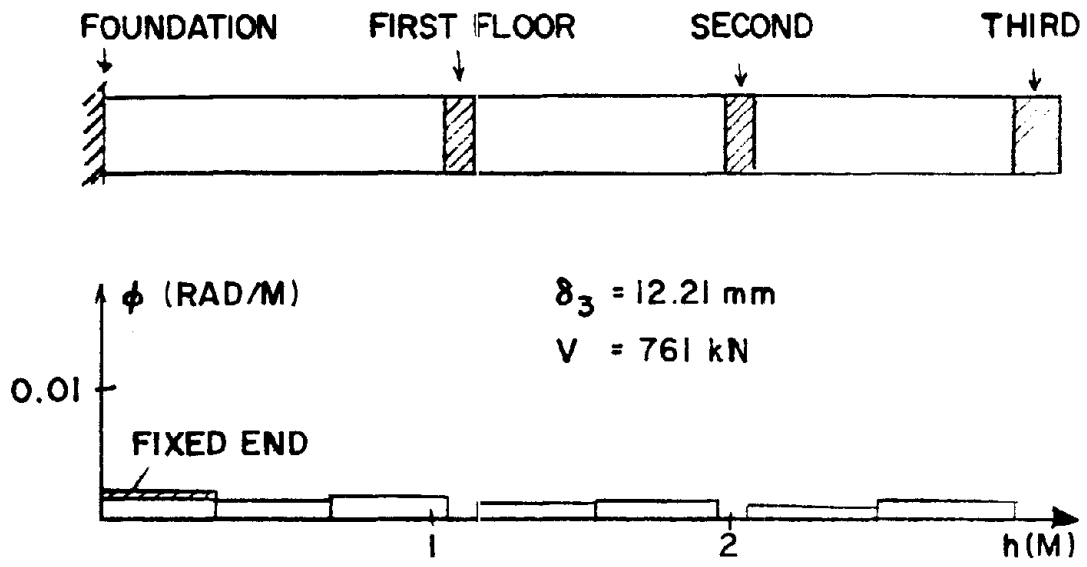


Fig. 5.13a At initiation of yielding

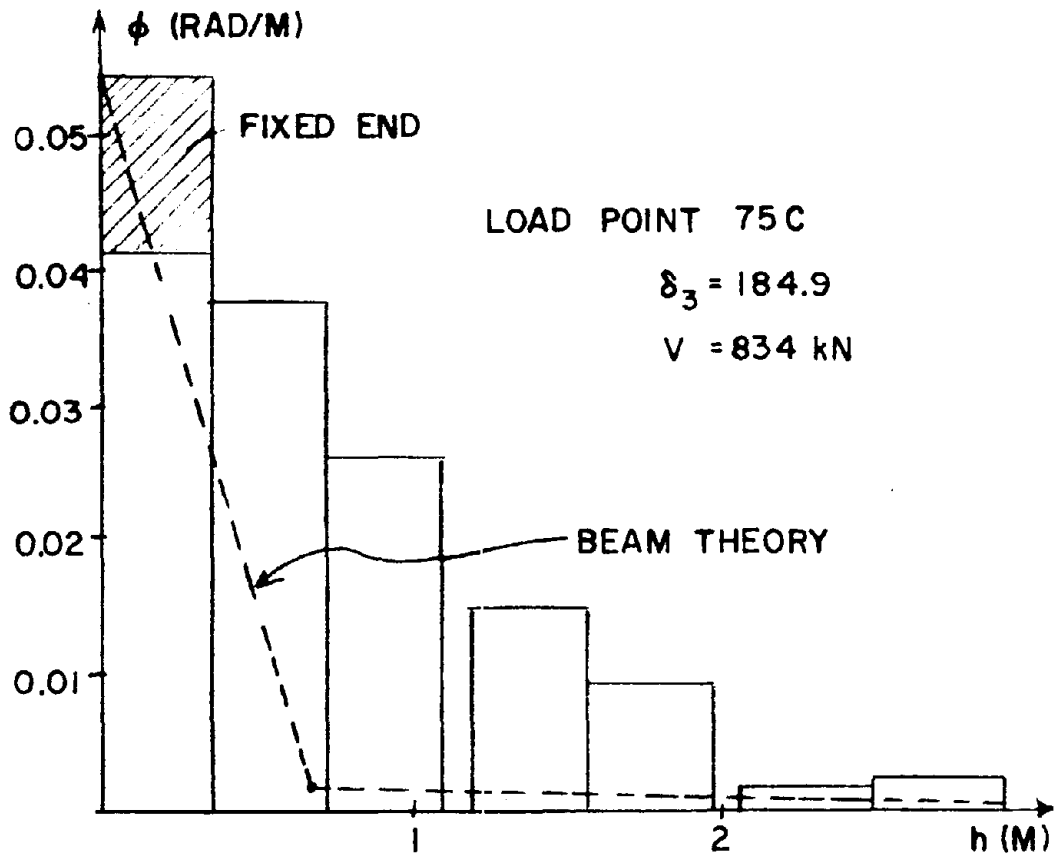


Fig. 5.13b Maximum displacement

Fig. 5.13 Curvature Distribution, Specimen 3

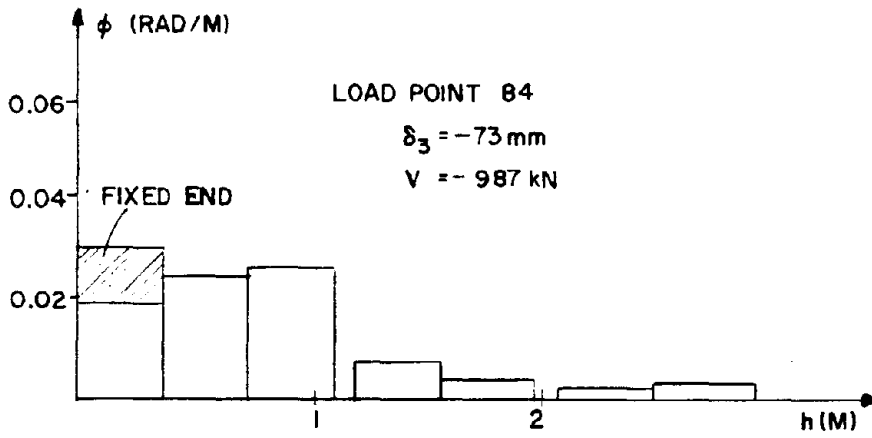


Fig. 5.14a Specimen 4

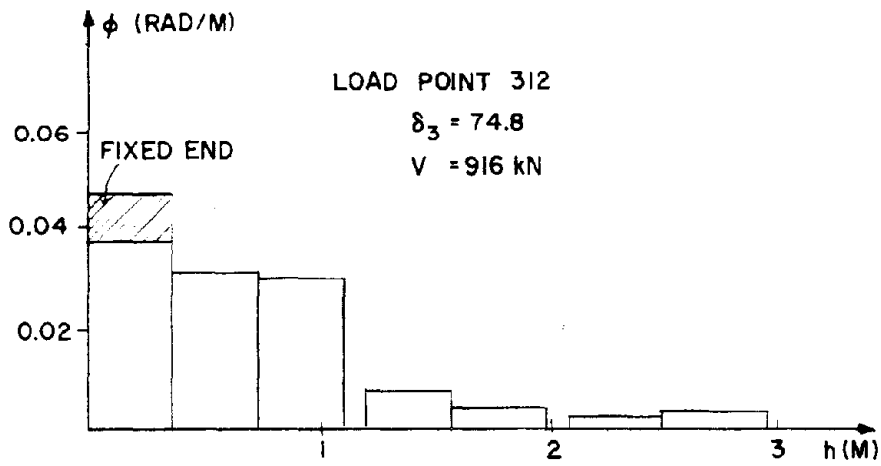


Fig. 5.14b Specimen 5

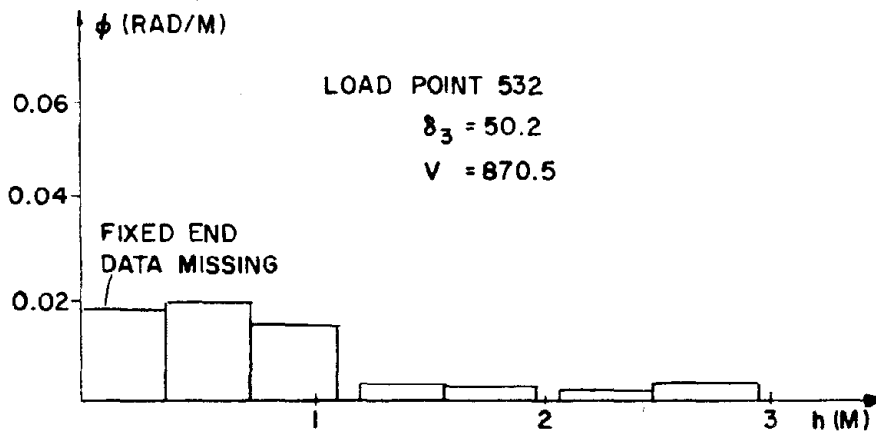


Fig. 5.14c Specimen 6

Fig. 5.14 Curvature Distribution, Specimens, 4, 5, and 6

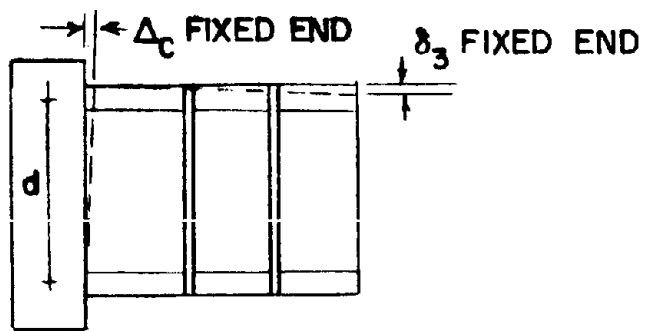


Fig. 5.15a Structural wall

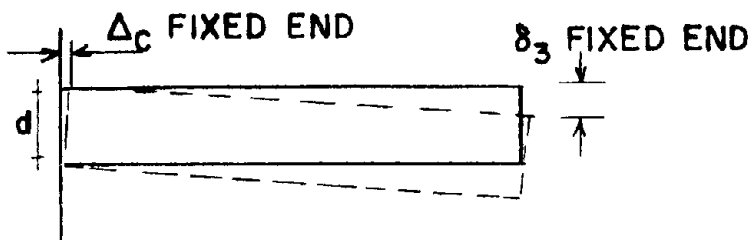


Fig. 5.15b Beam

Fig. 5.15 Effect of Fixed-End Rotation on Tip Displacement

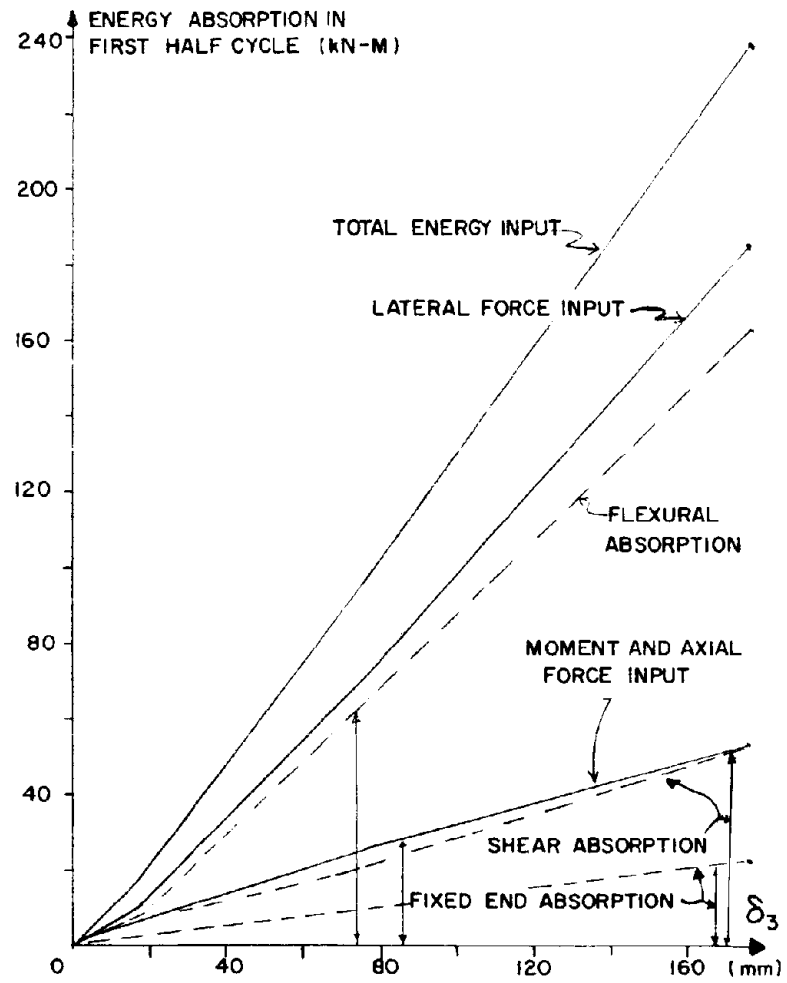


Fig. 5.16a Energy absorption, Specimen 3

Fig. 5.16 Energy Absorption Diagrams

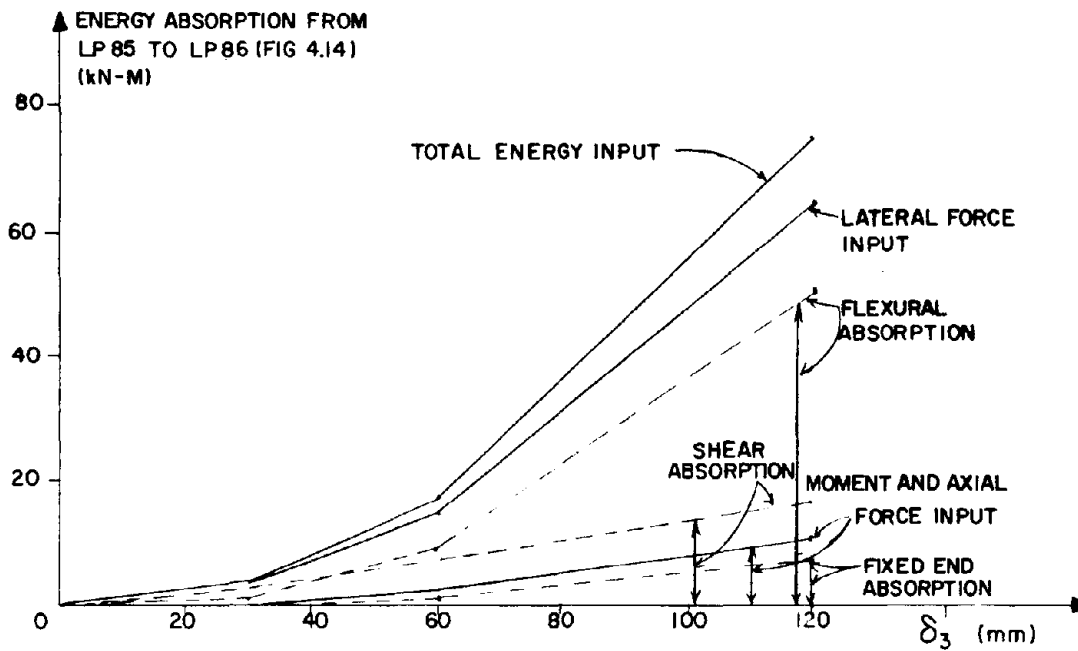


Fig. 5.16b Energy absorption, Specimen 4

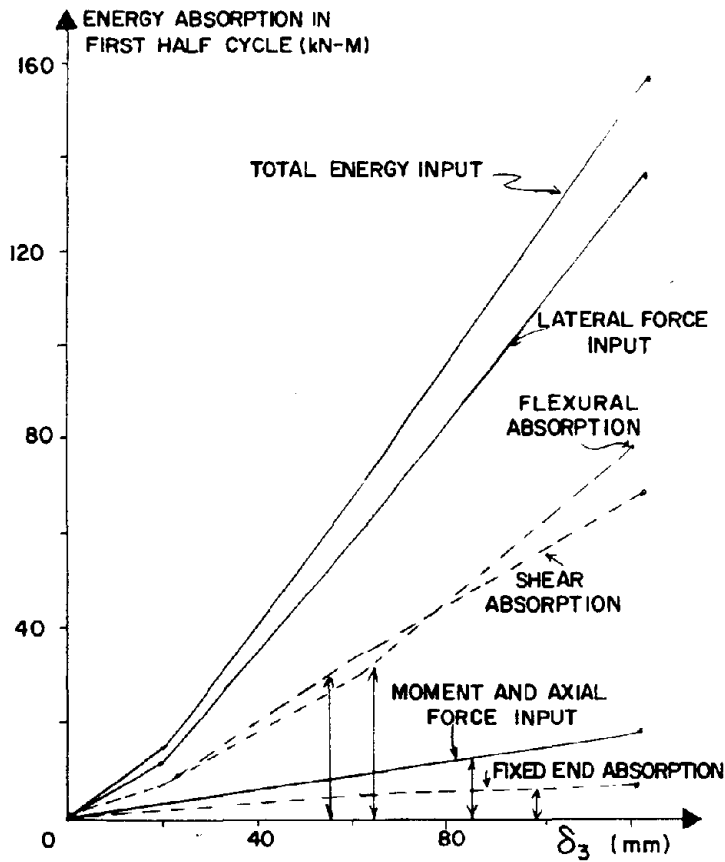


Fig. 5.16c Energy absorption, Specimen 4R

Fig. 5.16 Energy Absorption Diagrams

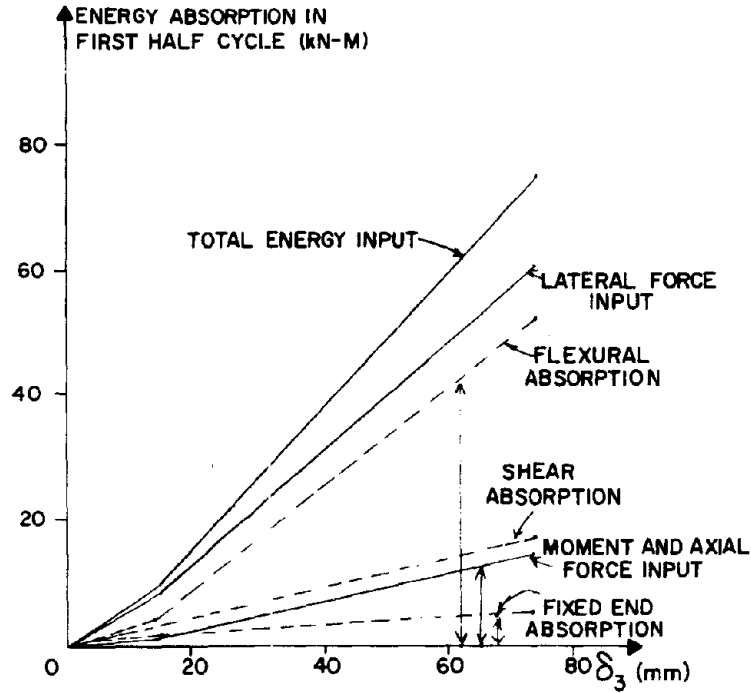


Fig. 5.16d Energy absorption, Specimen 5

Fig. 5.16 Energy Absorption Diagrams

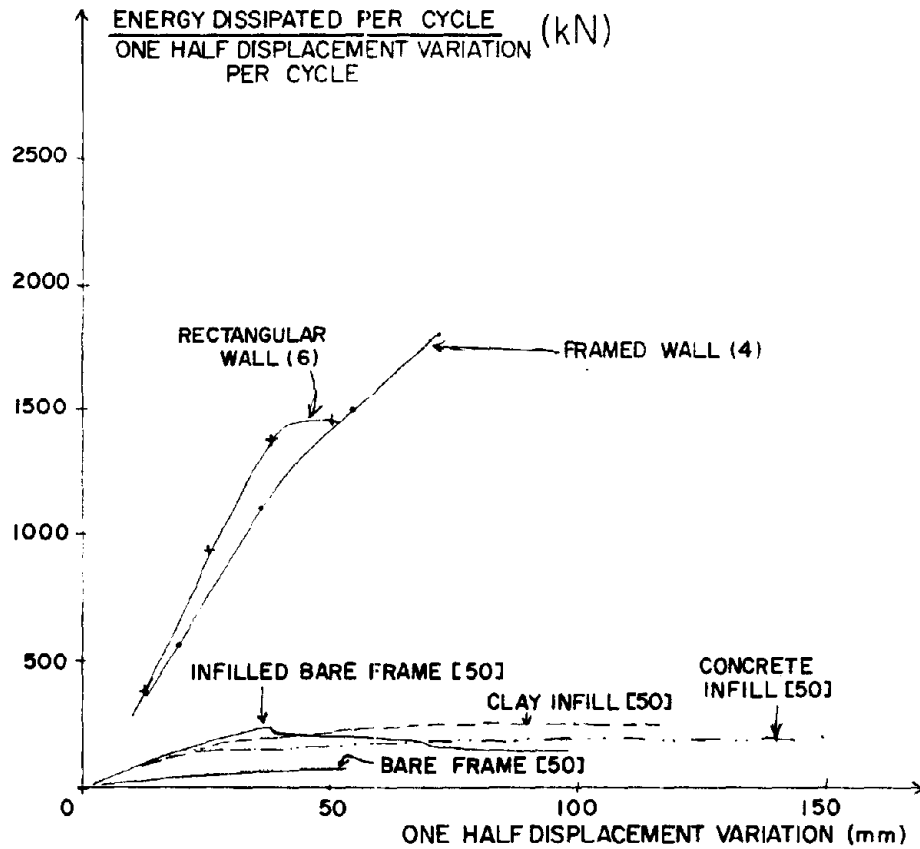


Fig. 5.17 Comparison of Energy Dissipation for Different Specimens

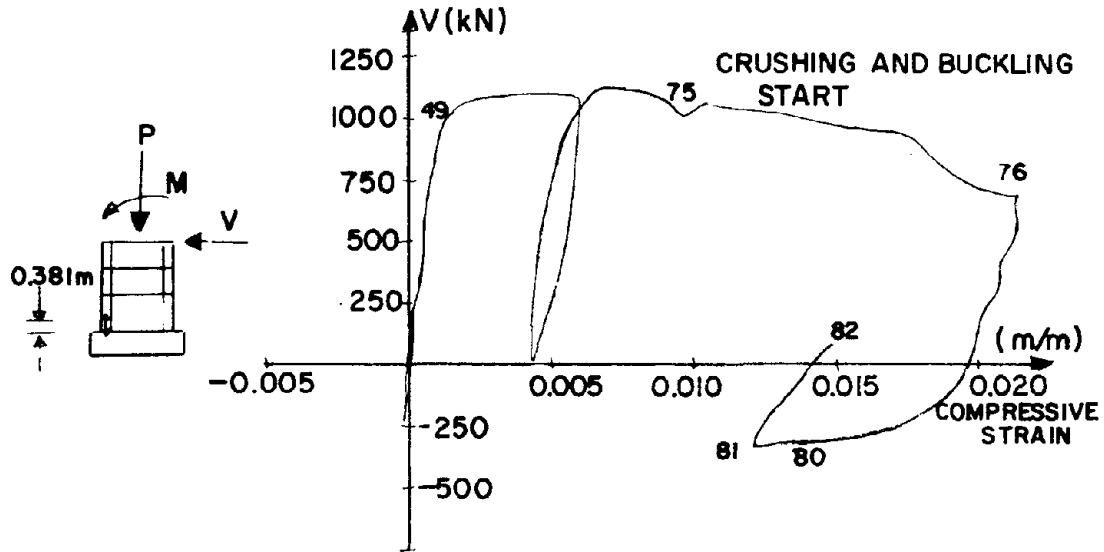


Fig. 5.18 Concrete Strain at Base of North Column (Gage C1), Framed Wall (Monotonic Loading), Specimen 3

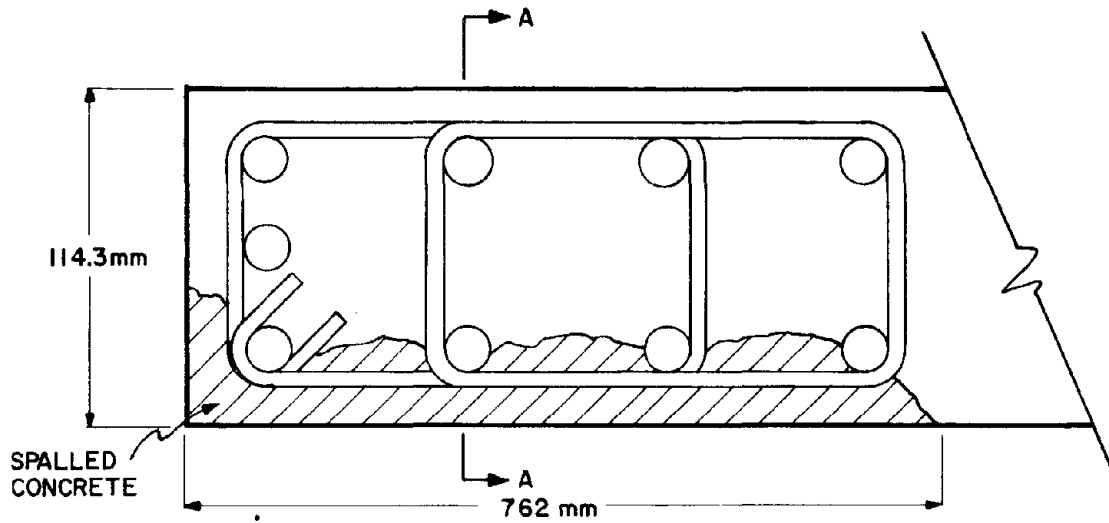


Fig. 5.19a Cross Section of Rectangular Boundary Element

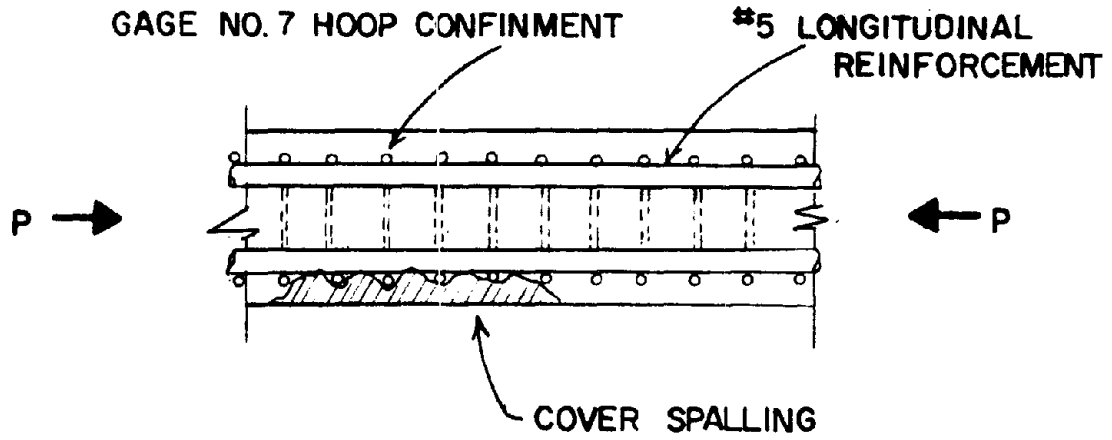


Fig. 5.19b Longitudinal section A-A

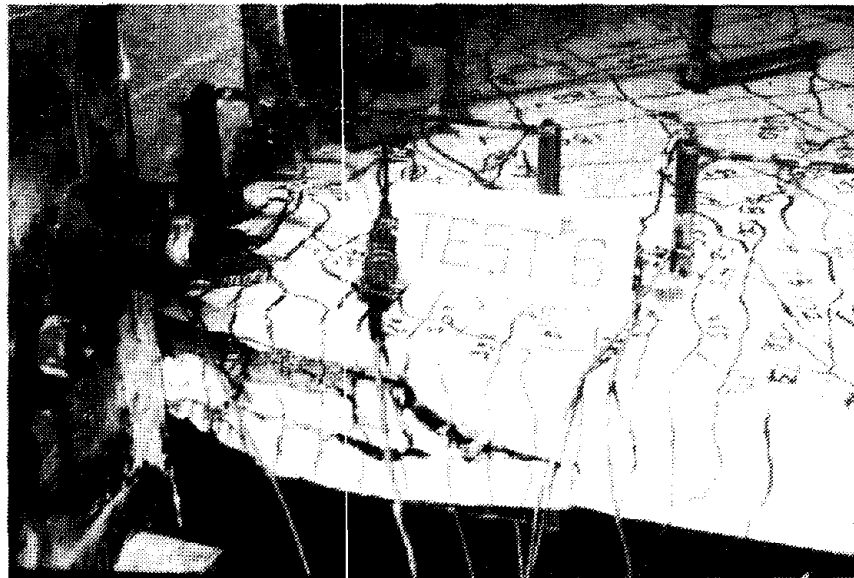


Fig. 5.19c Compression boundary element for Specimen 6

Fig. 5.19b,c Stability Failure Due to Asymmetric Cover Spalling

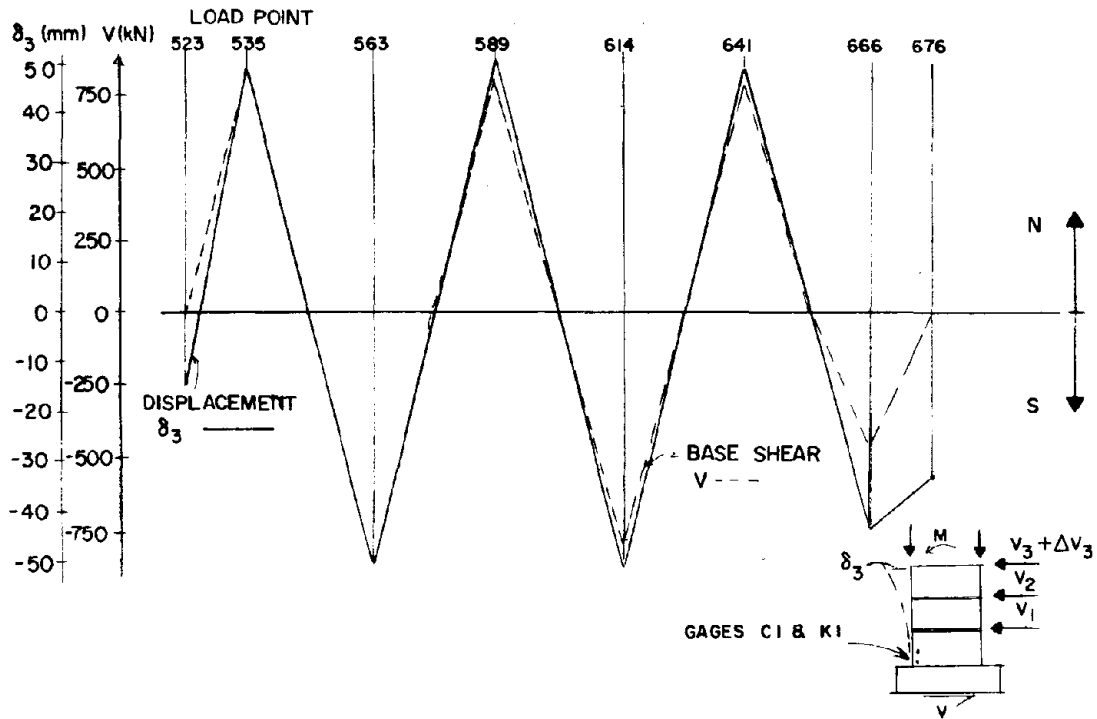


Fig. 5.20a Load and displacement histories for the last three cycles at ductility four and buckling, Specimen 6

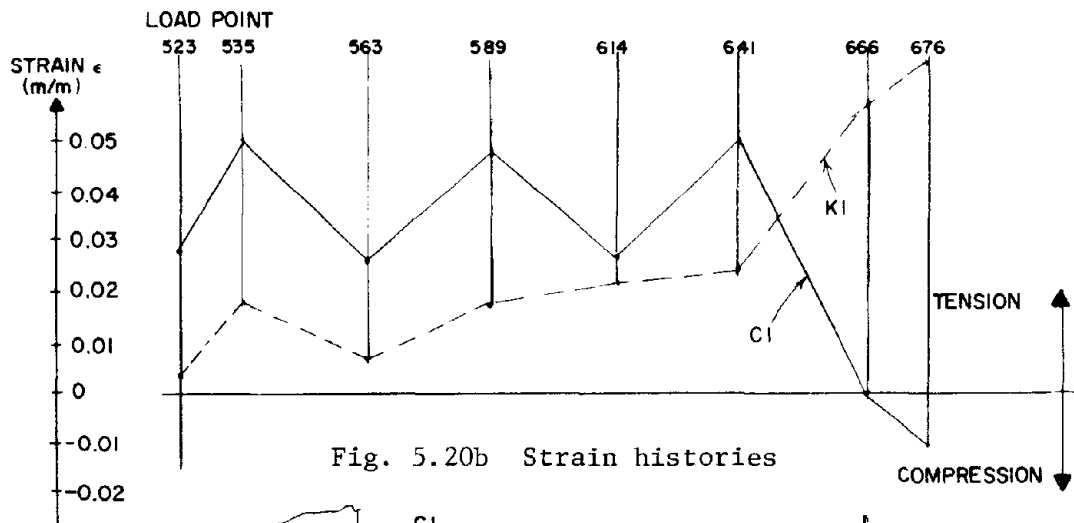


Fig. 5.20b Strain histories

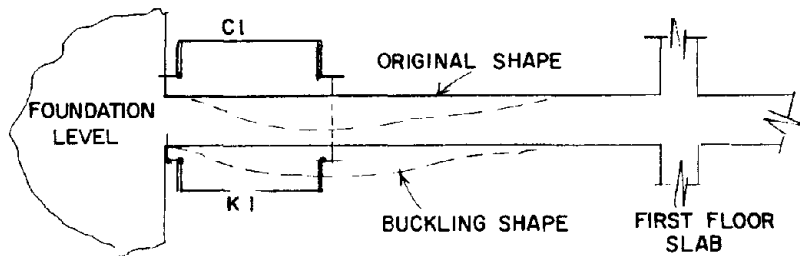


Fig. 5.20c Clip gage location

Fig. 5.20 Load Displacement and Strain Histories, Specimen 6

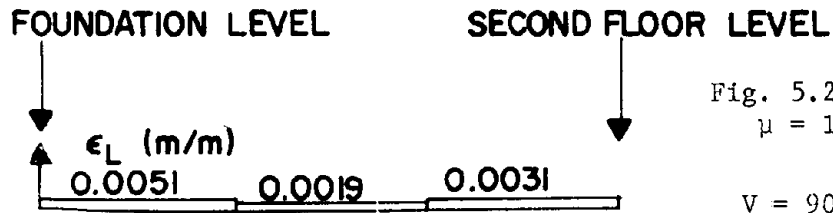


Fig. 5.21a Nominal
 $\mu = 1$ LP 49

$V = 901$ KN

$\delta_3 = 17.5$ mm

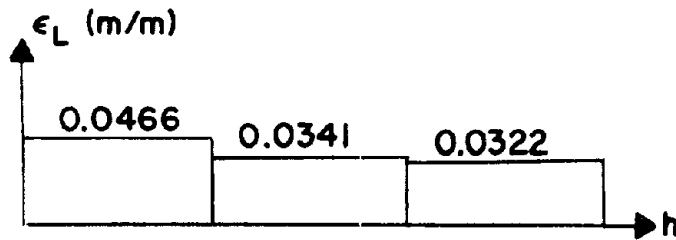


Fig. 5.21b LP 53

$V = 1032$ KN

$\delta_3 = 91.4$ mm

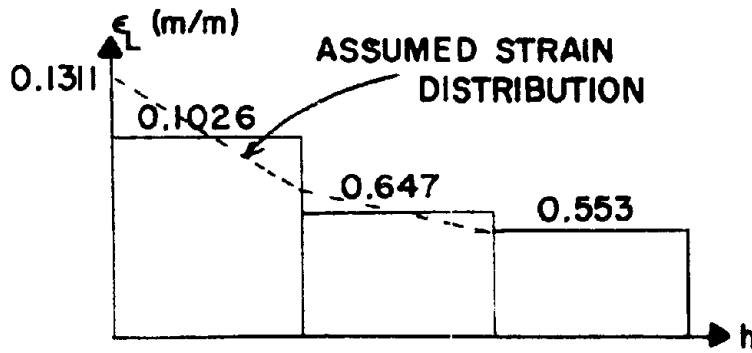


Fig. 5.21c LP 76
(Maximum displacement)

$V = 919$ KN

$\delta_3 = 185$ mm

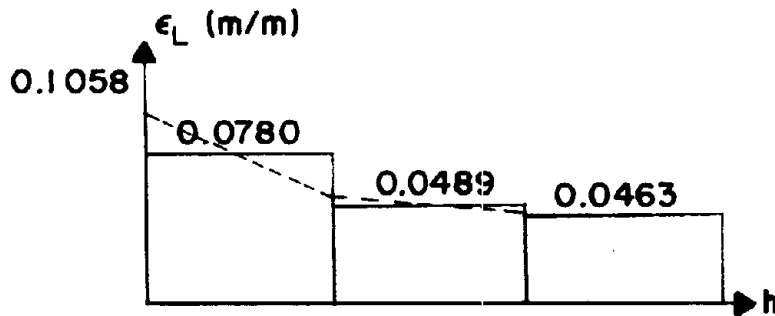


Fig. 5.21d LP 80
(South column buckling)

$V = 343$ KN

$\delta_3 = 114.5$ mm

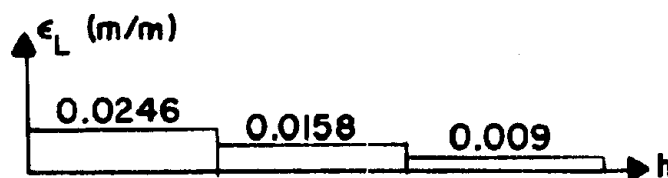


Fig. 5.21e Change in strain from c to d

Fig. 5.21 Average Strain Distribution Along South Column, Specimen 3

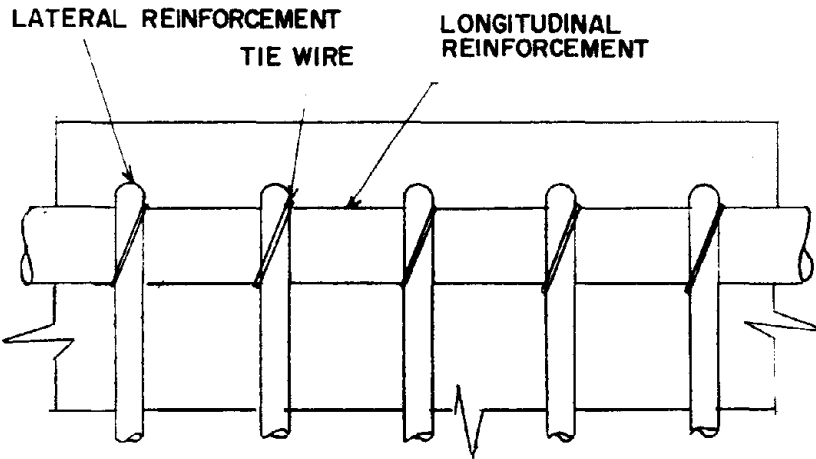


Fig. 5.22a Virgin concrete

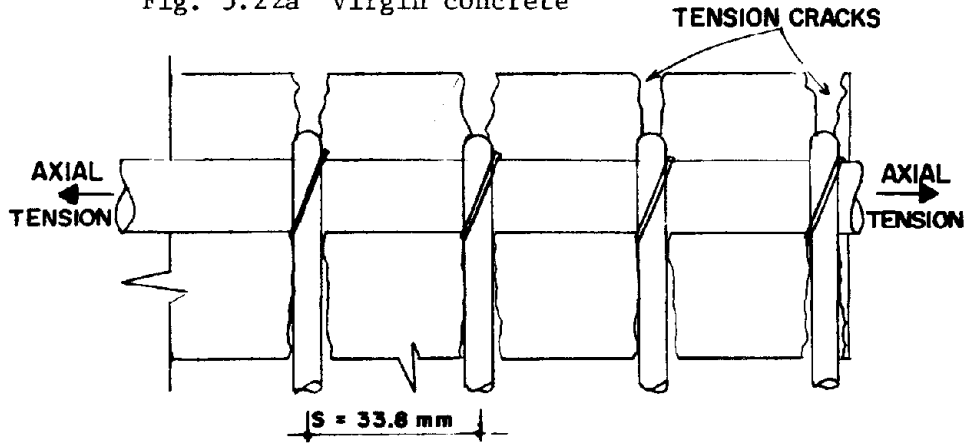


Fig 5.22b After application of tensile force

Fig. 5.22 Crack Spacing

◀ AREA OF CONCRETE IN CONTACT

● #6 STEEL BAR

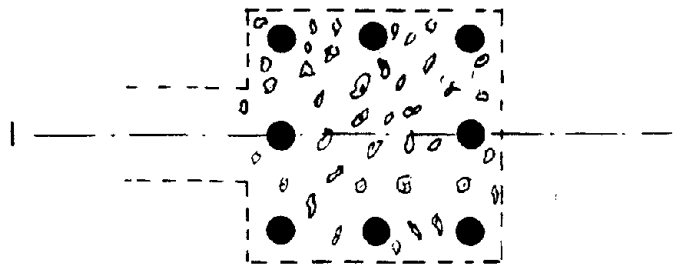


Fig. 5.23 Effective Compressive Section for Boundary Element of Specimen 3 at LP 80

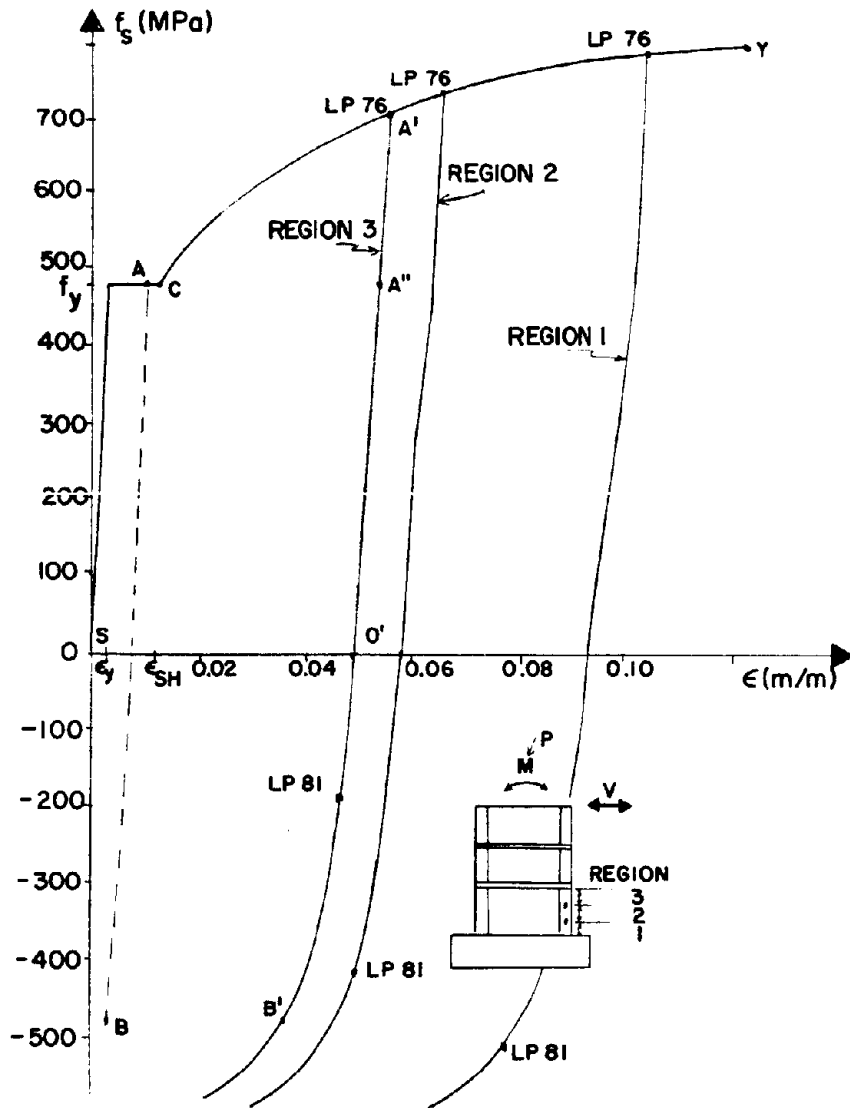


Fig. 5.24 Average Stress-Strain History for Steel in South Boundary Element of Specimen 3

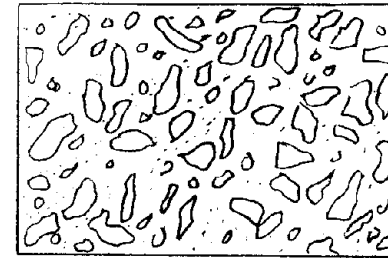


Fig. 5.25a Virgin concrete

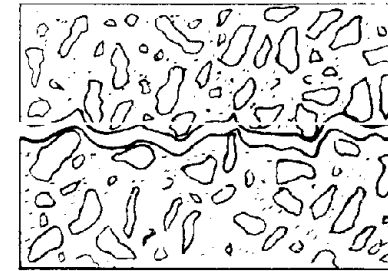


Fig. 5.25b Open crack

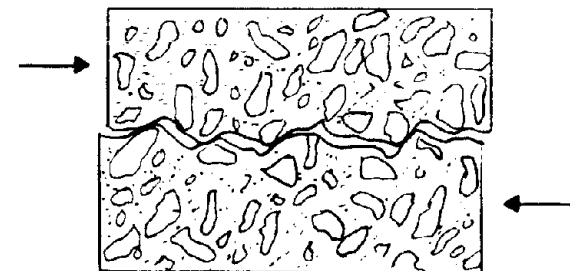


Fig. 5.25c Shear slippage

Fig. 5.25 Shear Slippage at Crack

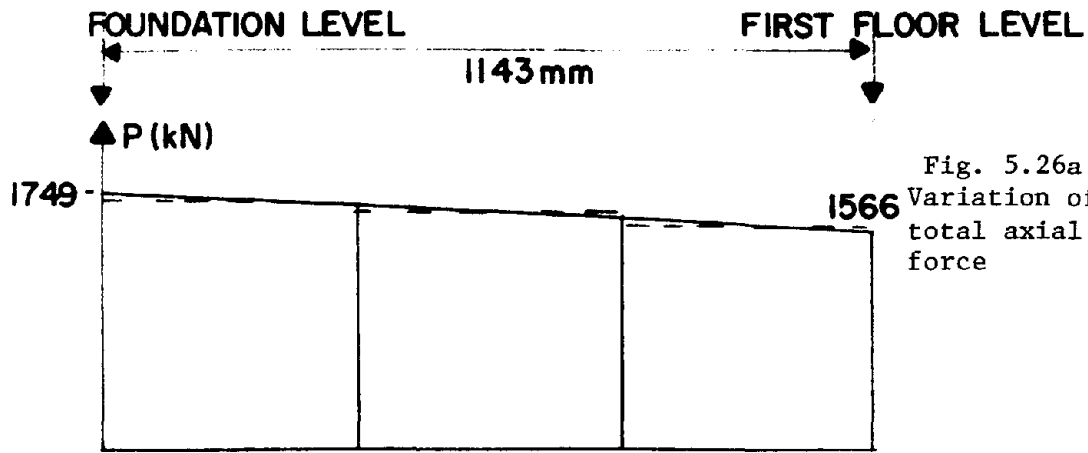


Fig. 5.26a
Variation of
total axial
force

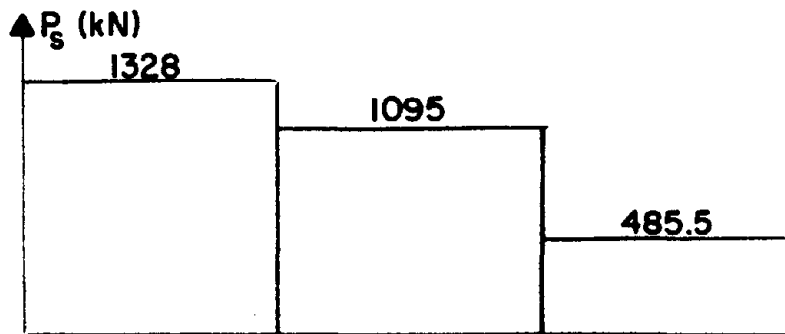


Fig. 5.26b
Force taken by
longitudinal
steel

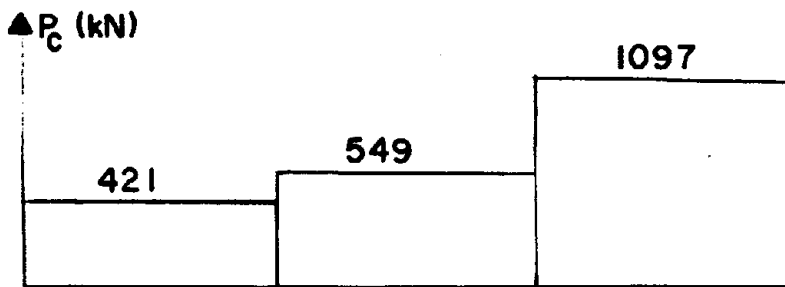


Fig. 5.26c
Force taken by
cracked concrete
5.26a,b

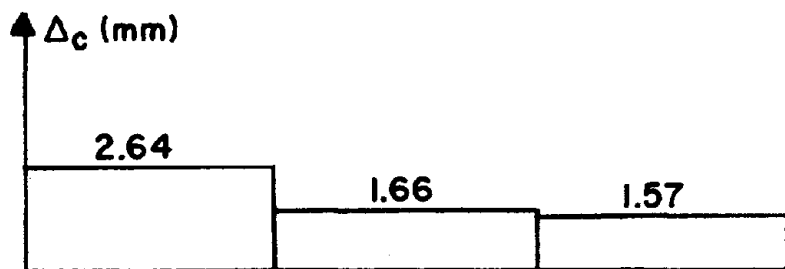


Fig. 5.26d
Average tension
crack widths,

Fig. 5.26 Variation of Axial Force Components and Crack Width Along South Boundary Element at LP 81, Specimen 3

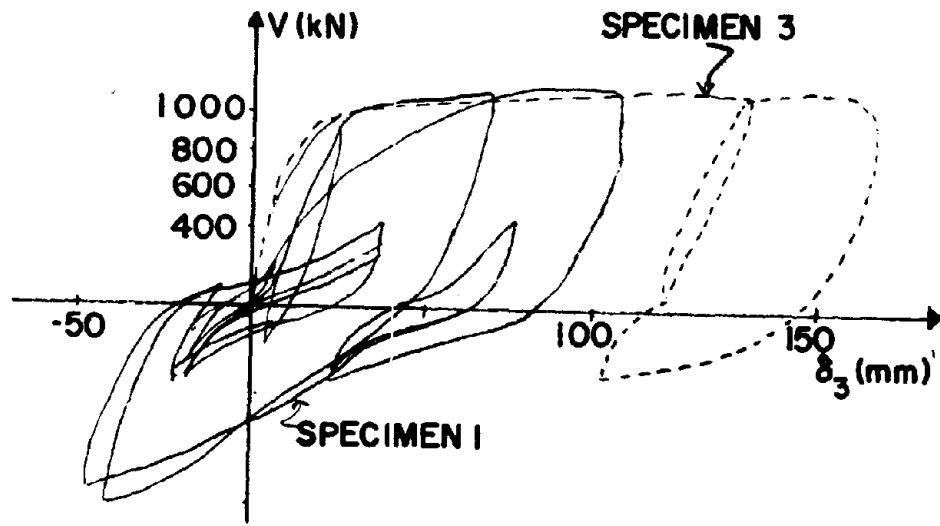


Fig. 5.27 Comparison of $V-\delta_3$ Diagrams for Specimens 1 and 3

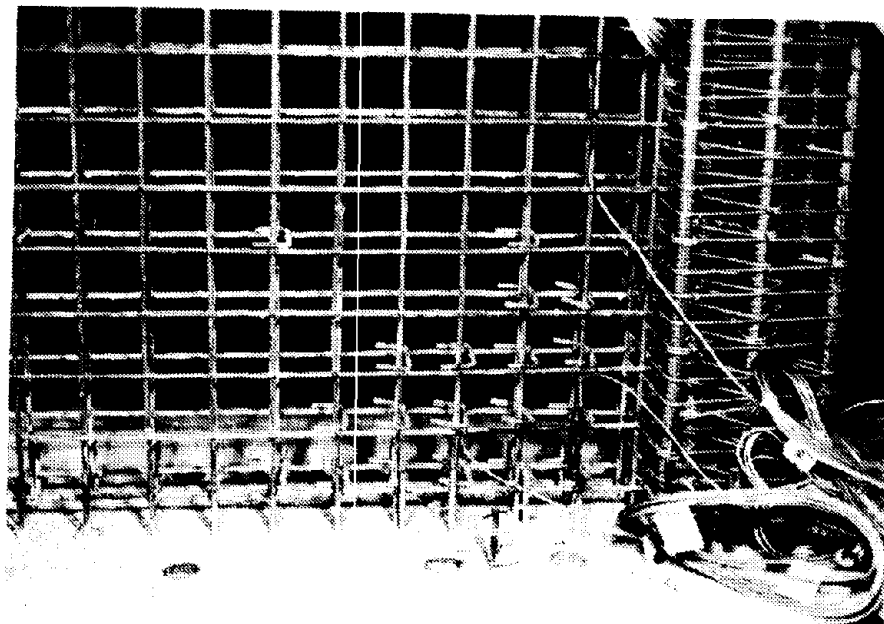


Fig. 5.28 Transverse Hoops in Critical Regions of Panel

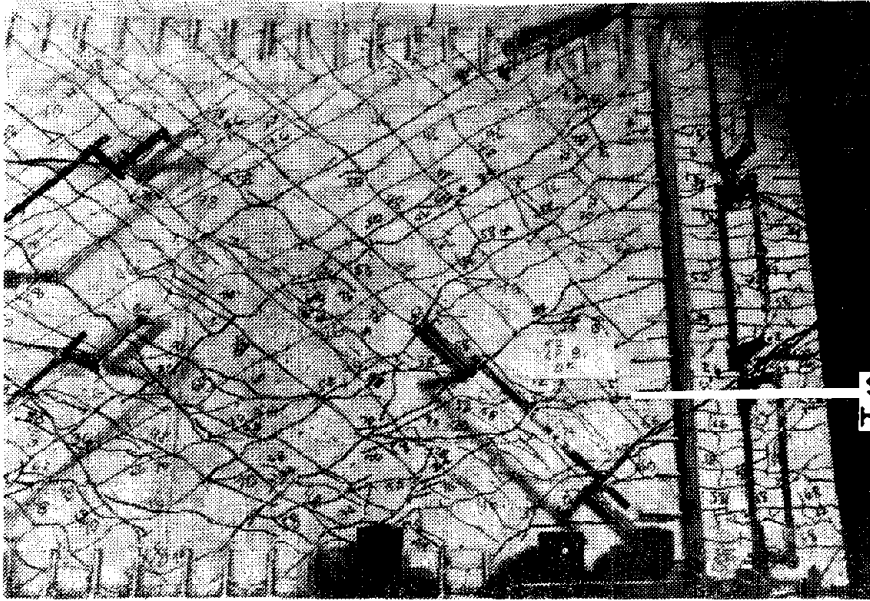


Fig. 5.29a
LP 81

SLIPPAGE ALONG
HORIZONTAL CRACK

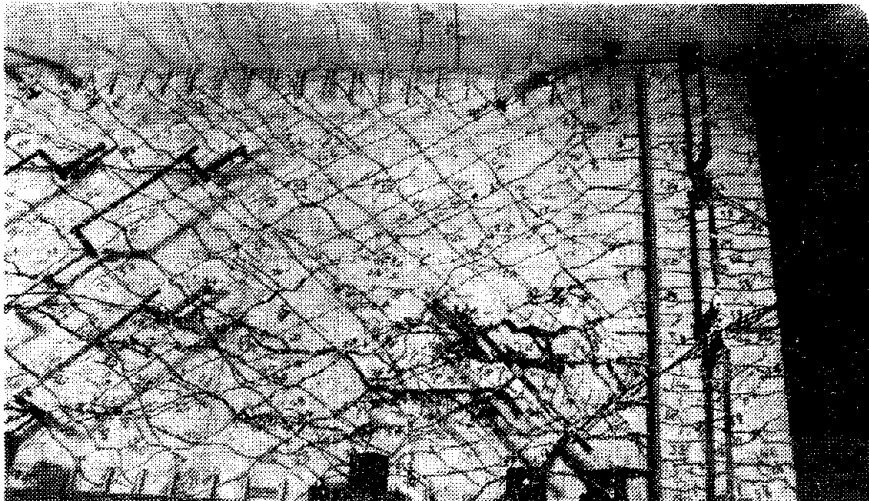


Fig. 5.29b
LP 91-92



Fig. 5.29c
LP 95

Fig. 5.29 Development of Crushing Band

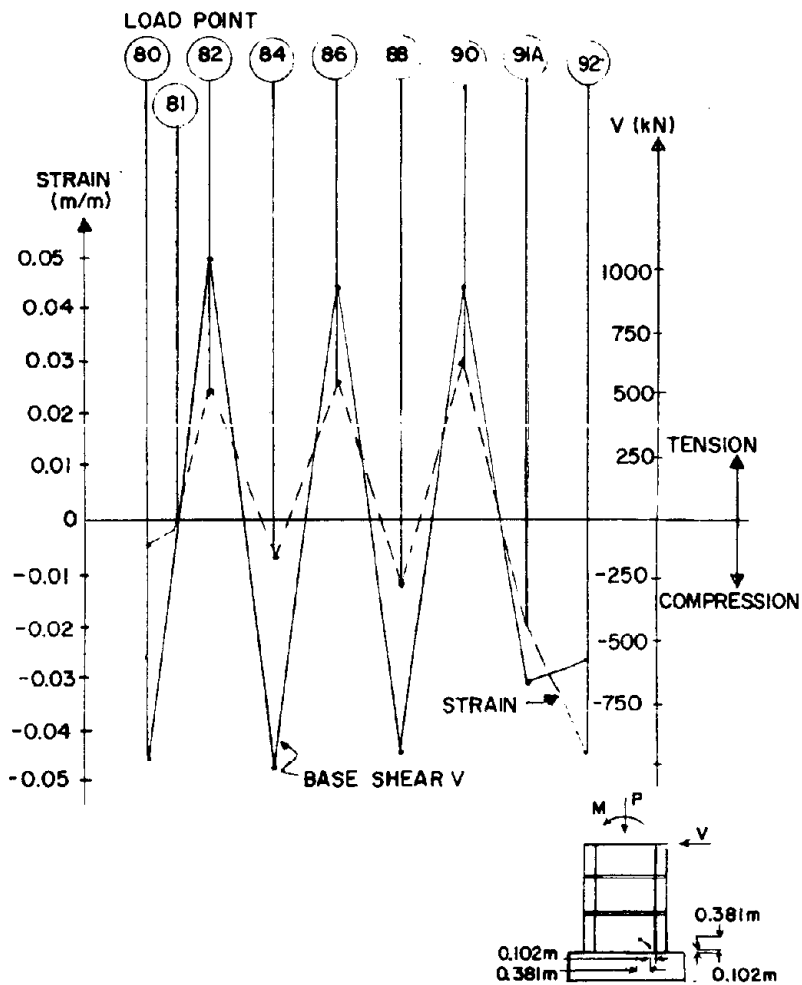


Fig. 5.30 Strain History for Gage W31, Specimen 4

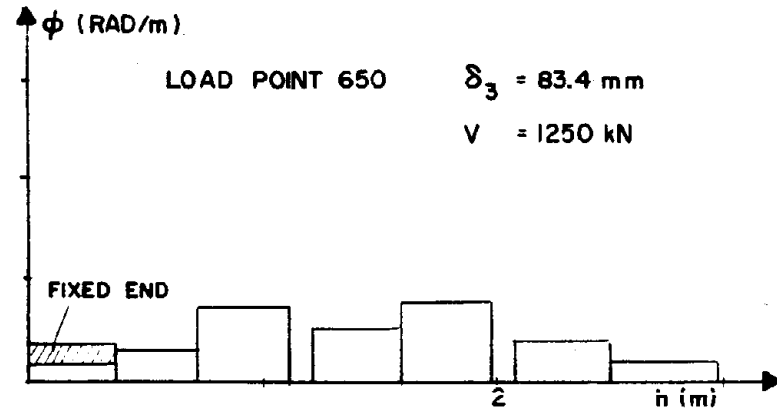


Fig. 5.31a Specimen 4R

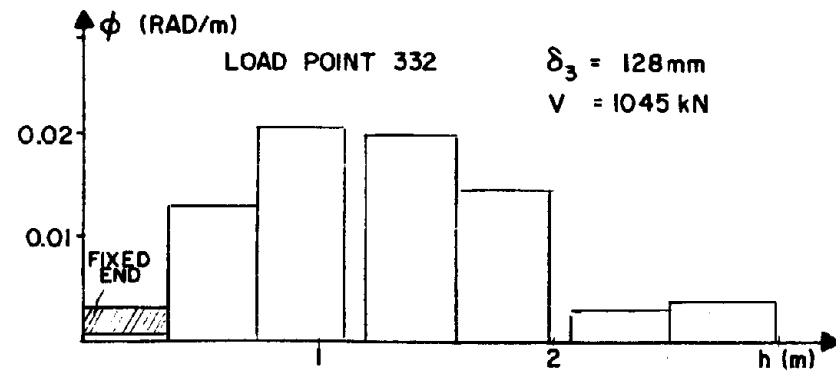


Fig. 5.31b Specimen 3R

Fig. 5.31ab Curvature Distribution at Maximum Displacement

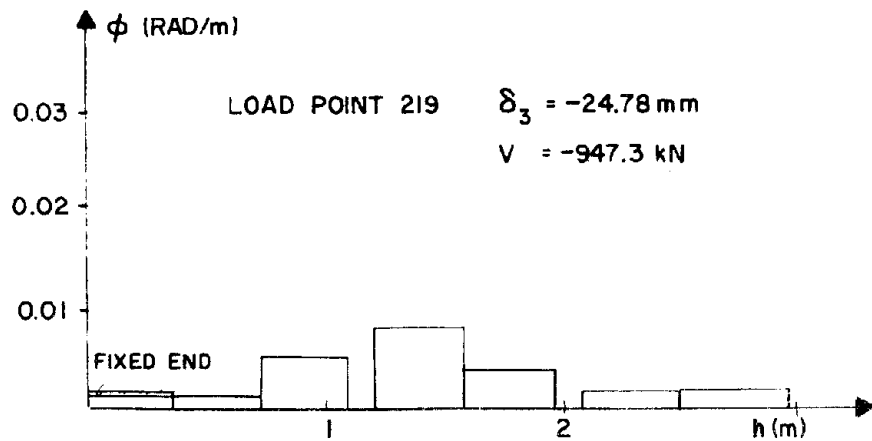


Fig. 5.31c Specimen 5R

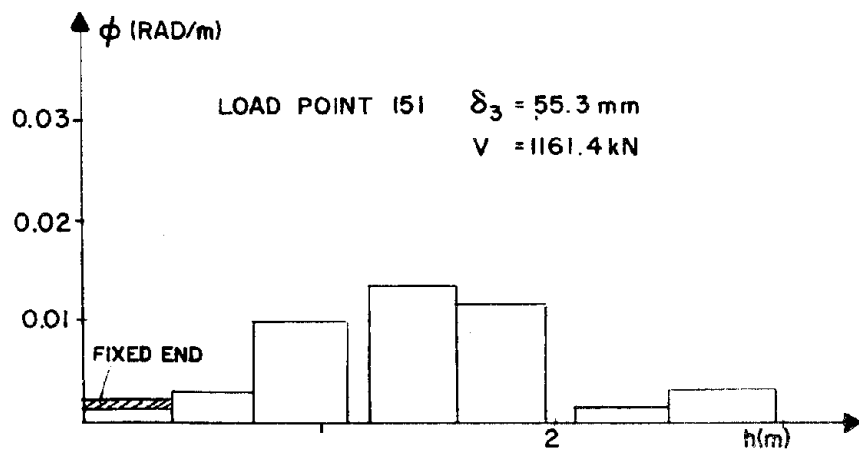


Fig. 5.31d Specimen 6R

Fig. 5.31cd Curvature Distribution at LP 151

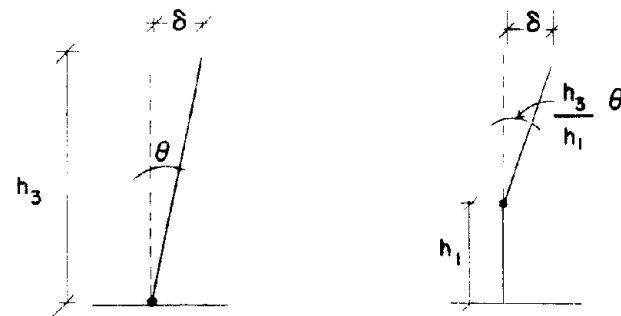


Fig. 5.32 Rotational Ductility Demand in Repaired Walls

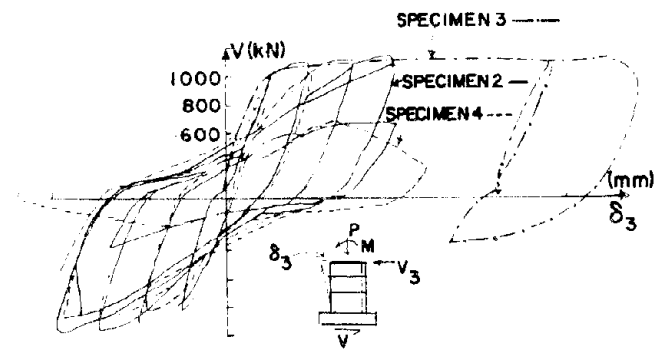


Fig. 5.33 Comparison of $V-\delta_3$ Diagrams for Specimens 1, 4, and 3

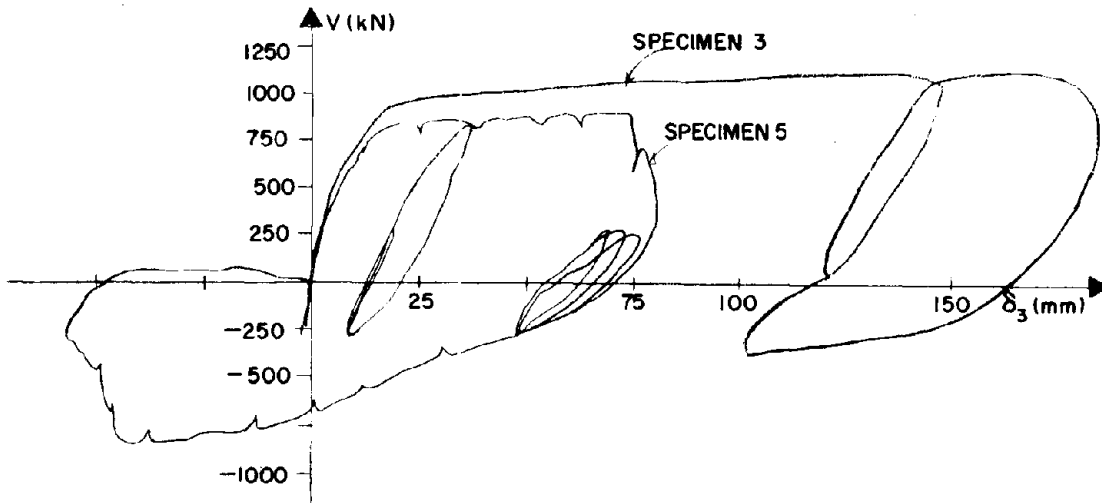


Fig. 5.34a Specimens 3 and 5

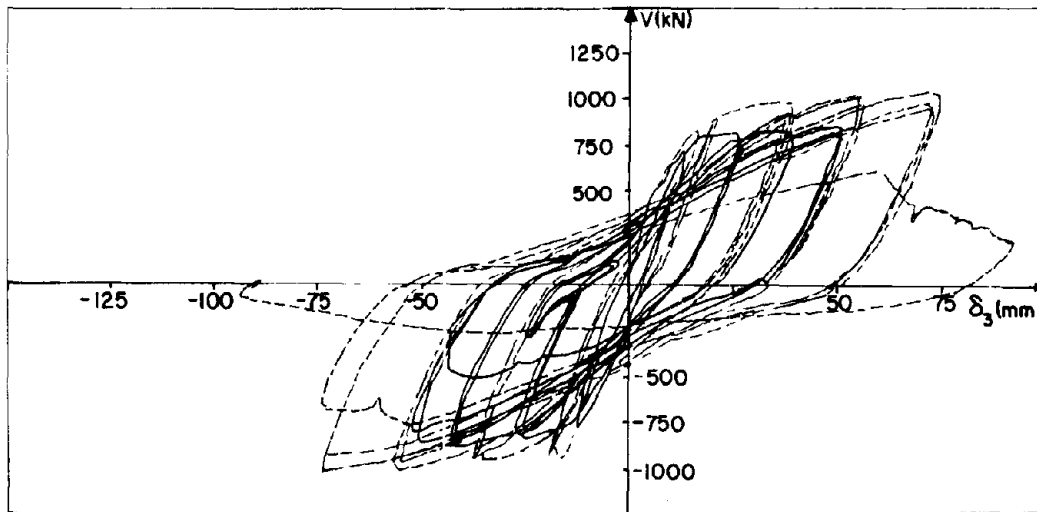
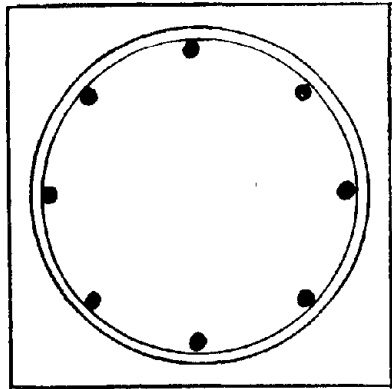
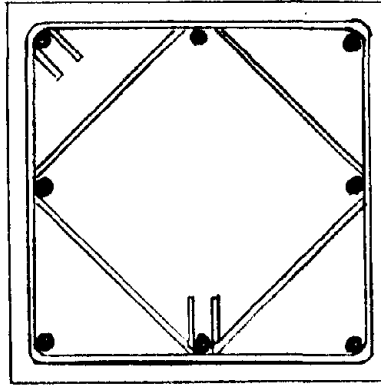
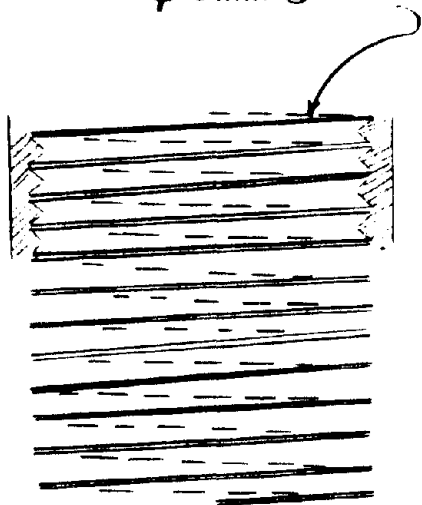


Fig. 5.34b Specimens 4 and 6

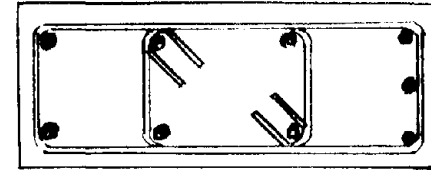
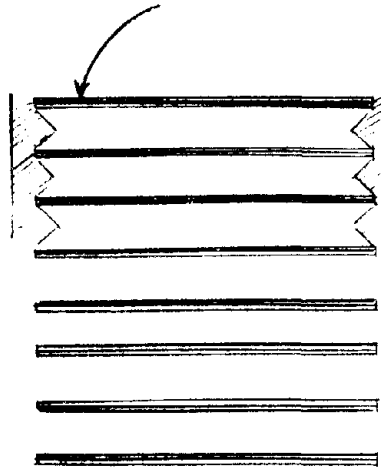
Fig. 5.34 Comparison of $V-\delta_3$ Diagrams



ϕ 5mm @ 21mm



GAGE No.7 @ 34mm



45°
SPALLED AREA

GAGE No.7 @ 34mm

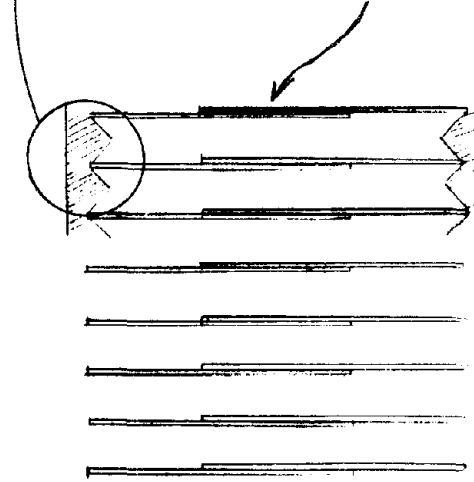


Fig. 5.35a Spiral for Specimens 1 and 2

Fig. 5.35b Hoops for Specimens 3 and 4

Fig. 5.35c Hoops for Specimens 5 and 6

Fig. 5.35 Confinement Arrangements for Boundary Elements of Structural Walls

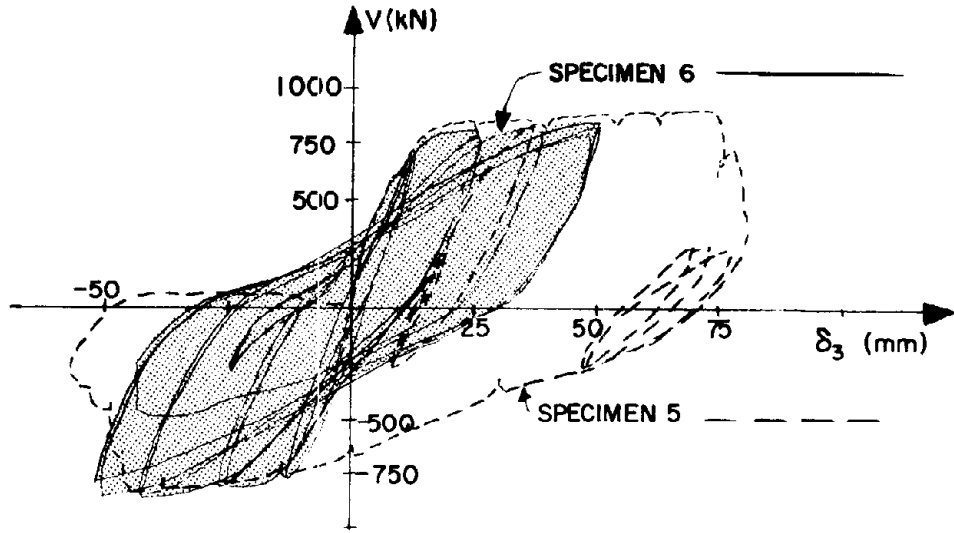


Fig. 5.36 Comparison of V - δ_3 Diagrams, Specimens 5 and 6

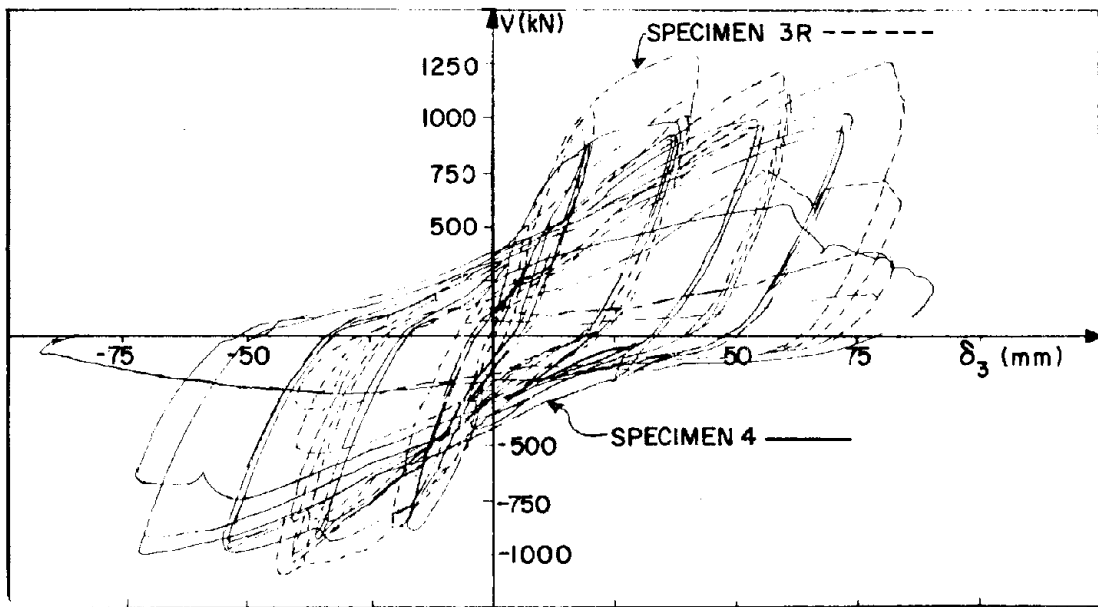


Fig. 5.37 Comparison of V - δ_3 Diagrams, Specimens 4 and 3R

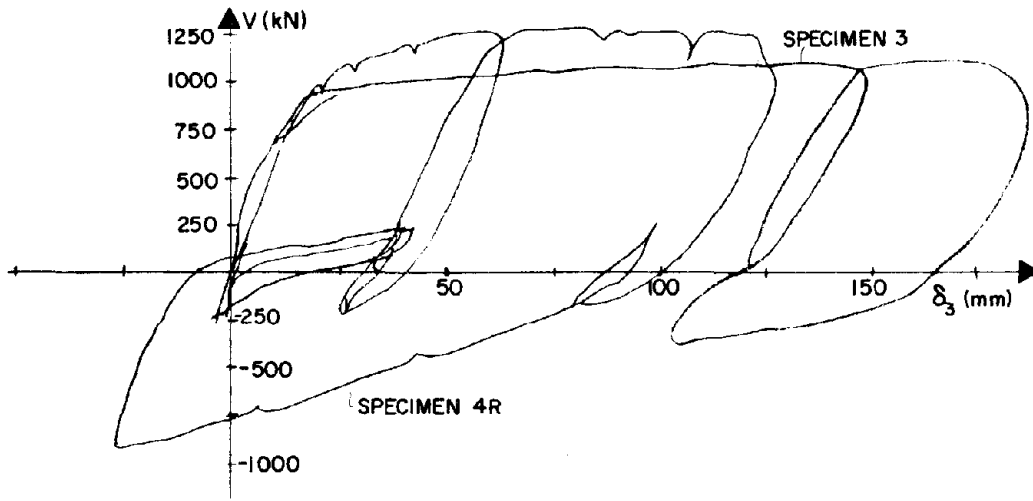


Fig. 5.38 Comparison of $V-\delta_3$ Diagrams, Specimens 3 and 4R

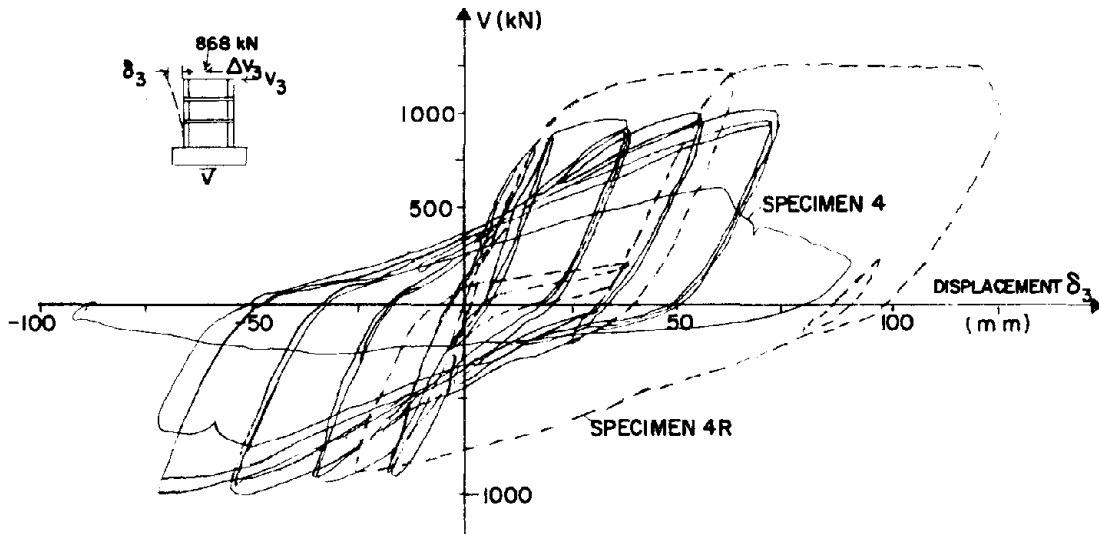


Fig. 5.39 Comparison of $V-\delta_3$ Diagrams, Specimens 4 and 4R

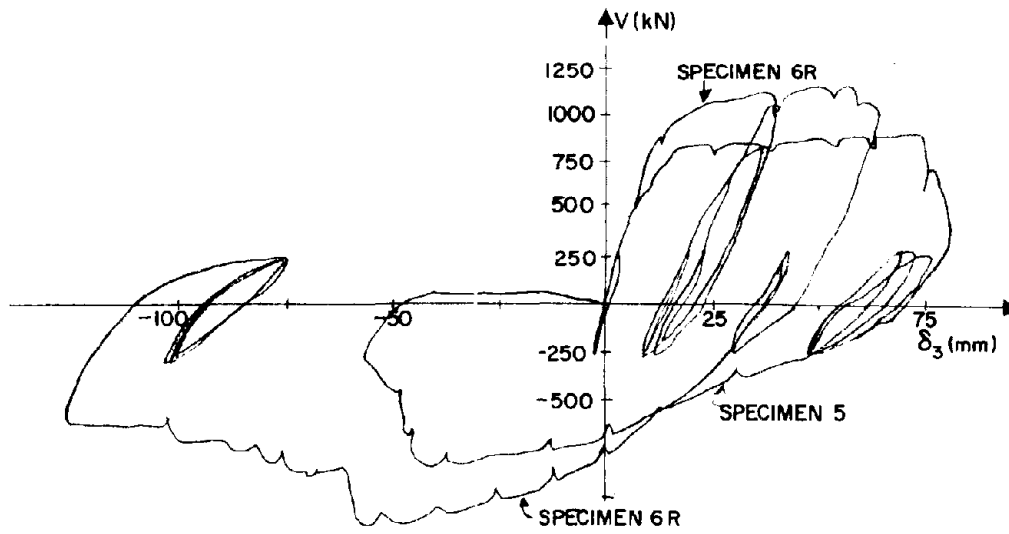


Fig. 5.40 Comparison of V - δ_3 Diagrams, Specimens 5 and 6R

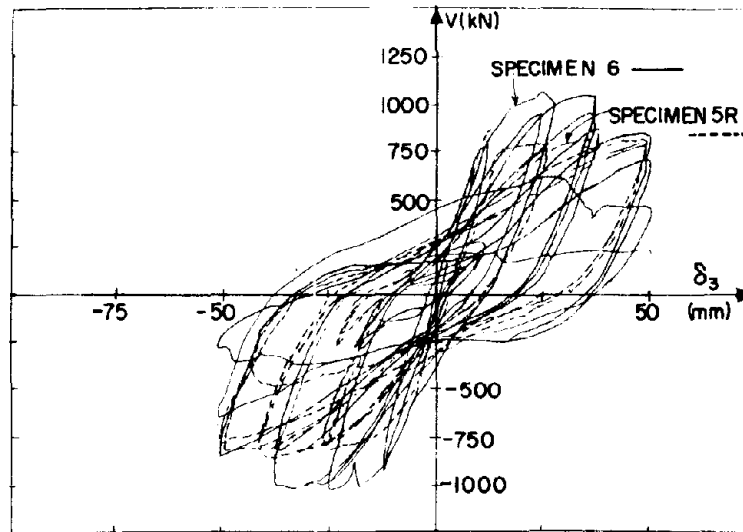


Fig. 5.41 Comparison of V - δ_3 Diagrams, Specimens 6 and 5R

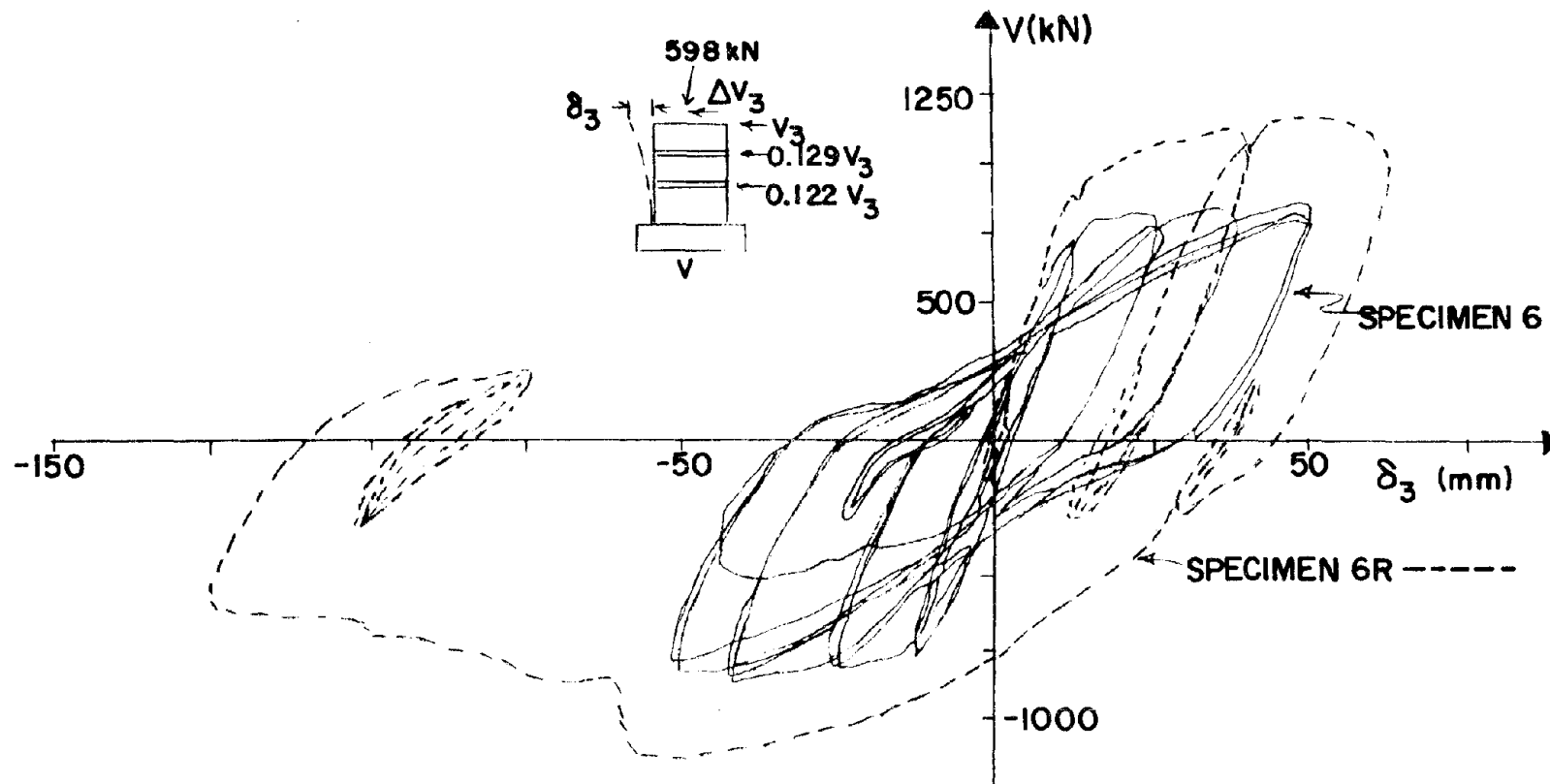


Fig. 5.42 Comparison of V - δ_3 Diagrams, Specimens 6 and 6R

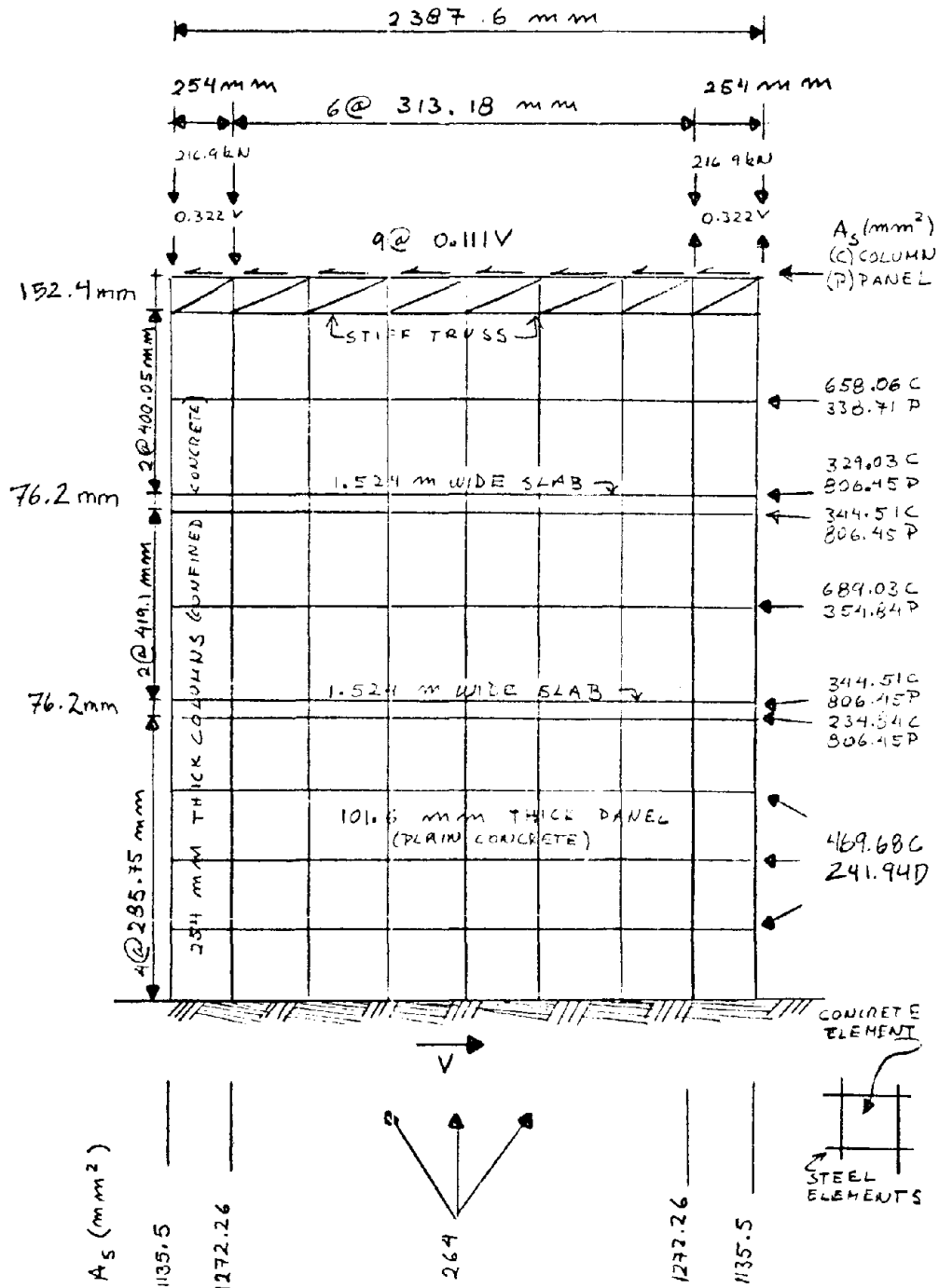


Fig. 6.1 Finite Element Modelling of Framed Wall for Monotonic Loading

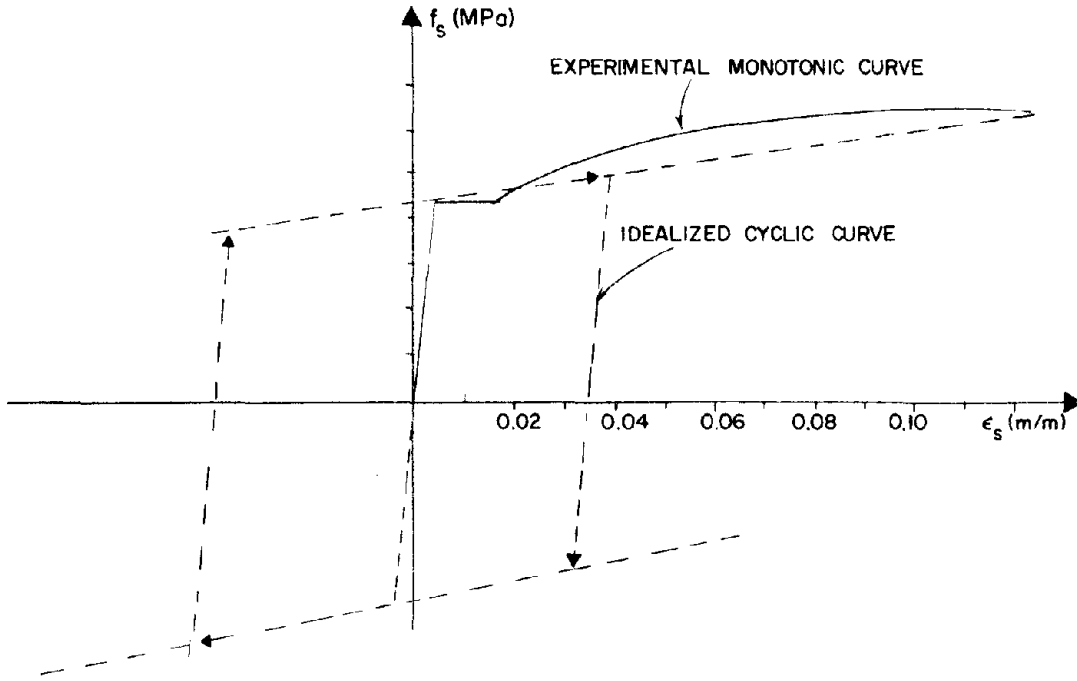


Fig. 6.2 Idealized Cyclic Stress-Strain Curve for No. 6 and No. 2 Steel Bars

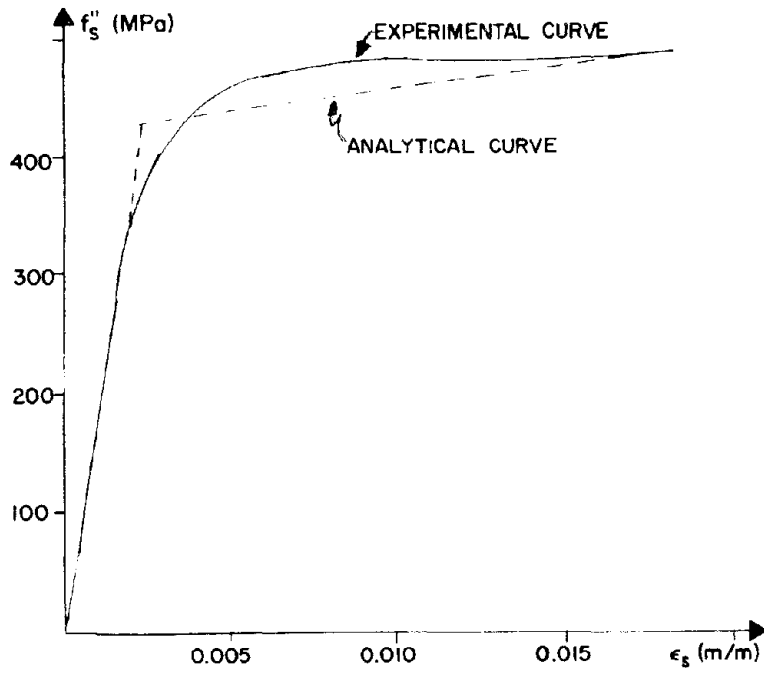


Fig. 6.3 Stress-Strain Diagram for Confining Reinforcement (Gage No. 7 Wire)

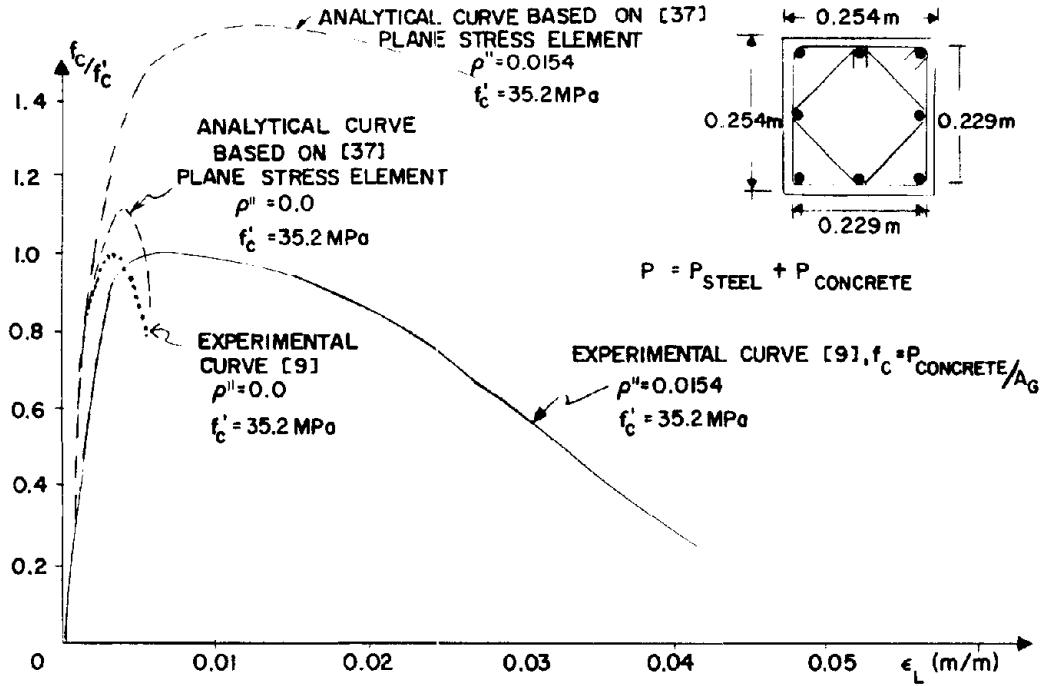


Fig. 6.4 f_c/f'_c vs. ϵ_L for Boundary Element

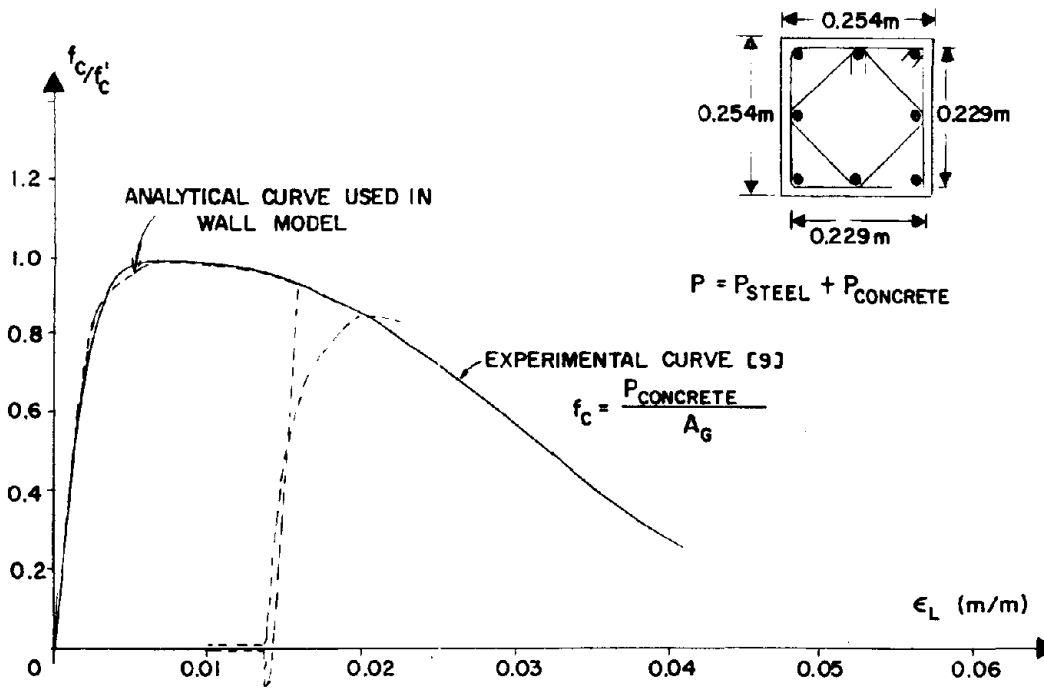


Fig. 6.5 f_c/f'_c vs. ϵ_L for Boundary Element

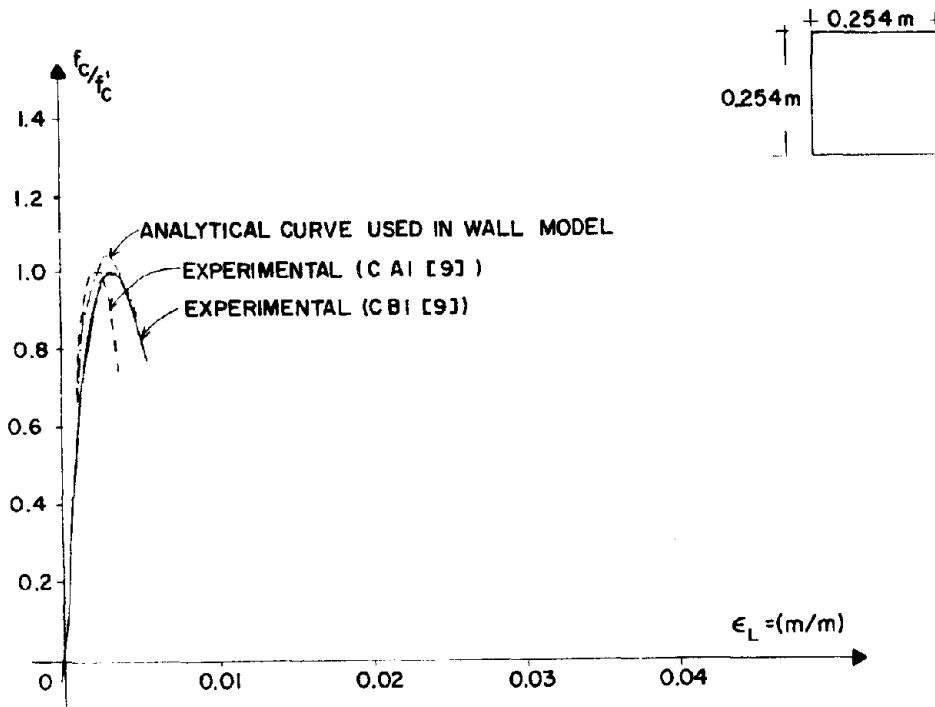


Fig. 6.6 f_c/f'_c vs. ϵ_L for Plain Concrete

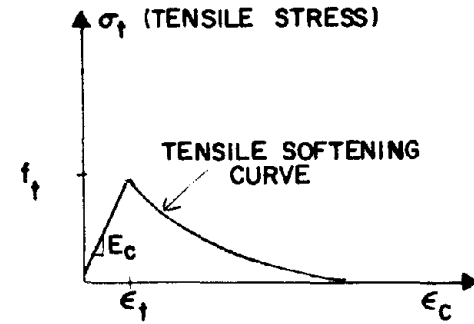


Fig. 6.7a Experimental Ref. 56

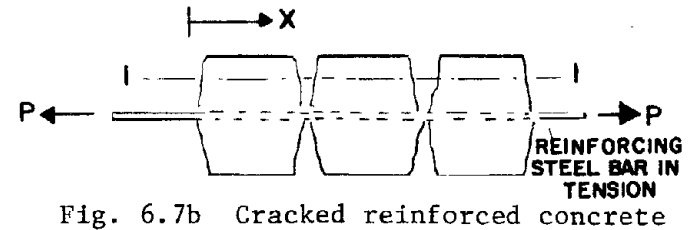


Fig. 6.7b Cracked reinforced concrete



Fig. 6.7c Concrete stress distribution along AXIS 1-1

Fig. 6.7 Tensile Softening

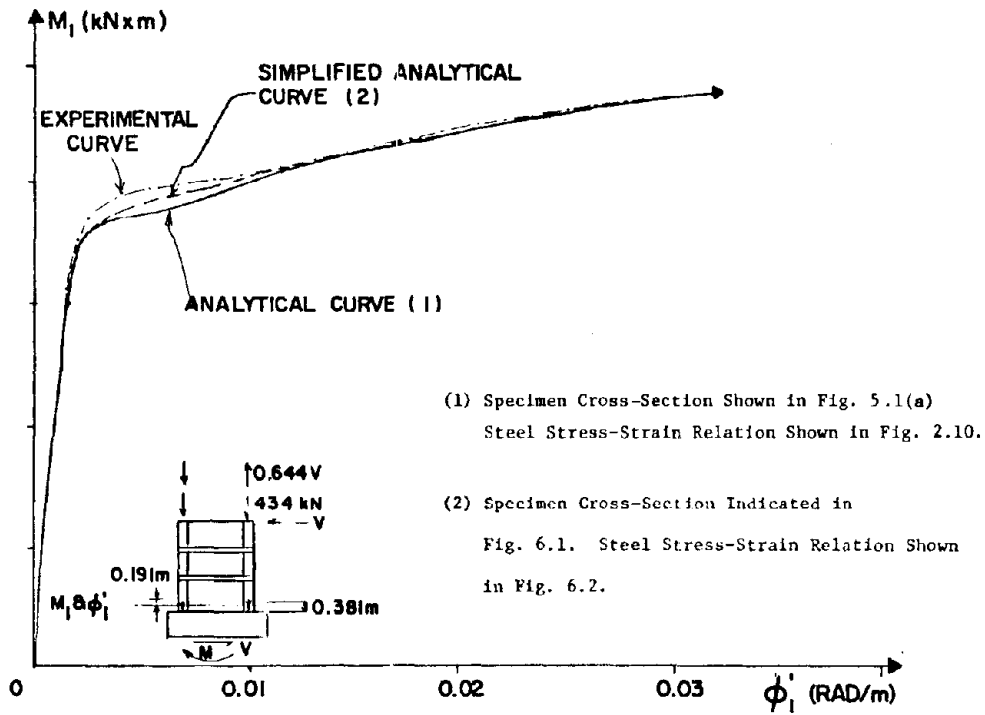


Fig. 6.8 Effect of Different Assumptions on $M-\delta$ Relation for Specimens

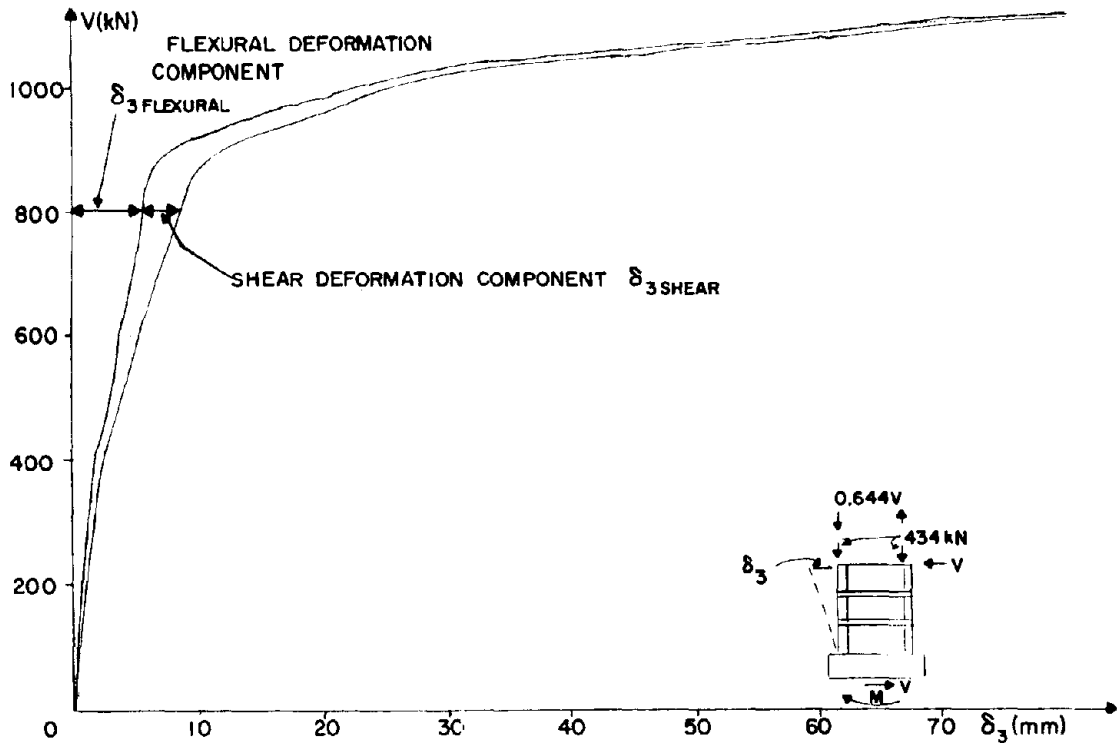


Fig. 6.9a Analytical force-displacement curve, Specimen 3

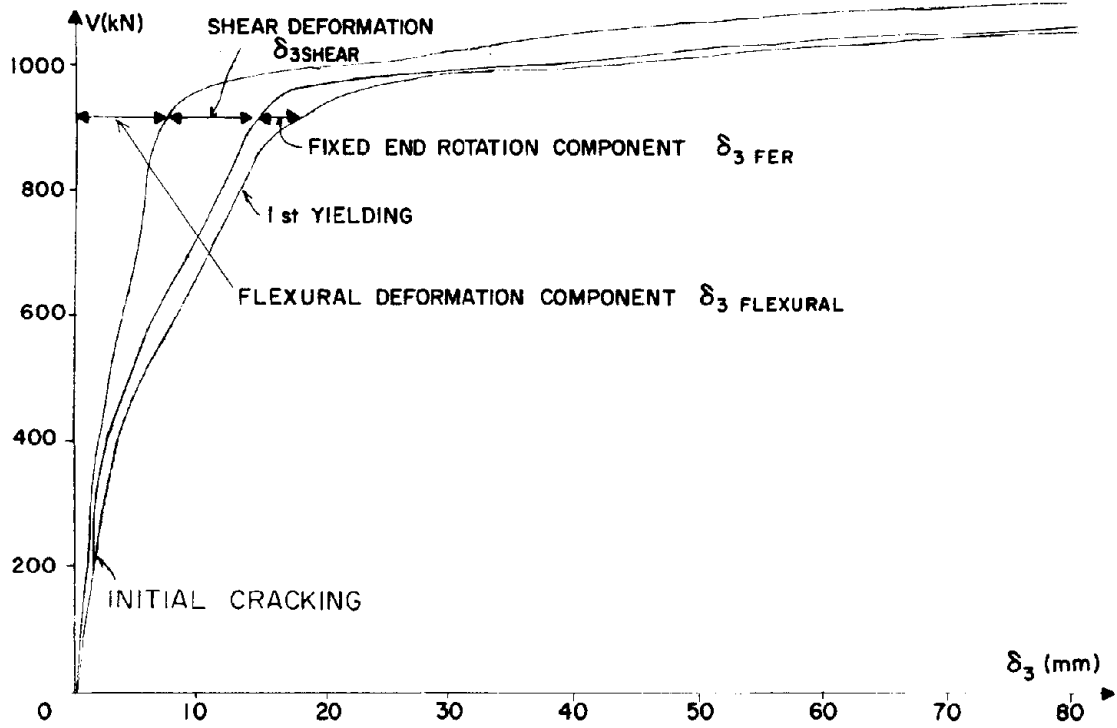


Fig. 6.9b Experimental force-displacement curve, Specimen 3

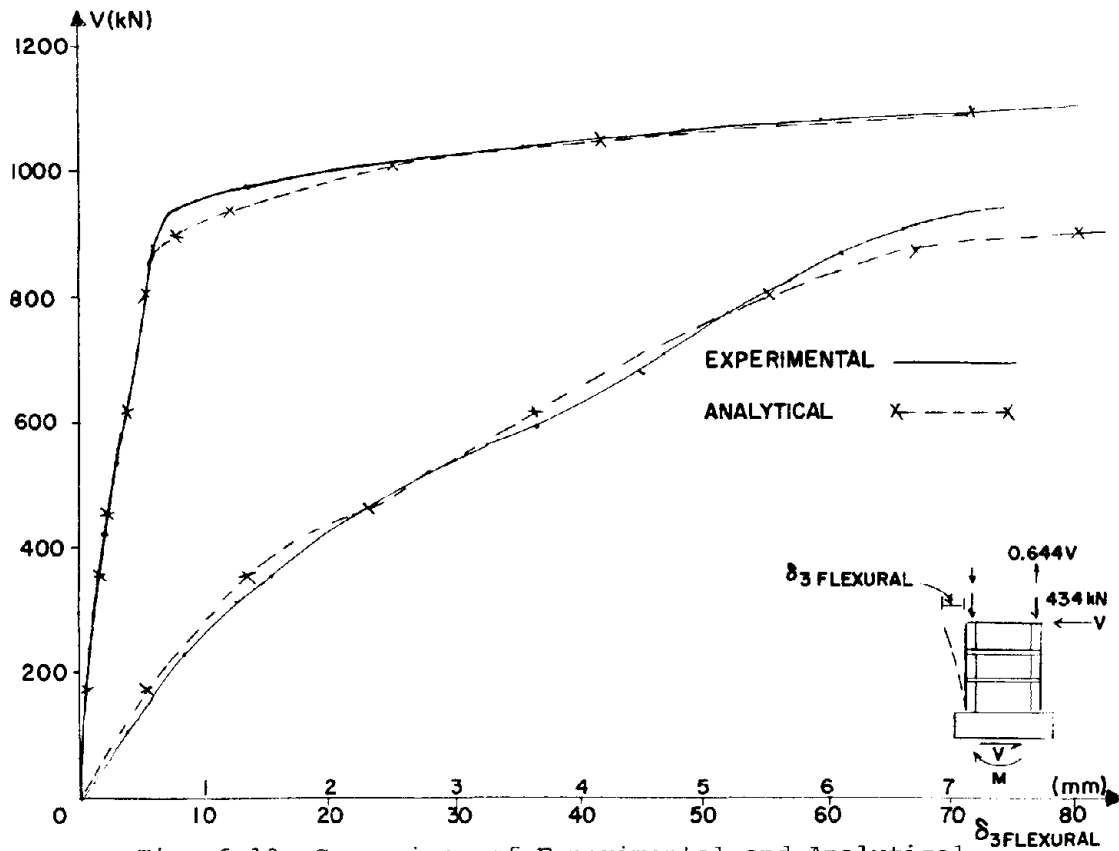


Fig. 6.10 Comparison of Experimental and Analytical Flexural Displacement Component, Specimen 3

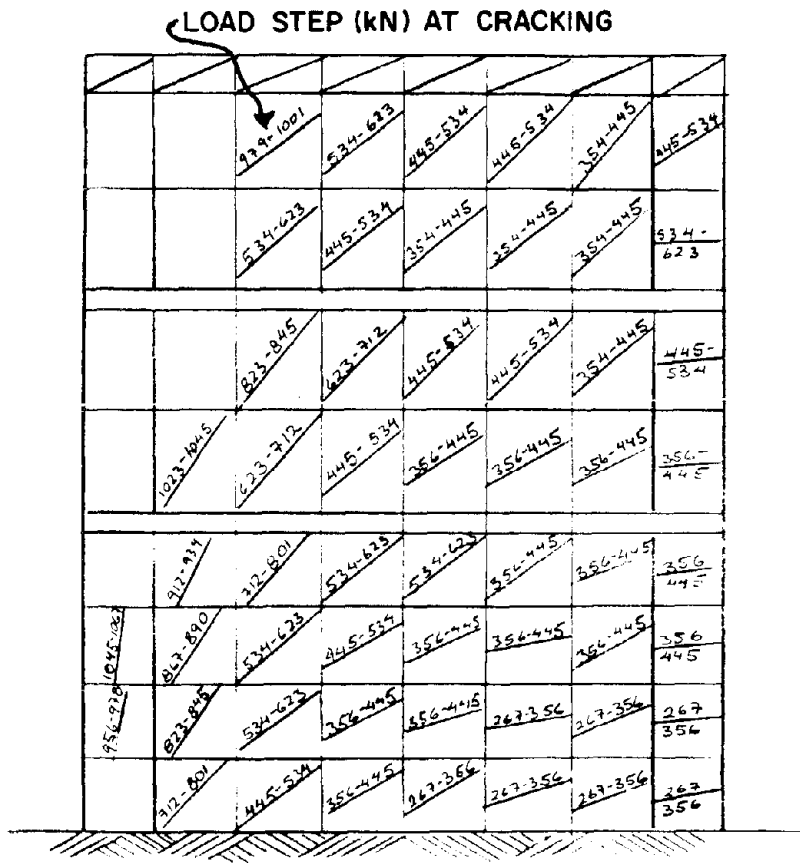


Fig. 6.11a Crack Pattern Analytical Prediction, Specimen 3

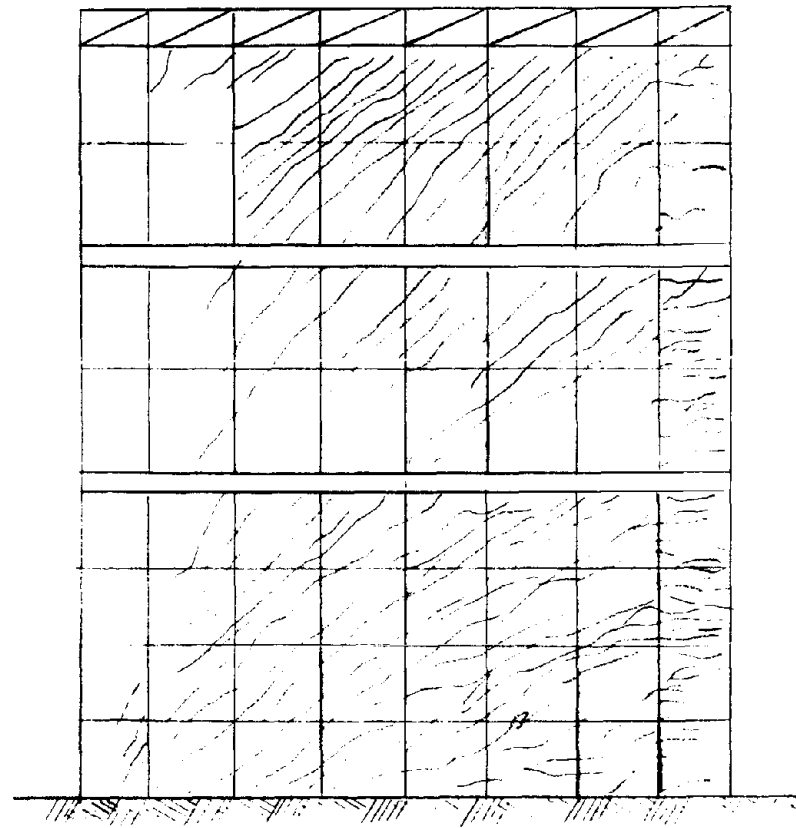


Fig. 6.11b Experimentally Obtained Crack Pattern, Specimen 3

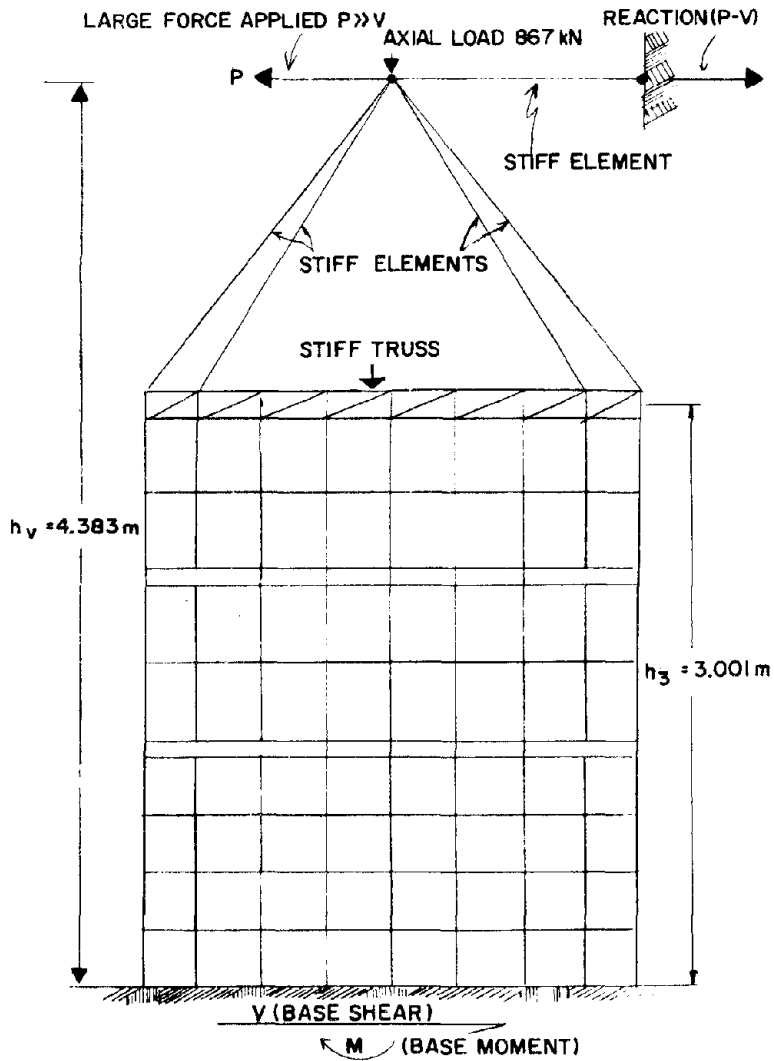


Fig. 6.12 Finite Element Modelling of Framed Wall for Displacement-Controlled Cyclic Loading

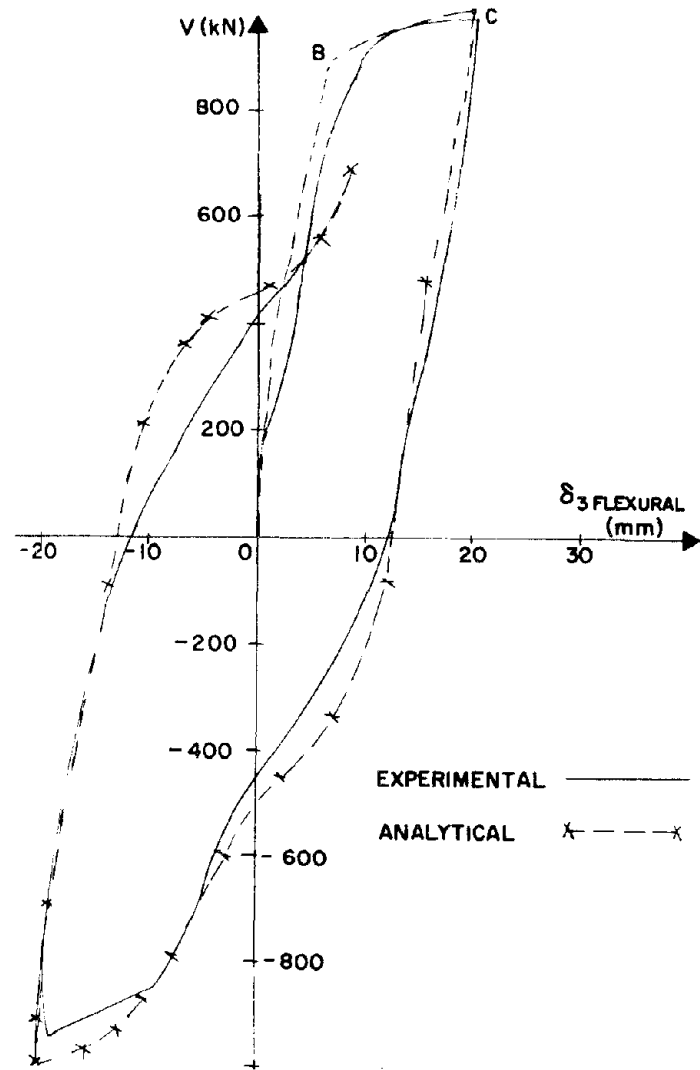


Fig. 6.13 Comparison of Experimental and Analytical Flexural Deformations, Specimen 4

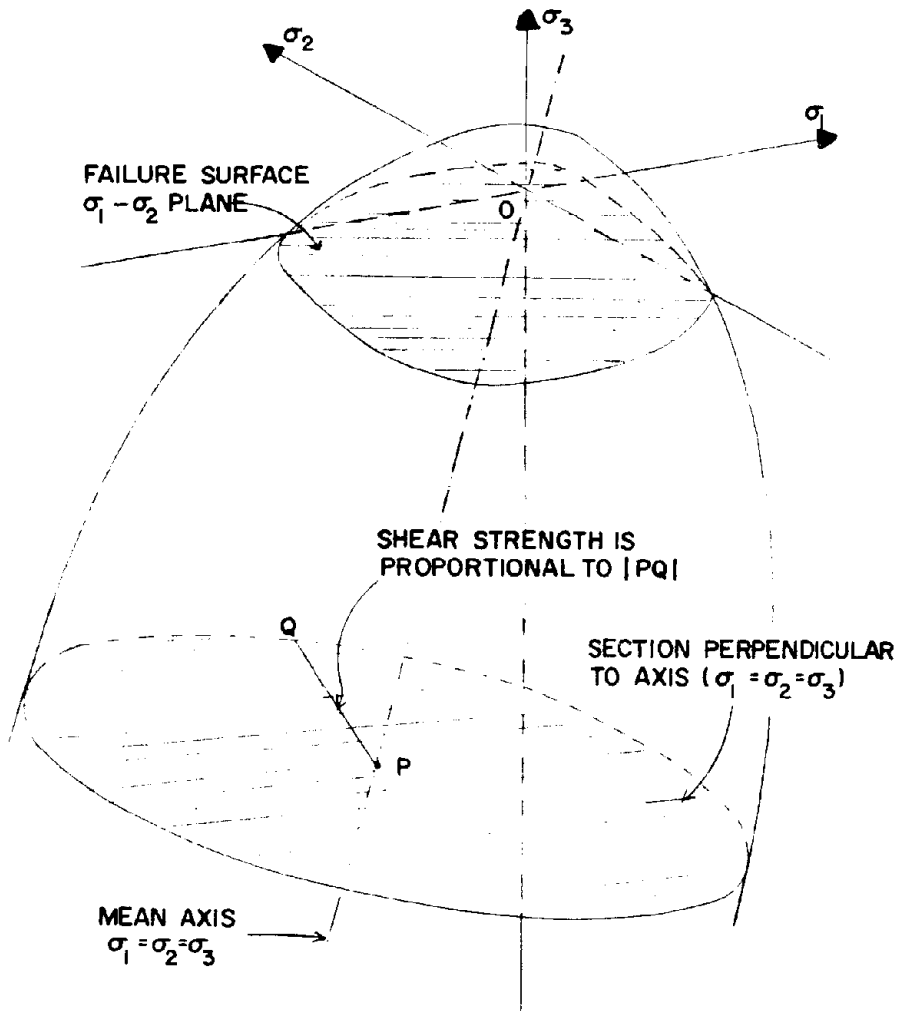


Fig. 6.14 Concrete Failure Surface in Three-Dimensional Stress Space

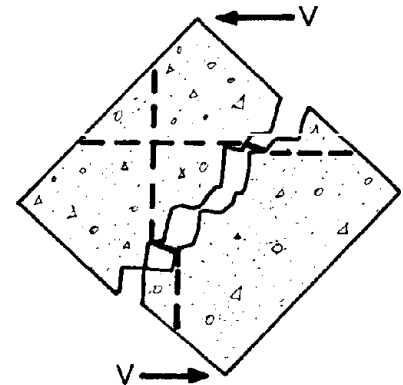


Fig. 6.15 Kinking Action in Panel Steel

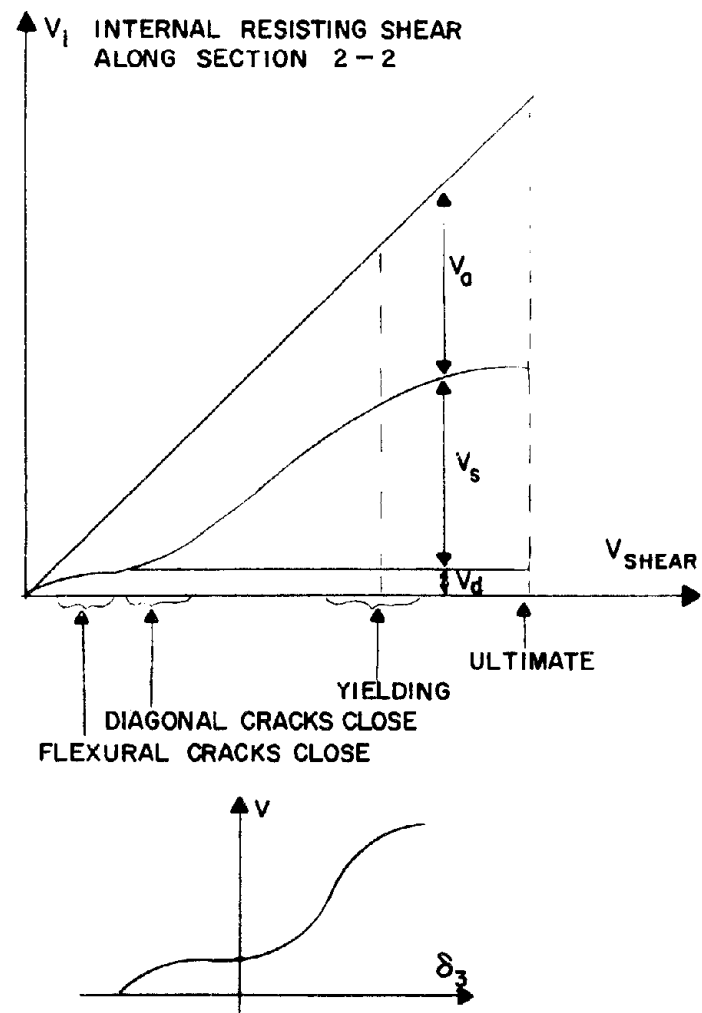
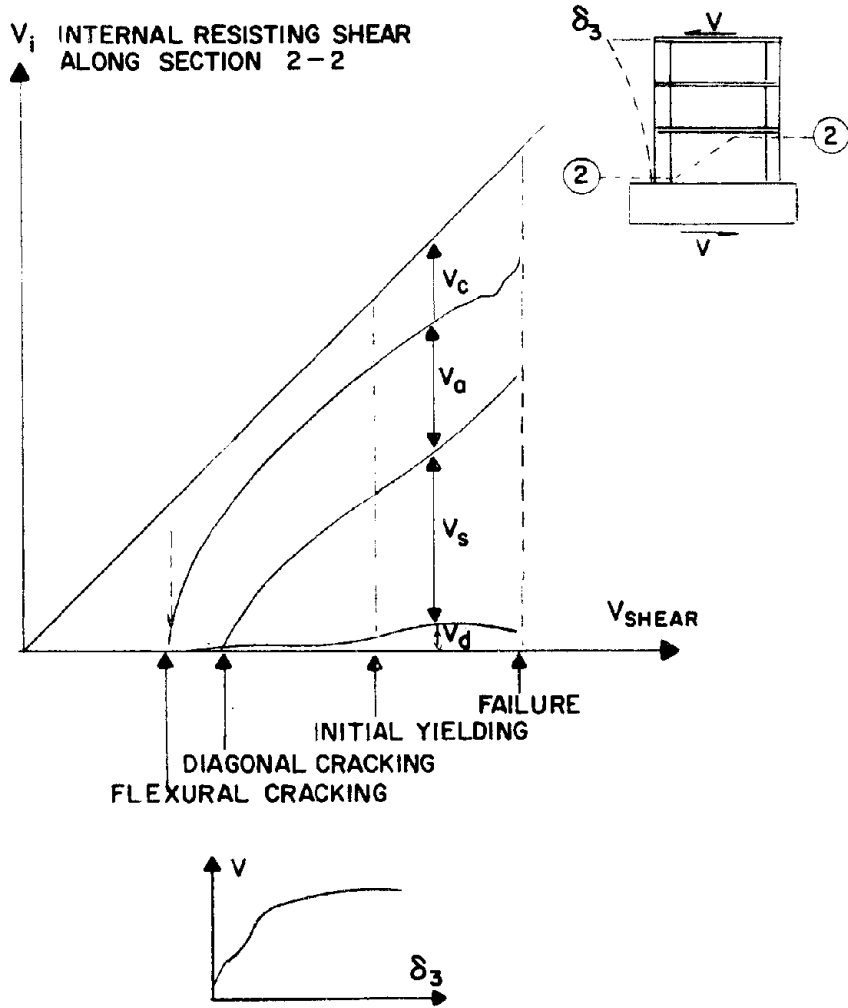


Fig. 6.16 Internal Shear Resisting Mechanisms

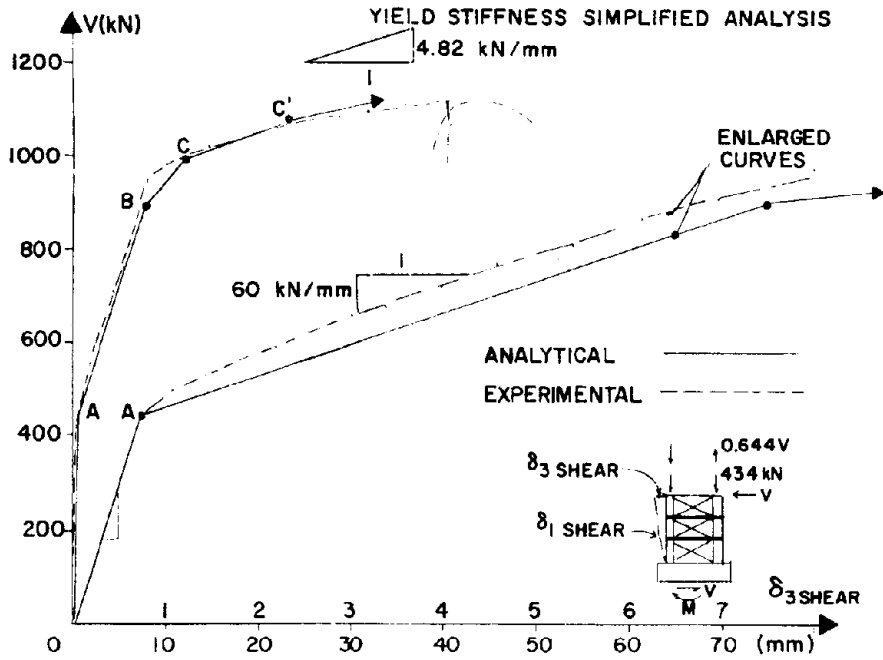


Fig. 6.17a Comparison of Experimental and Analytical Third-Floor Displacement Due to Shear Deformations, Specimen 3

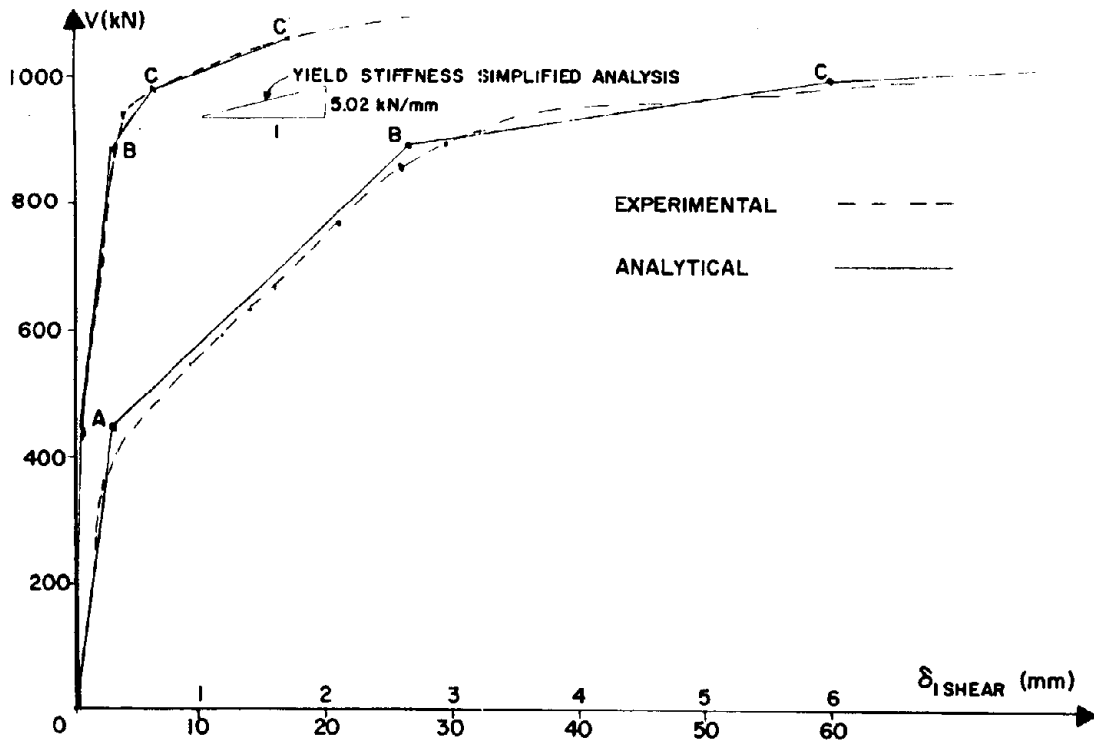


Fig. 6.17b Comparison of Experimental and Analytical First-Floor Displacements Due to Shear Deformations, Specimen 3

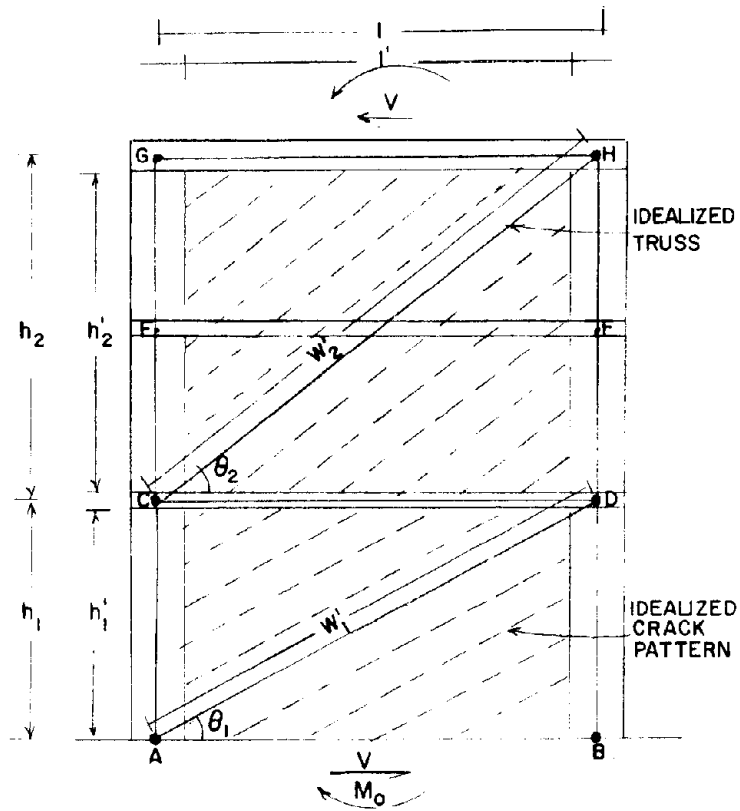


Fig. 6.18a Idealized Crack Pattern and Shear Deformation of Cracked Wall

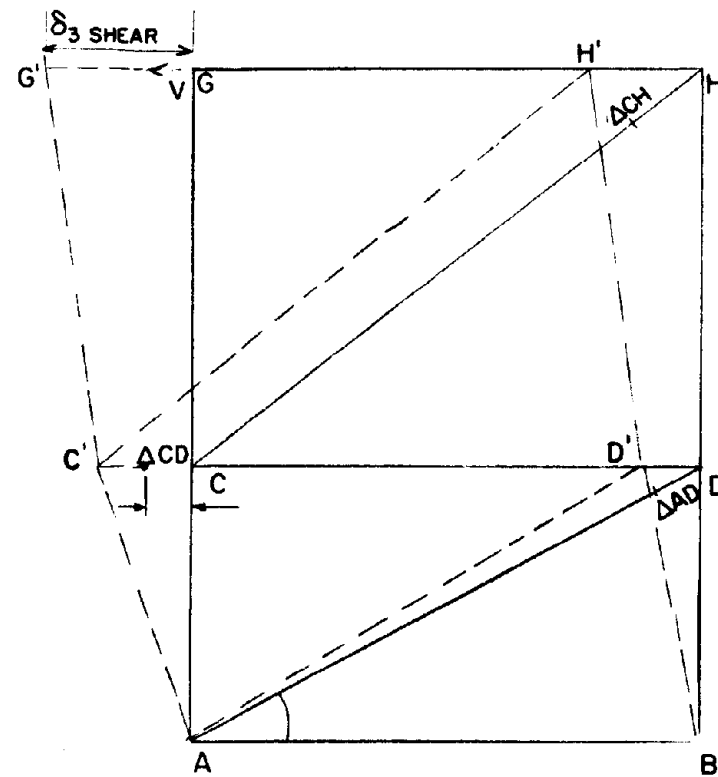


Fig. 6.18b Shear Deformation (Before Yield)

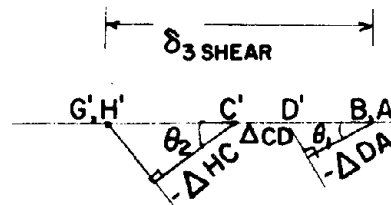


Fig. 6.18c Williot's Diagram

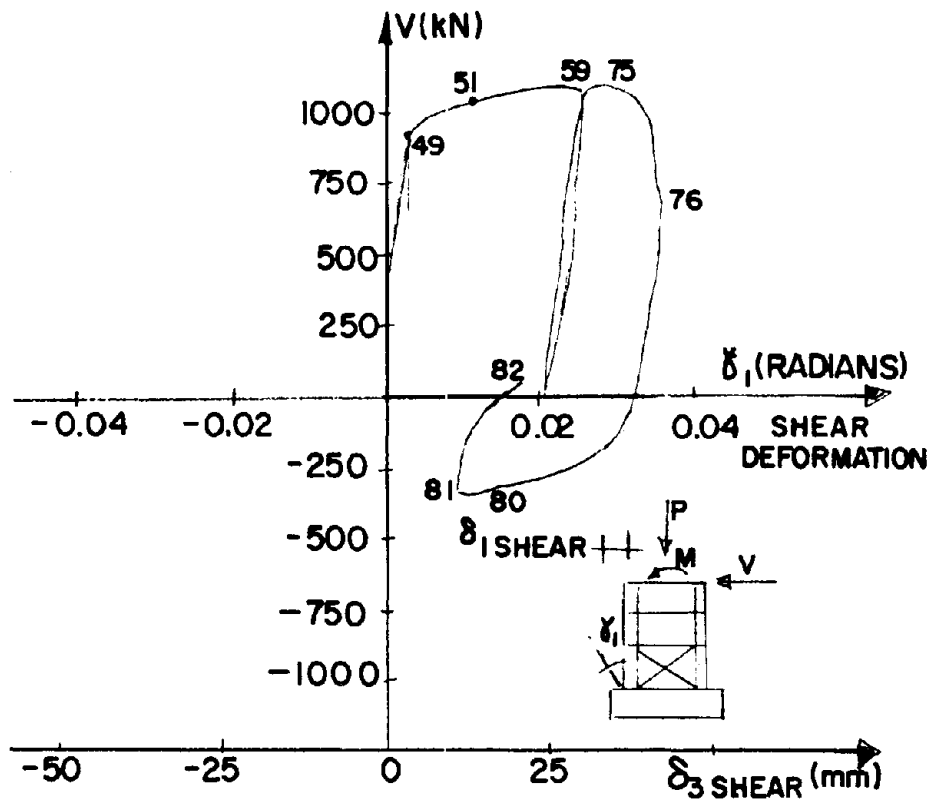


Fig. 6.19a Shear Deformation for First-Story Framed Wall (Monotonic Loading), Specimen 3

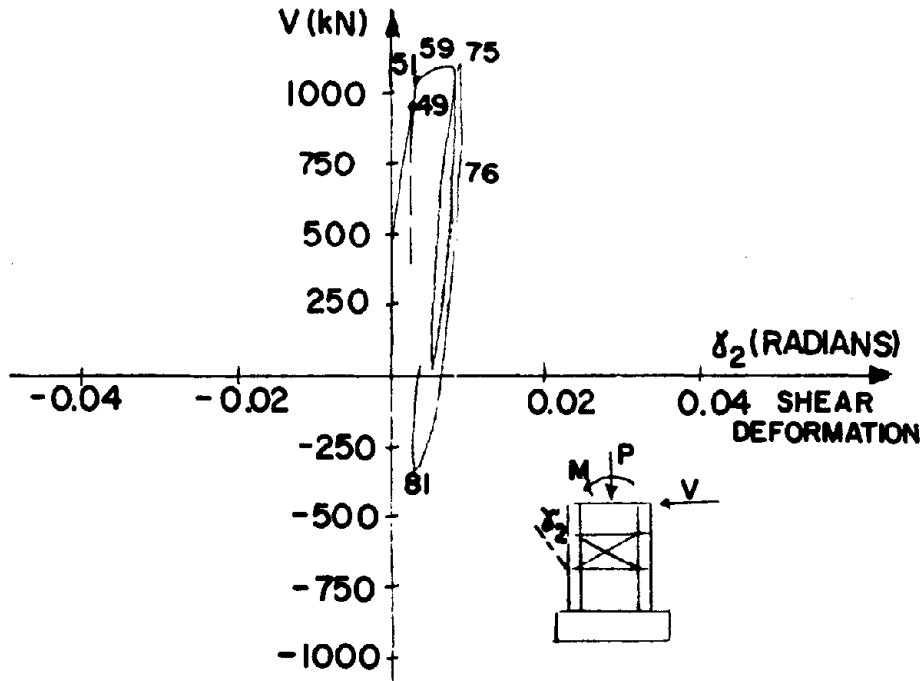


Fig. 6.19b Shear Deformation for Second-Story Framed Wall (Monotonic Loading), Specimen 3

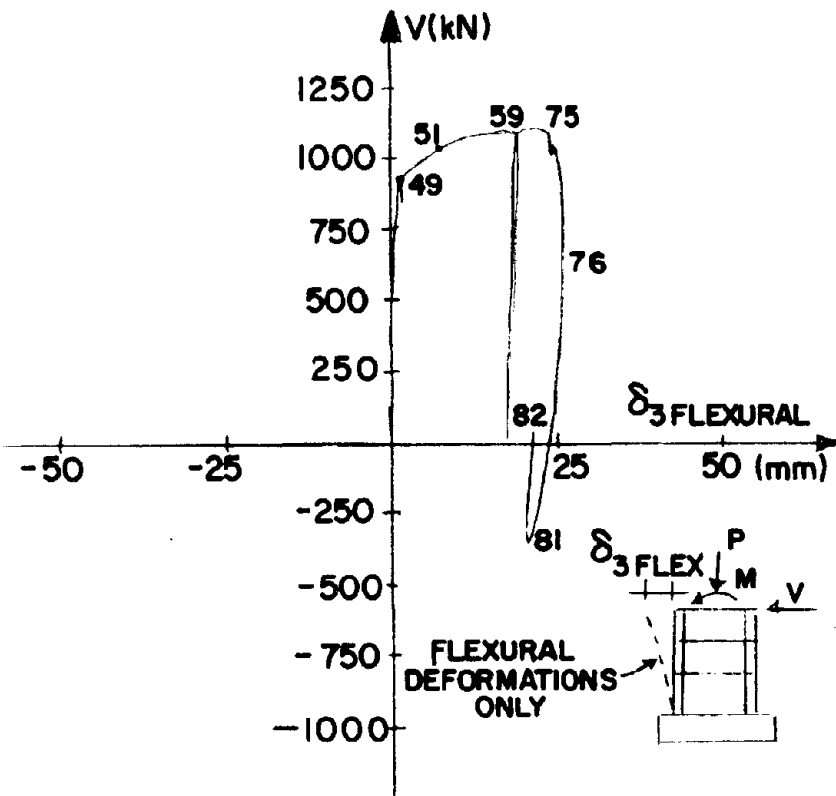


Fig. 6.20 Flexural Displacement at First-Floor of Framed Wall (Monotonic Loading), Specimen 3

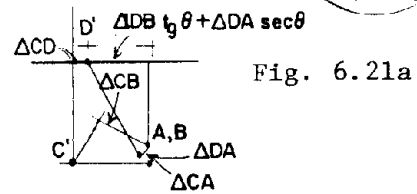
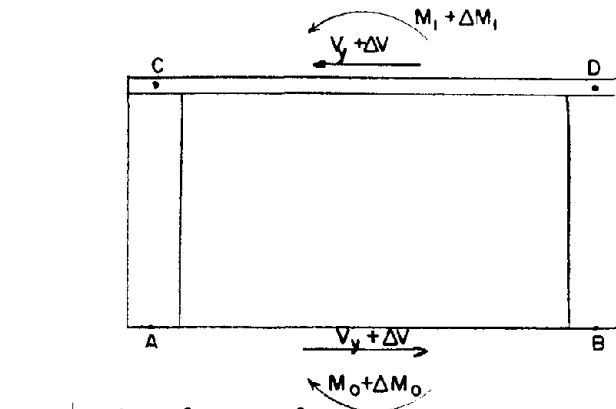


Fig. 6.21a

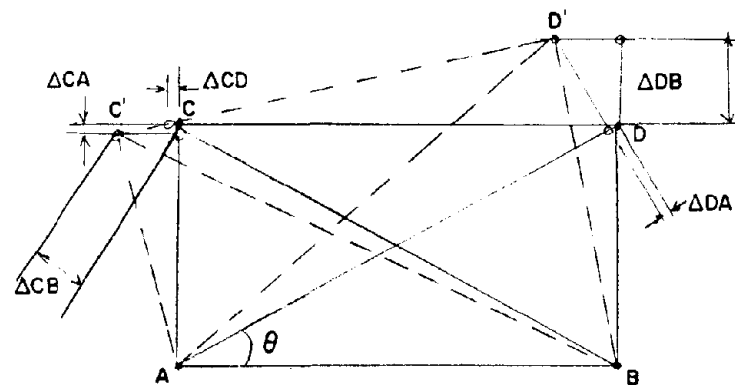


Fig. 6.21b

Fig. 6.21 Shear-Yielding Mechanism

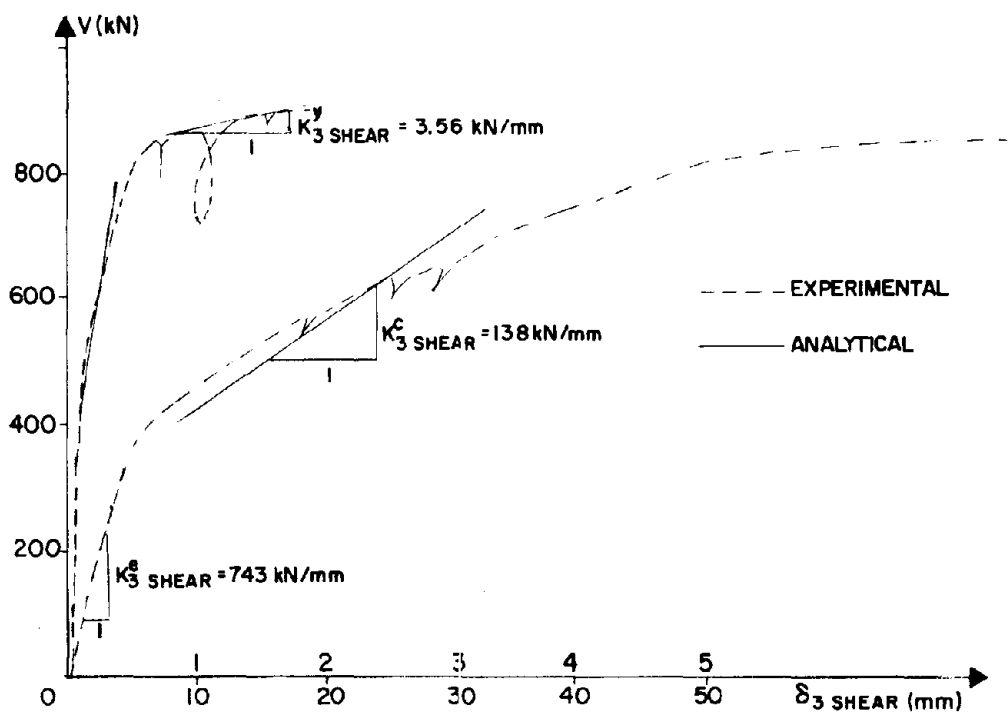


Fig. 6.22 Comparison of Shear Stiffness (Third-Floor Displacement), Specimen 5

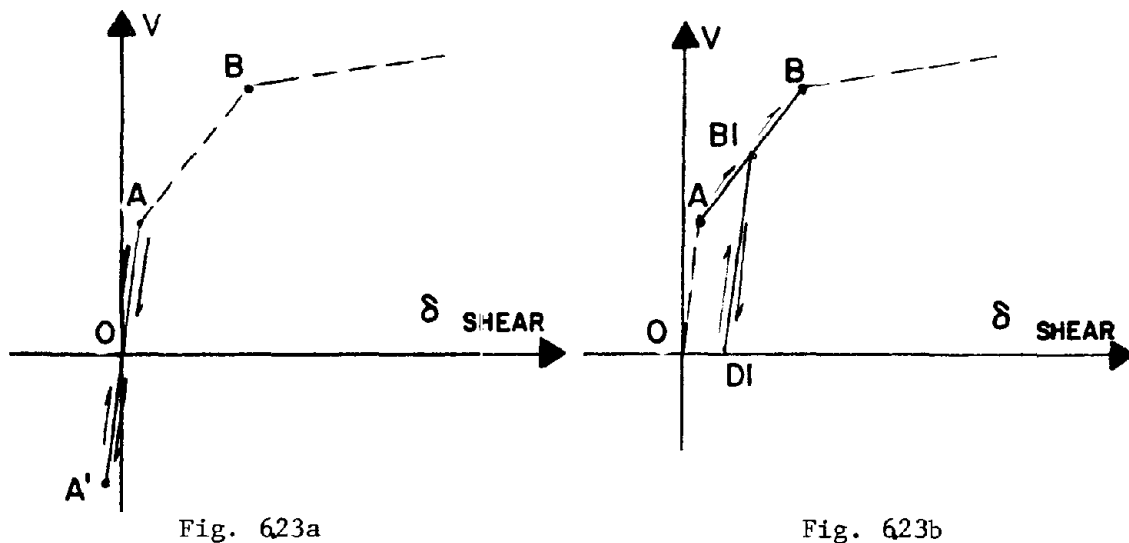


Fig. 6.23 Hysteretic Rule for Cyclic Shear Deformations

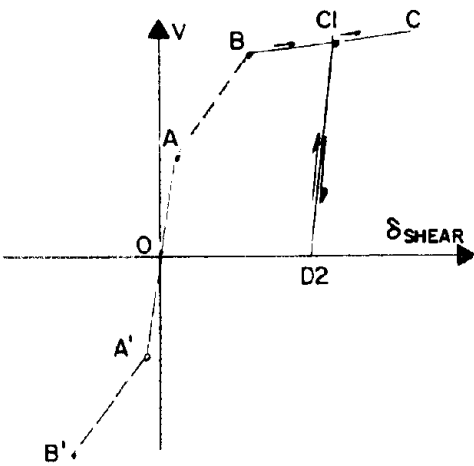


Fig. 6.23c

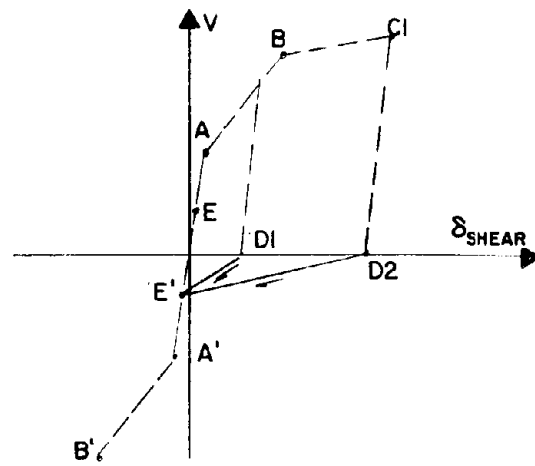


Fig. 6.23d

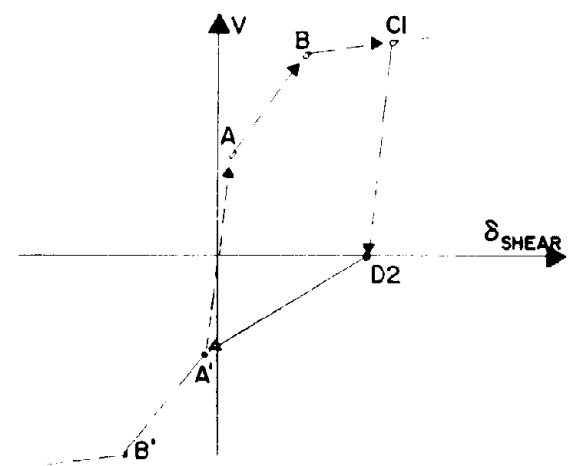


Fig. 6.23e

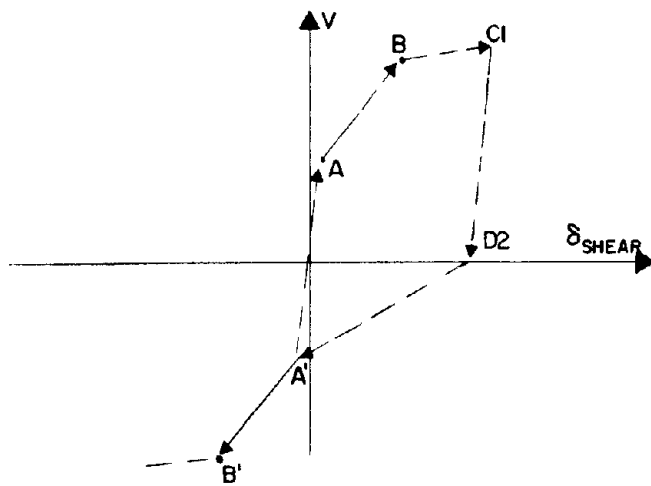


Fig. 6.23f

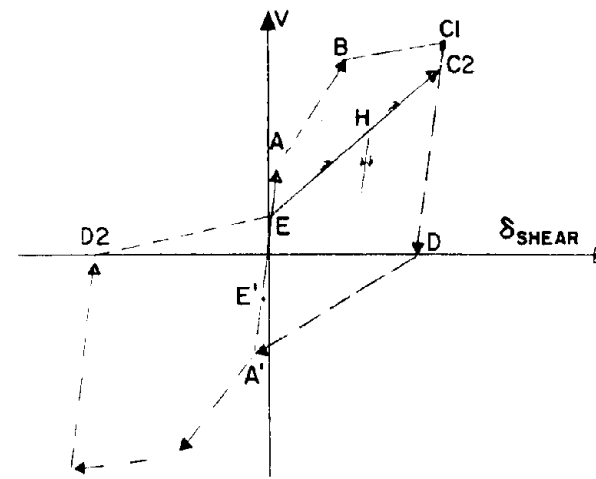


Fig. 6.23g

Fig. 6.23 Hysteretic Rule for Cyclic Shear Deformations

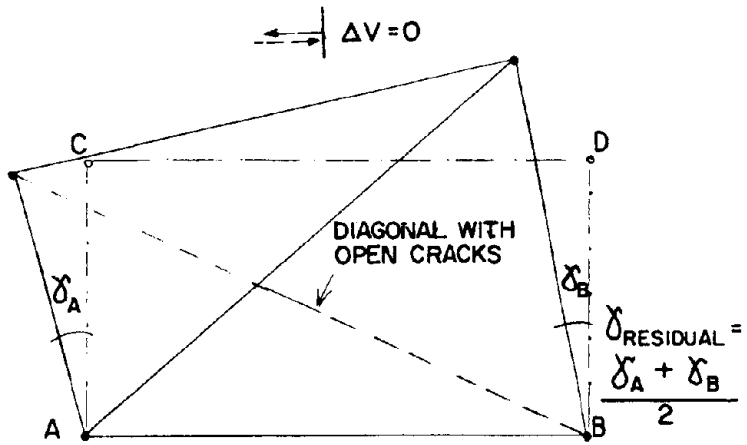


Fig. 6.24a Residual shear deformation

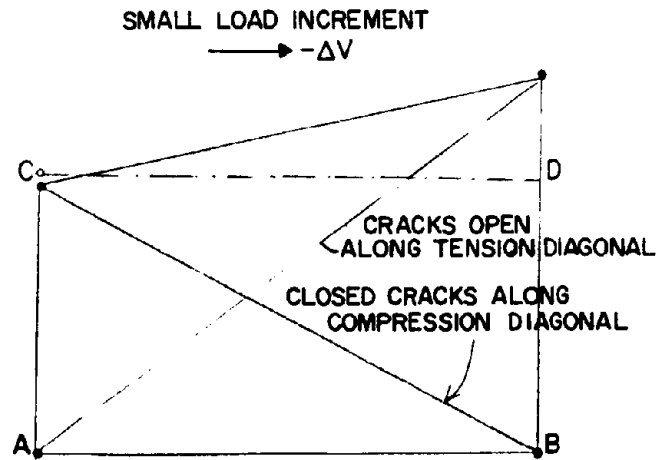


Fig. 6.24b Zero shear deformation

Fig. 6.24 Schematic Deformations of Panel with Open Diagonal Cracks

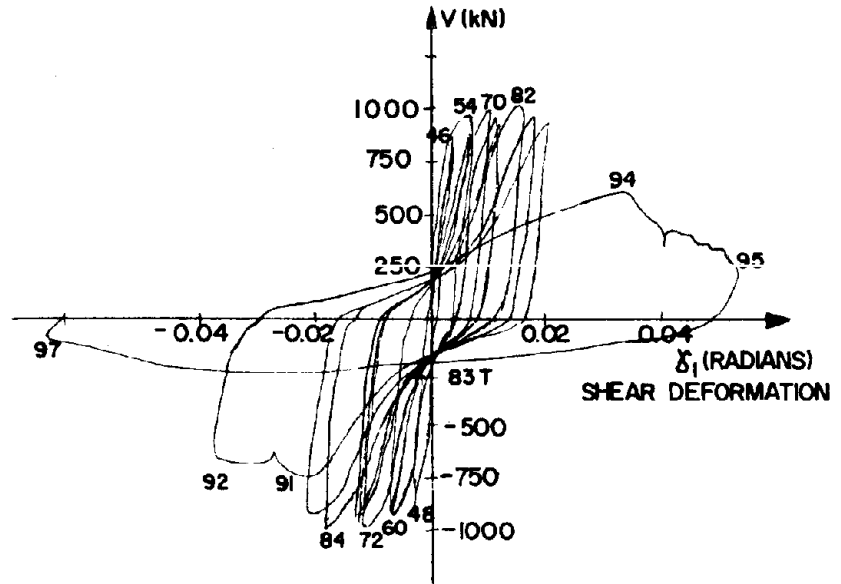


Fig. 6.25 Shear Deformation for First-Story Framed Wall (Cyclic Loading), Specimen 4

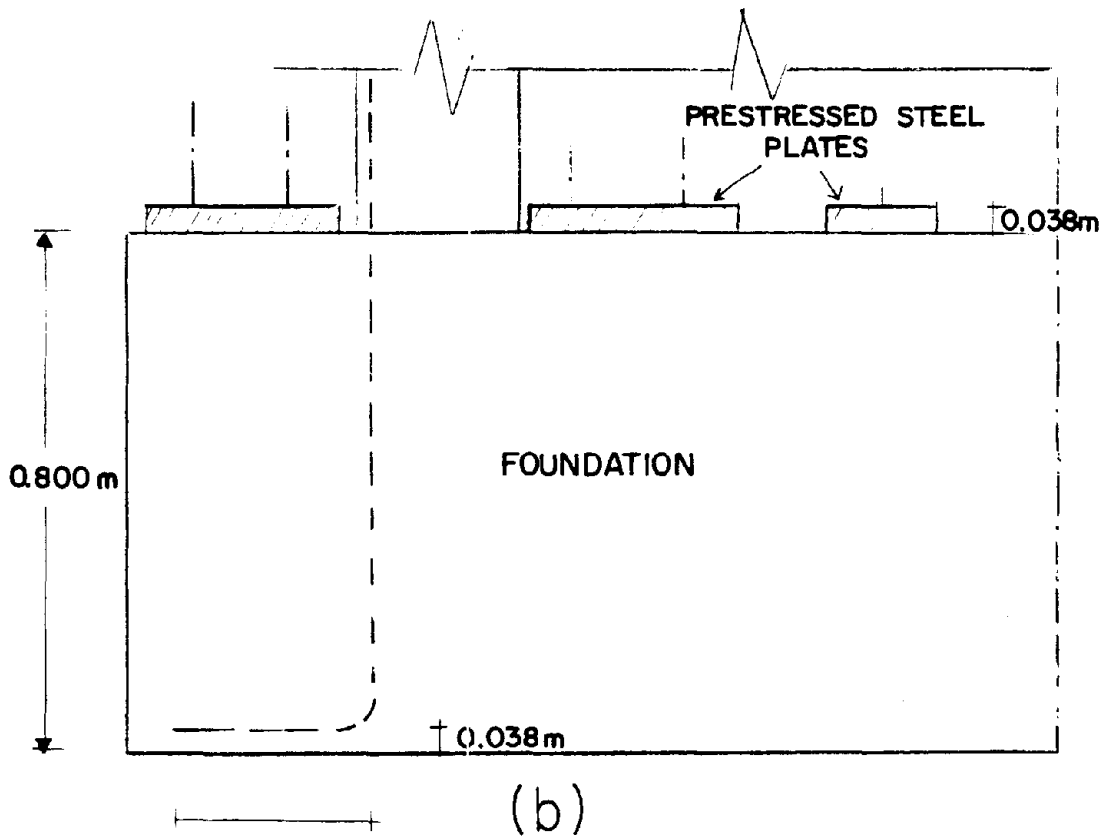
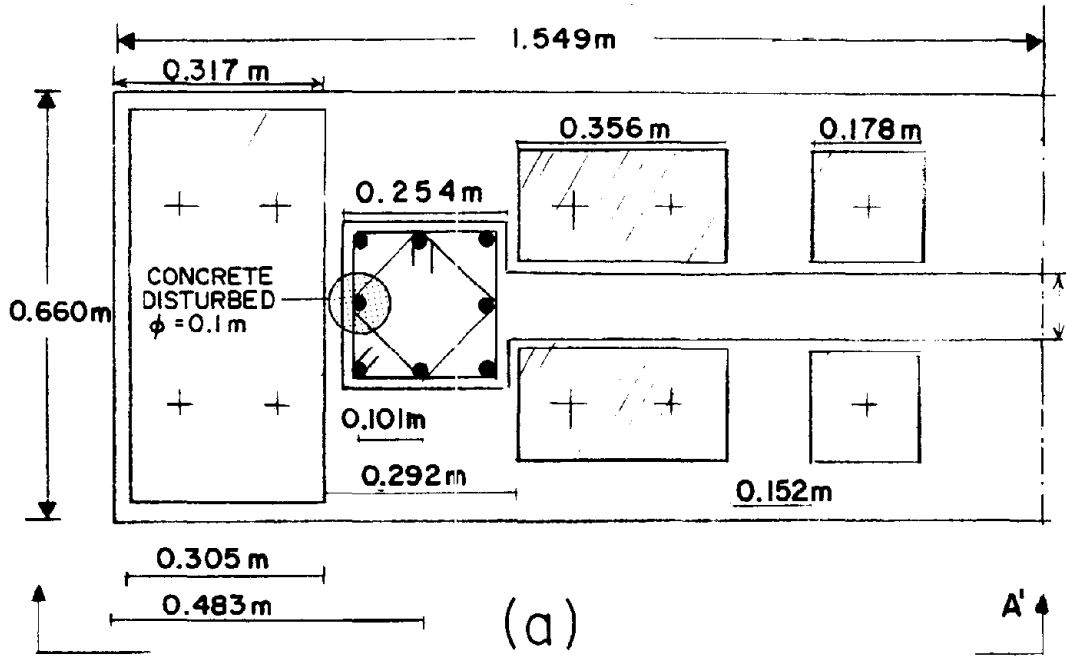


Fig. 6.28 Embedment Conditions for Longitudinal Reinforcement in the Foundation

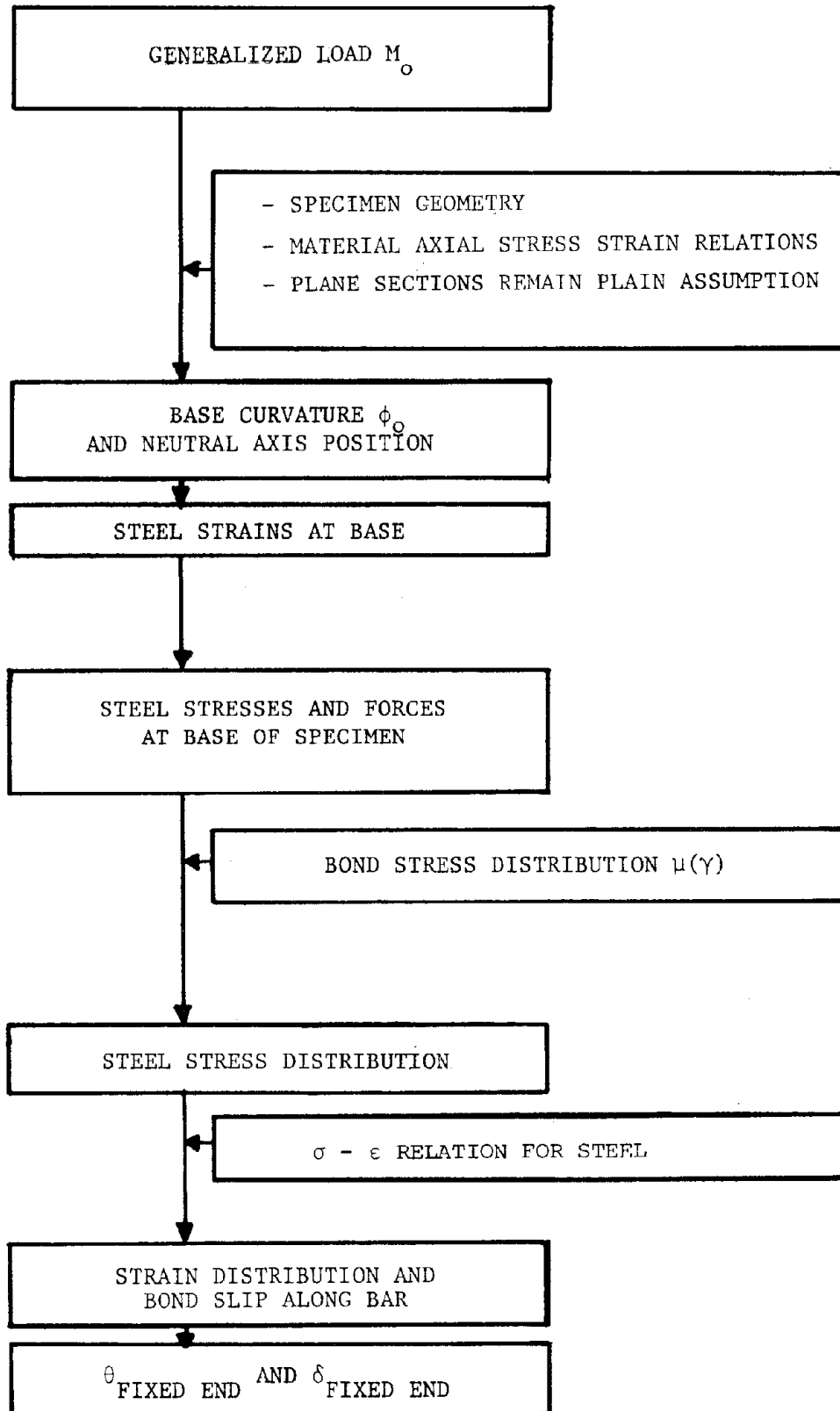


Fig. 6.29 Determination of Tip Displacement Due to Fixed-End Rotations

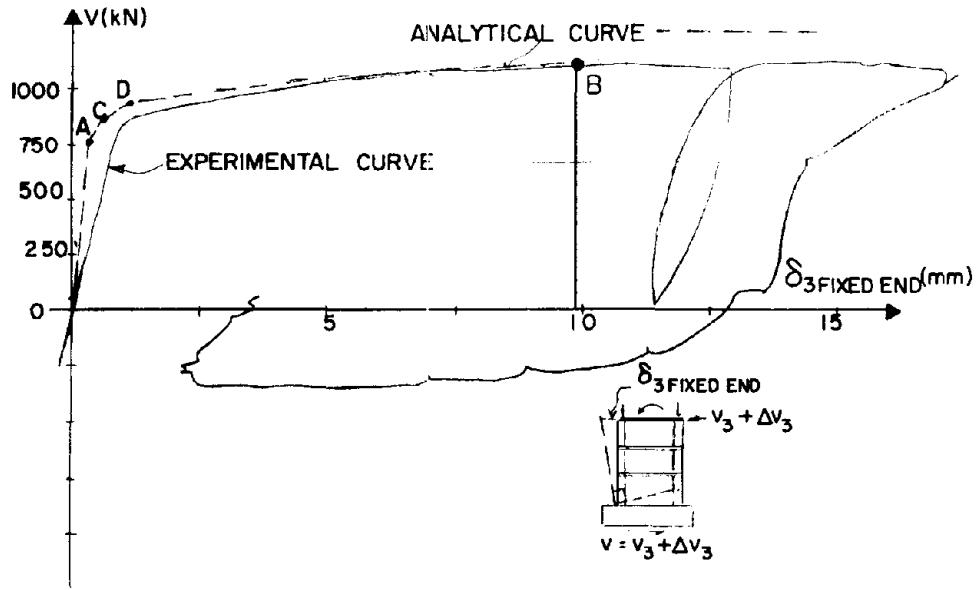


Fig. 6.30 Comparison of Experimental and Analytical Fixed-End Deformation Curves, Specimen 3

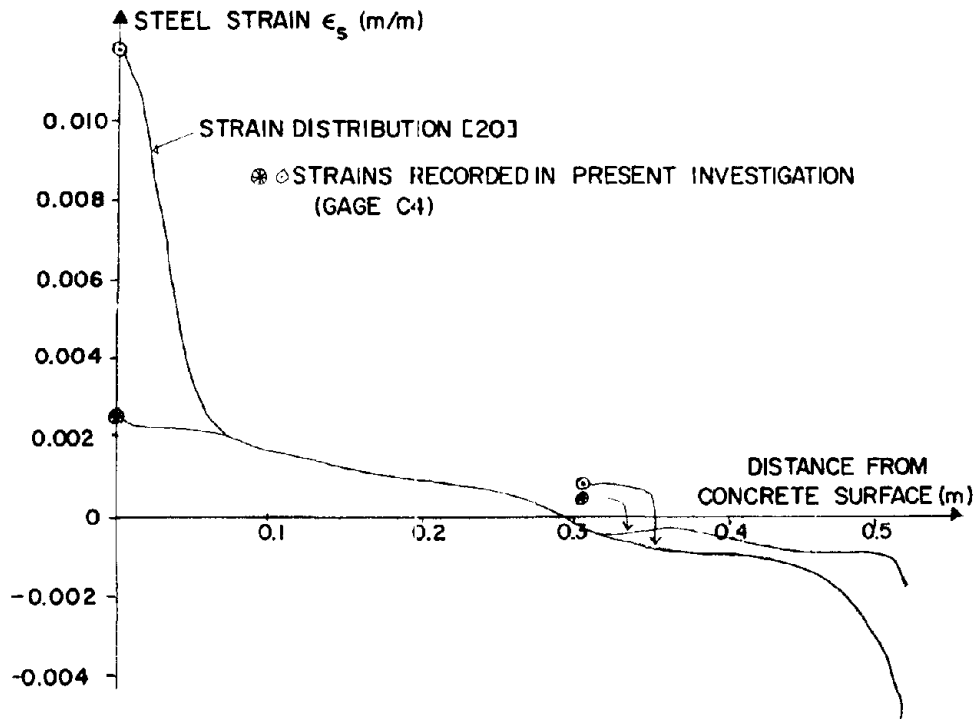


Fig. 6.31a Comparison of strain distribution curves for Ref. 20 and present investigation

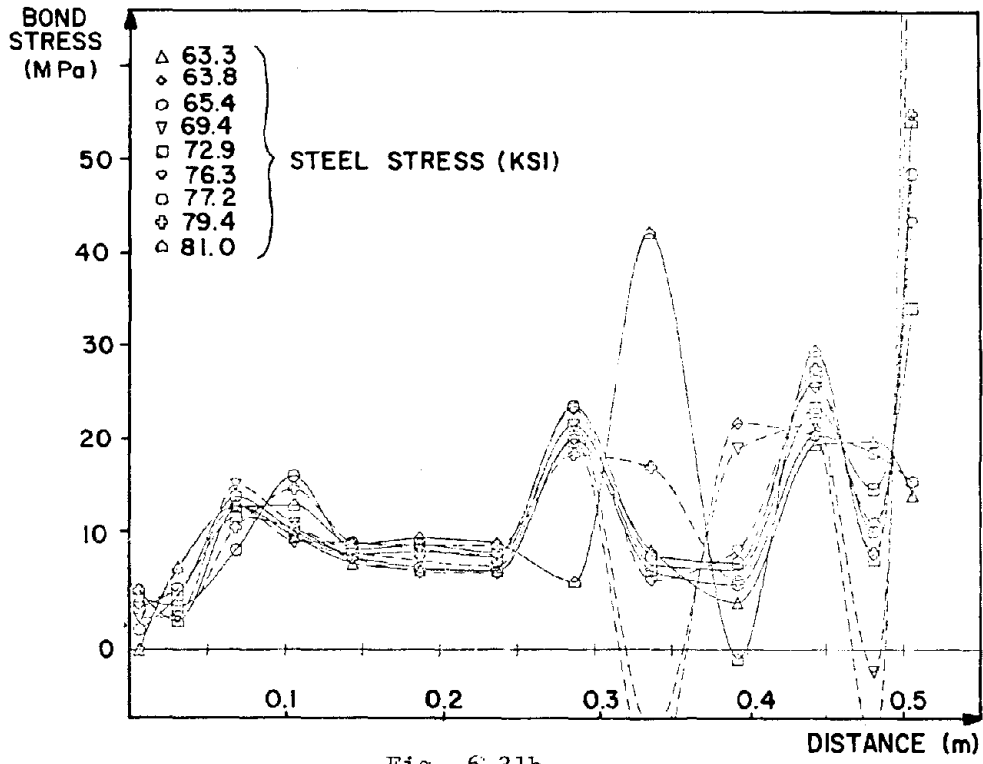


Fig. 6.31b

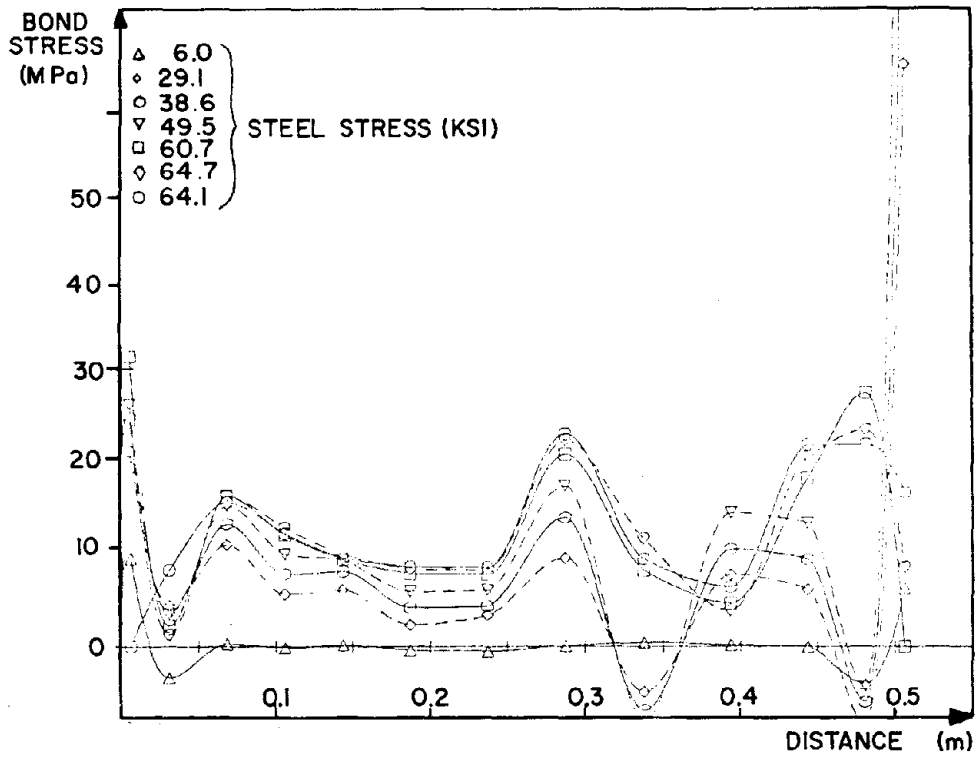
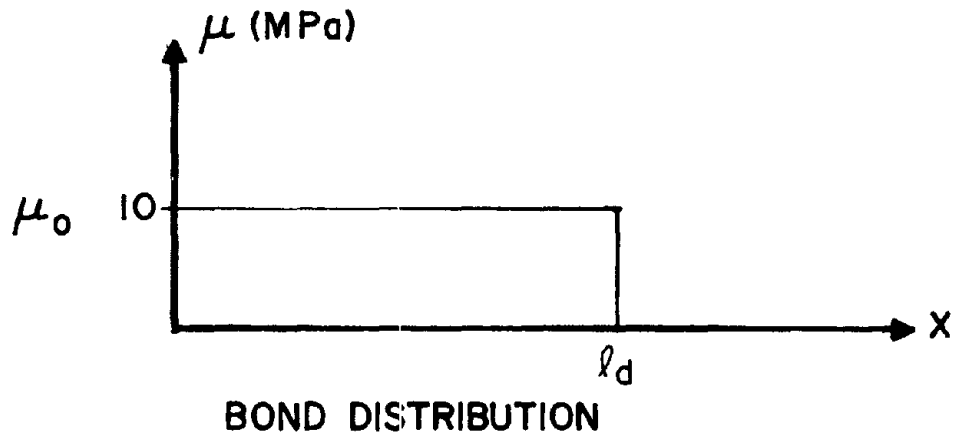
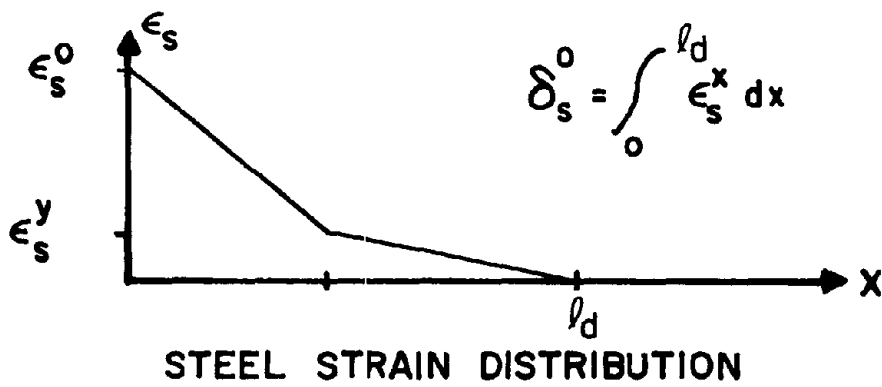
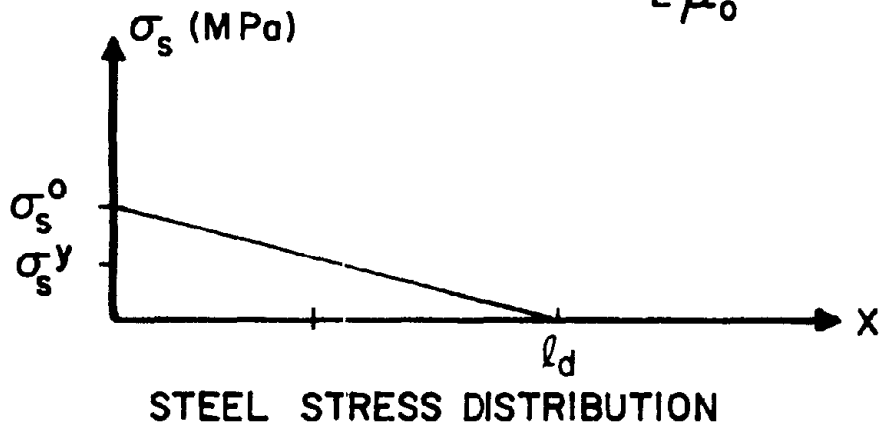


Fig. 6.31c

Fig. 6.31 Bond Stress Distribution for No. 6 Bar, Ref. 20



$$l_d = \frac{\sigma_s r}{2 \mu_0}$$



$$\delta_s^o = \int_0^{l_d} \epsilon_s^x dx$$

Fig. 6.32 Idealized Stress-Strain Distribution Along Embedded Bar for $\epsilon_s^o > \epsilon_s^y$

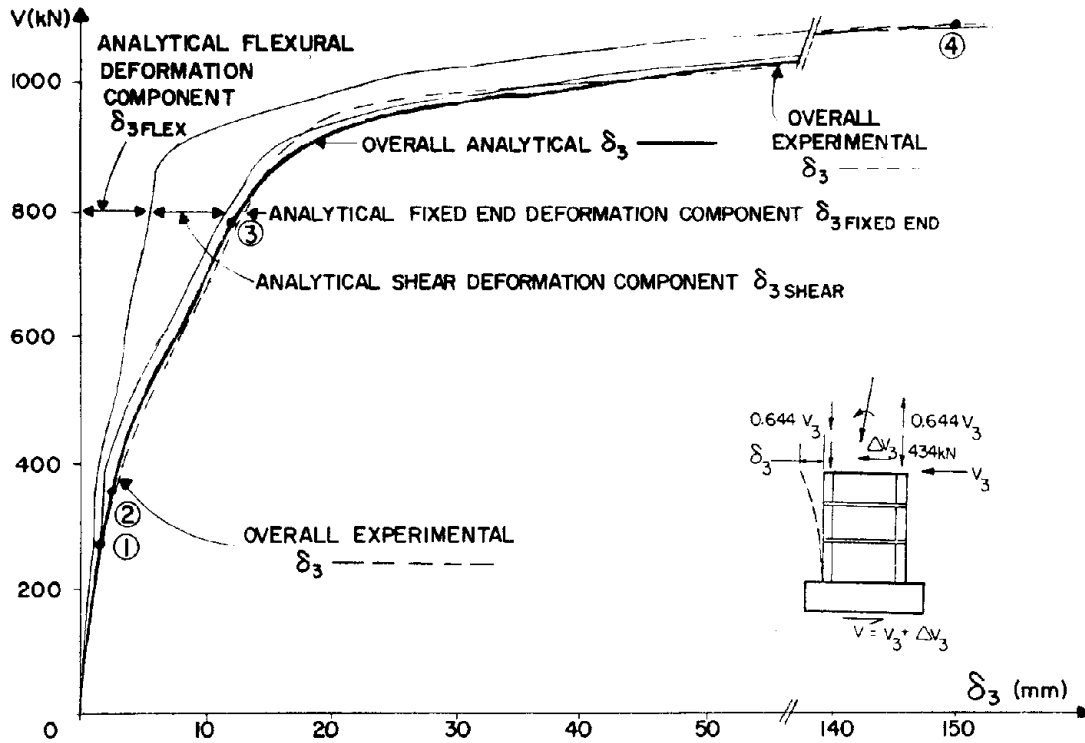


Fig. 6.33 Comparison of Experimental/Analytical Results for Overall Deformations

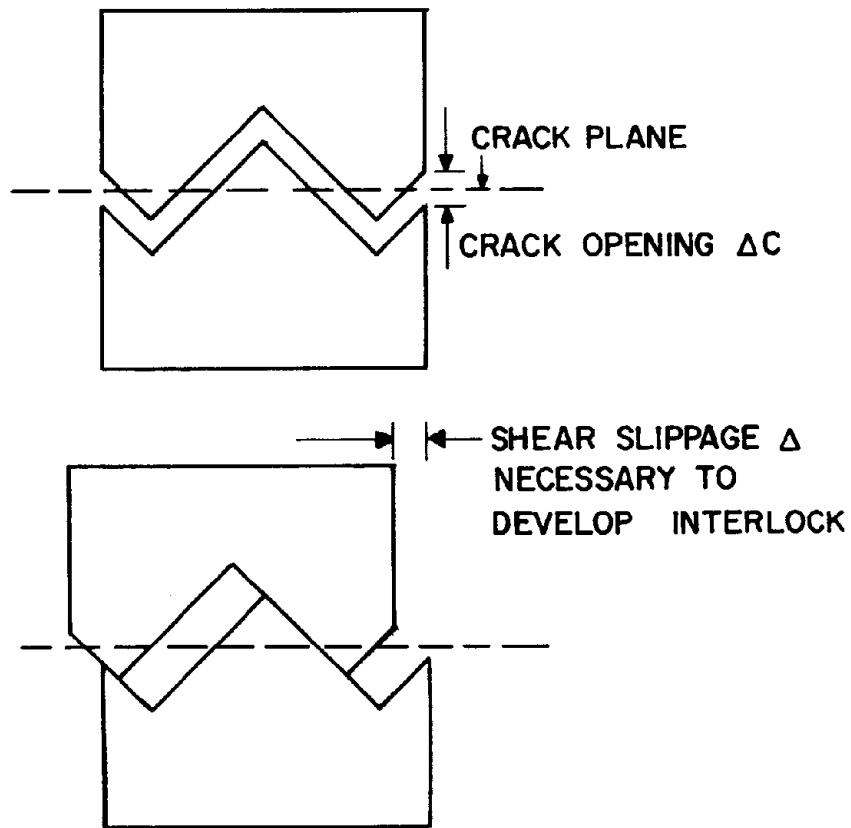


Fig. 7.1 Cracking Idealization

EERC REPORTS

EERC-1

EARTHQUAKE ENGINEERING RESEARCH CENTER REPORTS

NOTE: Numbers in parenthesis are Accession Numbers assigned by the National Technical Information Service; these are followed by a price code. Copies of the reports may be ordered from the National Technical Information Service, 5285 Port Royal Road, Springfield, Virginia, 22161. Accession Numbers should be quoted on orders for reports (PB --- ---) and remittance must accompany each order. Reports without this information were not available at time of printing. Upon request, EERC will mail inquirers this information when it becomes available.

- EERC 67-1 "Feasibility Study Large-Scale Earthquake Simulator Facility," by J. Penzien, J.G. Bouwkamp, R.W. Clough and D. Rea - 1967 (PB 187 905)A07
- EERC 68-1 Unassigned
- EERC 68-2 "Inelastic Behavior of Beam-to-Column Subassemblages Under Repeated Loading," by V.V. Bertero - 1968 (PB 184 888)A05
- EERC 68-3 "A Graphical Method for Solving the Wave Reflection-Refraction Problem," by H.D. McNiven and Y. Menqi - 1968 (PB 187 943)A03
- EERC 68-4 "Dynamic Properties of McKinley School Buildings," by D. Rea, J.G. Bouwkamp and R.W. Clough - 1968 (PB 187 902)A07
- EERC 68-5 "Characteristics of Rock Motions During Earthquakes," by H.B. Seed, I.M. Idriss and F.W. Kiefer - 1968 (PB 188 338)A03
- EERC 69-1 "Earthquake Engineering Research at Berkeley," - 1969 (PB 187 906)A11
- EERC 69-2 "Nonlinear Seismic Response of Earth Structures," by M. Dibaj and J. Penzien - 1969 (PB 187 904)A08
- EERC 69-3 "Probabilistic Study of the Behavior of Structures During Earthquakes," by R. Ruiz and J. Penzien - 1969 (PB 187 886)A06
- EERC 69-4 "Numerical Solution of Boundary Value Problems in Structural Mechanics by Reduction to an Initial Value Formulation," by N. Distefano and J. Schujman - 1969 (PB 187 942)A02
- EERC 69-5 "Dynamic Programming and the Solution of the Biharmonic Equation," by N. Distefano - 1969 (PB 187 941)A03
- EERC 69-6 "Stochastic Analysis of Offshore Tower Structures," by A.K. Malhotra and J. Penzien - 1969 (PB 187 903)A09
- EERC 69-7 "Rock Motion Accelerograms for High Magnitude Earthquakes," by H.B. Seed and I.M. Idriss - 1969 (PB 187 940)A02
- EERC 69-8 "Structural Dynamics Testing Facilities at the University of California, Berkeley," by R.M. Stephen, J.G. Bouwkamp, R.W. Clough and J. Penzien - 1969 (PB 189 111)A04
- EERC 69-9 "Seismic Response of Soil Deposits Underlain by Sloping Rock Boundaries," by H. Dezfulian and H.B. Seed - 1969 (PB 189 114)A03
- EERC 69-10 "Dynamic Stress Analysis of Axisymmetric Structures Under Arbitrary Loading," by S. Ghosh and E.L. Wilson - 1969 (PB 189 026)A10
- EERC 69-11 "Seismic Behavior of Multistory Frames Designed by Different Philosophies," by J.C. Anderson and V. V. Bertero - 1969 (PB 190 662)A10
- EERC 69-12 "Stiffness Degradation of Reinforcing Concrete Members Subjected to Cyclic Flexural Moments," by V.V. Bertero, B. Bresler and H. Ming Liao - 1969 (PB 202 942)A07
- EERC 69-13 "Response of Non-Uniform Soil Deposits to Travelling Seismic Waves," by H. Dezfulian and H.B. Seed - 1969 (PB 191 023)A03
- EERC 69-14 "Damping Capacity of a Model Steel Structure," by D. Rea, R.W. Clough and J.G. Bouwkamp - 1969 (PB 190 663)A06
- EERC 69-15 "Influence of Local Soil Conditions on Building Damage Potential during Earthquakes," by H.B. Seed and I.M. Idriss - 1969 (PB 191 036)A03
- EERC 69-16 "The Behavior of Sands Under Seismic Loading Conditions," by M.L. Silver and H.B. Seed - 1969 (AD 714 982)A07
- EERC 70-1 "Earthquake Response of Gravity Dams," by A.K. Chopra - 1970 (AD 709 640)A03
- EERC 70-2 "Relationships between Soil Conditions and Building Damage in the Caracas Earthquake of July 29, 1967," by H.B. Seed, I.M. Idriss and H. Dezfulian - 1970 (PB 195 762)A05
- EERC 70-3 "Cyclic Loading of Full Size Steel Connections," by E.P. Popov and R.M. Stephen - 1970 (PB 213 545)A04
- EERC 70-4 "Seismic Analysis of the Charaima Building, Caraballeda, Venezuela," by Subcommittee of the SEAONC Research Committee: V.V. Bertero, P.F. Fratessa, S.A. Mahin, J.H. Sexton, A.C. Scordelis, E.L. Wilson, L.A. Wyllie, H.B. Seed and J. Penzien, Chairman - 1970 (PB 201 455)A06

EERC-2

- EERC 70-5 "A Computer Program for Earthquake Analysis of Dams," by A.K. Chopra and P. Chakrabarti - 1970 (AD 723 994)A05
- EERC 70-6 "The Propagation of Love Waves Across Non-Horizontally Layered Structures," by J. Lysmer and L.A. Drake 1970 (PB 197 896)A03
- EERC 70-7 "Influence of Base Rock Characteristics on Ground Response," by J. Lysmer, H.B. Seed and P.B. Schnabel 1970 (PB 197 897)A03
- EERC 70-8 "Applicability of Laboratory Test Procedures for Measuring Soil Liquefaction Characteristics under Cyclic Loading," by H.B. Seed and W.H. Peacock - 1970 (PB 198 016)A03
- EERC 70-9 "A Simplified Procedure for Evaluating Soil Liquefaction Potential," by H.B. Seed and I.M. Idriss - 1970 (PB 198 009)A03
- EERC 70-10 "Soil Moduli and Damping Factors for Dynamic Response Analysis," by H.B. Seed and I.M. Idriss - 1970 (PB 197 869)A03
- EERC 71-1 "Koyna Earthquake of December 11, 1967 and the Performance of Koyna Dam," by A.K. Chopra and P. Chakrabarti 1971 (AD 731 496)A06
- EERC 71-2 "Preliminary In-Situ Measurements of Anelastic Absorption in Soils Using a Prototype Earthquake Simulator," by R.D. Borcherdt and P.W. Rodgers - 1971 (PB 201 454)A03
- EERC 71-3 "Static and Dynamic Analysis of Inelastic Frame Structures," by F.L. Porter and G.H. Powell - 1971 (PB 210 135)A06
- EERC 71-4 "Research Needs in Limit Design of Reinforced Concrete Structures," by V.V. Bertero - 1971 (PB 202 943)A04
- EERC 71-5 "Dynamic Behavior of a High-Rise Diagonally Braced Steel Building," by D. Rea, A.A. Shah and J.G. Bouwkamp 1971 (PB 203 584)A06
- EERC 71-6 "Dynamic Stress Analysis of Porous Elastic Solids Saturated with Compressible Fluids," by J. Chaboussi and E. L. Wilson - 1971 (PB 211 396)A06
- EERC 71-7 "Inelastic Behavior of Steel Beam-to-Column Subassemblages," by H. Krawinkler, V.V. Bertero and E.P. Popov 1971 (PB 211 335)A14
- EERC 71-8 "Modification of Seismograph Records for Effects of Local Soil Conditions," by P. Schnabel, H.B. Seed and J. Lysmer - 1971 (PB 214 450)A03
- EERC 72-1 "Static and Earthquake Analysis of Three Dimensional Frame and Shear Wall Buildings," by E.L. Wilson and H.H. Dovey - 1972 (PB 212 904)A05
- EERC 72-2 "Accelerations in Rock for Earthquakes in the Western United States," by P.B. Schnabel and H.B. Seed - 1972 (PB 213 100)A03
- EERC 72-3 "Elastic-Plastic Earthquake Response of Soil-Building Systems," by T. Minami - 1972 (PB 214 868)A08
- EERC 72-4 "Stochastic Inelastic Response of Offshore Towers to Strong Motion Earthquakes," by M.K. Kaul - 1972 (PB 215 713)A05
- EERC 72-5 "Cyclic Behavior of Three Reinforced Concrete Flexural Members with High Shear," by E.P. Popov, V.V. Bertero and H. Krawinkler - 1972 (PB 214 555)A05
- EERC 72-6 "Earthquake Response of Gravity Dams Including Reservoir Interaction Effects," by P. Chakrabarti and A.K. Chopra - 1972 (AD 762 330)A08
- EERC 72-7 "Dynamic Properties of Pine Flat Dam," by D. Rea, C.Y. Liaw and A.K. Chopra - 1972 (AD 763 928)A05
- EERC 72-8 "Three Dimensional Analysis of Building Systems," by E.L. Wilson and H.H. Dovey - 1972 (PB 222 438)A06
- EERC 72-9 "Rate of Loading Effects on Uncracked and Repaired Reinforced Concrete Members," by S. Mahin, V.V. Bertero, D. Rea and M. Atalay - 1972 (PB 224 520)A08
- EERC 72-10 "Computer Program for Static and Dynamic Analysis of Linear Structural Systems," by E.L. Wilson, K.-J. Bathe, J.E. Peterson and H.H. Dovey - 1972 (PB 220 437)A04
- EERC 72-11 "Literature Survey - Seismic Effects on Highway Bridges," by T. Iwasaki, J. Penzien and R.W. Clough - 1972 (PB 215 613)A19
- EERC 72-12 "SHAKE-A Computer Program for Earthquake Response Analysis of Horizontally Layered Sites," by P.B. Schnabel and J. Lysmer - 1972 (PB 220 207)A06
- EERC 73-1 "Optimal Seismic Design of Multistory Frames," by V.V. Bertero and H. Kamil - 1973
- EERC 73-2 "Analysis of the Slides in the San Fernando Dams During the Earthquake of February 9, 1971," by H.B. Seed, K.L. Lee, I.M. Idriss and F. Makdasi - 1973 (PB 223 402)A14

EERC-3

- EERC 73-3 "Computer Aided Ultimate Load Design of Unbraced Multistory Steel Frames," by M.B. El-Hafez and G.H. Powell 1973 (PB 248 315)A09
- EERC 73-4 "Experimental Investigation into the Seismic Behavior of Critical Regions of Reinforced Concrete Components as Influenced by Moment and Shear," by M. Celebi and J. Penzien - 1973 (PB 215 884)A09
- EERC 73-5 "Hysteretic Behavior of Epoxy-Repaired Reinforced Concrete Beams," by M. Celebi and J. Penzien - 1973 (PB 239 568)A03
- EERC 73-6 "General Purpose Computer Program for Inelastic Dynamic Response of Plane Structures," by A. Kanaan and G.H. Powell - 1973 (PB 221 260)A08
- EERC 73-7 "A Computer Program for Earthquake Analysis of Gravity Dams Including Reservoir Interaction," by P. Chakrabarti and A.K. Chopra - 1973 (AD 766 271)A04
- EERC 73-8 "Behavior of Reinforced Concrete Deep Beam-Column Subassemblages Under Cyclic Loads," by O. Küstü and J.G. Bouwkamp - 1973 (PB 246 117)A12
- EERC 73-9 "Earthquake Analysis of Structure-Foundation Systems," by A.K. Vaish and A.K. Chopra - 1973 (AD 766 272)A07
- EERC 73-10 "Deconvolution of Seismic Response for Linear Systems," by R.B. Reimer - 1973 (PB 227 179)A08
- EERC 73-11 "SAP IV: A Structural Analysis Program for Static and Dynamic Response of Linear Systems," by K.-J. Bathe, E.L. Wilson and F.E. Peterson - 1973 (PB 221 967)A09
- EERC 73-12 "Analytical Investigations of the Seismic Response of Long, Multiple Span Highway Bridges," by W.S. Tseng and J. Penzien - 1973 (PB 227 816)A10
- EERC 73-13 "Earthquake Analysis of Multi-Story Buildings Including Foundation Interaction," by A.K. Chopra and J.A. Gutierrez - 1973 (PB 222 970)A03
- EERC 73-14 "ADAP: A Computer Program for Static and Dynamic Analysis of Arch Dams," by R.W. Clough, J.M. Raphael and S. Mojtahedi - 1973 (PB 223 763)A09
- EERC 73-15 "Cyclic Plastic Analysis of Structural Steel Joints," by R.B. Pinkney and R.W. Clough - 1973 (PB 226 843)A08
- EERC 73-16 "QIAD-4: A Computer Program for Evaluating the Seismic Response of Soil Structures by Variable Damping Finite Element Procedures," by I.M. Idriss, J. Lysmer, R. Hwang and H.B. Seed - 1973 (PB 229 424)A05
- EERC 73-17 "Dynamic Behavior of a Multi-Story Pyramid Shaped Building," by R.M. Stephen, J.P. Hollings and J.G. Bouwkamp - 1973 (PB 240 718)A06
- EERC 73-18 "Effect of Different Types of Reinforcing on Seismic Behavior of Short Concrete Columns," by V.V. Bertero, J. Hollings, O. Küstü, R.M. Stephen and J.G. Bouwkamp - 1973
- EERC 73-19 "Olive View Medical Center Materials Studies, Phase I," by B. Bresler and V.V. Bertero - 1973 (PB 235 986)A06
- EERC 73-20 "Linear and Nonlinear Seismic Analysis Computer Programs for Long Multiple-Span Highway Bridges," by W.S. Tseng and J. Penzien - 1973
- EERC 73-21 "Constitutive Models for Cyclic Plastic Deformation of Engineering Materials," by J.M. Kelly and P.P. Gillis 1973 (PB 226 024)A03
- EERC 73-22 "DRAIN - 2D User's Guide," by G.H. Powell - 1973 (PB 227 016)A05
- EERC 73-23 "Earthquake Engineering at Berkeley - 1973," (PB 226 033)A11
- EERC 73-24 Unassigned
- EERC 73-25 "Earthquake Response of Axisymmetric Tower Structures Surrounded by Water," by C.Y. Liaw and A.K. Chopra 1973 (AD 773 052)A09
- EERC 73-26 "Investigation of the Failures of the Olive View Stairtowers During the San Fernando Earthquake and Their Implications on Seismic Design," by V.V. Bertero and R.G. Collins - 1973 (PB 235 106)A13
- EERC 73-27 "Further Studies on Seismic Behavior of Steel Beam-Column Subassemblages," by V.V. Bertero, H. Krawinkler and E.P. Popov - 1973 (PB 234 172)A06
- EERC 74-1 "Seismic Risk Analysis," by C.S. Oliveira - 1974 (PB 235 920)A06
- EERC 74-2 "Settlement and Liquefaction of Sands Under Multi-Directional Shaking," by R. Pyke, C.K. Chan and H.B. Seed 1974
- EERC 74-3 "Optimum Design of Earthquake Resistant Shear Buildings," by D. Ray, K.S. Pister and A.K. Chopra - 1974 (PB 231 172)A06
- EERC 74-4 "LUSH - A Computer Program for Complex Response Analysis of Soil-Structure Systems," by J. Lysmer, T. Udaka, H.B. Seed and R. Hwang - 1974 (PB 236 796)A05

EERC-4

- EERC 74-5 "Sensitivity Analysis for Hysteretic Dynamic Systems: Applications to Earthquake Engineering," by D. Ray 1974 (PB 233 213)A06
- EERC 74-6 "Soil Structure Interaction Analyses for Evaluating Seismic Response," by H.B. Seed, J. Lysmer and R. Hwang 1974 (PB 236 519)A04
- EERC 74-7 Unassigned
- EERC 74-8 "Shaking Table Tests of a Steel Frame - A Progress Report," by R.W. Clough and D. Tang - 1974 (PB 240 869)A03
- EERC 74-9 "Hysteretic Behavior of Reinforced Concrete Flexural Members with Special Web Reinforcement," by V.V. Bertero, E.P. Popov and T.Y. Wang - 1974 (PB 236 797)A07
- EERC 74-10 "Applications of Reliability-Based, Global Cost Optimization to Design of Earthquake Resistant Structures," by E. Vitiello and K.S. Pister - 1974 (PB 237 231)A06
- EERC 74-11 "Liquefaction of Gravelly Soils Under Cyclic Loading Conditions," by R.T. Wong, H.B. Seed and C.K. Chan 1974 (PB 242 042)A03
- EERC 74-12 "Site-Dependent Spectra for Earthquake-Resistant Design," by H.B. Seed, C. Ugas and J. Lysmer - 1974 (PB 240 953)A03
- EERC 74-13 "Earthquake Simulator Study of a Reinforced Concrete Frame," by P. Hidalgo and R.W. Clough - 1974 (PB 241 944)A13
- EERC 74-14 "Nonlinear Earthquake Response of Concrete Gravity Dams," by N. Pal - 1974 (AD/A 006 583)A06
- EERC 74-15 "Modeling and Identification in Nonlinear Structural Dynamics - I. One Degree of Freedom Models," by N. Distefano and A. Rath - 1974 (PB 241 548)A06
- EERC 75-1 "Determination of Seismic Design Criteria for the Dumbarton Bridge Replacement Structure, Vol. I: Description, Theory and Analytical Modeling of Bridge and Parameters," by F. Baron and S.-H. Pang - 1975 (PB 259 407)A15
- EERC 75-2 "Determination of Seismic Design Criteria for the Dumbarton Bridge Replacement Structure, Vol. II: Numerical Studies and Establishment of Seismic Design Criteria," by F. Baron and S.-H. Pang - 1975 (PB 259 408)A11 (For set of EERC 75-1 and 75-2 (PB 259 406))
- EERC 75-3 "Seismic Risk Analysis for a Site and a Metropolitan Area," by C.S. Oliveira - 1975 (PB 248 134)A09
- EERC 75-4 "Analytical Investigations of Seismic Response of Short, Single or Multiple-Span Highway Bridges," by M.-C. Chen and J. Penzien - 1975 (PB 241 454)A09
- EERC 75-5 "An Evaluation of Some Methods for Predicting Seismic Behavior of Reinforced Concrete Buildings," by S.A. Mahin and V.V. Bertero - 1975 (PB 246 306)A16
- EERC 75-6 "Earthquake Simulator Study of a Steel Frame Structure, Vol. I: Experimental Results," by R.W. Clough and D.T. Tang - 1975 (PB 243 981)A13
- EERC 75-7 "Dynamic Properties of San Bernardino Intake Tower," by D. Rea, C.-Y. Liaw and A.K. Chopra - 1975 (AD/A008 406) A05
- EERC 75-8 "Seismic Studies of the Articulation for the Dumbarton Bridge Replacement Structure, Vol. I: Description, Theory and Analytical Modeling of Bridge Components," by F. Baron and R.E. Hamati - 1975 (PB 251 539)A07
- EERC 75-9 "Seismic Studies of the Articulation for the Dumbarton Bridge Replacement Structure, Vol. 2: Numerical Studies of Steel and Concrete Girder Alternates," by F. Baron and R.E. Hamati - 1975 (PB 251 540)A10
- EERC 75-10 "Static and Dynamic Analysis of Nonlinear Structures," by D.P. Mondkar and G.H. Powell - 1975 (PB 242 434)A08
- EERC 75-11 "Hysteretic Behavior of Steel Columns," by E.P. Popov, V.V. Bertero and S. Chandramouli - 1975 (PB 252 365)A11
- EERC 75-12 "Earthquake Engineering Research Center Library Printed Catalog," - 1975 (PB 243 711)A26
- EERC 75-13 "Three Dimensional Analysis of Building Systems (Extended Version)," by E.L. Wilson, J.P. Hollings and H.H. Dovey - 1975 (PB 243 989)A07
- EERC 75-14 "Determination of Soil Liquefaction Characteristics by Large-Scale Laboratory Tests," by P. De Alba, C.K. Chan and H.B. Seed - 1975 (NUREG 0027)A08
- EERC 75-15 "A Literature Survey - Compressive, Tensile, Bond and Shear Strength of Masonry," by R.L. Mayes and R.W. Clough - 1975 (PB 246 292)A10
- EERC 75-16 "Hysteretic Behavior of Ductile Moment Resisting Reinforced Concrete Frame Components," by V.V. Bertero and E.P. Popov - 1975 (PB 246 388)A05
- EERC 75-17 "Relationships Between Maximum Acceleration, Maximum Velocity, Distance from Source, Local Site Conditions for Moderately Strong Earthquakes," by H.B. Seed, R. Murarka, J. Lysmer and I.M. Idriss - 1975 (PB 248 172)A03
- EERC 75-18 "The Effects of Method of Sample Preparation on the Cyclic Stress-Strain Behavior of Sands," by J. Mullis, C.K. Chan and H.B. Seed - 1975 (Summarized in EERC 75-28)

EERC-5

- EERC 75-19 "The Seismic Behavior of Critical Regions of Reinforced Concrete Components as Influenced by Moment, Shear and Axial Force," by M.B. Atalay and J. Penzien - 1975 (PB 258 842)A11
- EERC 75-20 "Dynamic Properties of an Eleven Story Masonry Building," by R.M. Stephen, J.P. Hollings, J.G. Bouwkamp and D. Jurukovski - 1975 (PB 246 945)A04
- EERC 75-21 "State-of-the-Art in Seismic Strength of Masonry - An Evaluation and Review," by R.L. Mayes and R.W. Clough - 1975 (PB 249 040)A07
- EERC 75-22 "Frequency Dependent Stiffness Matrices for Viscoelastic Half-Plane Foundations," by A.K. Chopra, P. Chakrabarti and G. Dasgupta - 1975 (PB 248 121)A07
- EERC 75-23 "Hysteretic Behavior of Reinforced Concrete Framed Walls," by T.Y. Wong, V.V. Bertero and E.P. Popov - 1975
- EERC 75-24 "Testing Facility for Subassemblages of Frame-Wall Structural Systems," by V.V. Bertero, E.P. Popov and T. Endo - 1975
- EERC 75-25 "Influence of Seismic History on the Liquefaction Characteristics of Sands," by H.B. Seed, K. Mori and C.K. Chan - 1975 (Summarized in EERC 75-28)
- EERC 75-26 "The Generation and Dissipation of Pore Water Pressures during Soil Liquefaction," by H.B. Seed, P.P. Martin and J. Lysmer - 1975 (PB 252 648)A03
- EERC 75-27 "Identification of Research Needs for Improving Aseismic Design of Building Structures," by V.V. Bertero - 1975 (PB 248 136)A05
- EERC 75-28 "Evaluation of Soil Liquefaction Potential during Earthquakes," by H.B. Seed, I. Arango and C.K. Chan - 1975 (NUREG 0026)A13
- EERC 75-29 "Representation of Irregular Stress Time Histories by Equivalent Uniform Stress Series in Liquefaction Analyses," by H.B. Seed, I.M. Idriss, F. Makdisi and N. Banerjee - 1975 (PB 252 635)A03
- EERC 75-30 "FLUSH - A Computer Program for Approximate 3-D Analysis of Soil-Structure Interaction Problems," by J. Lysmer, T. Udaka, C.-F. Tsai and H.B. Seed - 1975 (PB 259 332)A07
- EERC 75-31 "ALUSH - A Computer Program for Seismic Response Analysis of Axisymmetric Soil-Structure Systems," by E. Berger, J. Lysmer and H.B. Seed - 1975
- EERC 75-32 "TRIP and TRAVEL - Computer Programs for Soil-Structure Interaction Analysis with Horizontally Travelling Waves," by T. Udaka, J. Lysmer and H.B. Seed - 1975
- EERC 75-33 "Predicting the Performance of Structures in Regions of High Seismicity," by J. Penzien - 1975 (PB 248 130)A03
- EERC 75-34 "Efficient Finite Element Analysis of Seismic Structure - Soil - Direction," by J. Lysmer, H.B. Seed, T. Udaka, R.N. Hwang and C.-F. Tsai - 1975 (PB 253 570)A03
- EERC 75-35 "The Dynamic Behavior of a First Story Girder of a Three-Story Steel Frame Subjected to Earthquake Loading," by R.W. Clough and L.-Y. Li - 1975 (PB 248 841)A05
- EERC 75-36 "Earthquake Simulator Study of a Steel Frame Structure, Volume II - Analytical Results," by D.T. Tang - 1975 (PB 252 926)A10
- EERC 75-37 "ANSR-I General Purpose Computer Program for Analysis of Non-Linear Structural Response," by D.P. Mondkar and G.H. Powell - 1975 (PB 252 386)A08
- EERC 75-38 "Nonlinear Response Spectra for Probabilistic Seismic Design and Damage Assessment of Reinforced Concrete Structures," by M. Murakami and J. Penzien - 1975 (PB 259 530)A05
- EERC 75-39 "Study of a Method of Feasible Directions for Optimal Elastic Design of Frame Structures Subjected to Earthquake Loading," by N.D. Walker and K.S. Pister - 1975 (PB 257 781)A06
- EERC 75-40 "An Alternative Representation of the Elastic-Viscoelastic Analogy," by G. Dasgupta and J.L. Sackman - 1975 (PB 252 173)A03
- EERC 75-41 "Effect of Multi-Directional Shaking on Liquefaction of Sands," by H.B. Seed, R. Pyke and G.R. Martin - 1975 (PB 258 781)A03
- EERC 76-1 "Strength and Ductility Evaluation of Existing Low-Rise Reinforced Concrete Buildings - Screening Method," by T. Okada and B. Bresler - 1976 (PB 257 906)A11
- EERC 76-2 "Experimental and Analytical Studies on the Hysteretic Behavior of Reinforced Concrete Rectangular and T-Beams," by S.-Y.M. Ma, E.P. Popov and V.V. Bertero - 1976 (PB 260 843)A12
- EERC 76-3 "Dynamic Behavior of a Multistory Triangular-Shaped Building," by J. Petrovski, R.M. Stephen, E. Gartenbaum and J.G. Bouwkamp - 1976 (PB 273 279)A07
- EERC 76-4 "Earthquake Induced Deformations of Earth Dams," by N. Serff, H.B. Seed, F.I. Makdisi & C.-Y. Chang - 1976 (PB 292 065)A08

EERC-6

- EERC 76-5 "Analysis and Design of Tube-Type Tall Building Structures," by H. de Clercq and G.H. Powell - 1976 (PB 252 220)A10
- EERC 76-6 "Time and Frequency Domain Analysis of Three-Dimensional Ground Motions, San Fernando Earthquake," by T. Kubo and J. Penzien (PB 260 556)A11
- EERC 76-7 "Expected Performance of Uniform Building Code Design Masonry Structures," by R.L. Mayes, Y. Omote, S.W. Chen and R.W. Clough - 1976 (PB 270 098)A05
- EERC 76-8 "Cyclic Shear Tests of Masonry Piers, Volume 1 - Test Results," by R.L. Mayes, Y. Omote, R.W. Clough - 1976 (PB 264 424)A06
- EERC 76-9 "A Substructure Method for Earthquake Analysis of Structure - Soil Interaction," by J.A. Gutierrez and A.K. Chopra - 1976 (PB 257 783)A08
- EERC 76-10 "Stabilization of Potentially Liquefiable Sand Deposits using Gravel Drain Systems," by H.B. Seed and J.R. Booker - 1976 (PB 258 820)A04
- EERC 76-11 "Influence of Design and Analysis Assumptions on Computed Inelastic Response of Moderately Tall Frames," by G.H. Powell and D.G. Row - 1976 (PB 271 409)A06
- EERC 76-12 "Sensitivity Analysis for Hysteretic Dynamic Systems: Theory and Applications," by D. Ray, K.S. Pister and E. Polak - 1976 (PB 262 859)A04
- EERC 76-13 "Coupled Lateral Torsional Response of Buildings to Ground Shaking," by C.L. Kan and A.K. Chopra - 1976 (PB 257 907)A09
- EERC 76-14 "Seismic Analyses of the Banco de America," by V.V. Bertero, S.A. Mahin and J.A. Hollings - 1976
- EERC 76-15 "Reinforced Concrete Frame 2: Seismic Testing and Analytical Correlation," by R.W. Clough and J. Gidwani - 1976 (PB 261 323)A08
- EERC 76-16 "Cyclic Shear Tests of Masonry Piers, Volume 2 - Analysis of Test Results," by R.L. Mayes, Y. Omote and R.W. Clough - 1976
- EERC 76-17 "Structural Steel Bracing Systems: Behavior Under Cyclic Loading," by E.P. Popov, K. Takanashi and C.W. Roeder - 1976 (PB 260 715)A05
- EERC 76-18 "Experimental Model Studies on Seismic Response of High Curved Overcrossings," by D. Williams and W.G. Godden - 1976 (PB 269 548)A08
- EERC 76-19 "Effects of Non-Uniform Seismic Disturbances on the Dumbarton Bridge Replacement Structure," by F. Baron and R.E. Hamati - 1976 (PB 282 981)A16
- EERC 76-20 "Investigation of the Inelastic Characteristics of a Single Story Steel Structure Using System Identification and Shaking Table Experiments," by V.C. Matzen and H.D. McNiven - 1976 (PB 258 453)A07
- EERC 76-21 "Capacity of Columns with Splice Imperfections," by E.P. Popov, R.M. Stephen and R. Philbrick - 1976 (PB 260 378)A04
- EERC 76-22 "Response of the Olive View Hospital Main Building during the San Fernando Earthquake," by S. A. Mahin, V.V. Bertero, A.K. Chopra and R. Collins - 1976 (PB 271 425)A14
- EERC 76-23 "A Study on the Major Factors Influencing the Strength of Masonry Prisms," by N.M. Mostaghel, R.L. Mayes, R. W. Clough and S.W. Chen - 1976 (Not published)
- EERC 76-24 "GADFLEA - A Computer Program for the Analysis of Pore Pressure Generation and Dissipation during Cyclic or Earthquake Loading," by J.R. Booker, M.S. Rahman and H.B. Seed - 1976 (PB 263 947)A04
- EERC 76-25 "Seismic Safety Evaluation of a R/C School Building," by B. Bresler and J. Axley - 1976
- EERC 76-26 "Correlative Investigations on Theoretical and Experimental Dynamic Behavior of a Model Bridge Structure," by K. Kawashima and J. Penzien - 1976 (PB 263 388)A11
- EERC 76-27 "Earthquake Response of Coupled Shear Wall Buildings," by T. Srichatrapimuk - 1976 (PB 265 157)A07
- EERC 76-28 "Tensile Capacity of Partial Penetration Welds," by E.P. Popov and R.M. Stephen - 1976 (PB 262 899)A03
- EERC 76-29 "Analysis and Design of Numerical Integration Methods in Structural Dynamics," by H.M. Hilber - 1976 (PB 264 410)A06
- EERC 76-30 "Contribution of a Floor System to the Dynamic Characteristics of Reinforced Concrete Buildings," by L.E. Malik and V.V. Bertero - 1976 (PB 272 247)A13
- EERC 76-31 "The Effects of Seismic Disturbances on the Golden Gate Bridge," by F. Baron, M. Arikan and R.E. Hamati - 1976 (PB 272 279)A09
- EERC 76-32 "Infilled Frames in Earthquake Resistant Construction," by R.E. Klingner and V.V. Bertero - 1976 (PB 265 892)A13

EERC-7

- UCB/EERC-77/01 "PLUSH - A Computer Program for Probabilistic Finite Element Analysis of Seismic Soil-Structure Interaction," by M.P. Romo Organista, J. Lysmer and H.B. Seed - 1977
- UCB/EERC-77/02 "Soil-Structure Interaction Effects at the Humboldt Bay Power Plant in the Ferndale Earthquake of June 7, 1975," by J.E. Valera, H.B. Seed, C.F. Tsai and J. Lysmer - 1977 (PB 265 795)A04
- UCB/EERC-77/03 "Influence of Sample Disturbance on Sand Response to Cyclic Loading," by K. Mori, H.B. Seed and C.K. Chan - 1977 (PB 267 352)A04
- UCB/EERC-77/04 "Seismological Studies of Strong Motion Records," by J. Shoja-Taheri - 1977 (PB 269 655)A10
- UCB/EERC-77/05 "Testing Facility for Coupled-Shear Walls," by L. Li-Hyung, V.V. Bertero and E.P. Popov - 1977
- UCB/EERC-77/06 "Developing Methodologies for Evaluating the Earthquake Safety of Existing Buildings," by No. 1 - B. Bresler; No. 2 - B. Bresler, T. Okada and D. Zisling; No. 3 - T. Okada and B. Bresler; No. 4 - V.V. Bertero and B. Bresler - 1977 (PB 267 354)A08
- UCB/EERC-77/07 "A Literature Survey - Transverse Strength of Masonry Walls," by Y. Omote, R.L. Mayes, S.W. Chen and R.W. Clough - 1977 (PB 277 933)A07
- UCB/EERC-77/08 "DRAIN-TABS: A Computer Program for Inelastic Earthquake Response of Three Dimensional Buildings," by R. Guendelman-Israel and G.H. Powell - 1977 (PB 270 693)A07
- UCB/EERC-77/09 "SUBWALL: A Special Purpose Finite Element Computer Program for Practical Elastic Analysis and Design of Structural Walls with Substructure Option," by D.Q. Le, H. Peterson and E.P. Popov - 1977 (PB 270 567)A05
- UCB/EERC-77/10 "Experimental Evaluation of Seismic Design Methods for Broad Cylindrical Tanks," by D.P. Clough (PB 272 280)A13
- UCB/EERC-77/11 "Earthquake Engineering Research at Berkeley - 1976," - 1977 (PB 273 507)A09
- UCB/EERC-77/12 "Automated Design of Earthquake Resistant Multistory Steel Building Frames," by N.D. Walker, Jr. - 1977 (PB 276 526)A09
- UCB/EERC-77/13 "Concrete Confined by Rectangular Hoops Subjected to Axial Loads," by J. Vallenias, V.V. Bertero and E.P. Popov - 1977 (PB 275 165)A06
- UCB/EERC-77/14 "Seismic Strain Induced in the Ground During Earthquakes," by Y. Sugimura - 1977 (PB 284 201)A04
- UCB/EERC-77/15 "Bond Deterioration under Generalized Loading," by V.V. Bertero, E.P. Popov and S. Viathanatepa - 1977
- UCB/EERC-77/16 "Computer Aided Optimum Design of Ductile Reinforced Concrete Moment Resisting Frames," by S.W. Zagajeski and V.V. Bertero - 1977 (PB 280 137)A07
- UCB/EERC-77/17 "Earthquake Simulation Testing of a Stepping Frame with Energy-Absorbing Devices," by J.M. Kelly and D.F. Tsztoo - 1977 (PB 273 506)A04
- UCB/EERC-77/18 "Inelastic Behavior of Eccentrically Braced Steel Frames under Cyclic Loadings," by C.W. Roeder and E.P. Popov - 1977 (PB 275 526)A15
- UCB/EERC-77/19 "A Simplified Procedure for Estimating Earthquake-Induced Deformations in Dams and Embankments," by F.I. Makdisi and H.B. Seed - 1977 (PB 276 820)A04
- UCB/EERC-77/20 "The Performance of Earth Dams during Earthquakes," by H.B. Seed, F.I. Makdisi and P. de Alba - 1977 (PB 276 821)A04
- UCB/EERC-77/21 "Dynamic Plastic Analysis Using Stress Resultant Finite Element Formulation," by P. Lukunapvasit and J.M. Kelly - 1977 (PB 275 453)A04
- UCB/EERC-77/22 "Preliminary Experimental Study of Seismic Uplift of a Steel Frame," by R.W. Clough and A.A. Huckelbridge - 1977 (PB 278 769)A08
- UCB/EERC-77/23 "Earthquake Simulator Tests of a Nine-Story Steel Frame with Columns Allowed to Uplift," by A.A. Huckelbridge - 1977 (PB 277 944)A09
- UCB/EERC-77/24 "Nonlinear Soil-Structure Interaction of Skew Highway Bridges," by M.-C. Chen and J. Penzien - 1977 (PB 276 176)A07
- UCB/EERC-77/25 "Seismic Analysis of an Offshore Structure Supported on Pile Foundations," by D.D.-N. Liou and J. Penzien - 1977 (PB 283 180)A06
- UCB/EERC-77/26 "Dynamic Stiffness Matrices for Homogeneous Viscoelastic Half-Planes," by G. Dasgupta and A.K. Chopra - 1977 (PB 279 654)A06
- UCB/EERC-77/27 "A Practical Soft Story Earthquake Isolation System," by J.M. Kelly, J.M. Eiding and C.J. Derham - 1977 (PB 276 814)A07
- UCB/EERC-77/28 "Seismic Safety of Existing Buildings and Incentives for Hazard Mitigation in San Francisco: An Exploratory Study," by A.J. Meltsner - 1977 (PB 281 970)A05
- UCB/EERC-77/29 "Dynamic Analysis of Electrohydraulic Shaking Tables," by D. Rea, S. Abedi-Hayati and Y. Takahashi - 1977 (PB 282 569)A04
- UCB/EERC-77/30 "An Approach for Improving Seismic - Resistant Behavior of Reinforced Concrete Interior Joints," by B. Galunic, V.V. Bertero and E.P. Popov - 1977 (PB 290 870)A06

EERC-8

- UCB/EERC-78/01 "The Development of Energy-Absorbing Devices for Aseismic Base Isolation Systems," by J.M. Kelly and D.F. Tsztoo - 1978 (PB 284 978)A04
- UCB/EERC-78/02 "Effect of Tensile Prestrain on the Cyclic Response of Structural Steel Connections, by J.G. Bouwkamp and A. Mukhopadhyay - 1978
- UCB/EERC-78/03 "Experimental Results of an Earthquake Isolation System using Natural Rubber Bearings," by J.M. Eidingcr and J.M. Kelly - 1978 (PB 281 686)A04
- UCB/EERC-78/04 "Seismic Behavior of Tall Liquid Storage Tanks," by A. Niwa - 1978 (PB 284 017)A14
- UCB/EERC-78/05 "Hysteretic Behavior of Reinforced Concrete Columns Subjected to High Axial and Cyclic Shear Forces," by S.W. Zagajeski, V.V. Bertero and J.G. Bouwkamp - 1978 (PB 283 858)A13
- UCB/EERC-78/06 "Inelastic Beam-Column Elements for the ANSR-I Program," by A. Riahi, D.G. Row and G.H. Powell - 1978
- UCB/EERC-78/07 "Studies of Structural Response to Earthquake Ground Motion," by O.A. Lopez and A.K. Chopra - 1978 (PB 282 790)A05
- UCB/EERC-78/08 "A Laboratory Study of the Fluid-Structure Interaction of Submerged Tanks and Caissons in Earthquakes," by R.C. Byrd - 1978 (PB 284 957)A08
- UCB/EERC-78/09 "Model for Evaluating Damageability of Structures," by I. Sakamoto and B. Bresler - 1978
- UCB/EERC-78/10 "Seismic Performance of Nonstructural and Secondary Structural Elements," by I. Sakamoto - 1978
- UCB/EERC-78/11 "Mathematical Modelling of Hysteresis Loops for Reinforced Concrete Columns," by S. Nakata, T. Sproul and J. Penzien - 1978
- UCB/EERC-78/12 "Damageability in Existing Buildings," by T. Blejwas and B. Bresler - 1978
- UCB/EERC-78/13 "Dynamic Behavior of a Pedestal Base Multistory Building," by R.M. Stephen, E.L. Wilson, J.G. Bouwkamp and M. Button - 1978 (PB 286 650)A08
- UCB/EERC-78/14 "Seismic Response of Bridges - Case Studies," by R.A. Imbsen, V. Nutt and J. Penzien - 1978 (PB 286 503)A10
- UCB/EERC-78/15 "A Substructure Technique for Nonlinear Static and Dynamic Analysis," by D.G. Row and G.H. Powell - 1978 (PB 288 077)A10
- UCB/EERC-78/16 "Seismic Risk Studies for San Francisco and for the Greater San Francisco Bay Area," by C.S. Oliveira - 1978
- UCB/EERC-78/17 "Strength of Timber Roof Connections Subjected to Cyclic Loads," by P. Gülkan, R.L. Mayes and R.W. Clough - 1978
- UCB/EERC-78/18 "Response of K-Braced Steel Frame Models to Lateral Loads," by J.G. Bouwkamp, R.M. Stephen and E.P. Popov - 1978
- UCB/EERC-78/19 "Rational Design Methods for Light Equipment in Structures Subjected to Ground Motion," by J.L. Sackman and J.M. Kelly - 1978 (PB 292 357)A04
- UCB/EERC-78/20 "Testing of a Wind Restraint for Aseismic Base Isolation," by J.M. Kelly and D.E. Chitty - 1978 (PB 292 833)A03
- UCB/EERC-78/21 "APOLLO - A Computer Program for the Analysis of Pore Pressure Generation and Dissipation in Horizontal Sand Layers During Cyclic or Earthquake Loading," by P.P. Martin and H.B. Seed - 1978 (PB 292 835)A04
- UCB/EERC-78/22 "Optimal Design of an Earthquake Isolation System," by M.A. Bhatti, K.S. Pister and E. Polak - 1978 (PB 294 735)A06
- UCB/EERC-78/23 "MASH - A Computer Program for the Non-Linear Analysis of Vertically Propagating Shear Waves in Horizontally Layered Deposits," by P.P. Martin and H.B. Seed - 1978 (PB 293 101)A05
- UCB/EERC-78/24 "Investigation of the Elastic Characteristics of a Three Story Steel Frame Using System Identification," by I. Kaya and H.D. McNiven - 1978
- UCB/EERC-78/25 "Investigation of the Nonlinear Characteristics of a Three-Story Steel Frame Using System Identification," by I. Kaya and H.D. McNiven - 1978
- UCB/EERC-78/26 "Studies of Strong Ground Motion in Taiwan," by Y.M. Hsiung, B.A. Bolt and J. Penzien - 1978
- UCB/EERC-78/27 "Cyclic Loading Tests of Masonry Single Piers: Volume 1 - Height to Width Ratio of 2," by P.A. Hidalgo, R.L. Mayes, H.D. McNiven and R.W. Clough - 1978
- UCB/EERC-78/28 "Cyclic Loading Tests of Masonry Single Piers: Volume 2 - Height to Width Ratio of 1," by S.-W.J. Chen, P.A. Hidalgo, R.L. Mayes, R.W. Clough and H.D. McNiven - 1978
- UCB/EERC-78/29 "Analytical Procedures in Soil Dynamics," by J. Lysmer - 1978

EERC-9

- UCB/EERC-79/01 "Hysteretic Behavior of Lightweight Reinforced Concrete Beam-Column Subassemblages," by B. Forzani, E.P. Popov, and V.V. Bertero - 1979
- UCB/EERC-79/02 "The Development of a Mathematical Model to Predict the Flexural Response of Reinforced Concrete Beams to Cyclic Loads, Using System Identification," by J.F. Stanton and H.D. McNiven - 1979
- UCB/EERC-79/03 "Linear and Nonlinear Earthquake Response of Simple Torsionally Coupled Systems," by C.L. Kan and A.K. Chopra - 1979
- UCB/EERC-79/04 "A Mathematical Model of Masonry for Predicting Its Linear Seismic Response Characteristics," by Y. Mengi and H.D. McNiven - 1979
- UCB/EERC-79/05 "Mechanical Behavior of Light Weight Concrete Confined by Different Types of Lateral Reinforcement," by M.A. Manrique and V.V. Bertero - 1979
- UCB/EERC-79/06 "Static Tilt Tests of a Tall Cylindrical Liquid Storage Tank," by R.W. Clough and A. Niwa - 1979
- UCB/EERC-79/07 "The Design of Steel Energy Absorbing Restrainers and Their Incorporation Into Nuclear Power Plants for Enhanced Safety: Volume 1 - Summary Report," by P.N. Spencer, V.F. Zackay, and E.R. Parker - 1979
- UCB/EERC-79/08 "The Design of Steel Energy Absorbing Restrainers and Their Incorporation Into Nuclear Power Plants for Enhanced Safety: Volume 2 - The Development of Analyses for Reactor System Piping," "Simple Systems" by M.C. Lee, J. Penzien, A.K. Chopra, and K. Suzuki "Complex Systems" by G.H. Powell, E.L. Wilson, R.W. Clough and D.G. Row - 1979
- UCB/EERC-79/09 "The Design of Steel Energy Absorbing Restrainers and Their Incorporation Into Nuclear Power Plants for Enhanced Safety: Volume 3 - Evaluation of Commercial Steels," by W.S. Owen, R.M.N. Pelloux, R.O. Ritchie, M. Faral, T. Ohhashi, J. Toplosky, S.J. Hartman, V.F. Zackay, and E.R. Parker - 1979
- UCB/EERC-79/10 "The Design of Steel Energy Absorbing Restrainers and Their Incorporation Into Nuclear Power Plants for Enhanced Safety: Volume 4 - A Review of Energy-Absorbing Devices," by J.M. Kelly and M.S. Skinner - 1979
- UCB/EERC-79/11 "Conservatism In Summation Rules for Closely Spaced Modes," by J.M. Kelly and J.L. Sackman - 1979

EERC-10

- UCB/EERC-79/12 "Cyclic Loading Tests of Masonry Single Piers Volume 3 - Height to Width Ratio of 0.5," by P.A. Hidalgo, R.L. Mayes, H.D. McNiven and R.W. Clough - 1979
- UCB/EERC-79/13 "Cyclic Behavior of Dense Coarse-Grain Materials in Relation to the Seismic Stability of Dams," by N.G. Banerjee, H.B. Seed and C.K. Chan - 1979
- UCB/EERC-79/14 "Seismic Behavior of R/C Interior Beam Column Subassemblages," by S. Viathanatapa, E.P. Popov and V.V. Bertero - 1979
- UCB/EERC-79/15 "Optimal Design of Localized Nonlinear Systems with Dual Performance Criteria Under Earthquake Excitations," by M.A. Bhatti - 1979
- UCB/EERC-79/16 "OPTDYN - A General Purpose Optimization Program for Problems with or without Dynamic Constraints," by M.A. Bhatti, E. Polak and K.S. Pister - 1979
- UCB/EERC-79/17 "ANSR-II, Analysis of Nonlinear Structural Response, Users Manual," by D.P. Mondkar and G.H. Powell - 1979
- UCB/EERC-79/18 "Soil Structure Interaction in Different Seismic Environments," A. Gomez-Masso, J. Lysmer, J.-C. Chen and H.B. Seed - 1979
- UCB/EERC-79/19 "ARMA Models for Earthquake Ground Motions," by M.K. Chang, J.W. Kwiatkowski, R.F. Nau, R.M. Oliver and K.S. Pister - 1979
- UCB/EERC-79/20 "Hysteretic Behavior of Reinforced Concrete Structural Walls," by J.M. Vallenias, V.V. Bertero and E.P. Popov - 1979
- UCB/EERC-79/21 "Studies on High-Frequency Vibrations of Buildings I: The Column Effects," by J. Lubliner - 1979
- UCB/EERC-79/22 "Bond Deterioration of Reinforcing Bars Embedded in Confined Concrete Blocks," by S. Viathanatapa, E.P. Popov and V.V. Bertero - 1979
- UCB/EERC-79/23 "Shaking Table Study of Single-Story Masonry Houses, Volume 1: Test Structures 1 and 2," by P. Gülkan, R.L. Mayes and R.W. Clough - 1979
- UCB/EERC-79/24 "Shaking Table Study of Single-Story Masonry Houses, Volume 2: Test Structures 3 and 4," by P. Gülkan, R.L. Mayes and R.W. Clough - 1979
- UCB/EERC-79/25 "Shaking Table Study of Single-Story Masonry Houses, Volume 3: Summary, Conclusions and Recommendations," by R.W. Clough, P. Gülkan and R.L. Mayes